



Universiteit Gent  
Faculteit Wetenschappen  
Vakgroep Fysica en Sterrenkunde

<sup>2</sup> No title yet

<sup>3</sup> No sub-title neither, obviously...

---

<sup>4</sup> Alexis Fagot

5



Thesis to obtain the degree of  
Doctor of Philosophy in Physics  
Academic years 2012-2017





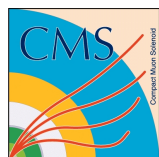


Universiteit Gent  
Faculteit Wetenschappen  
Vakgroep Fysica en Sterrenkunde

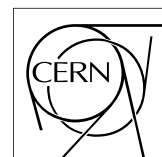
Promotoren: Dr. Michael Tytgat  
Prof. Dr. Dirk Ryckbosch

Universiteit Gent  
Faculteit Wetenschappen  
Vakgroep Fysica en Sterrenkunde  
Proeftuinstraat 86, B-9000 Gent, België  
Tel.: +32 9 264.65.28  
Fax.: +32 9 264.66.97

17



Thesis to obtain the degree of  
Doctor of Philosophy in Physics  
Academic years 2012-2017





## Acknowledgements

<sup>19</sup> Ici on remerciera tous les gens que j'ai pu croiser durant cette aventure et qui m'ont permis de passer  
<sup>20</sup> un bon moment

<sup>21</sup> *Gent, ici la super date de la mort qui tue de la fin d'écriture*  
<sup>22</sup> *Alexis Fagot*



# Table of Contents

23

24	<b>Acknowledgements</b>	i
25	<b>Nederlandse samenvatting</b>	vii
26	<b>English summary</b>	ix
27	<b>1 Introduction</b>	1-1
28	1.1 A story of High Energy Physics . . . . .	1-1
29	1.2 Organisation of this study . . . . .	1-1
30	<b>2 Investigating the TeV scale</b>	2-1
31	2.1 The Standard Model of Particle Physics . . . . .	2-2
32	2.1.1 A history of particle physics . . . . .	2-2
33	2.1.2 Construction and test of the model . . . . .	2-11
34	2.1.3 Investigating the TeV scale . . . . .	2-12
35	2.2 The Large Hadron Collider & the Compact Muon Solenoid . . . . .	2-14
36	2.2.1 LHC, the most powerful particle accelerator . . . . .	2-14
37	2.2.1.1 Particle acceleration . . . . .	2-15
38	2.2.2 CMS, a multipurpose experiment . . . . .	2-18
39	2.2.2.1 The silicon tracker, core of CMS . . . . .	2-20
40	2.2.2.2 The calorimeters, measurement of particle's energy . . . . .	2-20
41	2.2.2.3 The muon system, corner stone of CMS . . . . .	2-22
42	<b>3 Muon Phase-II Upgrade</b>	3-1
43	3.1 High Luminosity LHC and muon system requirements . . . . .	3-2
44	3.2 Necessity for improved electronics . . . . .	3-5
45	3.3 New detectors and increased acceptance . . . . .	3-8
46	3.3.1 Improved forward resistive plate chambers . . . . .	3-9
47	3.3.2 Gas electron multipliers . . . . .	3-12
48	3.3.3 Installation schedule . . . . .	3-19
49	3.4 Implications of the different upgrades on the Level-1 Trigger. Improvement of	
50	physics performance. . . . .	3-20
51	3.5 Ecofriendly gas studies . . . . .	3-24
52	<b>4 Physics of Resistive plate chambers</b>	4-1
53	4.1 Principle . . . . .	4-1
54	4.2 Rate capability and time resolution of Resistive Plate Chambers . . . . .	4-3
55	4.2.1 Operation modes . . . . .	4-3
56	4.2.2 Standard gas mixture for RPCs operated in collider experiments . . . . .	4-5
57	4.2.3 Detector designs and performance . . . . .	4-9
58	4.2.3.1 Double gap RPC . . . . .	4-11

59	4.2.3.2 Multigap RPC (MRPC) . . . . .	4-13
60	4.2.3.3 Charge distribution and performance limitations . . . . .	4-16
61	4.3 Signal formation . . . . .	4-18
62	4.3.1 Energy loss at intermediate energies . . . . .	4-19
63	4.3.2 Primary ionization . . . . .	4-23
64	4.3.3 Development and propagation of avalanches . . . . .	4-26
65	4.3.4 Drift and diffusion of the electron cloud . . . . .	4-30
66	4.3.5 Space charge effect . . . . .	4-32
67	<b>5 Longevity studies and Consolidation of the present CMS RPC subsystem</b>	<b>5-1</b>
68	5.1 Resistive Plate Chambers at CMS . . . . .	5-1
69	5.1.1 Overview . . . . .	5-1
70	5.1.2 The present RPC system . . . . .	5-2
71	5.1.3 Pulse processing of CMS RPCs . . . . .	5-3
72	5.2 Testing detectors under extreme conditions . . . . .	5-4
73	5.2.1 The Gamma Irradiation Facilities . . . . .	5-6
74	5.2.1.1 GIF . . . . .	5-6
75	5.2.1.2 GIF++ . . . . .	5-8
76	5.3 Preliminary tests at GIF . . . . .	5-10
77	5.3.1 Resistive Plate Chamber test setup . . . . .	5-10
78	5.3.2 Data Acquisition . . . . .	5-12
79	5.3.3 Geometrical acceptance of the setup layout to cosmic muons . . . . .	5-12
80	5.3.3.1 Description of the simulation layout . . . . .	5-13
81	5.3.3.2 Simulation procedure . . . . .	5-15
82	5.3.3.3 Results . . . . .	5-16
83	5.3.4 Photon flux at GIF . . . . .	5-16
84	5.3.4.1 Expectations from simulations . . . . .	5-16
85	5.3.4.2 Dose measurements . . . . .	5-21
86	5.3.5 Results and discussions . . . . .	5-22
87	5.4 Longevity tests at GIF++ . . . . .	5-23
88	5.4.1 Description of the Data Acquisition . . . . .	5-26
89	5.4.2 RPC current, environmental and operation parameter monitoring . . . . .	5-27
90	5.4.3 Measurement procedure . . . . .	5-28
91	5.4.4 Longevity studies results . . . . .	5-28
92	<b>6 Investigation on high rate RPCs</b>	<b>6-1</b>
93	6.1 Rate limitations and ageing of RPCs . . . . .	6-1
94	6.1.1 Low resistivity electrodes . . . . .	6-1
95	6.1.2 Low noise front-end electronics . . . . .	6-1
96	6.2 Construction of prototypes . . . . .	6-1
97	6.3 Results and discussions . . . . .	6-1
98	<b>7 Conclusions and outlooks</b>	<b>7-1</b>
99	7.1 Conclusions . . . . .	7-1
100	7.2 Outlooks . . . . .	7-1

---

<b>A A data acquisition software for CAEN VME TDCs</b>	<b>A-1</b>
A.1 GIF++ DAQ file tree . . . . .	A-1
A.2 Usage of the DAQ . . . . .	A-2
A.3 Description of the readout setup . . . . .	A-3
A.4 Data read-out . . . . .	A-3
A.4.1 V1190A TDCs . . . . .	A-4
A.4.2 DataReader . . . . .	A-6
A.4.3 Data quality flag . . . . .	A-10
A.5 Communications . . . . .	A-12
A.5.1 V1718 USB Bridge . . . . .	A-13
A.5.2 Configuration file . . . . .	A-13
A.5.3 WebDCS/DAQ intercommunication . . . . .	A-17
A.5.4 Example of inter-process communication cycle . . . . .	A-18
A.6 Software export . . . . .	A-18
<b>B Details on the offline analysis package</b>	<b>B-1</b>
B.1 GIF++ Offline Analysis file tree . . . . .	B-1
B.2 Usage of the Offline Analysis . . . . .	B-2
B.2.1 Output of the offline tool . . . . .	B-3
B.2.1.1 ROOT file . . . . .	B-3
B.2.1.2 CSV files . . . . .	B-5
B.3 Analysis inputs and information handling . . . . .	B-6
B.3.1 Dimensions file and IniFile parser . . . . .	B-6
B.3.2 TDC to RPC link file and Mapping . . . . .	B-7
B.4 Description of GIF++ setup within the Offline Analysis tool . . . . .	B-9
B.4.1 RPC objects . . . . .	B-9
B.4.2 Trolley objects . . . . .	B-10
B.4.3 Infrastructure object . . . . .	B-11
B.5 Handeling of data . . . . .	B-12
B.5.1 RPC hits . . . . .	B-13
B.5.2 Clusters of hits . . . . .	B-14
B.6 DAQ data Analysis . . . . .	B-15
B.6.1 Determination of the run type . . . . .	B-16
B.6.2 Beam time window calculation for efficiency runs . . . . .	B-17
B.6.3 Data loop and histogram filling . . . . .	B-18
B.6.4 Results calculation . . . . .	B-19
B.6.4.1 Rate normalisation . . . . .	B-19
B.6.4.2 Rate and activity . . . . .	B-21
B.6.4.3 Strip masking tool . . . . .	B-23
B.6.4.4 Output CSV files filling . . . . .	B-25
B.7 Current data Analysis . . . . .	B-29



<sup>141</sup>

<sup>142</sup>

## Nederlandse samenvatting –Summary in Dutch–

<sup>143</sup> Le resume en Neerlandais (j'aurais peut-être pu apprendre la langue juste pour ça...).



## English summary

<sup>145</sup> Le meme résume mais en Anglais (on commencera par la hein!).



# List of Figures

146

147	2.1	Through the gold foil experiment Rutherford could show that most of the mass of atoms was contained in a positively charged nucleus and could then propose a more accurate atomic model than that of Thomson. . . . .	2-3
148	2.2	Figure 2.2a: Meson octet. Figure 2.2b: Baryon octet. Figure 2.2c: Baryon decuplet. . . . .	2-8
149	2.3	The elementary particles of the Standard Model are showed along with their names and properties. Their interactions with the strong, weak and electromagnetic forces have been explicated using color squares. In the left column, the scalar higgs boson is depicted, while the central is focused on the matter particles, the fermions, and the right on the force carriers, the gauge bosons. The role of the Higgs boson in electroweak symmetry breaking is highlighted, and the corresponding way properties of the various particles differ in the (high-energy) symmetric phase (top) and the (low-energy) broken-symmetry phase (bottom) are showed. . . . .	2-11
150	2.4	CERN accelerator complex. . . . .	2-15
151	2.5	Pictures of the different accelerators. From top to bottom: first the LINAC 2 and the <i>Pb</i> source of LINAC 3. Then the Booster and the LEIR. Finally, the PS, the SPS and the LHC. . . . .	2-16
152	2.6	Figure 2.6a: schematics of the LHC cryodipoles. 1: Superconducting Coils, 2: Beam pipe, 3: Heat exchanger Pipe, 4: Helium-II Vessel, 5: Superconducting Bus-bar, 6: Iron Yoke, 7: Non-Magnetic Collars, 8: Vacuum Vessel, 9: Radiation Screen, 10: Thermal Shield, 11: Auxiliary Bus-bar Tube, 12: Instrumentation Feed Throughs, 13: Protection Diode, 14: Quadrupole Bus-bars, 15: Spool Piece Bus-bars. Figure 2.6b: magnetic field and resulting motion force applied on the beam particles. . . . .	2-17
153	2.7	Figure 2.7a: picture of the LHC quadrupoles. Figure 2.7b: magnetic fields and resulting focussing force applied on the beam by 2 consecutive quadrupoles. . . . .	2-18
154	2.8	Picture of the CMS barrel. The red outer layer is the muon system hosted into the red iron return yokes. The calorimeters are the blue cylinder inside in magnet solenoid and the tracker is the inner yellow cylinder built around the beam pipe. . . . .	2-19
155	2.9	View of the CMS apparatus and of its different components. . . . .	2-19
156	2.10	Slice showing CMS sub-detectors and how particles interact with them. . . . .	2-20
157	2.11	CMS tracker. . . . .	2-20
158	2.12	Figure 2.12a: picture of the ECAL. Figure 2.12b: picture of the lead tungstate crystals composing the ECAL. . . . .	2-21
159	2.13	CMS hadron calorimeter barrel. . . . .	2-21
160	2.14	A quadrant of the muon system, showing DTs (yellow), RPCs (blue), and CSCs (green). . . . .	2-22
161	2.15	Figure 2.15a: Barrel wheel with its detector rings and return yokes. Figure 2.15b: CSC endcap disk with the 2 CSC stations. The outer station is made of 10 deg detectors while the inner station is made of 20 deg detectors. Figure 2.15c: RPC endcap disk. The inner station is not equipped and the inner CSC station can be seen. . . . .	2-23
162			
163			
164			
165			
166			
167			
168			
169			
170			
171			
172			
173			
174			
175			
176			
177			
178			
179			
180			
181			
182			
183			
184			
185			

- 186    2.16 Figure 2.16a: Cross section of a DT module showing the two superlayers measur-  
 187    ing the  $\phi$  coordinate, perpendicular to the cross section plane, and the superlayer  
 188    measuring the  $\eta$  coordinate, placed in between the two others with honeycomb and  
 189    parallel to the cross section plane. The DT detector is sandwiched in between 2  
 190    RPCs whose readout strips are perpendicular to the cross section plane, measuring  
 191    the  $\phi$  coordinate. Figure 2.16b: A DT cell is shown together with its electric field.  
 192    The path of a muon through a superlayer is shown. . . . . 2-23
- 193    2.17 Figure 2.17a: cathode strips and anode wire layout of a CSC panel. Figure 2.17b  
 194    avalanche development and charge collection by anode wires and induction on cath-  
 195    ode strips inside of a CSC panel. . . . . 2-24
- 196    2.18 Muon track reconstruction through the 6 panels of a CMS CSC using the infor-  
 197    mation of anode wire groups and cathode strip charge distribution combined with  
 198    comparator bits to decide on which half strip the muon is more likely to have passed. 2-24
- 199    2.19 Double gap layout of CMS RPCs. Muons passing through the gas volumes will cre-  
 200    ate electron-ions pairs by ionising the gas. this ionisation will immediately translate  
 201    into a developing avalanche. . . . . 2-25
- 202    3.1 Detailed timeline projection of for LHC and HL-LHC operation until 2039 show-  
 203    ing the evolution of the instantaneous and integrated luminosity as designed (Fig-  
 204    ure 3.1a) and in the ultimate case where the instantaneous luminosity is increased to  
 205     $7.5 \times 10^{34} \text{ cm}^{-2}\text{s}^{-1}$  (Figure 3.1b) [20, 22]. . . . . 3-2
- 206    3.2 Absorbed dose in the CMS cavern after an integrated luminosity of 3000 fb. Using  
 207    the interaction point as reference, R is the transverse distance from the beamline and  
 208    Z is the distance along the beamline. . . . . 3-3
- 209    3.3 A quadrant of the muon system, showing DTs (yellow), RPCs (blue), and CSCs  
 210    (green). The locations of new forward muon detectors for Phase-II are contained  
 211    within the dashed box and indicated in red for GEM stations (ME0, GE1/1, and  
 212    GE2/1) and dark blue for improved RPC (iRPC) stations (RE3/1 and RE4/1). . . . . 3-4
- 213    3.4 Figure 3.4a: Extrapolated fraction of failing channels of the present DT MiC1 elec-  
 214    tronics as a function of the integrated luminosity for different scenari until LS4. Fig-  
 215    ure 3.4b: Comparison of the current (left) and upgraded (right) DT data processing.  
 216    So far, the data is sent to service cavern of CMS facility via copper-to-optical-fiber  
 217    translators (CuOF) by each MiC1. There, data including RPCs and outer hadron  
 218    calorimeter is combined into trigger primitives (TPG) and transmitted by the Twin-  
 219    Mux system to CMS Track Finder. The time-to-digital converter (TDC) data is col-  
 220    lected and sent to the CMS data acquisition system (DAQ) by the micro read-out  
 221    server ( $\mu$ ROS). After the upgrade, the TDC data will be sent via optical links to  
 222    a patch panel inside the experimental cavern by each MiC2, and transferred to the  
 223    back-end, where triggering and event building will be performed. . . . . 3-6
- 224    3.5 Figure 3.5a: The event loss fractions as a function of the instantaneous luminosity is  
 225    compared for CFEBs (Phase-1) and DCFEBs (Phase-II) at different CSC locations.  
 226    HL-LHC luminosity is marked with the dashed brown line. Figure 3.5b: Comparison  
 227    of the current (left) and upgraded (right) CSC data processing. A part of the con-  
 228    nections in between ALCTs and DCFEBs, and the trigger mother boards (TMBs)  
 229    and data acquisition mother boards (DMBs) will be upgraded toward optical data  
 230    transfer. The detector dependent units (DDUs) used as interface in between CSCs'  
 231    front-end electronics and the CMS DAQ will be replaced by new FED boards. . . . . 3-7
- 232    3.6 Comparison of the simulated time residuals in between reconstructed and true muon  
 233    times without (blue) and with (red) the upgraded RPC link system. . . . . 3-8

234	3.7	RMS of the multiple scattering displacement as a function of muon $p_T$ for the proposed forward muon stations. All of the electromagnetic processes such as bremsstrahlung and magnetic field effect are included in the simulation. . . . .	3-9
235			
236			
237	3.8	Simulation of the impact of RPC hit inclusion onto the local trigger primitive efficiency in station 3 (left) and station 4 (right). The contribution of iRPC starts above $ \eta  = 1.8$ . . . . .	3-9
238			
239			
240	3.9	Expected hit rate due to neutrons, photons, electrons and positrons at HL-HLC instantaneous luminosity of $5 \times 10^{34} \text{ cm}^{-2}\text{s}^{-1}$ in RE3/1 and RE4/1 chambers. The sensitivities of iRPCs used in the simulation for each particle are reported and differ from one endcap disk to another as the energies of the considered particles varies with the increasing distance from the interaction point. . . . .	3-10
241			
242			
243			
244			
245	3.10	Measured average charge per avalanche as a function of the effective electric field for different gas gap thickness in double gap RPCs using HPL electrodes. . . . .	3-11
246			
247	3.11	The PETIROC time jitter as a function of the input signal amplitude, measured with and without internal clocks. . . . .	3-12
248			
249	3.12	Schematics of a GEM showing the cathode on top, the GEM foil separating the gas volume into the drift region, in between the cathode and foil, and the induction region, in between the GEM foil and the anode, and the anode on which a 2D readout is installed. A negative voltage is applied on the cathode while the anode is connected to the ground. . . . .	3-13
250			
251			
252			
253			
254	3.13	Left: Picture of a CMS GEM foil provided by a scanning electron microscope. Right: Representation of the electric field lines in a GEM hole and of the amplification that electrons and ions undergo in the hole's volume due to the very intense electric field. . . . .	3-14
255			
256			
257	3.14	Schematic representation of CMS triple GEMs. The gas volume is divided into 4 areas. The drift area is the region where the primary electrons are created before being amplified a first time while passing through the first GEM foil. Then the process of drift and amplification is repeated twice in following two transfer areas and GEM foils. Finally, the charges have been amplified enough to induce current in the read-out strips while in the last drift area. The dimensions, potentials and electric fields are provided. . . . .	3-14
258			
259			
260			
261			
262			
263			
264	3.15	Simulated efficiency and rate of the standalone Level-1 muon trigger using tracks reconstructed in CSCs and all GEM stations compared with Phase-I values in the case where only CSCs are used or CSCs+GE1/1. The zones of inefficiency of the CSC subsystem are compensated by the addition of GEMs during Phase-II and the trigger rates is kept from increasing due to the high luminosity. . . . .	3-15
265			
266			
267			
268			
269	3.16	Figure 3.16a: Simulated resolution of the muon direction measurement $\Delta\phi$ with Phase-II conditions. In the second endcap station, the resolution is compared in the case of CSCs (ME2/1) alone and CSCs+GEMs (GE2/1+ME2/1) while a similar resolution measurement is given in the case of the first station (GE1/1+ME1/1). Figure 3.16b: The addition of GEM detectors on stations 1 and 2 (ME0 is considered to contribute to station station 1) as redundant system to CSCs allows to improve the muon momentum improvement through a more accurate measurement of the local bending angles $\phi_1$ and $\phi_2$ . . . . .	3-16
270			
271			
272			
273			
274			
275			
276			
277	3.17	Schematics of the data communication chain for DAQ of the GEM subsystems. The sending of trigger data via optical links to the CSC OTMBs is only done for GE1/1 and GE2/1 to match the data with ME1/1 and ME2/1. . . . .	3-16
278			
279			

280 3.18 Figure 3.18a: Energy spectrum of GIF++  $^{137}Cs$  source as measured by the GE1/1  
 281 detector installed in GIF++. Figure 3.18b: Evolution of the normalized gain of the  
 282 GE1/1 detector installed at in GIF++ as a function of the integrated charge per unit  
 283 area. The first part of the study, up to a charge of  $55\text{ mC/cm}^2$  had been done in the  
 284 former Gamma Irradiation Facility (GIF) that has now been dismantled following  
 285 the construction of GIF++. No variation of the normalized gain can be observed  
 286 after an accumulation of  $110\text{ mC/cm}^2$  . . . . . 3-17

287 3.19 Figure 3.19a: Comparison of the gas gain as a function of the divider voltage before  
 288 and after the irradiation of a triple-GEM by neutrons in CHARM. Figure 3.19b:  
 289 Comparison of the gas gain as a function of the divider voltage before and after the  
 290 irradiation of a triple-GEM by alpha particles. . . . . 3-18

291 3.20 Data flow of the Level-1 Trigger during Phase-II operations. . . . . 3-20

292 3.21 Comparison of Phase-II DT trigger primitives algorithmic efficiency for segments  
 293 obtained with 2 super-layers (quality  $\geq 6/8$ ) and 1 super-layer only (quality = 4/4).  
 294 The simulation was done by generating  $2 \times 10^6$  muons. The candidate tracks with  
 295 correct time identification is showed with open symbols. . . . . 3-21

296 3.22 Simulated spatial (3.22a) and angular (3.22b) resolution of the algorithm using 8  
 297 aligned hits in both super-layers (quality = 8/8) and 4 aligned hits in only one super-  
 298 layer (quality = 4/4). The contribution of intermediate quality tracks (6 aligned hits)  
 299 is negligible in the angular range shown. [Be careful to update this caption as it  
 300 uses a text to close to the published one.] . . . . . 3-21

301 3.23 Efficiency of the L1 trigger in the endcap region after Phase-II upgrade in the case  
 302 CSC/GEM/RPC hits are requested in at least 2 stations out of four (3.23a) and in all  
 303 four stations (3.23b). . . . . 3-22

304 3.24 Resolution of the LCT ambiguous events thanks to the combination of CSC and  
 305 iRPC readout data. Using CSCs only, 2 pairs of hits are possible. . . . . 3-23

306 3.25 The angular resolution on reconstructed muon tracks in the GEM overlap region  
 307  $2.0 < |\eta| < 2.15$  is compared for Phase-II conditions in the case CSC are alone  
 308 (Figure 3.25a) and in the case the GEMs' data, including ME0, is combined to which  
 309 of CSCs (Figure 3.25b). . . . . 3-23

310 3.26 Comparison of L1 trigger performances for prompt muons with and without the  
 311 addition of GEMs in the region  $2.1 < |\eta| < 2.4$  at Phase-II conditions. GEMs would  
 312 allow a reduction of the trigger accept rate by an order of magnitude (Figure 3.26a)  
 313 while increasing the trigger efficiency (Figure 3.26b). . . . . 3-24

314 3.27 The efficiency (solid lines) and streamer probability (dashed lines) of  $HFO/CO_2$   
 315 (Figure 3.27a) and  $CF_3I/CO_2$  (Figure 3.27b) based gas mixtures as a function of  
 316 the effective high-voltage are compared with the present CMS RPC gas mixture  
 317 represented in black. The detector used for the study is a single gap RPC with similar  
 318 properties than CMS RPCs. The streamer probability is defined as the proportion of  
 319 events with a deposited charge greater than  $20\text{ pC}$ . . . . . 3-25

320 4.1 Different phases of the avalanche development in the RPC gas volume subjected to  
 321 a constant electric field  $E_0$ . a) An avalanche is initiated by the primary ionisation  
 322 caused by the passage of a charged particle through the gas volume. b) Due to  
 323 its growing size, the avalanche starts to locally influence the electric field. c) The  
 324 electrons, lighter than the cations reach the anode first. d) The ions reach the cathode.  
 325 While the charges have not recombined, the electric field in the small region around  
 326 the avalanche stays affected and locally blinds the detector. . . . . 4-2

- 327        4.2 Movement of the charge carriers in an RPC. Figure 4.2a: Voltage across an RPC  
 328        whose electrode have a relative permittivity of 5 at the moment the tension s applied.  
 329        Figure 4.2b: After the charge carriers moved, the electrodes are charged and there  
 330        is no voltage drop over the electrodes anymore. The full potential is applied on the  
 331        gas gap only. Figure 4.2c: The streamer discharge initiated by a charged particle  
 332        transports electrons and cations towards the anode and cathode respectively. . . . . 4-4
- 333        4.3 Typical oscilloscope pulses in streamer mode (Figure 4.3a) and avalanche mode(Figure 4.3b).  
 334        In the case of streamer mode, the very small avalanche signal is visible. . . . . 4-4
- 335        4.4 Rate capability comparison for the streamer and avalanche mode of operation. An  
 336        order of magnitude in rate capability for a maximal efficiency drop of 10% is gained  
 337        by using the avalanche mode over the streamer mode. . . . . 4-5
- 338        4.5 Comparison of the charge distribution of signals induced by cosmic muons in an  
 339        RPC operated with a gas mixture of argon, butane and bromotrifluoromethane ( $CF_3Br$ ).  
 340        The  $Ar/C_4H_{10}$  is kept constant at 60/40 in volume while the total amount of  $CF_3Br$   
 341        in the mixture is varied: 0% (Figure 4.5a), 4% (Figure 4.5b) and 8% (Figure 4.5c) [39]. 4-6
- 342        4.6 Comparison of the efficiency and streamer probability, defined as the fraction of  
 343        events with an induced charge 10 times larger than that of the average avalanche,  
 344        with and without irradiation by a 24 GBq  $^{137}Cs$  source of an RPC successively  
 345        operated with a 90/10 mixture  $C_2H_2F_4/i-C_4H_{10}$  (Figure 4.6a) and a 70/5/10/15  
 346        mixture of  $Ar/i-C_4H_{10}/CO_2/C_2H_2F_4$  (Figure 4.6b) [40]. . . . . 4-6
- 347        4.7 Comparison of the fast charge ratio with and without irradiation by a 24 GBq  $^{137}Cs$   
 348        source of an RPC successively operated with a 90/10 mixture  $C_2H_2F_4/i-C_4H_{10}$   
 349        (Figure 4.7a) and a 70/5/10/15 mixture of  $Ar/i-C_4H_{10}/CO_2/C_2H_2F_4$  (Figure 4.7b).  
 350        The results are provided for both single gap and double gap operation [40]. . . . . 4-7
- 351        4.8 Efficiency (circles and stars with 30 mV and 100 mV thresholds respectively) and  
 352        streamer probability (opened circles) as function of the operating voltatge of a 2 mm  
 353        single gap HPL RPC flushed with a gas mixture containing (a) 5%, (b) 2%, (c) 1%  
 354        and (d) no  $SF_6$  [42]. . . . . 4-8
- 355        4.9 Evolution of the efficiency, working voltage, and voltage at 50% of maximum ef-  
 356        ficiency for CMS Barrel (Figure 4.9a) and Endcap (Figure 4.9b) RPCs obtained  
 357        through yearly voltage scans since 2011. The working voltage of each RPC is up-  
 358        dated after each voltage scan to ensure optimal operation [57]. . . . . 4-9
- 359        4.10 Comparison of the rate capability of 8 mm and 2 mm wide RPCs. The lines are  
 360        linear fits on the data [59]. . . . . 4-10
- 361        4.11 Distributions of the induced charge of fast signals on 2 mm (Figure 4.11a) and 8 mm  
 362        (Figure 4.11b) RPCs exposed to a radiation rate of 100 Hz/cm<sup>2</sup>. Average induced  
 363        charge of fast signals as a function of the high voltage applied on 2 mm and 8 mm  
 364        RPCs (Figure 4.11c). In the case of the 2 mm RPC, a saturation of the pre-amplifier  
 365        was observed. The average of the distribution is underestimated and the median is  
 366        showed together with the average to account for this bias [59]. . . . . 4-10
- 367        4.12 Time distributions of the leading, trailing, and average of both leading and traling  
 368        edges for 2 mm (top row) and 8 mm (bottom row) RPCs exposed to a 100 Hz/cm<sup>2</sup>  
 369        radiation rate. The data was collected with RPCs operated at the voltage correspond-  
 370        ing to the knee of the efficiency distribution, defined as the point where 95% of the  
 371        maximum efficiency is obtained [59]. . . . . 4-11

- 372     4.13 Possible double-gap RPC layouts: a) "standard" 1D double-gap RPC, as used in  
 373       CMS experiment, where the anodes are facing each other and a 1D read-out plane  
 374       is sandwiched in between them, b) double read-out double-gap RPC as used in AT-  
 375       LAS experiment, where the cathodes are facing each other and 2 read-out planes are  
 376       used on the outer surfaces. This last layout can offer the possibility to use a 2D  
 377       reconstruction by using orthogonal read-out planes. . . . . 4-12
- 378     4.14 Comparison of performance of CMS double and single gap RPCs using cosmic  
 379       muons [55]. Figure 4.14a: Comparison of efficiency sigmoids. Figure 4.14b: Volt-  
 380       age distribution at 95% of maximum efficiency. Figure 4.14c:  $\Delta_{10\%}^{90\%}$  distribution. . . 4-12
- 381     4.15 Representation of different RPC layouts (wide gap on Figure (a), double gap on  
 382       Figure (b) and multigap on Figure (c)), of the corresponding sensitive volume in  
 383       gray, and of the associated avalanche size [45]. . . . . 4-13
- 384     4.16 Time distributions of the leading, trailing, and average of both leading and trailing  
 385       edges for multigap RPCs consisting in two 4 mm (Figure 4.16a) and four 2 mm  
 386       (Figure 4.16b) exposed to a 100 Hz/cm<sup>2</sup> radiation rate. The data was collected with  
 387       RPCs operated at the voltage corresponding to the knee of the efficiency distribution,  
 388       defined as the point where 95% of the maximum efficiency is obtained [45]. . . . . 4-14
- 389     4.17 Presentation of a study of a possible ALICE MRPC cell using 250  $\mu\text{m}$  gas gaps,  
 390       620  $\mu\text{m}$  outer glass electrodes, and 550  $\mu\text{m}$  inner floating electrodes (Figure 4.17a),  
 391       and of its time resolution performance as a function of the applied high voltage for  
 392       different radiation levels referred through different filter settings of the 740 GBq  
<sup>137</sup>Cs source the former CERN GIF facility [60]. . . . . 4-14
- 394     4.18 Particle identification applied to electrons in the STAR experiment. The identifica-  
 395       tion is performed combining ToF and  $dE/dx$  measurements [65]. . . . . 4-15
- 396     4.19 Comparison of the detector performance of ALICE ToF MRPC [66] at fixed applied  
 397       voltage (in blue) and at fixed effective voltage (in red). The effective voltage is kept  
 398       fixed by increasing the applied voltage accordingly to the current drawn by the detector. 4-16
- 399     4.20 Ratio between total induced and drifting charge have been simulated for single gap,  
 400       double-gap and multigap layouts [67]. The total induced charge for a double-gap  
 401       RPC is a factor 2 higher than for a multigap. . . . . 4-17
- 402     4.21 Charge spectra have been simulated for single gap, double-gap and multigap lay-  
 403       outs [67]. It appears that when single gap shows a decreasing spectrum, double and  
 404       multigap layouts exhibit a spectrum whose peak is detached from the origin. The  
 405       detachment gets stronger as the number of gaps increases. . . . . 4-17
- 406     4.22 The maximal theoretical efficiency is simulated for single gap, double-gap and multi-  
 407       gap layouts [67] at a constant gap thickness of 2 mm and using an effective Townsend  
 408       coefficient of 9 mm<sup>-1</sup>. . . . . 4-18
- 409     4.23 Mass stopping power as a function of  $\beta\gamma = p/Mc$  for positive muons in copper [68].  
 410       The total stopping power is indicated with solid line and local components with  
 411       dashed lines. the vertical bands are used to indicate boundaries between different  
 412       approximations used at different energy range. . . . . 4-18
- 413     4.24 Mean mass stopping power for liquid hydrogen, as used in bubble chambers, gaseous  
 414       helium, carbon, aluminum, iron, tin, and lead without the inclusion of radiative effect  
 415       at higher  $\beta\gamma$  necessary for pions and muons in denser materials [68]. . . . . 4-20
- 416     4.25 Mean excitation energies normalized to the atomic number as adopted by the ICRU [68,  
 417       72, 73]. . . . . 4-21
- 418     4.26 Mean mass stopping power at minimum ionization as a function of the atomic num-  
 419       ber [68]. . . . . 4-21

420	4.27 Example of straggling function $f(\Delta)$ of particles passing through 1.2 cm of Argon 421 gas with a $\beta\gamma$ of 3.6 and represented with a solid line. The original Landau distribu- 422 tion is showed with a dashed line [74]. . . . .	4-22
423	4.28 Evolution of straggling functions $f(\Delta)$ of particles passing through a volume of 424 Argon gas with a $\beta\gamma$ of 3.6 with increasing thickness $x$ [74]. . . . .	4-22
425	4.29 Photo-absorption cross section as computed by HEED for nobles gases with different 426 electric shell numbers [70]. . . . .	4-24
427	4.30 Photo-absorption cross section as computed by HEED for typical RPC gas mix- 428 tures [70]. The RPC mixture with $CO_2$ corresponds to the mixture used by CALICE 429 SDHCAL [78] while the other one was foreseen for the experimenter ATLAS [79] but 430 has been changed since then. . . . .	4-24
431	4.31 Distributions of number of electrons (left) and energy loss (right) for a 5 GeV/c 432 muon passing through 1.2 mm of Helium (Figure 4.31a), Argon (Figure 4.31b) or a 433 typical RPC gas mixture (Figure 4.31c) [70]. . . . .	4-25
434	4.32 Figure 4.32a: Mean cluster density for muons through different gas volumes [70]. 435 Figure 4.32b: Distribution of the number of electrons per cluster for a 5 GeV/c 436 muon traveling through a mixture of 96.7% $C_2H_2F_4$ , 3% i- $C_4H_{10}$ and 0.3% $SF_6$ [70, 437 79]. . . . .	4-26
438	4.33 Townsend and attachment coefficient for a typical 96.7/3/0.3 mixture of $C_2H_2F_4$ /i- 439 $C_4H_{10}$ / $SF_6$ , at a temperature $T = 296.15$ K and a pressure $P = 1013$ hPa [70, 79]. . . . .	4-27
440	4.34 Comparison of the distribution law of Furry and the Poisson law for $\bar{n} = 5$ [82]. . . . .	4-28
441	4.35 Single-electron avalanche size distribution in a proportionnal counter filled with 442 methylal at different $E/p$ values. (a) 70, (b) 76.5, (c) 105, (d) 186.5, (e) 426V/cm torr [83].	4-28
443	4.36 Figure 4.36a: Comparison of avalanche size distributions for different values of 444 Townsend and attachment coefficients. The effective Townsend coefficient is the 445 same for both distributions. Figure 4.36b: Fluctuation in avalanche size for avalanche 446 started by a single electron with $\alpha = 13$ mm $^{-1}$ and $\eta = 3.5$ mm $^{-1}$ [79]. . . . .	4-30
447	4.37 Figure 4.37a: Electron mean drift velocity $v_D$ in pure $C_2H_2F_4$ and typical RPC 448 gas mixtures. Figure 4.37b: Transverse diffusion coefficient in pure $C_2H_2F_4$ and a 449 typical RPC gas mixture. Figure 4.37c: Longitudinal diffusion coefficient in pure 450 $C_2H_2F_4$ and a typical RPC gas mixture. All results are given with a pressure $P =$ 451 760 Torr and a temperature $T = 296.15$ K [70]. . . . .	4-31
452	4.38 Comparison of the free charge carriers in the gas after a time $t = 7.90$ ns in the case 453 where no diffusion is taken into account to simulate the avalanche (Figure 4.38a) 454 and in the case where the diffusion is implemented (Figure 4.38b) [70]. . . . .	4-31
455	4.39 Schematic representation of an avalanche and of the electric field deformation it 456 causes due to the local concentration of charge carriers [51]. . . . .	4-33
457	4.40 Evolution of the charge induced by an avalanche started by a single electron in a 458 1.2 mm thick RPC with an applied electric field of 54 kV/cm in the case space 459 charge is not taken into account (Figure 4.40a) and in the case it is implemented into 460 the simulation (Figure 4.40b). The total induced charge is correlated to the size of 461 the avalanche [70]. . . . .	4-34
462	4.41 Distributions of charge carriers within the gas volume of a 1.2 mm thick RPC and 463 the corresponding deformation of the electric field at different time steps with an 464 applied electric field of 55.5 kV/cm [70]. . . . .	4-35
465	5.1 Signals from the RPC strips are shaped by the FEE described on Figure 5.1a. Out- 466 put LVDS signals are then read-out by a TDC module connected to a computer or 467 converted into NIM and sent to scalers. Figure 5.1b describes how these converted 468 signals are put in coincidence with the trigger. . . . .	5-3

469	5.2 Description of the principle of a CFD. A comparison of threshold triggering (left)	
470	and constant fraction triggering (right) is shown in Figure 5.2a. Constant fraction	
471	triggering is obtained thanks to zero-crossing technique as explained in Figure 5.2b.	
472	The signal arriving at the input of the CFD is split into three components. A first	
473	one is delayed and connected to the inverting input of a first comparator. A sec-	
474	ond component is connected to the noninverting input of this first comparator. A	
475	third component is connected to the noninverting input of another comparator along	
476	with a threshold value connected to the inverting input. Finally, the output of both	
477	comparators is fed through an AND gate. . . . .	5-4
478	5.3 Figure 5.3a: The integrated charge per region (Barrel, Endcap) is extrapolated to	
479	HL-LHC integrated luminosity ( $3000 \text{ fb}^{-1}$ ) using the data accumulated in 2016 in	
480	every HV channels. Figure 5.3b: The hit rate per region (Barrel, Endcap) is linearly	
481	extrapolated to HL-LHC highest instantaneous luminosity ( $5 \times 10^{34} \text{ cm}^{-2}\text{s}^{-1}$ ) using	
482	the rate as a function of instantaneous luminosity recorded by RPCs in 2017 showing	
483	a linear dependence. . . . .	5-5
484	5.4 Background Fluka simulation compared to 2016 Data at $L = 10^{34} \text{ cm}^{-2}\text{s}^{-1}$ in	
485	the fourth endcap disk region. A mismatch in between simulation and data can be	
486	observed. [To be understood.] . . . . .	5-6
487	5.5 Layout of the test beam zone called X5c GIF at CERN. Photons from the radioactive	
488	source produce a sustained high rate of random hits over the whole area. The zone is	
489	surrounded by 8 m high and 80 cm thick concrete walls. Access is possible through	
490	three entry points. Two access doors for personnel and one large gate for material.	
491	A crane allows installation of heavy equipment in the area. . . . .	5-7
492	5.6 $^{137}\text{Cs}$ decays by $\beta^-$ emission to the ground state of $^{137}\text{Ba}$ (BR = 5.64%) and via the	
493	662 keV isomeric level of $^{137}\text{Ba}$ (BR = 94.36%) whose half-life is 2.55 min. . . . .	5-8
494	5.7 Floor plan of the GIF++ facility. When the facility downstream of the GIF++ takes	
495	electron beam, a beam pipe is installed along the beam line (z-axis). The irradiator	
496	can be displaced laterally (its center moves from $x = 0.65 \text{ m}$ to $2.15 \text{ m}$ ), to increase	
497	the distance to the beam pipe. . . . .	5-8
498	5.8 Simulated unattenuated current of photons in the xz plane (Figure 5.8a) and yz plane	
499	(Figure 5.8b) through the source at $x = 0.65 \text{ m}$ and $y = 0 \text{ m}$ . With angular correction	
500	filters, the current of 662 keV photons is made uniform in xy planes. . . . .	5-9
501	5.9 Description of the RPC setup. Dimensions are given in mm. A tent containing RPCs	
502	is placed at 1720 mm from the source container. The source is situated in the center	
503	of the container. RE-4-2-BARC-161 chamber is 160 mm inside the tent. This way,	
504	the distance between the source and the chambers plan is 2060 mm. Figure 5.9a	
505	provides a side view of the setup in the xz plane while Figure 5.9b shows a top view	
506	in the yz plane. . . . .	5-10
507	5.10 RE-4-2-BARC-161 chamber is inside the tent as described in Figure 5.9. In the top	
508	right, the two scintillators used as trigger can be seen. This trigger system has an	
509	inclination of $10^\circ$ relative to horizontal and is placed above half-partition B2 of the	
510	RPCs. PMT electronics are shielded thanks to lead blocks placed in order to protect	
511	them without stopping photons from going through the scintillators and the chamber. . . . .	5-11

512	5.11 Hit distributions over all 3 partitions of RE-4-2-BARC-161 chamber is showed on these plots. Top, middle and bottom figures respectively correspond to partitions A, B, and C. These plots show that some events still occur in other half-partitions than B2, which corresponds to strips 49 to 64, in front of which the trigger is placed, contributing to the inefficiency of detection of cosmic muons. In the case of partitions A and C, the very low amount of data can be interpreted as noise. On the other hand, it is clear that a little portion of muons reach the half-partition B1, corresponding to strips 33 to 48. . . . .	5-12
520	5.12 Results are derived from data taken on half-partition B2 only. On the 18 <sup>th</sup> of June 2014, data has been taken on chamber RE-2-BARC-161 at building 904 (Prevessin Site) with cosmic muons providing us a reference efficiency plateau of $(97.54 \pm 0.15)\%$ represented by a black curve. A similar measurement has been done at GIF on the 21 <sup>st</sup> of July with the same chamber giving a plateau of $(78.52 \pm 0.94)\%$ represented by a red curve. . . . .	5-13
526	5.13 Representation of the layout used for the simulations of the test setup. The RPC is represented as a yellow trapezoid while the two scintillators as blue cuboids looking at the sky. A green plane corresponds to the muon generation plane within the simulation. Figure 5.9a shows a global view of the simulated setup. Figure 5.9b shows a zommed view that allows to see the 2 scintillators as well as the full RPC plane. . . . .	5-14
531	5.14 $\gamma$ flux $F(D)$ is plot using values from table 5.1. As expected, the plot shows similar attenuation behaviours with increasing distance for each absorption factors. . . . .	5-17
533	5.15 Figure 5.15a shows the linear approximation fit done via formulae 5.7 on data from table 5.2. Figure 5.15b shows a comparison of this model with the simulated flux using a and b given in figure 5.15a in formulae 5.4 and the reference value $D_0 = 50\text{cm}$ and the associated flux for each absorption factor $F_0^{ABS}$ from table 5.1 . . . . .	5-19
537	5.16 Dose measurements has been done in a plane corresponding to the tents front side. This plan is 1900 mm away from the source. As explained in the first chapter, a lens-shaped lead filter provides a uniform photon flux in the vertical plan orthogonal to the beam direction. If the second line of measured fluxes is not taken into account because of lower values due to experimental equipments in the way between the source and the tent, the uniformity of the flux is well showed by the results. . . . .	5-21
543	5.17 . . . . .	5-22
544	5.18 Evolution of the maximum efficiency for RE2 (5.18a) and RE4 (5.18b) chambers with increasing extrapolated $\gamma$ rate per unit area at working point. Both irradiated (blue) and non irradiated (red) chambers are shown. . . . .	5-24
547	5.19 Evolution of the working point for RE2 (5.19a) and RE4 (5.19b) with increasing extrapolated $\gamma$ rate per unit area at working point. Both irradiated (blue) and non irradiated (red) chambers are shown. . . . .	5-24
550	5.20 Evolution of the maximum efficiency at HL-LHC conditions, i.e. a background hit rate per unit area of 300 Hz/cm <sup>2</sup> , with increasing integrated charge for RE2 (5.20a) and RE4 (5.20b) detectors. Both irradiated (blue) and non irradiated (red) chambers are shown. The integrated charge for non irradiated detectors is recorded during test beam periods and stays small with respect to the charge accumulated in irradiated chambers. . . . .	5-25
556	5.21 Comparison of the efficiency sigmoid before (triangles) and after (circles) irradiation for RE2 (5.21a) and RE4 (5.21b) detectors. Both irradiated (blue) and non irradiated (red) chambers are shown. . . . .	5-25
559	5.22 Evolution of the Bakelite resistivity for RE2 (5.22a) and RE4 (5.22b) detectors. Both irradiated (blue) and non irradiated (red) chambers are shown. . . . .	5-26

561	5.23 Evolution of the noise rate per unit area for the irradiated chamber RE2-2-BARC-9 only. . . . .	5-26
562		
563	A.1 (A.1a) View of the front panel of a V1190A TDC module [89]. (A.1b) View of the 564 front panel of a V1718 Bridge module [90]. (A.1c) View of the front panel of a 6U 565 6021 VME crate [91]. . . . .	A-3
566	A.2 Module V1190A <i>Trigger Matching Mode</i> timing diagram [89]. . . . .	A-4
567	A.3 Structure of the ROOT output file generated by the DAQ. The 5 branches ( <code>EventNumber</code> , 568 <code>number_of_hits</code> , <code>Quality_flag</code> , <code>TDC_channel</code> and <code>TDC_TimeStamp</code> ) are visible on 569 the left panel of the ROOT browser. On the right panel is visible the histogram cor- 570 responding to the variable <code>nHits</code> . In this specific example, there were approximately 571 50k events recorded to measure the gamma irradiation rate on the detectors. Each 572 event is stored as a single entry in the <code>TTree</code> . . . . .	A-10
573	A.4 The effect of the quality flag is explained by presenting the content of <code>TBranch</code> 574 <code>number_of_hits</code> of a data file without <code>Quality_flag</code> in Figure A.4a and the con- 575 tent of the same <code>TBranch</code> for data corresponding to a <code>Quality_flag</code> where all TDCs 576 were labelled as <code>GOOD</code> in Figure A.4b taken with similar conditions. It can be noted 577 that the number of entries in Figure A.4b is slightly lower then in Figure A.4a due 578 to the excluded events. . . . .	A-12
579	A.5 Using the same data as previously showed in Figure A.4, the effect of the quality 580 flag is explained by presenting the reconstructed hit multiplicity of a data file with- 581 out <code>Quality_flag</code> in Figure A.5a and the reconstructed content of the same RPC 582 partition for data corresponding to a <code>Quality_flag</code> where all TDCs were labelled as 583 <code>GOOD</code> in Figure A.5b taken with similar conditions. The artificial high content of bin 584 0 is completely suppressed. . . . .	A-12
585	A.6 WebDCS DAQ scan page. On this page, shifters need to choose the type of scan 586 (Rate, Efficiency or Noise Reference scan), the gamma source configuration at the 587 moment of data taking, the beam configuration, and the trigger mode. These in- 588 formation will be stored in the DAQ ROOT output. Are also given the minimal 589 measurement time and waiting time after ramping up of the detectors is over before 590 starting the data acquisition. Then, the list of HV points to scan and the number of 591 triggers for each run of the scan are given in the table underneath. . . . .	A-14
592	B.1 Example of expected hit time distributions in the cases of efficiency (Figure B.1a) 593 and noise/gamma rate per unit area (Figure B.1b) measurements as extracted from 594 the raw ROOT files. The unit along the x-axis corresponds to ns. The fact that 595 "the" muon peak is not well defined in Figure B.1a is due to the contribution of all 596 the RPCs being tested at the same time that don't necessarily have the same signal 597 arrival time. Each individual peak can have an offset with the ones of other detectors. 598 The inconsistancy in the first 100 ns of both time distributions is an artefact of the 599 TDCs and are systematically rejected during the analysis. . . . .	B-16
600	B.2 The effect of the quality flag is explained by presenting the reconstructed hit multi- 601 plicity of a data file without <code>Quality_flag</code> . The artificial high content of bin 0 is the 602 effect of corrupted data. . . . .	B-19
603		





# List of Tables

611

612	3.1	Details of the greenhouse fluorinated gases used in CMS and of their GWP [23]. . . . .	3-24
613	4.1	Properties of the most used electrode materials for RPCs. . . . .	4-3
614	5.1	Total photon flux ( $E\gamma \leq 662$ keV) with statistical error predicted considering a 615 $^{137}\text{Cs}$ activity of 740 GBq at different values of the distance $D$ to the source along 616      the x-axis of irradiation field [86]. . . . .	5-16
617	5.2	Correction factor $c$ is computed thanks to formulae 5.5 taking as reference $D_0 =$ 618      50 cm and the associated flux $F_0^{ABS}$ for each absorption factor available in table 5.1.	5-18
619	5.3	The data at $D_0$ in 1997 is taken from [86]. In a second step, using Equations 5.8 620      and 5.9, the flux at $D$ can be estimated in 1997. Then, taking into account the 621      attenuation of the source activity, the flux at $D$ can be estimated at the time of the 622      tests in GIF in 2014. Finally, assuming a sensitivity of the RPC to $\gamma$ $s = 2 \cdot 10^{-3}$ , 623      an estimation of the hit rate per unit area is obtained. . . . .	5-20
624	A.1	Inter-process communication cycles in between the webDCS and the DAQ through 625      file string signals. . . . .	A-19



# List of Acronyms

## A

**AFL** Almost Full Level

**ALCTs** anode local charged track boards

## B

**BARC**

Bhabha Atomic Research Centre

**BLT**

Block Transfer

**BMTF**

Barrel Muon Track Finder

**BNL**

Brookhaven National Laboratory

**BR**

Branching Ratio

## C

**CAEN**

Costruzioni Apparecchiature Elettroniche Nucleari S.p.A.

**CERN**

European Organization for Nuclear Research

**CFD**

Constant Fraction Discriminator

**CFEBs**

cathode front-end boards

**CMB**

Cosmic Microwave Background

**CMS**

Compact Muon Solenoid

**CSC**

Cathode Strip Chamber

**CuOF**

copper-to-optical-fiber translators

## D

**DAQ**

Data Acquisition

**DCS**

Detector Control Software

**DQM**

Data Quality Monitoring

662	<b>DT</b>	Drift Tube
663		
664		
665	<b>E</b>	
666		
667	<b>ECAL</b>	electromagnetic calorimeter
668	<b>EMTF</b>	Endcap Muon Track Finder
669		
670		
671	<b>F</b>	
672		
673	<b>FCC</b>	Future Circular Collider
674	<b>FEE</b>	Front-End Electronics
675	<b>FEB</b>	Front-End Board
676	<b>FWHM</b>	full-width-at-half-maximum
677		
678	<b>G</b>	
679		
680		
681	<b>GE-/-</b>	Find a good description
682	<b>GE1/1</b>	Find a good description
683	<b>GE2/1</b>	Find a good description
684	<b>GEANT</b>	GEometry ANd Tracking - a series of software toolkit platforms developed by CERN
685		
686	<b>GEB</b>	GEM Electronics board
687	<b>GEM</b>	Gas Electron Multiplier
688	<b>GIF</b>	Gamma Irradiation Facility
689	<b>GIF++</b>	new Gamma Irradiation Facility
690	<b>GWP</b>	Global Warming Potential
691		
692		
693	<b>H</b>	
694		
695	<b>HCAL</b>	hadron calorimeter
696	<b>HL-LHC</b>	High Luminosity LHC
697	<b>HPL</b>	High-pressure laminate
698	<b>HV</b>	High Voltage
699		
700		
701	<b>I</b>	
702		
703	<b>ICRU</b>	International Commission on Radiation Units & Measurements
704	<b>iRPC</b>	improved RPC

705	<b>IRQ</b>	Interrupt Request
706	<b>ISR</b>	Intersecting Storage Rings
707		
708		
709	<b>L</b>	
710		
711	<b>LEIR</b>	Low Energy Ion Ring
712	<b>LEP</b>	Large Electron-Positron
713	<b>LHC</b>	Large Hadron Collider
714	<b>LS1</b>	First Long Shutdown
715	<b>LS2</b>	Second Long Shutdown
716	<b>LS3</b>	Third Long Shutdown
717	<b>LV</b>	Low Voltage
718	<b>LVDS</b>	Low-Voltage Differential Signaling
719		
720		
721	<b>M</b>	
722		
723	<b>MiC1</b>	first version of Minicrate electronics
724	<b>mip's</b>	minimum ionizing particles
725	<b>MC</b>	Monte Carlo
726	<b>MCNP</b>	Monte Carlo N-Particle
727	<b>ME-/</b>	Find good description
728	<b>ME0</b>	Find good description
729	<b>MRPC</b>	Multigap RPC
730		
731		
732	<b>N</b>	
733		
734	<b>NIM</b>	Nuclear Instrumentation Module logic signals
735		
736		
737	<b>O</b>	
738		
739	<b>OH</b>	Optohybrid Board
740	<b>OMTF</b>	Overlap Muon Track Finder
741		
742		
743	<b>P</b>	
744		
745	<b>PAI</b>	Photo-Absorption Ionisation
746	<b>PAIR</b>	Photo-Absorption Ionisation with Relaxation
747	<b>PMT</b>	PhotoMultiplier Tube

748 PS Proton Synchrotron  
749 PU pile-up

750

751

## 752 Q

753

754 QCD Quantum Chromodynamics  
755 QED Quantum Electrodynamics

756

757

## 758 R

759

760 RE-/ Find a good description  
761 RE2/2 Find a good description  
762 RE3/1 Find a good description  
763 RE3/2 Find a good description  
764 RE4/1 Find a good description  
765 RE4/2 Find a good description  
766 RE4/3 Find a good description  
767 RMS Root Mean Square  
768 ROOT a framework for data processing born at CERN  
769 RPC Resistive Plate Chamber

770

771

## 772 S

773

774 SC Synchrocyclotron  
775 SLAC Stanford Linear Accelerator Center  
776 SM Standard Model  
777 SPS Super Proton Synchrotron  
778 SUSY supersymmetry

779

780

## 781 T

782

783 TDC Time-to-Digital Converter  
784 TDR Technical Design Report  
785 ToF Time-of-flight  
786 TPG trigger primitives

787

788

## 789 W

790

791 webDCS Web Detector Control System

792

793

794

795

796 YETS                   Year End Technical Stop



# 1

## Introduction

797

798

<sup>799</sup> **1.1 A story of High Energy Physics**

<sup>800</sup> **1.2 Organisation of this study**



# 2

801

802

## Investigating the TeV scale

803 „We may regard the present state of the universe as the effect of the  
804 past and the cause of the future. An intellect which at any given mo-  
805 ment knew all of the forces that animate nature and the mutual posi-  
806 tions of the beings that compose it, if this intellect were vast enough  
807 to submit the data to analysis, could condense into a single formula  
808 the movement of the greatest bodies of the universe and that of the  
809 lightest atom; for such an intellect nothing could be uncertain and  
810 the future just like the past would be present before its eyes.”

811

812 - Pierre Simon de Laplace, *A Philosophical Essay on Probabilities*, 1814

Throughout history, physics experiment became more and more powerful in order to investigate finer details of nature and helped understanding the elementary blocks of matter and the fundamental interactions that bond them in the microscopic world. Nowadays, the Standard Model (SM) of particle physics is the most accurate theory designed to explain the behaviour of particles and was able to make very precise predictions that are constantly verified, although some hints of new physics are visible as bricks are still missing to have a global comprehension of the Universe.

To highlight the limits of the SM and test the different alternative theories, ever more powerful machines are needed. This is in this context that the Large Hadron Collider (LHC) has been thought and built to accelerate and collide particles at energies exceeding anything that had been done before. Higher collision energies and high pile-up imply the use of enormous detectors to measure the properties of the interaction products. The Compact Muon Solenoid (CMS) is a multipurpose experiment that have been designed to study the proton-proton collisions of the LHC and give answers on various high energy physics scenari. Nevertheless, the luminosity delivered by the collider will in the future be increased to levels beyond the original plans to improve its discovery potential giving no choice to experiments such as CMS to upgrade their technologies to cope with the increased radiation levels and detection rates.

## 2.1 The Standard Model of Particle Physics

In this early 21<sup>st</sup> century it is now widely accepted that matter is made of elementary blocks referred to as *elementary particles*. The physics theory that classifies and describes the best the behaviour and interaction of such elementary particles is the so called Standard Model that formalizes 3 of the 4 fundamental interactions (electromagnetic, weak and strong interactions). It's development took place during the 20<sup>th</sup> century thanks to a strong collaboration in between the theoretical and experimental physicists.

### 2.1.1 A history of particle physics

The idea that nature is composed of elementary bricks, called *atomism*, is not contemporary as it was already discussed by Indian or Greek philosophers during antiquity. In Greece, atomism has been rejected by Aristotelianism as the existance of *atoms* would imply the existance of a void that would violate the physical principles of Aristotle philosophy. Aristotelianism has been considered as a reference in the european area until the 15<sup>th</sup> century and the italian *Rinascimento* where antic text and history started to be more deeply studied. The re-discovery of Platon's philosophy would allow to open the door to alternative theories and give a new approach to natural sciences where experimentation would become central. A new era of knowledge was starting. By the begining of the 17<sup>th</sup> century, atomism was re-discovered by philosophers and the very first attempt to estimate an *atom* size would be provided by Magnetus in 1646. Although his *atoms* correspond to what would nowadays be called *molecules*, Magnetus achieved feats by calculating that the number of molecules in a grain of incense would be of the order of  $10^{18}$  simply by considering the time necessary to smell it everywhere in a large church after the stick was lit on. It is now known that this number only falls short by 1 order of magnitude.

An alternative philosophy to atomism popularized by Descartes was corpuscularianism. Built on ever divisible corpuscles, contrary to atoms, it's principles would be mainly used by alchemists like Newton who would later develop a corpuscular theory of light. Boyle would combine together ideas of both atomism or corpuscularianism leading to mechanical philosophy. The 18<sup>th</sup> century have

seen the development of engineering providing philosophical thought experiments with repeatable demonstration and a new point of view to explain the composition of matter and Lavoisier would greatly contribute to chemistry and atomism by publishing in 1789 a list of 33 chemical elements corresponding to what is now called *atoms*. In the early 19<sup>th</sup> century Dalton would summarize the knowledge on composition of matter and Fraunhofer would invent the spectrometer and discover the spectral lines. The rise of atomic physics, chemistry and mathematical formalism would unravel the different atomic elements and ultimately, the 20<sup>th</sup> century would see the very first sub-atomic particles.

**Discovery of the inner structure of the atom**

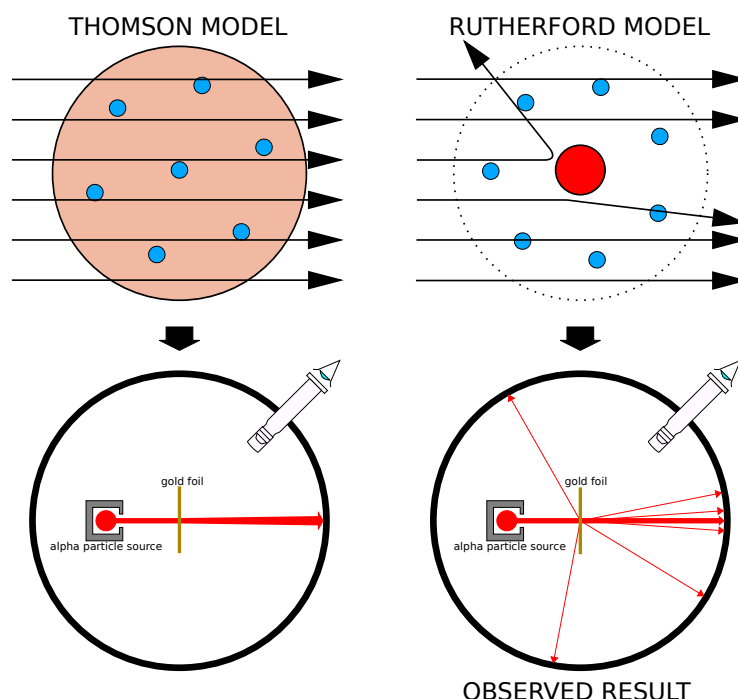


Figure 2.1: Through the gold foil experiment Rutherford could show that most of the mass of atoms was contained in a positively charged nucleus and could then propose a more accurate atomic model than that of Thomson.

The negative *electron* would be the first to be discovered in 1897 by Thomson after 3 decades of research on cathode rays by proving that the electrification observed in an electroscope, as reported by Perrin, was due to the rays themselves and that they had to be composed of electrically charged particles. In 1900, Becquerel would show the *beta rays* emitted by radium had the same charge over mass ratio than what measured by Thomson for cathode rays, pointing to electrons as a constituent of atoms. In 1907, Rutherford and Royds showed that *alpha* particles, once captured in a tube and subjected to an electric spark causing an electron avalanche, where helium ions as they could combine with 2 electrons to form a  ${}^4\text{He}$ . This discovery was directly followed by the constraint of the atom structure in 1909 through the gold foil experiment in which the deflection angle of alpha particles fired at a very thin gold foil was measured and highlighted atoms where mainly empty with

874 nearly all its mass contained into a tiny positively charged *nucleus*. With these two observations,  
 875 he could formulate the Rutherford model of the atom in 1911, shown together with the Thomson  
 876 plum pudding model in Figure 2.1. The link in between atomic number and number of positive and  
 877 negative charges contained into the atoms would fast be understood and the different kind of element  
 878 transmutation appeared to be purely nuclear processes making clear that the electromagnetic nature  
 879 of chemical transformation could not possibly change nuclei. Thus a new branch in physics appeared  
 880 to study nuclei exclusively: the nuclear physics.

881 Moreover, in 1913 quantum physics would be introduced into the atomic model by Bohr based  
 882 on the assumptions of Plank to explain spectral lines, and other observed quantum effects. The same  
 883 year, Moseley would confirm Borh's model and Debye would extend it by introducing elliptical  
 884 orbits.

885 By studying alpha emission and the product of their interaction with nitrogen gas, Rutherford  
 886 reported in 1919 the very first nuclear reaction leading to the discovery that the hydrogen nucleus was  
 887 composed of a single positively charged particle that was later baptised *proton*. This idea came from  
 888 1815 Prout's hypothesis proposing that all atoms are composed of "*protyles*" (i.e. hydrogen atoms).  
 889 By using scintillation detectors, Rutherford could highlight typical hydrogen nuclei signature and  
 890 understand that the impact of alpha particles with nitrogen would knock out an hydrogen nucleus  
 891 and produce an oxygen 17, as explicated in Formula 2.1 and would then postulate that protons are  
 892 building bricks of all elements.



893 With this assumption and the discovery of isotopes together with Aston, elements with identical  
 894 atomic number but different masses, Rutherford would propose that all elements' nuclei but hydrogen's are composed of both charged particles, protons, and of chargeless particles, which he called  
 895 *neutrons*, and that these neutral particles would help maintaining nuclei as one, as charged protons  
 896 were likely to electrostatically repulse each other, and introduced the idea of a new force, a *nuclear*  
 897 force. Though the first idea concerning neutrons was a bond state of protons and electrons as it was  
 898 known that the beta decay, emitting electrons, was taking place in the nucleus, it was then showed  
 899 that such a model would hardly be possible due to Heisenberg's uncertainty principle and by the  
 900 recently measured *spin* of both protons and electrons. The spin, discovered through the study of  
 901 the emission spectrum of alkali metals, would be understood as a "two-valued quantum degree of  
 902 freedom" and formalized by Pauli and extended by Dirac, to take the relativist case into account.  
 903 Measured to be  $\frac{1}{2}\hbar$  for both, it was impossible to arrange an odd number of half integer spins and  
 904 obtain a global nucleus spin that would be integer. Finally, in 1932, following the discovery of a new  
 905 neutral radiation, Chadwick could discover the neutron as an uncharged particle with a mass similar  
 906 to that of the proton whose half integer spin would reveal to be the solution to explain the nuclear  
 907 spin.

### 909 Development of the Quantum Electrodynamics

910 Historically, the development of the quantum theory revolved around the question of emission and  
 911 absorption of discrete amount of energy through light. Einstein used the initial intuition of Plank  
 912 about the black-body radiation to develop in 1905 a model to explain the photoelectric effect in  
 913 which light was described by discrete quanta now called *photons*. For this model, Einstein introduced  
 914 the concept of wave-particle duality as classical theory was not able to describe the phenomenon.  
 915 With the new understanding of atoms and of their structure, classical theories also proved unable

916 to explain atoms stability. Indeed, using classical mechanics, electrons orbiting around a nucleus  
 917 should radiate an energy proportional to their angular momentum and thus lose energy through  
 918 time and the spectrum of energy emission should then be continuous, but it was known since the  
 919 19<sup>th</sup> century and the discovery of spectral lines that the emission spectrum of material was discrete.

920 This was Bohr who first suggested that a quantum description of the atom was necessary in 1913.  
 921 Using the correspondence principle stating that at large enough numbers the quantum calculations  
 922 should give the same results than the classical theory, he proposed the very first quantum model  
 923 of the hydrogen atom explaining the line spectrum by introducing the principal quantum number  
 924  $n$  describing the electron shell. This model would then be improved by Sommerfeld that would  
 925 quantize the z-component of the angular momentum, leading to the second and third quantum  
 926 numbers, or azimuthal and magnetic quantum number,  $l$  and  $m$  defining for the second the orbital  
 927 angular momentum of the electrons on their shells and thus, the shape of the orbital, and for the third  
 928 the available orbital on the subshell for each electron. Nevertheless, although the model was not only  
 929 limited to spherical orbitals anymore, making the atom more realistic, the Zeeman effect couldn't be  
 930 completely explained by just using  $n$ ,  $l$  and  $m$ . A solution would be brought after the discovery of  
 931 Pauli in 1924, as Uhlenbeck, Goudsmit, and Kramers proposed in 1925 the idea of intrinsic rotation  
 932 of the electron, introducing a new angular momentum vector associated to the particle itself, and  
 933 not to the orbital, and associated to a new quantic number  $s$ , the *spin* projection quantum number  
 934 explaining the lift of degeneracy to an even number of energy levels.

935 The introduction of the *spin* happened 1 year after another attempt of improvement of the theory  
 936 was made by De Broglie in his PhD thesis. The original formulation of the quantum theory only  
 937 considered photons as energy quanta behaving as both waves and particles. De Broglie proposed  
 938 that all matter are described by waves and that their momentum is proportional to the oscillation of  
 939 quantized electromagnetic field oscillators. This interpretation was able to reproduce the previous  
 940 version of the quantum energy levels by showing that the quantum condition involves an integer  
 941 multiple of  $2\pi$ , as shown by Formula 2.2.

$$p = \hbar k \Leftrightarrow \int pdx = \hbar \int kdx = 2\pi\hbar n \quad (2.2)$$

942 Although the intuition of De Broglie about the wave-particle duality of all matter, his interpretation  
 943 was semiclassical and it's in 1926 that the first fully quantum mechanical wave-equation would  
 944 be introduced by Schrödinger to describe electron-like particles, reproducing the previous semiclassical  
 945 formulation without inconsistencies. This complexe equation describes the evolution of the  
 946 wave function  $\Psi$  of the quantum system, defined by its position vector  $\mathbf{r}$  and time  $t$  as an energy  
 947 conservation law, in which the hamiltonian of the system  $\hat{H}$  is explicit, by solving the Equation 2.3.

$$i\hbar \frac{\partial}{\partial t} |\Psi(\mathbf{r}, t)\rangle = \hat{H} |\Psi(\mathbf{r}, t)\rangle \quad (2.3)$$

948 In 1927, Dirac would go further in his paper about emission and absorption of radiation by  
 949 proposing a second quantization not only of the physical process at play but also of the electromagnetic  
 950 field, providing the ingredients to the first formulation of *Quantum Electrodynamics (QED)*  
 951 and the description of photon emission by electrons dropping into a lower energy state in which the  
 952 final number of particles is different than the initial one. To complete this model to the many-body  
 953 wave functions of identical particles, Jordan included creation and annihilation operators for fields  
 954 obeying Fermi-Dirac statistics leading to a model describing particles that would be referred to as  
 955 *fermions*. Nevertheless, in order to properly treat electromagnetism, the incorporation of the relativ-

ity theory developed by Einstein. Including gravity into quantum physics still is a challenge nowadays, but in 1928 Pauli and Jordan would show that special relativity's coordinate transformations could be applied to quantum fields as the field commutators were Lorentz invariant. Finally derived the same year, the Dirac equation, shown as Equation 2.4, similarly to Schrödinger's equation, is a single-particle equation but it incorporates special relativity in addition to quantum mechanics rules. It features the  $4 \times 4$  gamma matrices  $\gamma^\mu$  built using  $2 \times 2$  Pauli matrices and unitary matrix, the 4-gradient  $\partial_\mu$ , the rest mass  $m$  of any half integer spin massive particle described by the wave function  $\psi(x, t)$ , also called a Dirac spinor, and the speed of light  $c$ . In addition to perfectly reproduce the results obtained with quantum mechanics so far, it also provided with *negative-energy solutions* that would later be interpreted as a new form of matter, *antimatter* and give a theoretical justification to the Pauli equation that was phenomenologically constructed to account for the spin as in the non-relativistic limit, the Dirac equation is similar.

$$i\hbar\gamma^\mu\partial_\mu\psi - mc\psi = 0 \quad (2.4)$$

The successes of the QED was soon followed with theoretical problems as computations of any physical process involving photons and charged particles were showed to be only reliable at the first order of perturbation theory. At higher order of the theory, divergent contributions were appearing giving nonsensical results. Only two effects were contributing to these infinities.

- The self-energy of the electron (or positron), the energy that the particle has due its own interaction with its environment.
- The vacuum polarization, virtual electron–positron pairs produced by a background electromagnetic field in the vacuum which is not an "empty" space. These virtual pairs affect the charge and current distributions generated by the original electromagnetic field.

Solving this apparent problem was done by carefully defining the concepts of each observables, for example mass or charge, as these quantities are understood within the context of a non-interacting field equation, and that from the experiment point of view, they are abstractions as what is measured are "renormalized observables" shifted from there "bare" value by the interaction taking place in the measuring process. The infinities needed to be connected to corrections of mass and charge as those are fixed to finite values by experiment. This was the intuition of Bethe in 1947 who successfully computed the effect of such *renormalization* in the non-relativist case. Fully covariant formulations of QED including renormalization was achieved by 1949 by Tomonaga, Schwinger, Feynman and Dyson and Feynman is now famous for his association of diagrams to the term of the scattering matrix, greatly simplifying the representation and computation of interactions as the diagrams directly corresponded the measurable physical processes and would then be used in every quantum field theories. With the resolution of infinities, QED had mostly reached its final form, being still today the most accurate physical theory and would serve as a model to build all other quantum field theories.

### Development of the quark model and Quantum Chromodynamics

To explain the nuclear force that holds *nucleons* (protons and neutrons) together, Yukawa theoretically proposed in 1934 the existence of a force carrier called *meson* due to it's predicted mass in the range in between the electron and nucleon masses. Discovered in 1936 by Anderson and Neddermeyer, and confirmed using bubble chambers in 1937 by Street and Stevenson, a first meson

996 candidate was observed in the decay products of cosmic rays. Assuming it had the same electric  
 997 charge than electrons and protons, this particle was observed to have a curvature due to magnetic  
 998 field that was sharper than protons but smoother than electrons resulting in a mass in between that  
 999 of electrons and protons. But its properties were not compatible with Yukawa's theory, which was  
 1000 emphasized by the discovery of a new candidate in 1947, again in cosmic ray products using photo-  
 1001 graphic emulsions.

1002 This new candidate, although it had a similar mass than the already believed *meson*, would rather  
 1003 decay into it. For distinction, the first candidate would then be renamed "*mu meson*" when the second  
 1004 would be the "*pi meson*". The *mu meson* was behaving like a heavy electron and didn't participate  
 1005 in the strong interaction whereas the pion was believed to be the carrier of the nuclear interaction.  
 1006 This lead to classify the *mu* in a new category of particles called *leptons* together with the electron  
 1007 that shared similar properties and *the neutrino*, and be renamed *muon*. The *pi meson* was finally  
 1008 found to be a triplet of particles: a positively charged, a negatively charged, and a neutral particle.  
 1009 The neutral *pi meson* has been more difficult to identify as it wouldn't leave tracks on emulsions nor  
 1010 on bubble chambers and needed to be studied via it's decay products. It was ultimately identified in  
 1011 University of California's cyclotron in 1950 through the observation of its decay into 2 photons.

1012 Also discovered in 1947 but in cloud chamber photographs, the *K meson* as also been an im-  
 1013 portant step towards the establishment of the Standard Model. A triplet of particle, 2 charged and a  
 1014 neutral, with a mass roughly half that of a proton, were reported. These particles were baptised *K*  
 1015 *meson* in contrast to the "light" *pi* and *mu* "L-mesons". The particularity of the *K* were there very  
 1016 slow decays with a typical lifetime of the order of  $10^{-10}$ s much greater than the  $10^{-23}$ s of *pi*-proton  
 1017 reactions. The concept of *strangeness*, a new quantum number was then introduced by Pais as an  
 1018 attempt to explain this phenomenon as *strange* particles appeared as a pair production of a strange  
 1019 and anti-strange particle.

1020 With the development of synchrotrons, the particle *zoo* would grow to several dozens during the  
 1021 1950s as higher energies were reachable through acceleration. In 1961, a first classification system,  
 1022 called Eightfold Way, was proposed by Gell-Mann and finding its roots in the Gell-Mann–Nishijima  
 1023 formula, which relates the electric charge  $Q$ , the third component of the isospin  $I_3$ , the *baryon*  
 1024 number  $B$  and the strangeness  $S$ , as explicitated in Formula 2.5. The isospin was a quantum number  
 1025 introduced in 1932 to explain symmetries of the newly discovered neutron using representation  
 1026 theory of SU(2). The baryon number, was introduced by Nishijima as a quantum number for baryons,  
 1027 i.e. particles of the same family as nucleons. The mesons were classified in an octet and baryons of  
 1028 spin  $\pm \frac{1}{2}$  and  $\pm \frac{3}{2}$  were respectively classified into an octet and a decuplet, as shown in Figure 2.2. To  
 1029 complete the baryon decuplet, Gell-Mann predicted the existance of baryon  $\Omega^-$  which would later  
 1030 be discovered in 1964.

$$Q = I_3 + \frac{1}{2}(B + S) \quad (2.5)$$

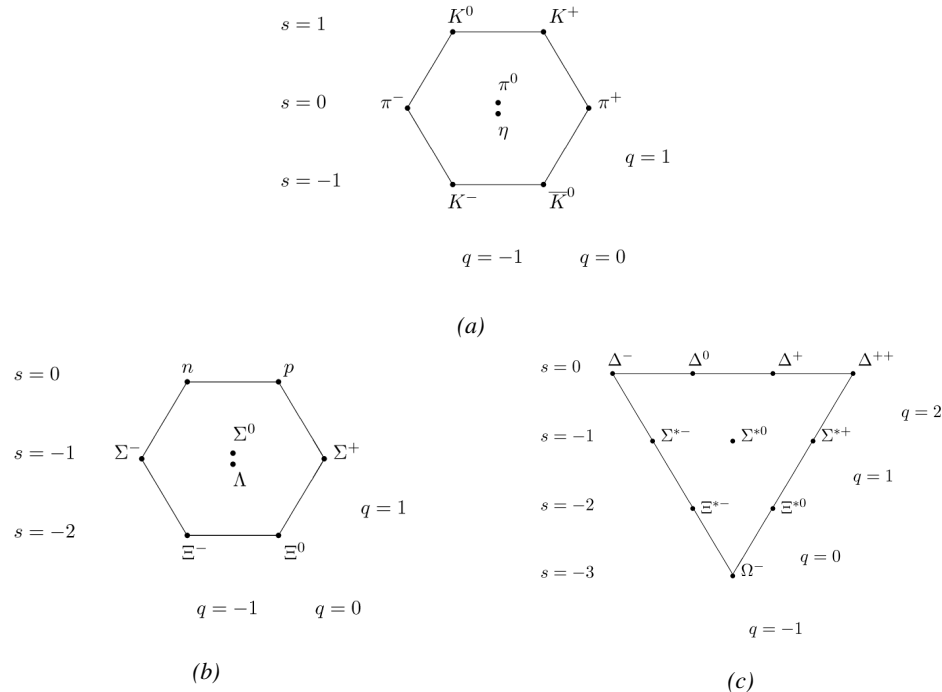


Figure 2.2: Figure 2.2a: Meson octet. Figure 2.2b: Baryon octet. Figure 2.2c: Baryon decuplet.

Strong of this classification using an SU(3) flavor symmetry, Gell-Mann, and independently Zweig, would propose a full theoretical model in which *hadrons* (strongly interacting particles, i.e. mesons and baryons) were not elementary particles anymore. They would rather be composed with 3 flavors of particles called *quarks* and there anti-particles. The 3 flavors were called *up*, *down* and *strange*. *Up* and *down* would be used to explain the nucleons and non-strange mesons, while *strange* would come into the composition of hadrons showing strangeness. *Up* and *down* flavors would be discovered in 1968 thanks to the deep inelastic scattering experiments conducted at the Stanford Linear Accelerator Center (SLAC), and *strange* could only be indirectly validated even though it provided a robust explanation to *kaon* ( $K$ ) and *pion* ( $\pi$ ). However, in the decade following the Gell-Mann-Zweig quark model proposition, several improvement to the model were brought, first by Glashow and Bjorken the same year that predicted the existence of a fourth quark flavor, the *charm*, that would equalize the then known number of quarks and leptons and finally in 1973 by Kobayashi and Maskawa that would increase the number of quarks to 6 to explain the experimental observation of CP violation. These two quarks would be referred to as *top* and *bottom* for the first time in 1975. It's only after these additions to the quark model that finally the *charm* would be discovered in 1974 at both SLAC and Brookhaven National Laboratory (BNL). A meson where the *charm* was bound with an *anti-charm*, called  $J/\psi$ , would help convince the physics community of the validity of the model. The *top* would be discovered soon after in 1977 in Fermilab and indicate the existence of the *bottom* that would resist to discovery until Fermilab's experiments CDF and D $\emptyset$  in 1995 due its very large mass and the energy needed to produce it.

As remarked by Struminsky, the original quark model proposal composed of 3 quarks should possess an additional quantum number due to mesons such as  $\Omega^-$  or  $\Delta^{++}$ . Indeed, these mesons are composed of 3 identical quarks, respectively 3 *strange* and *up* quark, with parallel spins, which

should be forbidden by the exclusion principle. Independentle, Greenberg and Han-Nambu proposed an additional SU(3) degree of freedom possessed by the quarks, that would later be refered to as *color charge gauge*, that could interact through *gluons*, the gauge boson octet corresponding to this degree of freedom. Nevertheless, as observing free quarks proved to be impossible, two visions of the quarks were argued mainly due to the failures to observe these particles free to prove their existence. On one side, Gell-Mann proposed to see quarks as mathematical construct instead of real particles, as they are always confined, implying that quantum field theory would not describe entirely the strong interaction. Opposed to this vision, Feynman on the contrary argued that quarks were real particles, that he would call *partons*, that should be described as all other particles by a distribution of position and momentum. The implications of quarks as point-like particles would be verified at SLAC and the concept of *color* would be added to the quark model in 1973 by Fritzsch and Leutwyler together with Gell-Mann to propose a description of the strong interaction through the theory of Quantum Chromodynamics (QCD). The discovery the same year of asymptotic freedom within the QCD by Groos, Politzer and Wilczek, allowed for very precise predictions thanks to the perturbation theory. Nowadays, the confinement of quarks is studied in experiments such as ALICE, through exploration of the quark-gluon plasma.

### 1070 The Weak interaction, spontaneous symmetry breaking, the Higgs mechanism and the Elec- 1071 troweak unification

1072 The weak interaction is the process that causes radioactive decays. Thanks to the neutron discovery,  
 1073 Fermi could explain in 1934 the beta radiations through the beta decay process in which the neutron  
 1074 decays into a proton by emitting an electron. Though the missing energy observed during this  
 1075 process triggered a huge debate about the apparent non conservation of energy, momentum and spin  
 1076 of the process, Fermi, as Pauli before him, proposed that the missing energy was due to a neutral  
 1077 not yet discovered particle that would then be baptised *neutrino*. The impossibility to detect such  
 1078 a particle would leave some members of the scientific community sceptical, but hints of energy  
 1079 conservation and of the existence of the neutrino were provided by measuring the energy spectrum  
 1080 of electrons emitted through beta decay, as there was a strict limit on their energy. It's only 30 years  
 1081 later in 1953 that it would be discovered by the team of Cowan and Reines using the principle of  
 1082 inverse beta decay described through Formula 2.6. The experiment consisted in placing water tanks  
 1083 sandwiched in between liquid scintillators near a nuclear reactor with an estimated neutrino flux of  
 1084  $5 \times 10^{13} \text{ s}^{-1} \text{ cm}^{-2}$ . However, in order to explain the absence of some reactions in the experiment  
 1085 of Cowan and Reines, and constraint the beta decay theory of Fermi and extend it to the case of  
 1086 the muon, Konopinski and Mahmoud proposed in 1953 that the muon decay would eject a particle  
 1087 similar to the neutrino and thus predicted the existence of a muon neutrino that would be different  
 1088 than the one involved in the beta decay, related to the electron. With this, the idea of lepton number  
 1089 would arise. The muon neutrino would successfully be detected in 1962 by Lederman, Schwartz and  
 1090 Steinberger.

$$\bar{\nu} + p \rightarrow n + e^+ \quad (2.6)$$

1091 The theory could not be valid though as the probability of interaction, called cross-section, would  
 1092 have been increasing without bond with the square of the energy. Fermi assumed in a two vector  
 1093 current coupling but Lee and Yang noted that an axial current could appear and would violate parity.  
 1094 The experiment of Wu in 1956 would confirm the parity violation and Gamow and Teller would try to  
 1095 account for it by describing Fermi's interaction through allowed (parity-violating) and superallowed

1096 (parity-conserving) decays. But the success of QED as a quantum field theory would spark the  
1097 development of such a theory to describe the weak interaction.

1098 As previously discussed, the great success of QED was built on an underlying symmetry, inter-  
1099 preted as a gauge invariance so that the effect of the force is the same in all space-time coordinates,  
1100 and of the possibility to renormalize it in order to absorb the infinities. Independently in 1958,  
1101 Glashow, and Salam and Ward used 1957 Schwinger ideas about vector intermediary for the decay  
1102 processes, could find a way to unite both the electromagnetic and weak interaction into a gauge  
1103 theory involving 4 gauge bosons, 3 of which were massive and carried out the weak interaction and  
1104 a massless boson carrying the electromagnetic interaction. Among the 3 massive bosons, 2 were  
1105 charged and 1 was neutral, similarly to the previously theorized *pi meson* vector of the Yukawa  
1106 model and all have a mass much greater than nucleons and thus a very short life time implying a  
1107 finite very short range contrary to the contact interaction originally proposed by Fermi.

1108 Breakthrough in other fields of physics contributed in giving theoretical support and interpreta-  
1109 tion to the unified electroweak theory. The stepping stone would be the use of spontaneous symmetry  
1110 breaking that was inspired to Nambu at the end of the 1950s following the development of the BCS  
1111 superconductivity mechanism in 1957. Cooper had shown that BCS pairs, pairs of electrons bound  
1112 together at low temperature, could have lower energy than the Fermi energy and where responsi-  
1113 ble for superconductivity. This lead to the discovery of Goldstone-Nambu bosons as a result of the  
1114 spontaneous breaking of the chiral symmetry in a theory describing nucleons and mesons devel-  
1115 opped by Nambu and Jona-Lasinio in 1961, and now understood as a low-energy approximation of  
1116 QCD. Similarly to mechanism of energy gap appearance in superconductivity, the nucleon mass  
1117 is suggested to the result of a self-energy of a fermion field and is studied through a four-fermion  
1118 interaction in which, as a consequence of the symmetry, bound states of nucleon-antinucleon pairs  
1119 appear and can be regarded as virtual pions. Though the symmetry is maintained in the equations,  
1120 the ground state is not preserved. Goldstone would later the same year show that the bound states  
1121 corresponds to spinless bosons with zero mass.

1122 Although the model in itself didn't revolutionize particle physics, spontaneous symmetry break-  
1123 ing would be generalized to quantum field theories. As all fundamental interactions are described  
1124 using gauge theories based on underlying symmetries, processes such as the chiral symmetry break-  
1125 ing would be introduced soon after the publication of Nambu and Jona-Lasinio. In 1962, Anderson,  
1126 following an idea of Schwinger who suggested that zero-mass vector bosons were not necessarily  
1127 required to describe the conservation of baryons contrary to the bosons emerging from chiral sym-  
1128 metry breaking, discussed the implications of spontaneous symmetry breaking in particles physics.  
1129 A model was finally independently built in 1964 by Brout and Englert, Higgs, and Guralnik, Hagen,  
1130 and Kibble, who discovered that combining an additional field into a gauge theory in order to break  
1131 the symmetry, the resulting gauge bosons acquire a nonzero mass. Moreover, Higgs stated that this  
1132 implied the existence of at least one new massive, i.e. self-interacting, scalar boson, that are now  
1133 known as *Higgs bosons* corresponding to this additional field. The Higgs mechanism today specific-  
1134 ally refers to the process through which the gauge bosons of the weak interaction acquire mass. In  
1135 1968, Weinberg could point to the Higgs mechanism to integrate a Higgs field into a new version  
1136 of the electroweak theory in which the spontaneous symmetry breaking mechanism of the Higgs  
1137 field would explicitly explain the masses of the weak interaction gauge bosons and the zero-mass  
1138 of photons.

### 1139 2.1.2 Construction and test of the model

1140 The Standard Model of particle physics was built in the middle of the 1970s after the experimental  
 1141 confirmation of the existence of quarks. It is based on the assembly of the models previously introduced  
 1142 and describing the fundamental interactions, except for gravitation, and their gauge bosons  
 1143 as well as the way elementary "matter" particles interact with the fields associated with these force  
 1144 carriers. In this sense, the development of QED and the unification of the electroweak interaction,  
 1145 of the Yukawa interaction and of QCD, and of the Higgs mechanism made it possible to explain most  
 1146 of contemporary physics.

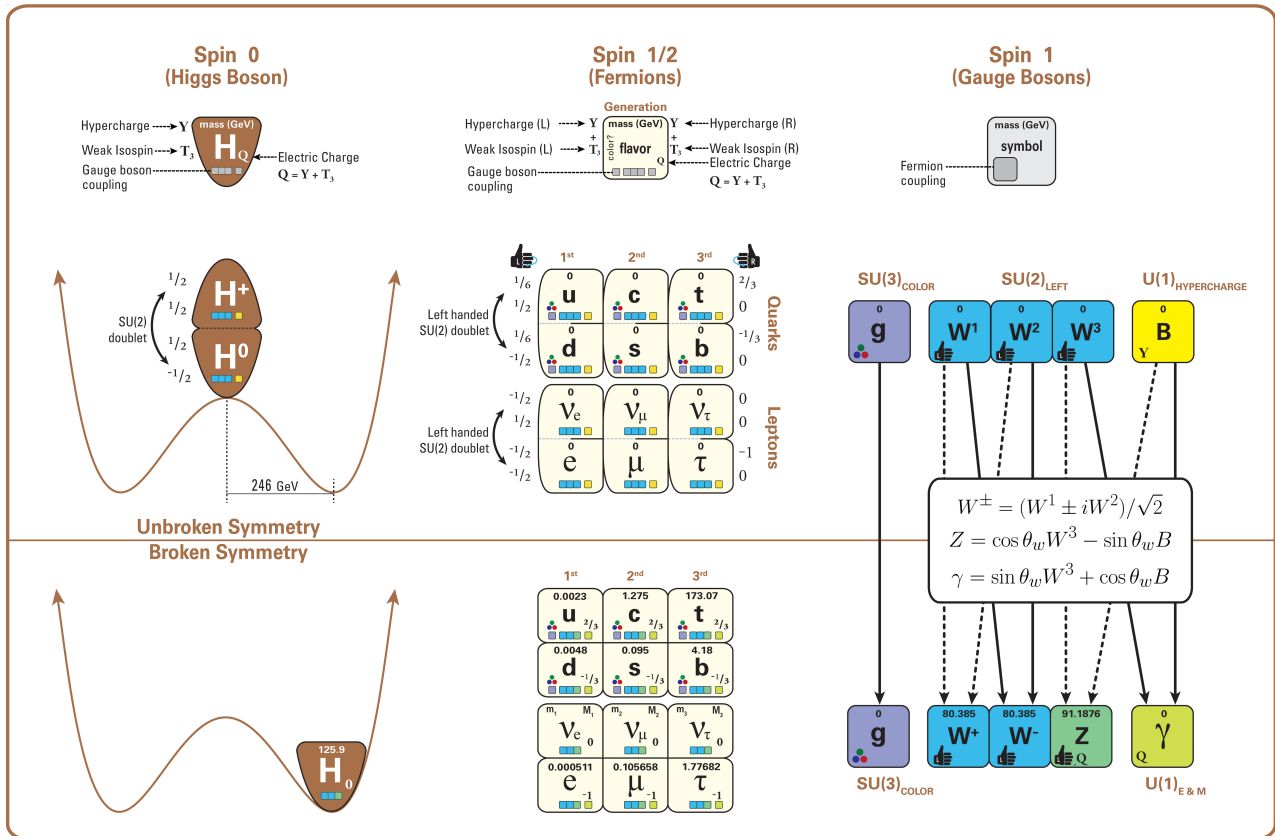


Figure 2.3: The elementary particles of the Standard Model are showed along with their names and properties. Their interactions with the strong, weak and electromagnetic forces have been explicited using color squares. In the left column, the scalar higgs boson is depicted, while the central is focused on the matter particles, the fermions, and the right on the force carriers, the gauge bosons. The role of the Higgs boson in electroweak symmetry breaking is highlighted, and the corresponding way properties of the various particles differ in the (high-energy) symmetric phase (top) and the (low-energy) broken-symmetry phase (bottom) are showed.

1147 In the SM, "matter" particles, are described by 12 fermion fields of spin  $\frac{1}{2}$  obeying the Fermi-  
 1148 Dirac statistics, i.e. subjected to the Pauli exclusion principle. To each fermion is associated its  
 1149 corresponding antiparticle. The fermions are classified according to the way they interact and, thus,  
 1150 according to the charges they carry. 6 of them are classified as quarks ( $u, d, c, s, t$ , and  $b$ ) and  
 1151 are subjected to all interactions and the 6 others as leptons ( $e^-, \mu^-, \tau^-, \nu_e, \nu_\mu$ , and  $\nu_\tau$ ). Leptons

1152 are not subjected to the strong interaction and among them, the 3 neutrinos only interact weakly as  
 1153 they are neutral particles, which explains why they are so difficult to detect. The gauge boson fields  
 1154 are the gluons  $g$  for the strong interaction, the photon  $\gamma$  for the electromagnetic interaction and the  
 1155 weak bosons  $W^+$ ,  $W^-$ , and  $Z^0$  for the weak interaction. Finally, the Higgs field  $H^0$  is responsible,  
 1156 through the spontaneous symmetry breaking, of the mixing of the massless electroweak boson fields  
 1157  $W_1$ ,  $W_2$ ,  $W_3$ , and  $B$  leading to the observable states  $\gamma$ ,  $W^+$ ,  $W^-$ , and  $Z^0$  that can gain mass while  
 1158 interacting with the Higgs field. This picture of the SM is summarized through Figure 2.3 where the  
 1159 antifermions are not showed.

1160 When the model was first finalized, the existence of the weak gauge bosons, of the charm, of the  
 1161 third quark generation composed of top and bottom quarks to explain the observed CP violation was  
 1162 not proven but the predictions were measured with good precision in the years following. First, the  
 1163 charm quark would be discovered in 1974, followed by the bottom quark in 1977. The weak bosons  
 1164 would be discovered during the next decade in 1983. The top quark would resist until 1995 due to  
 1165 its very large mass but would offer the last piece of the elementary QCD particles. The very last  
 1166 predicted elementary particle of the model that was not observed yet would prove to be very difficult  
 1167 to observe. The Higgs boson needed the start of the LHC to finally be observed in 2012. A few years  
 1168 more of tests were necessary to measure its properties to confirm the observation of a scalar boson  
 1169 compatible with the predicted Higgs boson  $H^0$ . Even though only quark-antiquark (mesons) and 3  
 1170 quark states (baryons) were observed, exotic hadrons were not forbidden by QCD and no limit of  
 1171 quark is imposed by the theory. Moreover, gluons could form bound states by themselves and with  
 1172 quarks. These two types of states are called *glueballs* and *hybrid hadrons*. For decades, experi-  
 1173 ments have been conducted without confirmation of such possible states existing. Nevertheless, in  
 1174 2014, tetraquarks were observed by LHCb, one of LHC's main experiments, and in 2015, the same  
 1175 experiment reported the discovery of pentaquarks making the SM one of the best tested theories of  
 1176 physics.

### 1177 2.1.3 Investigating the TeV scale

1178 Even though the SM is a well tested theory, several hints of physics going beyond its scope have  
 1179 been observed. First of all, gravity is not explained through this model and huge difficulties are en-  
 1180 countered when trying to include gravitation. The strength of gravitational interaction is expected to  
 1181 be negligible at the scale of elementary particles, nevertheless, adding gravitation in the perspective  
 1182 of developing a "theory of everything" leads to divergent integrals that could not be fixed through  
 1183 renormalization.

1184 Moreover, the SM considers neutrinos to be massless but it was shown in the late 1960s by the  
 1185 Homestake experiment that the flux of solar neutrinos (i.e.  $\nu_e$ ) measured didn't match the predicted  
 1186 values due to neutrino oscillations, confirmed in the early 2000s by the Sudbury Neutrino Obser-  
 1187 vatory. This oscillation implies that neutrinos that can be observed are a superposition of massive  
 1188 neutrino states. The research on neutrino oscillation is already quite advanced with experiments  
 1189 looking at atmospheric, reactor or beam neutrinos in order to determine the elements of the mixing  
 1190 matrix similar to the CKM matrix describing the mixing of quarks. Nevertheless, no answer to the  
 1191 origin of neutrino mass is provided.

1192 Another intriguing fact is that the universe is dominated by matter. However, the SM predicted  
 1193 that matter and antimatter should have been created in equal amounts and no mechanism is able to  
 1194 explain this matter-antimatter asymmetry. Although this asymmetry is seen from the visible uni-  
 1195 verse, it may be possible that other unknown regions of the Universe are dominated by antimatter.

1196 Another possibility to explain the apparent asymmetry would be the existence of a electric dipole  
1197 in any fundamental particle that would permit matter and antimatter particles to decay at different  
1198 rates.

1199 The discrepancy of velocity dispersion of stars in galaxies with respect to the visible mass they  
1200 contain is known since the end of the 19<sup>th</sup> century where Kelvin proposed that this problem could  
1201 be solved if a "*great majority of [the stars] would be dark bodies*". Throughout the 20<sup>th</sup> century,  
1202 physicists like Kapteyn, Zwicky, showed the first hints of a "*dark matter*" by studying star veloc-  
1203 ities and galactic clusters, followed by robust measurements of galaxy rotation curves by Babcock  
1204 which suggested that the mass-to-luminosity ratio was different from what would be expected from  
1205 watching the visible light. Later in the 1970s, Rubin and Ford from direct light observations and  
1206 Rogstad and Shostak from radio measurements showed that the radial velocity of visible objects in  
1207 galaxies was increasing with increasing distance to the center of the galaxy. Finally observation of  
1208 lensing effect by galaxy clusters, temperature distribution of hot gas in galaxies and clusters, and  
1209 the anisotropies in the Cosmic Microwave Background (CMB) kept on pointing to a "*dark matter*".  
1210 From all the data accumulated, the visible matter would only account to no more than 5% of the total  
1211 content on the visible universe. Alternative theories have tried to investigate modified versions of  
1212 the General Relativity as this theory is only well tested at the scale of the solar system but is not suf-  
1213 ficiently tested on wider ranges or even theories in which gravitation is not a fundamental force but  
1214 rather an emergent one, but so far, such theories have difficulties to reproduce all the experimental  
1215 observations as easily as through dark matter.

1216 A possible theory to offer dark matter candidates would be supersymmetry (SUSY) which pro-  
1217 poses a relationship in between bosons and fermions. In this model, each elementary particle,  
1218 through a spontaneous spacetime symmetry breaking mechanism would have a *super partner* from  
1219 the other family of particles. On top of providing heavy dark matter candidates, supersymmetry  
1220 could also help solving the *Hierarchy problem*, the very large scale difference in between the weak  
1221 interaction and gravity, although, as mentioned before, in the case gravity is found not to be a funda-  
1222 mental force, this problem would automatically fade.

1223  
1224 All these different aspects of physics beyond the Standard Model of particle physics and the  
1225 Standard model itself can be tested through the use of very energetic and intense hadron and ion col-  
1226 liders. The LHC at CERN is a perfect tool to seek answers to these open questions except maybe for  
1227 the gravity as gravity is extremely weak at particles level. For example, one of LHCb experiment's  
1228 goal is to investigate CP-violation and thus baryonic asymmetry. In 2017, the collaboration has an-  
1229 nounced to have so far a  $3.3\sigma$  statistical significance over a CP-violation through the study of the  
1230 decays of  $\Lambda_b^0$  and  $\overline{\Lambda}_b^0$  into a proton (or antiproton) and 3 pions. Many analysis teams are also working  
1231 hard on supersymmetry both in ATLAS and CMS collaborations, the two multipurpose experiments  
1232 of LHC, even though no evidence of a supersymmetrical theory was seen, the few hint having the  
1233 tendency to confirm the standard model. These experiments also have the possibility to investigate  
1234 ways to explain Majorana neutrino mass through Yukawa interactions of scalar particles.

1235 The higher the center-of-mass energy, the smaller details the experiments will be able to see, the  
1236 heavier the potential particle creation barrier will be, the stronger the cross-section of certain rare  
1237 decay channels will be. As a comparison, with collisions happening at 14 TeV, the LHC is approxi-  
1238 mately 2 orders of magnitude more sensitive to the Higgs than the Tevatron was with its already very  
1239 powerful 2 TeV. All these advantages eventually lead to new discoveries and deeper understanding  
1240 of the models describing our Universe. But the LHC only is a step forward to gather more precise  
1241 tests of the Standard Model and new knowledge about the physics beyond it. A successful physics

1242 campaign will probably serve to justify the building of new accelerators with even greater discovery  
1243 potential like for example the Future Circular Collider (FCC) that would push even further the study  
1244 of the unanswered questions of contemporary physics.

## 1245 2.2 The Large Hadron Collider & the Compact Muon Solenoid

1246 Throughout its history, CERN has played a leading role in high energy particle physics. Large re-  
1247 gional facilities such as CERN were thought after the second world war in an attempt to increase  
1248 international scientific collaboration and allows scientists to share the forever increasing costs of  
1249 experiment facilities required due to the need for increasing the energy in the center of mass to  
1250 deeper probe matter. The construction of the first accelerators at the end of the 50s, the Synchro-  
1251 cyclotron (SC) and the Proton Synchrotron (PS), was directly followed by the first observation of  
1252 antinuclei in 1965 [1]. Strong from the experience of the Intersecting Storage Rings (ISR), the very  
1253 first proton-proton collider that showed hints that protons are not elementary particles, the Super  
1254 Proton Synchrotron (SPS) was built in the 70s to investigate the structure of protons, the preference  
1255 for matter over antimatter, the state of matter in the early universe or exotic particles, and lead to  
1256 the discovery in 1983 of the W and Z bosons [2–5]. These newly discovered particles and the elec-  
1257 troweak interaction would then be studied in details by the Large Electron-Positron (LEP) collider  
1258 that will help to prove in 1989 that there only are three generations of elementary particles [6]. The  
1259 LEP would then be dismantled in 2000 to allow for the LHC to be constructed in the existing tunnel.

### 1260 2.2.1 LHC, the most powerful particle accelerator

1261 The LHC has always been considered as an option to the future of CERN. At the moment of the  
1262 construction of the LEP beneath the border between France and Switzerland, the tunnel was built in  
1263 order to accomodate what would be a Large Hadron Collider with a dipole field of 10 T and a beam  
1264 energy in between 8 and 9 TeV [7] directly followed in 1985 with the creation of a 'Working Group  
1265 on the Scientific and Technological Future of CERN' to investigate such a collider [8]. The decision  
1266 was finally taken almost 10 years later, in 1994, to construct the LHC in the LEP tunnel [9] and the  
1267 approval of the 4 main experiments that would take place at the 4 interaction points would come in  
1268 1997 [10] and 1998 [11]:

- 1269 • ALICE [12] has been designed in the purpose of studying quark-gluon plasma that is believed  
1270 to have been a state of matter that existed in the very first moment of the universe.
- 1271 • ATLAS [13] and CMS [14] are general purpose experiments that have been designed with  
1272 the goal of continuing the exploration of the Standard Model and investigate new physics.
- 1273 • LHCb [15] has been designed to investigate the preference of matter over antimatter in the  
1274 universe through the CP violation.

1275 These large scale experiments, as well as the full CERN accelerator complex, are displayed on  
1276 Figure 2.4. The LHC is a 27 km long hadron collider and the most powerful accelerator used for  
1277 particle physics since 2008 [16]. The LHC was originally designed to collide protons at a center-  
1278 of-mass energy of 14 TeV and luminosity of  $10^{34} \text{ cm}^{-2}\text{s}^{-1}$ , as well as  $Pb$  ions at a center-of-mass  
1279 energy of 2.8 TeV/A with a peak luminosity of  $10^{27} \text{ cm}^{-2}\text{s}^{-1}$ . Run 1 of LHC, when the center-of-  
1280 mass energy only was half of the nominal LHC energy, was enough for both CMS and ATLAS to

discover the Higgs boson [17] and for LHCb to discover pentaquarks [18] and confirm the existance of tetraquarks [19]. Nevertheless, after the Third Long Shutdown (LS3) (2024-2026), the accelerator will be in the so called High Luminosity LHC (HL-LHC) configuration [20], increasing its instantaneous luminosity to  $10^{35} \text{ cm}^{-2}\text{s}^{-1}$  for  $pp$  collisions and to  $4.5 \times 10^{27} \text{ cm}^{-2}\text{s}^{-1}$ , boosting the discovery potential of the LHC. The HL-LHC phase should last at least another 10 years depending on the breakthrough this machine would lead to. Already a new accelerating device, the FCC, as been proposed to prepare the future of high energy physics after the LHC.

### CERN's Accelerator Complex

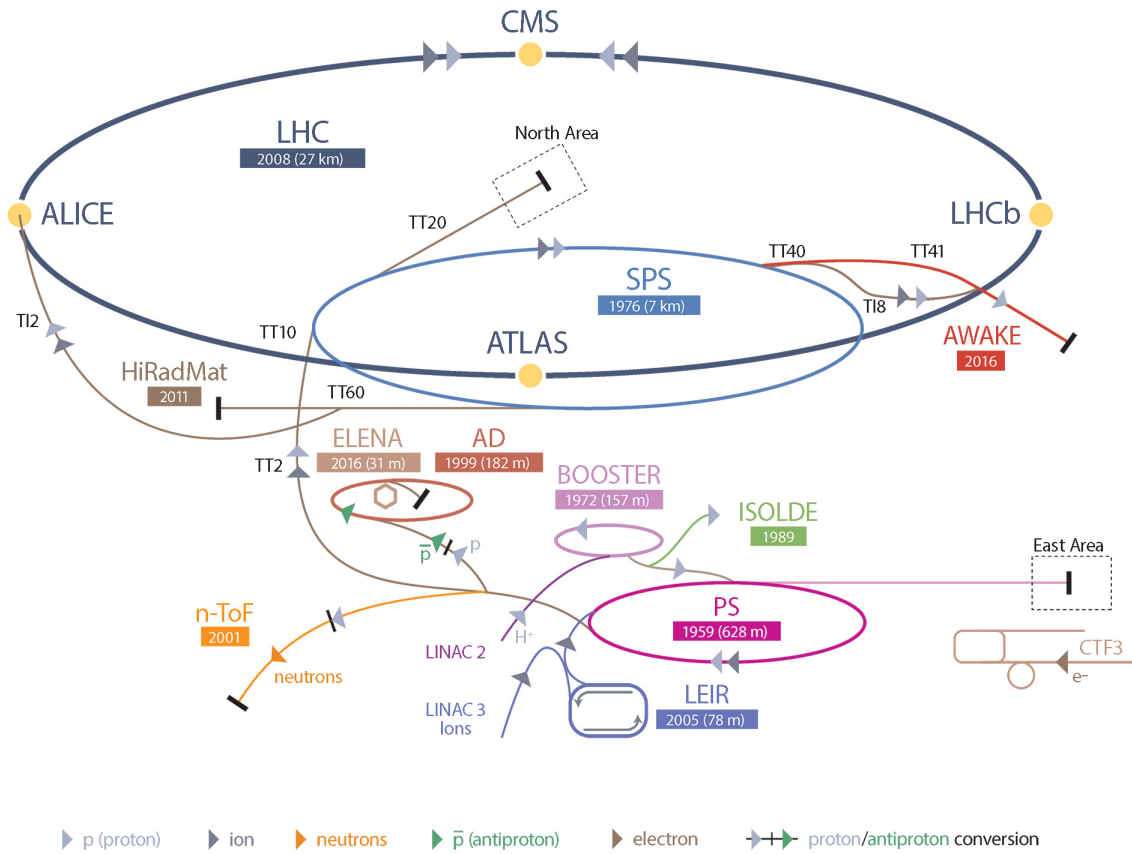


Figure 2.4: CERN accelerator complex.

#### 2.2.1.1 Particle acceleration

The LHC is the last of a long series of accelerating devices. Before being accelerated by the LHC, the particles need to pass through different acceleration stages. All these acceleration stages are visible on Figure 2.4 and pictures of the accelerators are showed in Figure 2.5.

The story of accelerated protons at CERN starts with a bottle of hydrogen gas injected into the source chamber of the linear particle accelerator *LINAC 2* in which a strong electric field strips the

1295 electron off the hydrogen molecules only to keep their nuclei, the protons. The cylindrical conductors,  
 1296 alternatively positively or negatively charged by radiofrequency cavities, accelerate protons by  
 1297 pushing them from behind and pulling them from the front and ultimately give them an energy of  
 1298 50 MeV, increasing their mass by 5% in the process.

1299

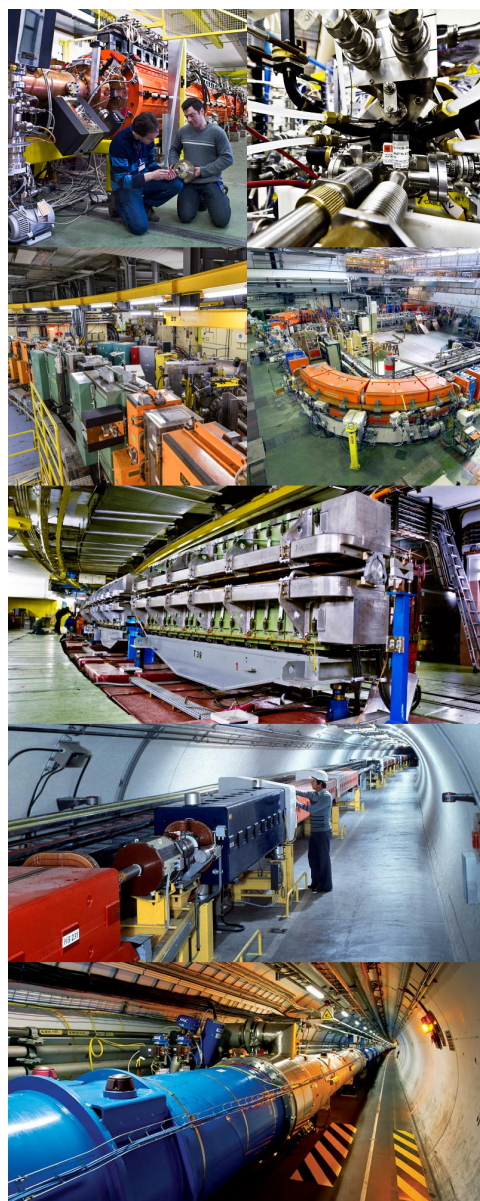


*Figure 2.5: Pictures of the different accelerators. From top to bottom: first the LINAC 2 and the Pb source of LINAC 3. Then the Booster and the LEIR. Finally, the PS, the SPS and the LHC.*

1300 When exiting the LINAC 2, the protons are divided into 4 bunches and injected into the 4 superimposed  
 1301 synchrotron rings of the *Booster* where they are then accelerated to reach an energy of

1302 1.4 GeV before being injected into the PS. Before the Booster was operational in 1972, the protons  
 1303 were directly injected into the PS from the LINAC 2 but the low injection energy limited the amount  
 1304 of protons that could be accelerated at once by the PS. With the Booster, the PS accepts approxi-  
 1305 mately 100 times more particles.

1306

1307 The 4 proton bunches are thus sent as one to the PS where their energy eventually reaches  
 1308 26 GeV. Since the 70s, the main goal of this 628 m circumference synchrotron has been to sup-  
 1309 ply other machines with accelerated particles. Nowadays, not only the PS accelerates protons, it also  
 1310 accelerates heavy ions from the *Low Energy Ion Ring (LEIR)*. Indeed, the LHC experiments are not  
 1311 only designed to study *pp*-collisions but also *Pb*-collisions. Lead is first injected into the dedicated  
 1312 linear collider *LINAC 3*, that accelerate the ions using the same principle than LINAC 2. Electrons  
 1313 are striped off the lead ions all along the acceleration process and eventually, only bare nuclei are  
 1314 injected in the LEIR whose goal is to transform the long ion pulses received into short dense bunches  
 1315 for LHC. Ions injected and stored in the PS were aceelerated by the LEIR from 4.2 MeV to 72 MeV.

1316

1317 Directly following the PS, is finally the last acceleration stage before the LHC, the 7 km long  
 1318 *SPS*. The SPS accelerates the protons to 450 GeV and inject proton in both LHC accelerator rings  
 1319 that will increase their energy up to 7 TeV. When the LHC runs with heavy lead ions for ALICE  
 1320 and LHCb, ions are injected and accelerated to reach the energy of 2.8 TeV/A.

1321

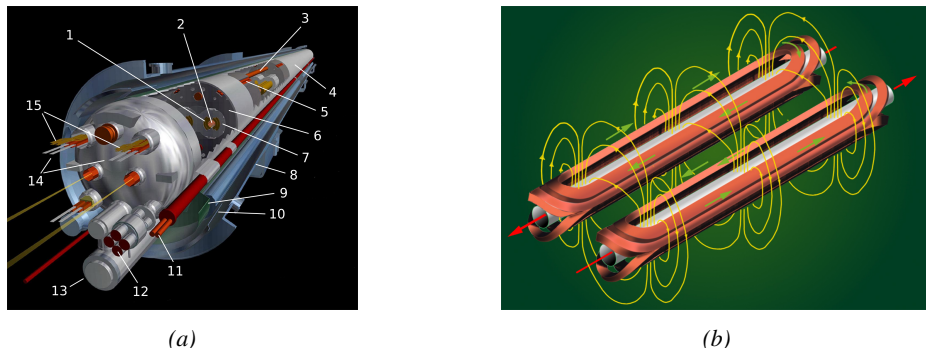
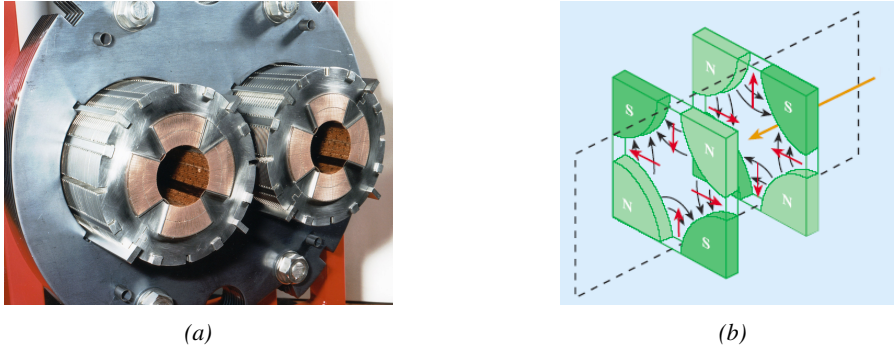


Figure 2.6: Figure 2.6a: schematics of the LHC cryodipoles. 1: Superconducting Coils, 2: Beam pipe, 3: Heat exchanger Pipe, 4: Helium-II Vessel, 5: Superconducting Bus-bar, 6: Iron Yoke, 7: Non-Magnetic Collars, 8: Vacuum Vessel, 9: Radiation Screen, 10: Thermal Shield, 11: Auxiliary Bus-bar Tube, 12: Instrumentation Feed Throughs, 13: Protection Diode, 14: Quadrupole Bus-bars, 15: Spool Piece Bus-bars. Figure 2.6b: magnetic field and resulting motion force applied on the beam particles.

1322

1323 The LHC beams are not continuous and are rather organised in bunch of paticles. When in *pp*-  
 1324 collision mode, the beams are composed of 2808 bunches of  $1.15 \times 10^{11}$  protons separated by 25 ns.  
 1325 When in *Pb* collision mode, the 592 *Pb* bunches are on the contrary composed of  $2.2 \times 10^8$  ions  
 1326 separated by 100 ns. The two parrallel proton beams of the LHC are contained in a single twin-  
 1327 bore magnet due to the space restriction in the LEP tunnel. Indeed, building 2 completely separate  
 1328 accelerator rings next to each other was impossible. The dipoles of the 1232 twin-bore magnets are  
 1329 showed in Figure 2.6 alongside the magnetic field generated along the dipole section to accelerate the  
 1330 particles. The dipoles generate a nominal field of 8.33 T, needed to give protons and lead nucleons  
 their nominal energy. Some 392 quadrupoles, presented in Figure 2.7, are also used to focus to the

1331 beams, as well as other multipoles to correct smaller imperfections.



1332 *Figure 2.7a: picture of the LHC quadrupoles. Figure 2.7b: magnetic fields and resulting focussing force applied on the beam by 2 consecutive quadrupoles.*

## 2.2.2 CMS, a multipurpose experiment

1333 Among the four main LHC experiments is the Compact Muon Solenoid used as a multipurpose tool to  
1334 investigate the SM and physics beyond its scope. Proposed through a letter of intention in 1992 [14],  
1335 and as its name suggests, this very compact detector's uses the muons as a clear tag of most of SM  
1336 and new physics interesting channels. In the original 1997 Technical Design Report (TDR) [21], the  
1337 very first sentences were stating that "*Muons are an unmistakable signature of most of the physics*  
1338 *LHC is designed to explore. The ability to trigger on and reconstruct muons at the highest luminosities is central to the concept of CMS, the Compact Muon Solenoid.*" CMS participated in the  
1339 discovery of the Higgs boson and the measurement of its properties and couplings together with  
1340 ATLAS and is also actively involved in the search for SUSY and heavy ion collisions. Other exotic  
1341 physics are also being investigated using the data collected by CMS.  
1342

1343 The CMS apparatus in itself is the heaviest detector ever built starring a SI15m diameter and a  
1344 29 m length for a total weight of 14 kT. A thick 4 T solenoid magnet located at the beam interaction  
1345 point hosts trackers and calorimeters. Extending in all directions around the magnet, heavy iron  
1346 return yokes are installed to extend the magnetic field and support a muon system. The apparatus  
1347 consists of a barrel, referring to the magnet and the detectors contained in it and the part of the muon  
1348 system built directly in the cylinder around the magnet, and of 2 endcaps in the forward and back-  
1349 ward region of the detector that closes the apparatus and complete the detection coverage along the  
1350 beam line. A front view on the barrel is provided in Figure 2.8 while a detailed view of the apparatus  
1351 is given in Figure 2.9.

1352 In order to efficiently detect all long leaving particles and measure their properties with good  
1353 precision, the CMS detector uses an onion like layout around of the interaction point in order to  
1354 maximize the covered solid angle. As detailed in Figure 2.10, in the innermost region of the detector,  
1355 closest to the interaction point, the silicon tracker records the trajectory of charged particles. Around  
1356 it, the electromagnetic calorimeter (ECAL) stops and measure the energy deposition of electrons  
1357 and photons. In the next layer, the hadron calorimeter (HCAL), hadrons are stopped and their energy  
1358 measured. These layers are contained inside of the magnet of CMS, the superconducting solenoid.  
1359 Outside of the magnet are the muon chambers embedded into iron return yokes used to control the  
1360

1361 magnetic field and gives muons, the only particles traveling completely through the whole detector, a  
 1362 double bending helping in reconstructing their energy and trajectory. Note that photons and neutral  
 1363 hadrons are differentiated from electrons and charged hadrons in the calorimeters by the fact that  
 1364 don't interact with the silicon tracker and that they are not influenced by the magnetic field.

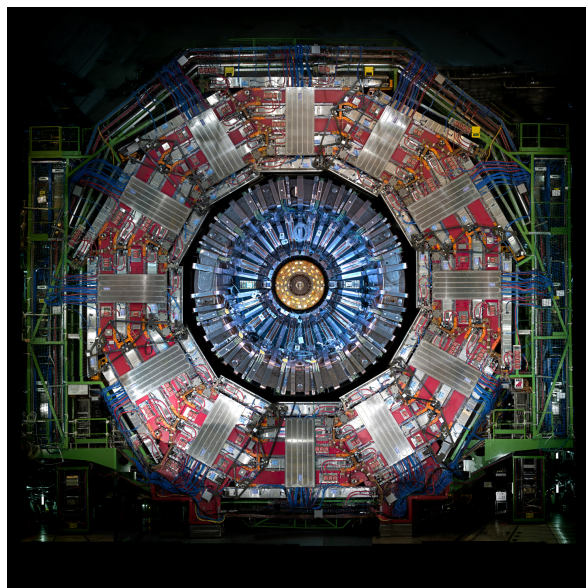


*Figure 2.8: Picture of the CMS barrel. The red outer layer is the muon system hosted into the red iron return yokes. The calorimeters are the blue cylinder inside in magnet solenoid and the tracker is the inner yellow cylinder built around the beam pipe.*

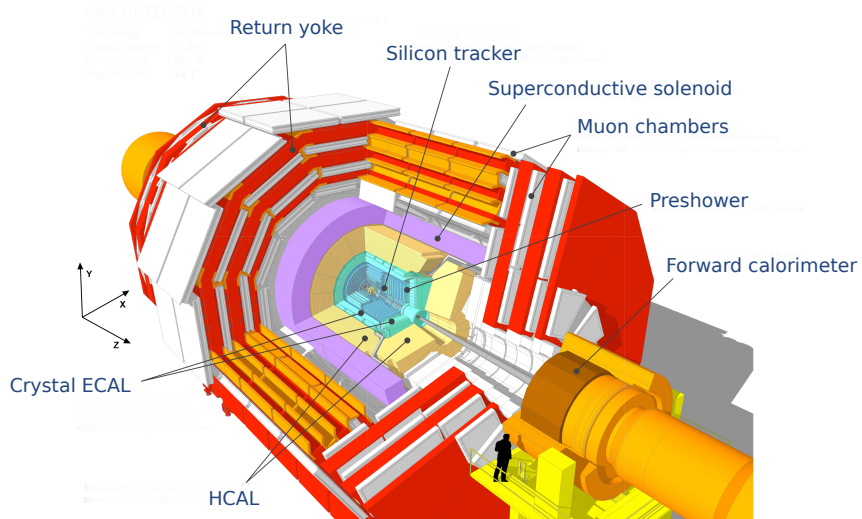


*Figure 2.9: View of the CMS apparatus and of its different components.*

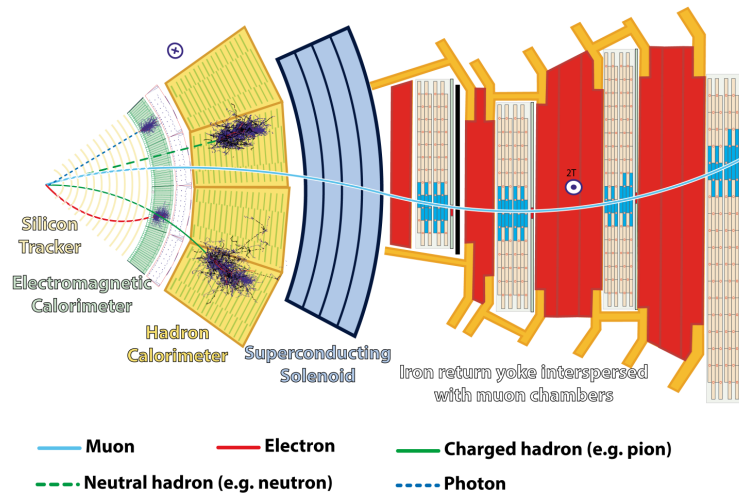


Figure 2.10: Slice showing CMS sub-detectors and how particles interact with them.

### 2.2.2.1 The silicon tracker, core of CMS

The silicon tracker visible on Figure 2.11 is divided into 2 different sub-systems: the *pixel detector* at the very core and the *microstrip detector* around it. This system is composed of 75 million individual readout channels with up to 6000 channels per squared centimeter for the pixels making it the world's biggest silicon detector. This density allows for measurements of the particle tracks with a precision of the order of  $10\ \mu\text{m}$ . This is necessary to reconstruct all the different interaction vertices with precision and have a precise measure of the curvature of the charged particles traveling through the magnetic field to estimate their charge and momentum.

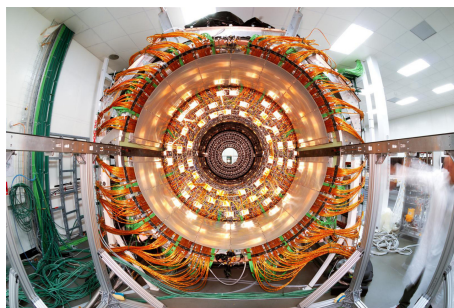
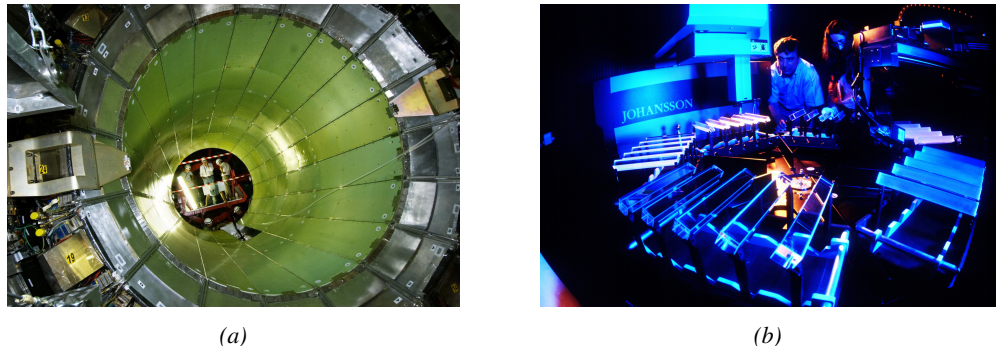


Figure 2.11: CMS tracker.

### 2.2.2.2 The calorimeters, measurement of particle's energy

The ECAL directly surrounding the tracker is composed of crystals of lead tungstate,  $\text{PbWO}_4$ , a very dense but optically transparent material used to stop high energy electrons and photons. These crystal blocks basically are extremely dense scintillators which scintillate in fast, short light bursts proportionally to the energy deposition. The light is yielded rapidly and contained at 80% in the corresponding 25 ns lasting bunch crossing. Each crystal is isolated from the other by the carbon fiber matrix they are embedded in. It is composed of a barrel containing more than 60,000 crystals

1380 and of closing endcaps containing another 15,000 crystals. In front of the ECAL endcap is installed  
 1381 a preshower detector made out of two layers of lead and silicon strip detectors to increase the spatial  
 1382 resolution close to the beam line for pion-photon and single-double photon discrimination purposes.  
 1383 Figure 2.12 shows the calorimeter inside of the magnet and the crystals.



*Figure 2.12: Figure 2.12a: picture of the ECAL. Figure 2.12b: picture of the lead tungstate crystals composing the ECAL.*

1384 The next layer is the HCAL measuring the hadrons momentum and providing indirect hints of  
 1385 non interacting neutral particles, such as neutrinos, as missing transverse momentum. Several layers  
 1386 of brass or steel are interleaved with plastic scintillators readout by photodiodes using wavelength-  
 1387 shifting fibers. The HCAL is also composed of a barrel, showed in Figure 2.13 and of endcaps. It  
 1388 also features forward calorimeters on both sides of CMS in the region very close to the beam line at  
 1389 high pseudorapidity ( $3.0 < |\eta| < 5.0$ ). The role of these forward calorimeters, made using steel and  
 1390 quartz fibers, is to measure very energetic hadrons.



*Figure 2.13: CMS hadron calorimeter barrel.*

1391 Finally, in the outer region of the apparatus, a muon system is used to trigger on potentially  
 1392 interesting event by identifying muons. Indeed, the muon system is a very important part of the  
 1393 CMS trigger infrastructure designed to efficiently select data from the enormous data flow received  
 1394 by the detectors as the LHC delivers collisions at a rate of 40 MHz with a pile-ip of 20 to 30 collisions  
 1395 per bunch crossing during Phase-I and up to 200 during Phase-II, representing billions of interactions  
 1396 per second among which a large quantity are low energy collisions that are not likely to produce new  
 1397 reactions, and which is physically impossible for nowadays technologies to cope with. Working at  
 1398 a maximum rate of 100 kHz, the trigger system is able to select the 100,000 more interesting events

1399 by looking at the energy distribution of the interaction products and clear signatures like muons  
 1400 reconstructed by the muon system. the vast majority of these events will not finally be stored after  
 1401 physics tests are applied.

#### 1402 2.2.2.3 The muon system, corner stone of CMS

1403 The challenge for the muon system is to provide a robust and fast measurement of muons. Three  
 1404 different subsystems, and soon 4 after LS2, compose the muon system as showed in Figure 2.14 in  
 1405 which a quadrant of the CMS detector focused on muon system. Drift Tube (DT) are found in the  
 1406 barrel region covering the low pseudorapidity region where particles transverse momentum is lower  
 1407 and Cathode Strip Chamber (CSC) are found in the endcap region covering higher pseudorapidity  
 1408 region closer to beam line where particles have a stronger momentum. The redundancy of the system  
 1409 is insured by Resistive Plate Chamber (RPC) in both the barrel and endcap region. Nevertheless, the  
 1410 region closest to the beam line ( $|\eta| > 1.8$ ) was not equipped with RPCs. This lack of redundancy  
 1411 in the high pseudo rapidity region will be solved during LS2, the following Year End Technical  
 1412 Stop (YETS) in 2021 and 2022, and LS3 where the necessary services, detectors and Link System,  
 1413 that collects the data and synchronizes them, will be installed.

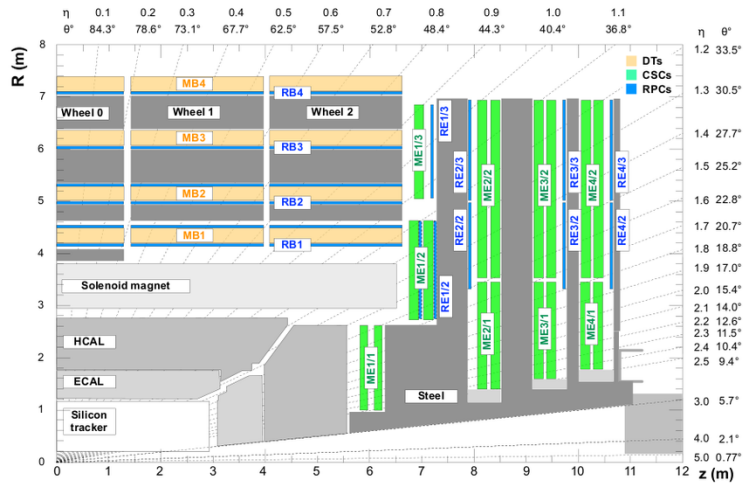
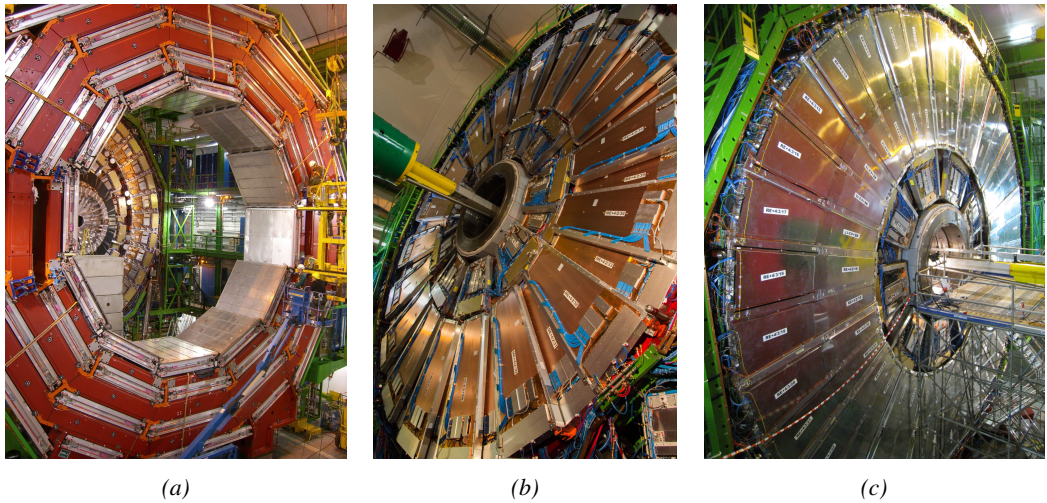


Figure 2.14: A quadrant of the muon system, showing DTs (yellow), RPCs (blue), and CSCs (green).

1414 The barrel region is divided into 5 *wheels* made out of 4 *rings* of detectors with iron return yokes  
 1415 in between them whereas the endcaps are made out of 4 disks, each divided into pseudorapidity  
 1416 stations, 2 for CSCs (except for the first disk where 3 stations are equipped) and 3 for RPCs, although  
 1417 only 2 RPCs stations are equipped at present. The wheels and disks are showed in Figure 2.15. So  
 1418 far, each subsystem was dedicated to a particular task. DTs, in the barrel, and CSCs, in the endcaps,  
 1419 are used mainly for their spatial resolution. Indeed, DTs' resolution is of the order of 100 μm along  
 1420 both the  $(r - \phi)$  and  $(r - z)$  components while the resolution of CSCs is similar but varies in a range  
 1421 from 50 μm to 140 μm depending on the distance to the beamline. On the other hand, RPCs are used  
 1422 for their time resolution as they can deliver an information on the muon tracks within 1.5 ns.

1423 The 250 CMS DTs, found in the barrel covering the pseudorapidity region  $0 < |\eta| < 1.2$   
 1424 and whose structure is shown in Figure 2.16, are composed of 3 *superlayers* of DT cells. Two of  
 1425 these superlayers are dedicated to measuring the  $\phi$  coordinate of the muons and while the last one

measures the  $\eta$  (or  $z$ ) coordinate. Each superlayer consists on 4 layers of 60 to 70 DT cells arranged in quincunx to allow for a precise reconstruction of the muon path through the DT layers. Each DT cell is a rectangular aluminium gas volume with a central anode wire. Cathode strips are placed on the narrow surface of the cells and electrode strips are placed on the wide surface to help shaping the electric field to ensure a consistent drift velocity of electrons in the drift volume. These detectors are operated using a 85/15 mixture of  $Ar$  and  $CO_2$ .



*Figure 2.15: Figure 2.15a: Barrel wheel with its detector rings and return yokes. Figure 2.15b: CSC endcap disk with the 2 CSC stations. The outer station is made of 10 deg detectors while the inner station is made of 20 deg detectors. Figure 2.15c: RPC endcap disk. The inner station is not equipped and the inner CSC station can be seen.*

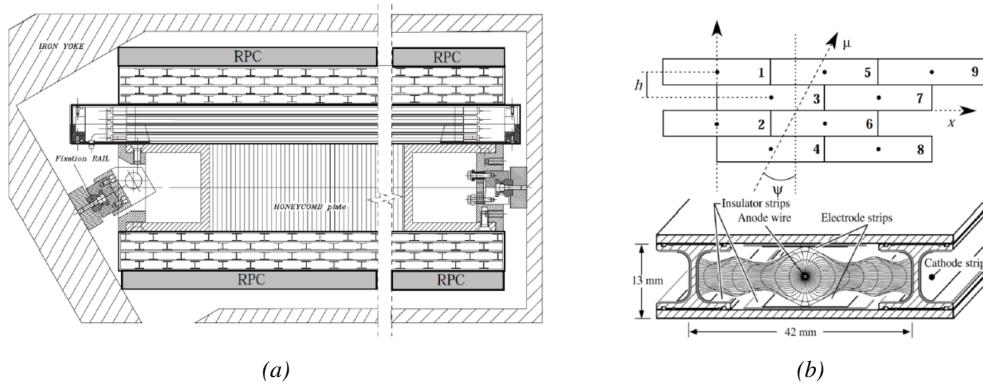


*Figure 2.16: Figure 2.16a: Cross section of a DT module showing the two superlayers measuring the  $\phi$  coordinate, perpendicular to the cross section plane, and the superlayer measuring the  $\eta$  coordinate, placed in between the two others with honeycomb and parallel to the cross section plane. The DT detector is sandwiched in between 2 RPCs whose readout strips are perpendicular to the cross section plane, measuring the  $\phi$  coordinate. Figure 2.16b: A DT cell is shown together with its electric field. The path of a muon through a superlayer is shown.*

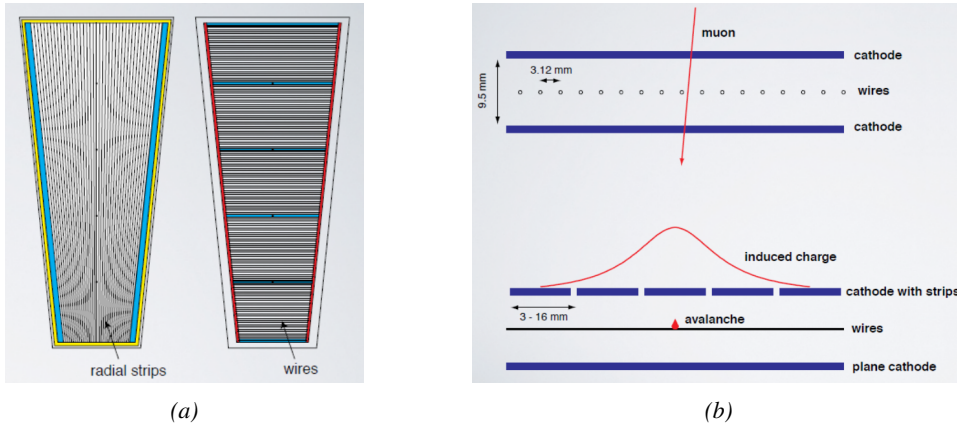


Figure 2.17: Figure 2.17a: cathode strips and anode wire layout of a CSC panel. Figure 2.17b avalanche development and charge collection by anode wires and induction on cathode strips inside of a CSC panel.

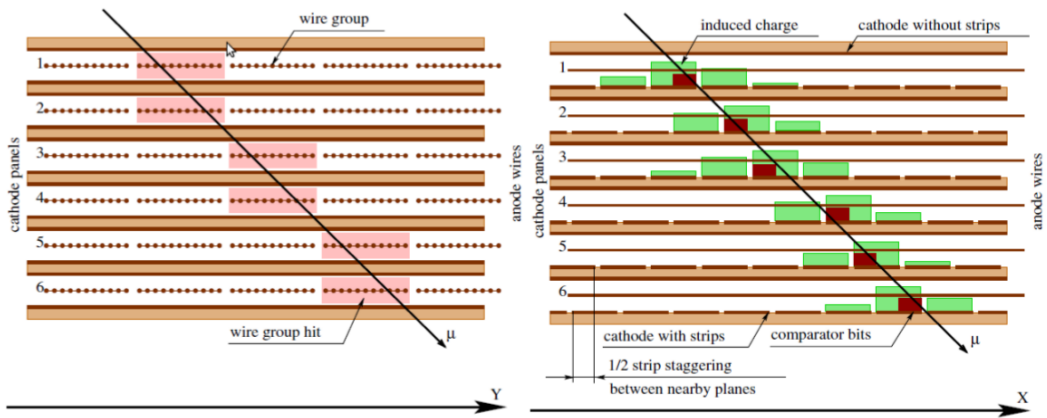


Figure 2.18: Muon track reconstruction through the 6 panels of a CMS CSC using the information of anode wire groups and cathode strip charge distribution combined with comparator bits to decide on which half strip the muon is more likely to have passed.

1432 The 540 CMS CSCs, found in the endcaps covering the pseudorapidity region  $0.9 < |\eta| < 2.5$   
 1433 and described through Figure 2.17, are composed of 6 panels of CSC, each panel consisting in  
 1434 a wide gas volume of 9.5 mm (7 mm in the case of ME1/1 station) containing anode wires and  
 1435 whose surfaces are cathodes. The top cathode is a wide copper plane of the size of the gas volume.  
 1436 The bottom cathode is divided into thin trapezoidal copper strips radially arranged to measure the  
 1437 azimuthal coordinate  $\phi$  with a pitch ranging from 8 to 16 mm. The  $0.50 \mu\text{m}$  anode wires are placed  
 1438 perpendicularly to the strips to measure radial coordinate  $r$  and are grouped by 10 to 15 with a wire  
 1439 to wire space of 3.2 mm. In the specific case of ME1/1 placed against the HCAL endcap, the  $0.30 \mu\text{m}$   
 1440 anode wires have a wire to wire distance of 2.5 mm and are not disposed perpendicularly to the strips  
 1441 but slightly tilted by an angle of 29 deg to compensate for the lorentz force due to the very strong  
 1442 local magnetic field of 4 T. These detectors are operated with a 40/50/10 mixture of Ar, CO<sub>2</sub> and  
 1443 CF<sub>4</sub>. Combining the information of the multiple CSC panels, the detectors achieve a very precise  
 1444 measurement of the muon track.

Despite their excellent spatial resolution, the wire chambers (DTs and CSCs) are limited in terms of time resolution by the fact that the charge needs to drift towards the anode wire and be collected before having the confirmation that a particle was detected as the drift volume is not used to develop avalanches. Indeed, the stronger electric field close to the anode wire triggers the avalanche and the gain of the detector. Due to the drift, the time resolution is thus limited at best to approximately 2 to 3 ns. In addition, even though the intrinsic time resolution of the tracking chambers is rather good compared to the 25 ns in between successive collisions, the processing time of the trigger system doesn't allow for very fast triggering as it provides a time precision of only 12.5 ns. Thus, detectors fully dedicated to timing measurement have been installed as a redundant system. These detectors are RPCs, also gaseous detectors but that use current induction instead of charge collection allowing for a time resolution of the order of 1.5 ns only. Theoretically, depending on the design used, RPCs could reach a time resolution of the order of 10 ps but in the context of LHC where bunch crossing happen every 25 ns, a time resolution of 1.5 ns is sufficient to accurately assign the right bunch crossing to each detected muon.

The 1056 RPCs equipping the CMS muon system both in the barrel and endcap regions and covering the pseudorapidity region  $0 < |\eta| < 1.6$  are composed of two layers of RPC *gaps* as described in Figure 2.19. Each gap consists in two resistive electrodes made out of 2 mm thick Bakelite enclosing a 2 mm thick gas volume containing a 95.2/4.5/0.3 mixture of  $C_2H_2F_4$ ,  $i - C_4H_{10}$  and  $SF_6$ . Due to this geometry, the electric field inside of a gap is homogeneous and linear at every point in the gas translating into a uniform development of avalanches in the gas volume as soon as a passing muon ionises the gas. The two gaps sandwich a readout copper strip plane. A negative voltage is applied on the outer electrodes, used as cathodes, and the inner electrodes, the anodes, are simply connected to the ground as well as the readout panel that picks up the current induced by the accumulated charge of the growing avalanches in one or both of the gas gaps. This OR system allows for a lower gain (i.e. a lower electric field) on both gaps to reach the maximal efficiency of such a detector.

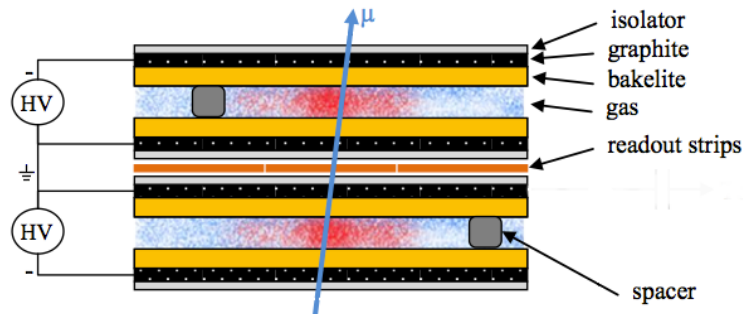


Figure 2.19: Double gap layout of CMS RPCs. Muons passing through the gas volumes will create electron-ion pairs by ionising the gas. this ionisation will immediately translate into a developing avalanche.



# 3

1471

1472

## Muon Phase-II Upgrade

1473 The very first proton beam successfully circulated in the LHC in September 2008 directly followed  
1474 by an incident leading to mechanical damage that would delay the LHC program for a year until  
1475 November 2009, the very first collisions at a center-of-mass energy of 7 TeV taking place in March  
1476 2010. The energy of the beam would be increased after a First Long Shutdown (LS1) starting early  
1477 2013 after less than 3 years of data taking. Nevertheless, this first data taking period at only 7 TeV  
1478 was sufficient to claim the discovery of a new particle compatible with the Higgs boson in July 2012.  
1479 During the 2 years of shutdown, the upgrade of the accelerator allowed for several maintainances  
1480 along the beam pipes, repair and consolidation of magnet connection and high-current splices. But  
1481 not only the LHC was upgraded. Indeed, the experiments at the 4 collision points also took the  
1482 advantage of this time to upgrade their system in prevision of the next LHC run (Run-II) until  
1483 2018 and the Second Long Shutdown (LS2) as the luminosity and energy of the beam would be  
1484 continuously increasing. By the end of Run-II, the luminosity will have reached twice its nominal  
1485 value when the center-of-mass energy has already got close to its nominal value by reaching an  
1486 historical 13 TeV for the first time in 2017.

1487 The next long shutdown will occur at the end of this year and will again be the occasion for sim-  
1488 ilar maintenance and consolidation in prevision of Run-III and the future upgrade of LS3. Still, the  
1489 main occupation of LS2 on LHC side will be the upgrade of LHC injectors. On the experiments side,  
1490 LHCb and ALICE will, in a very tight schedule, implement major upgrades while ATLAS and CMS  
1491 will wait until LS3 to upgrade their detectors in prevision of high luminosity *LHC-Phase-II*. ALICE  
1492 main challenge is an upgrade of their apparatus to cope with the 50 kHz  $Pb - Pb$  collisions. Simi-  
1493 larly, LHCb will upgrade their frontend readout electronics to cope with the full 40 MHz collisions  
1494 delivered by LHC. ATLAS will perform standard maintenance and CMS will focus on the urgent up-  
1495 grade of the pixel detector and on the installation of new muon detectors in order to take profit of LS2  
1496 time to mitigate the upgrade of detectors foreseen during LS3. Run-III will start in 2021 with the LHC  
1497 at its nominal center-of-mass energy and will bring LHC-Phase-I to an end at the end of 2023. By  
1498 then the luminosity will only increase to reach 2.5 times the nominal luminosity but during these 3  
1499 years of run, the LHC will deliver as much integrated luminosity as what what brought during the al-

most 7 years of both Run-I and II of data taking. Phase-I will end with an overall  $300 \text{ fb}^{-1}$  delivered.

1501

### 3.1 High Luminosity LHC and muon system requirements

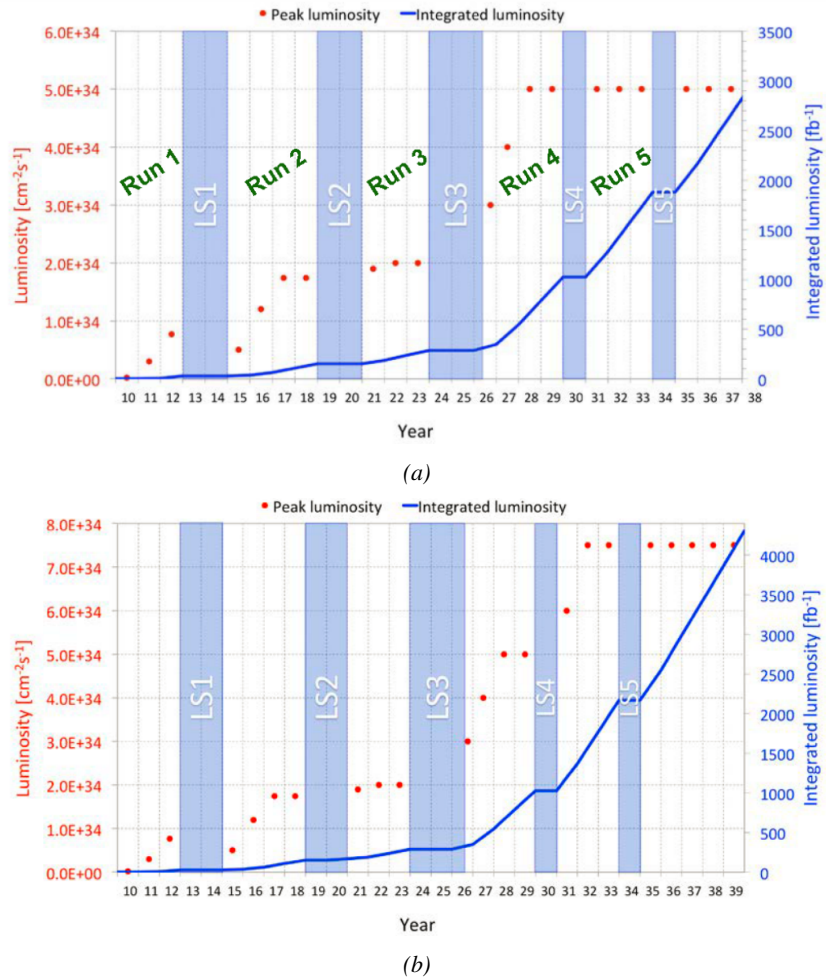


*Figure 3.1: Detailed timeline projection of for LHC and HL-LHC operation until 2039 showing the evolution of the instantaneous and integrated luminosity as designed (Figure 3.1a) and in the ultimate case where the instantaneous luminosity is increased to  $7.5 \times 10^{34} \text{ cm}^{-2}\text{s}^{-1}$  (Figure 3.1b) [20, 22].*

After approximately 15 years of operation, the LHC will undergo a new series of upgrade during the LS3 in order to boost its discovery potential as showed in Figure 3.1. This moment onward is what is referred to HL-LHC or Phase-II. The goal is to aim for a luminosity 5 to 7 times stronger than the nominal one trying to reach even 10 times this value if possible. Increasing the luminosity means that the beam size at the collision points needs to be reduced to boost the number of collisions per bunch crossing. For this purpose, new focusing and bending magnets, and collimators will be installed at the collision points as well as newly developed "crab cavities" that will tilt the particle

1503

1504

1505

1506

1507

1508

1509

1510 bunched just prior to the collisions by giving them transverse momentum and thus increasing their  
 1511 meeting area. In addition, the full proton injection line will be upgraded.

1512 Over its full lifetime, the HL-LHC is expected to deliver an outstanding integrated luminosity of  
 1513  $3000 \text{ fb}^{-1}$  leading, in the case of Higgs studies to measuring the couplings of the boson to a precision  
 1514 of 2 to 5% thanks to the estimated 15 millions of Higgs created every year providing a more precise  
 1515 measurement of potential deviations from the theoretical predictions. SUSY and heavy gauge boson  
 1516 studies would also see their mass range limits pushed away by at least 1 TeV and could lead to a new  
 1517 breakthrough. SUSY is a particularly important topic as it could give an answer to why the Higgs  
 1518 boson can stay so light while coupled to heavy particles by introducing the contributions of the super  
 1519 partners on top of providing dark matter candidates. Finally, the increase of luminosity will give the  
 1520 possibility to investigate "exotic" mode like for example the models introducing extra dimensions to  
 1521 explain the hierarchy problem.

1522 On the experiments side, the pile-up (PU) will be increased up to 150 to 200 interactions per  
 1523 bunch crossing in ATLAS and CMS, making necessary an strong upgrade of the trigger system and  
 1524 of the inner trackers and of the calorimeters. Both ATLAS and CMS will also need to upgrade  
 1525 the muon trigger at the level of the endcaps mainly focusing on the coverage near the beam line in  
 1526 order to increase the detection acceptance and event selection. Moreover, the increased luminosity  
 1527 will also lead to an increased background rate and a faster ageing of the detectors. This PhD work  
 1528 takes place into this very specific context of muon detector consolidation and certification for the  
 1529 HL-LHC period in order to provide the CMS experiment with robust new detectors and confirm that  
 1530 the present system will survive through the next 20 years of HL-LHC.

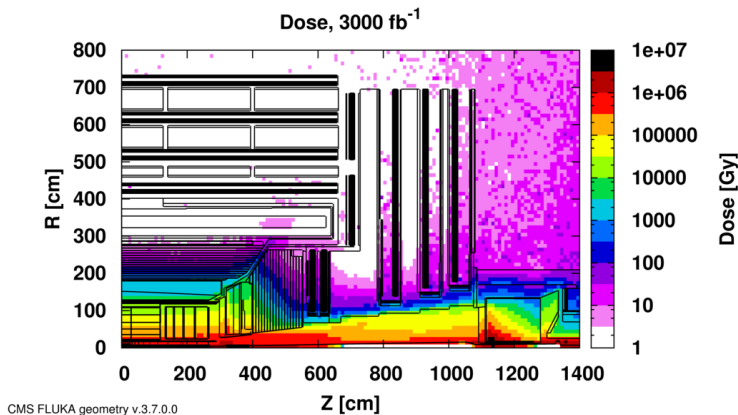
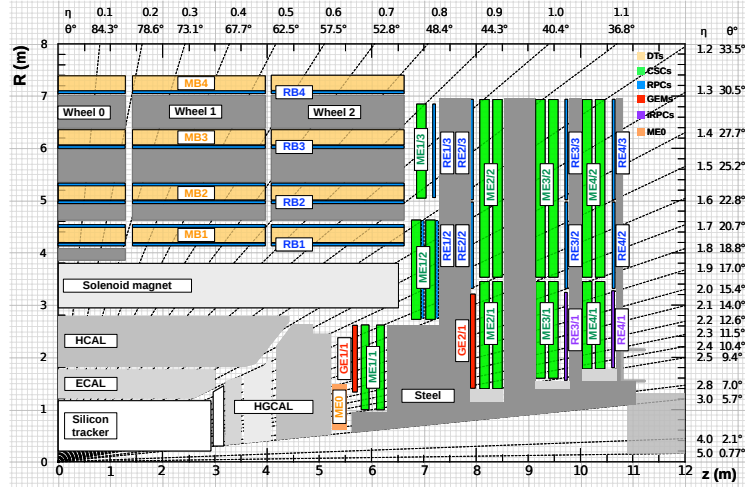


Figure 3.2: Absorbed dose in the CMS cavern after an integrated luminosity of  $3000 \text{ fb}^{-1}$ . Using the interaction point as reference,  $R$  is the transverse distance from the beamline and  $Z$  is the distance along the beamline.

1531 The end of 2018 will mark the beginning of LS2 and the start of Phase-II upgrade activities.  
 1532 From the HL-LHC period onwards, i.e. past LS3, the performance degradation due to integrated  
 1533 radiation as well as the average number of inelastic collisions per bunch crossing, seen as pile-up  
 1534 into the detectors' readout that far exceeds this of the original LHC plans, will rise substantially and  
 1535 become a major challenge for all of the LHC experiments, like CMS, that were forced to address  
 1536 an upgrade program for Phase-II [23]. Dealing with the data from the muon detectors will force  
 1537 to upgrade the detectors and electronics towards the most recent technologies. Simultaneously, this  
 1538 will push new latency requirements onto the Level-1 trigger and the Data Acquisition (DAQ) that

will only be fulfilled by upgrading the system with electronics having deeper buffering and faster processing. Simulations of the expected distribution of absorbed dose in the CMS detector under HL-LHC conditions show, in Figure 3.2, that detectors placed close to the beam line will have to withstand high irradiation, the radiation dose being of the order of a few tens of Gy.



**Figure 3.3:** A quadrant of the muon system, showing DTs (yellow), RPCs (blue), and CSCs (green). The locations of new forward muon detectors for Phase-II are contained within the dashed box and indicated in red for GEM stations (ME0, GE1/1, and GE2/1) and dark blue for improved RPC (iRPC) stations (RE3/I and RE4/1).

The increase of irradiation close to the beam line will affect the background rate seen by the muon detectors in this area and tracking muons will prove to be difficult as this region is not yet equipped with all the detectors that were already foreseen for Phase-I. Improving this situation will come with the increase of hit numbers recorded along the particle track to reduce the ambiguity on muon versus background detection. Moreover, the measurement of small production cross-section and/or decay branching ratio processes, such as the Higgs boson coupling to charge leptons, and in particular to muons, or the  $B_s \rightarrow \mu^+ \mu^-$  decay, is of major interest and specific upgrades in the forward regions of the detector will be required to maximize the physics acceptance to the largest possible solid angle.

To ensure proper trigger performance within the present coverage, the muon system will be completed with new chambers and the electronics of the present system will need to be upgraded to ensure an efficient triggering. Figure 3.3 shows the addition of Gas Electron Multiplier (GEM) and improved RPC (iRPC) in the pseudo-rapidity region  $1.6 < |\eta| < 2.4$  to complete the redundancy of the already existing CSCs as originally scheduled in the CMS Technical Proposal [24]. A first step into this direction will be taken by installing GEMs on the first endcap disk in position GE1/1 during LS2, during which preparations for the future installation of more GEMs and RPCs will take place by installing the needed services. During the YETS following LS2, iRPCs will be installed on the third and fourth endcap disks in position RE3/1 and RE4/1, and more GEMs will equip the second endcap in position GE2/1 and the inner layer, closest to the HCAL endcap called ME0 during LS3, finally completing the redundant coverage of the muon system and extending it a little by extending the reach to  $|\eta| = 2.8$ , the redundancy in the region  $2.4 < |\eta| < 2.8$  being maintained by the 6 GEM layers contained in each ME0 detector that provide enough tracking points to efficiently reject

1565 neutron-induced background.

1566 Nevertheless, the region beyond  $|\eta| > 2.8$  and extending to  $|\eta| = 5.0$  only is covered by the  
 1567 forward HCAL detectors and lack redundant muon detector coverage. Extensions of the tracker in  
 1568 the context of HL-LHC will increase its coverage up to  $|\eta| = 4.0$  but the identification of muons and  
 1569 measurement of their energy with reasonable precision only using the tracker is nearly impossible.  
 1570 Thus, this increased tracker coverage range needs to be put in parallel with a matching muon detector  
 1571 and will open doors to multi-lepton final states in which leptons are likely to have a low transverse  
 1572 momentum and to be found near the beam line.

1573

1574 Finally, as the muon system is composed only of gaseous detectors, strong environmental con-  
 1575 cerns have risen over the last years as the European directives will restrict the use of fluorine based  
 1576 gas mixtures. Both the CSC and RPC subsystems, using  $CF_4$ ,  $C_2H_2F_4$ , or  $SF_6$ , will need to adapt  
 1577 their working gas in order to strongly reduce the greenhouse potential of the mixtures released into  
 1578 the atmosphere due to gas leaks.

## 1579 3.2 Necessity for improved electronics

1580 Drift Tubes and Cathode Strip Chambers are important components used to identify and measure  
 1581 muons, especially thanks to their spatial resolution of the order of  $100\ \mu m$ . Nevertheless, the lumi-  
 1582 nosity and irradiation during HL-LHC will cause serious event loss and ageing on the electronics of  
 1583 these subsystems that will comprise the triggering and data transferring needs of CMS. Thus, elec-  
 1584 tronics upgrade are foreseen to address these expected problems. While only the RPCs' electronic  
 1585 system is able to operate under Phase-II requirements, DTs and CSCs will need to improve their  
 1586 trigger accept rate and latency to ensure that Level-1 trigger threshold stays at the same level [25],  
 1587 and DAQ data transfer rate, that respectively need to achieve a minimum of  $500\ kHz$ , get down to  
 1588  $12.5\ \mu s$  [26], and increase to  $1082\ Gbit/s$  DTs and to  $1026\ Gbit/s$  for CSCs. As of today, the Level-  
 1589 1 trigger accept rate of DTs doesn't reach  $300\ kHz$  while this of CSCs is below  $250\ kHz$  but the  
 1590 foreseen upgrades are expected to increase the rate way beyond the requirement in the of DTs and  
 1591 up to  $4\ MHz$  for CSCs [23].

1592 The first version of Minicrate electronics (MiC1) used by DTs don't allow for high enough  
 1593 trigger rate. In addition to this problem, it was showed that these electronics contain components  
 1594 that are not radiation hard enough to sustain HL-LHC conditions and thus, a too large number of  
 1595 channels may fail due to radiations. Considering the most optimistic scenario, at least 19% of the  
 1596 channels could have failed by LS4, as explicitated in Figure 3.4, far before the end of the HL-LHC  
 1597 campain. The MiC1 will be replaced on each detector by an improved version referred to as MiC2  
 1598 while front-end electronics and high-voltage modules will not need any replacement. On the other  
 1599 hand, CSCs showed that there electronics would be able to live through the 10 years of Phase-II but  
 1600 the limited buffer depth might cause memory overflows and readout inefficiencies with a fraction  
 1601 of event loss ranging from 5 to more than 10% at an instantaneous luminosity similar to which of  
 1602 HL-LHC depending on the expected background, as showed on Figure 3.5 through the different  
 1603 detector positions. Thus the replacement of CSCs' cathode front-end boards (CFEBs) by digital  
 1604 ones, DCFEBS, with deeper buffer would permit to make event loss negligible and satisfy HL-LHC  
 1605 requirements [23].

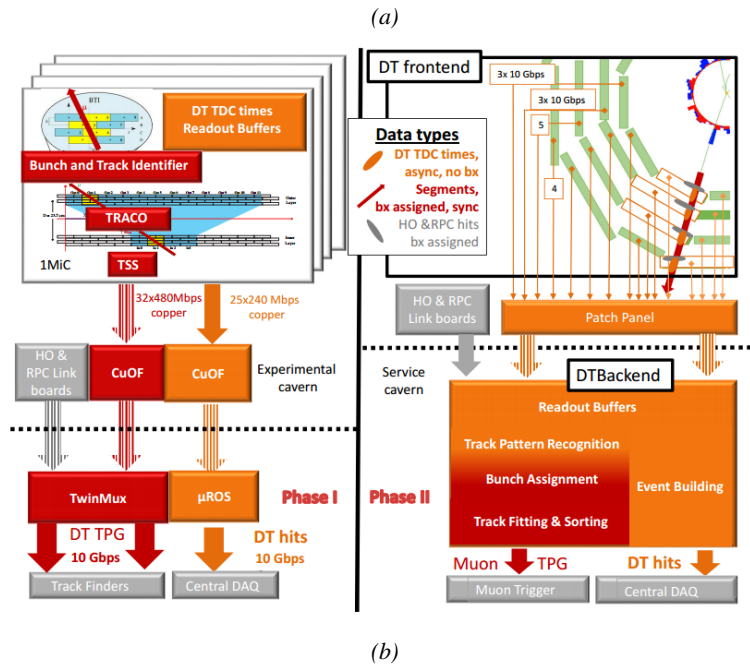
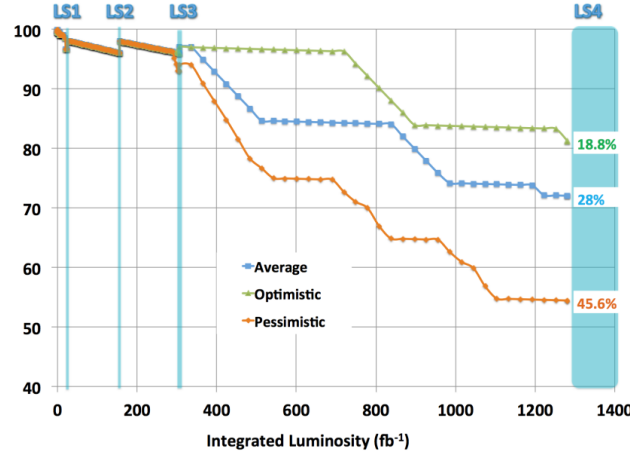


*Figure 3.4: Figure 3.4a: Extrapolated fraction of failing channels of the present DT MiC1 electronics as a function of the integrated luminosity for different scenari until LS4. Figure 3.4b: Comparison of the current (left) and upgraded (right) DT data processing. So far, the data is sent to service cavern of CMS facility via copper-to-optical-fiber translators (CuOF) by each MiC1. There, data including RPCs and outer hadron calorimeter is combined into trigger primitives (TPG) and transmitted by the TwinMux system to CMS Track Finder. The time-to-digital converter (TDC) data is collected and sent to the CMS data acquisition system (DAQ) by the micro read-out server ( $\mu$ ROS). After the upgrade, the TDC data will be sent via optical links to a patch panel inside the experimental cavern by each MiC2, and transferred to the back-end, where triggering and event building will be performed.*

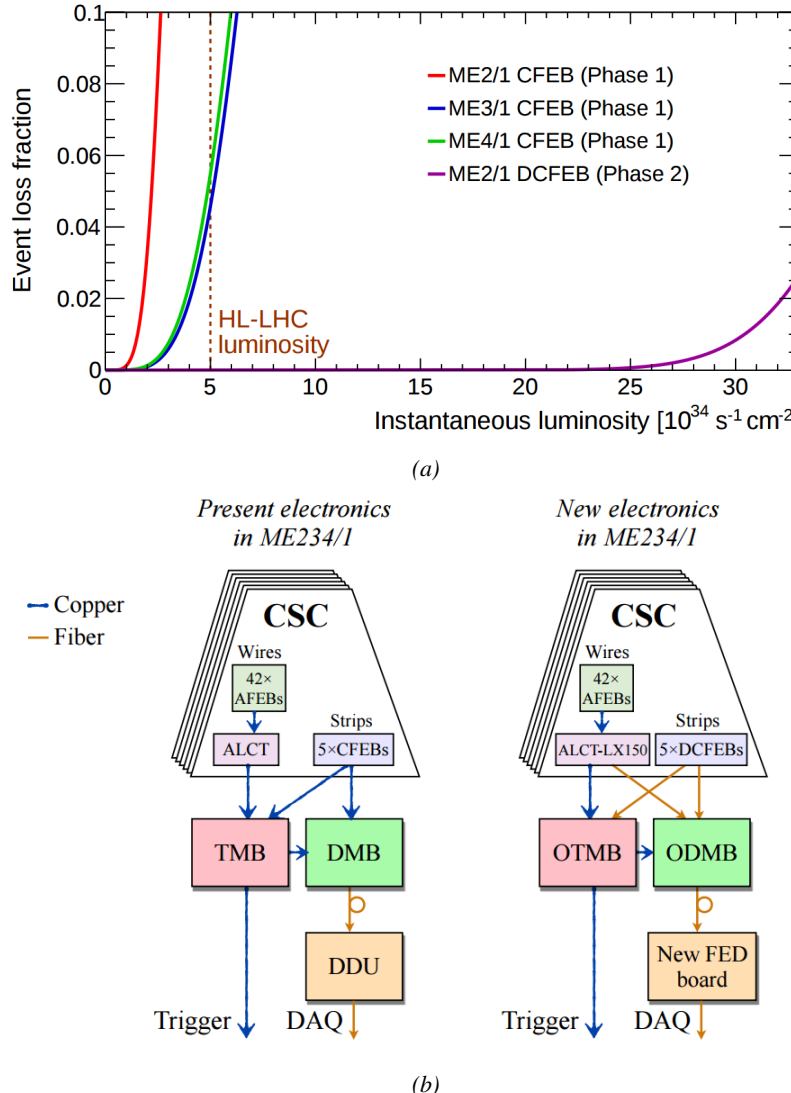
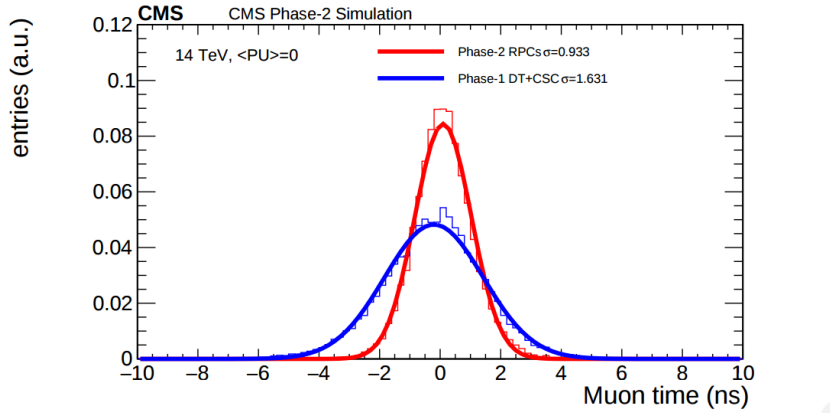


Figure 3.5: Figure 3.5a: The event loss fractions as a function of the instantaneous luminosity is compared for CFEBs (Phase-1) and DCFEBs (Phase-II) at different CSC locations. HL-LHC luminosity is marked with the dashed brown line. Figure 3.5b: Comparison of the current (left) and upgraded (right) CSC data processing. A part of the connections in between ALCTs and DCFEBs, and the trigger mother boards (TMBs) and data acquisition mother boards (DMBs) will be upgraded toward optical data transfer. The detector dependent units (DDUs) used as interface in between CSCs' front-end electronics and the CMS DAQ will be replaced by new FED boards.

All these new DT and CSC electronics will be connected to the trigger electronics via optical links to ensure a faster communication. The main change will come from the new DT minicrate modules which will not anymore be responsible for trigger and event building logic which will be transferred to the back-end electronics instead located in the service cavern via the patch panels to which the Time-to-Digital Converter (TDC) data will be sent. The trigger and data transfer logic will barely change for CSCs. The existing copper cable connections of cathode and anode FEBs (CFEBs,

and AFEBs which data is transmitted through the ALCTs) toward the trigger and data mother boards (TMBs and DMBs) will simply be replaced by optical fibers and the TMBs and DMBs upgraded with optical versions (OTMBS and ODMBs). As a new feature, the full anode wire data from ALCTs will be sent to the ODMBs causing a lack of FPGA memory resources in these ALCT boards that will thus need replacement.



*Figure 3.6: Comparison of the simulated time residuals in between reconstructed and true muon times without (blue) and with (red) the upgraded RPC link system.*

The upgrade on the side of Resistive Plate Chambers will then not come from their on-board electronics but from the Link System located in the service cavern of CMS and that connects the front-end electronics data of RPCs into CMS trigger processors. The main motivation for such an upgrade is that the electronic board composing the link system are built using obsolete components and weak components that can easily suffer from the electromagnetic noise. These components may be the source of failing channels throughout Phase-II. Moreover, these link boards were originally designed only to match RPC digitized signals with the corresponding bunch crossing. Due to this feature, the time resolution of the full RPC chain is thus limited to 25 ns and does not exploit the full time resolution of the detectors. This would make the synchronization of the RPC system easier and allow to have a finer offline background removal within the 25 ns in between bunch crossings thanks to the order of magnitude gained in terms of time resolution.

Upgrading RPC link system will require the installation of 1376 new link boards and 216 control boards. The new boards will make use of the recent progress made with fast FPGAs and will be a great improvement to the ASICs formerly used as they will be able to process signals from several detectors in parallel. The benefit from using the full RPC time resolution thanks to the upgraded link system can be seen through Figure 3.6 where the resolution of the RPC system itself is better than that of DTs and CSCs that was used until now.

### 3.3 New detectors and increased acceptance

In the present muon system, the redundancy of was assured by RPCs used for their good timing performances. The extension of the muon system towards higher pseudo-rapidity in order to complete the redundancy in this very region and to contribute to the precision of muon momentum measurements will require muon chambers with a spatial resolution less or comparable to the contribution

<sup>1639</sup> muon of multiple scattering through the detector volume [21]. Most of the plausible physics is  
<sup>1640</sup> covered only considering muons with  $p_T < 100$  GeV thus, in order to match CMS requirements,  
<sup>1641</sup> a spatial resolution of  $\mathcal{O}(\text{few mm})$  will be necessary for the proposed new RPC stations while the  
<sup>1642</sup> GEMs will need a resolution better than 1 mm, as showed by the simulation in Figure 3.7.

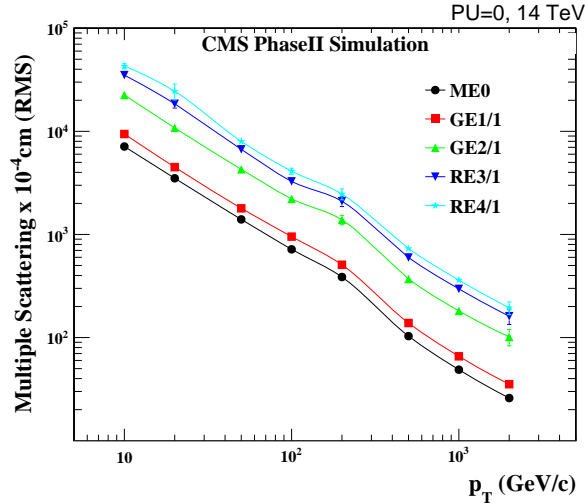


*Figure 3.7: RMS of the multiple scattering displacement as a function of muon  $p_T$  for the proposed forward muon stations. All of the electromagnetic processes such as bremsstrahlung and magnetic field effect are included in the simulation.*

### <sup>1643</sup> 3.3.1 Improved forward resistive plate chambers

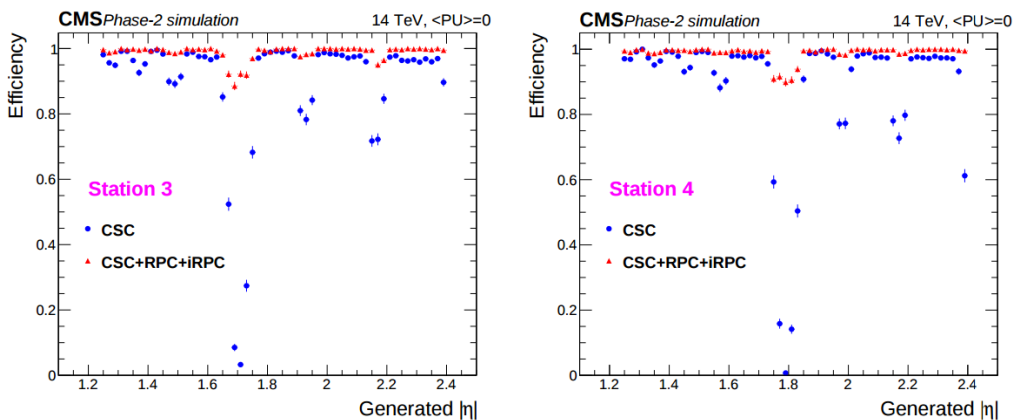


*Figure 3.8: Simulation of the impact of RPC hit inclusion onto the local trigger primitive efficiency in station 3 (left) and station 4 (right). The contribution of iRPC starts above  $|\eta| = 1.8$ .*

<sup>1644</sup> Figure 3.3 shows that the iRPCs that will equip the third and fourth endcap disks in position RE3/1  
<sup>1645</sup> and RE4/1 will finally be the partners of the CSCs in position ME3/1 and ME4/1 and complete  
<sup>1646</sup> Phase-I plans but bringing the needed upgrades in the scope of Phase-II as the older chambers are

not suitable to equip the forward region of CMS due to HL-LHC rates and charge deposition. By completing the redundancy, more track along the muon trajectory will be available and the lever arm will be improved. The benefits from extending the redundancy of the muon system with iRPCs to the forward most region is showed in Figure 3.8 in which the trigger efficiency is showed with and without RPCs in which it is possible to see that the efficiency of CMS trigger with the complete redundancy is improved is above 95% in the region  $|\eta| > 1.8$  as the iRPCs help filling the holes in the CSC system.

1654

The detectors that will be installed in the coming years will be similar to the already existing RPC system. 18 of the new chambers, each spanning  $20^\circ$  in  $\varphi$  around the beam axis with 96 radially oriented trapezoidal read-out strips, will cover each muon endcap disk leading to the production of 72 iRPCs. The main difference with the old RPC chambers is that these detectors will not have readout strips segmented in  $\eta$  as by using fast front-end electronics the strips will be read-out on both sides allowing for a radial spatial resolution of the order of 2 cm in order to contribute to the better reconstruction of muon in the forward region where the bending of muons by the magnetic field is low. This is motivated by the fact that, in the case a  $\eta$  segmentation was used, at least 5 pseudorapidity partitions would have been necessary to reach the minimal radial spatial resolution ( $\approx 20$  cm). Having only one strip read-out from both along the chamber reduces by 60% the total number of channels and the necessary cabling and allows for a better spatial resolution. The strip pitch will range from 6.0 mm (5.9 mm) on the high pseudo-rapidity end to 12.3 mm (10.9 mm) on the low one on position RE3/1 (RE4/1). The spatial resolution in the direction perpendicular to the strips should reach approximately 3 mm, better than the minimal needed resolution (Figure 3.7), and the overall time resolution of the new installation will be equally 1.5 ns, as for the present due to the same link system being used.

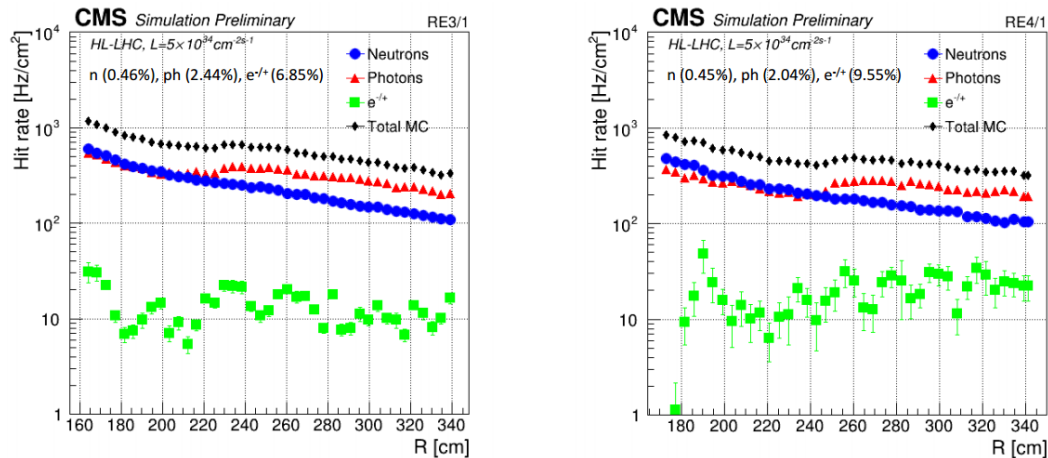


*Figure 3.9: Expected hit rate due to neutrons, photons, electrons and positrons at HL-HLC instantaneous luminosity of  $5 \times 10^{34} \text{ cm}^{-2}\text{s}^{-1}$  in RE3/1 and RE4/1 chambers. The sensitivities of iRPCs used in the simulation for each particle are reported and differ from one endcap disk to another as the energies of the considered particles varies with the increasing distance from the interaction point.*

Nevertheless, having only a single strip instead of pseudo-rapidity segmentation will increase the probability of double hits in the same channel. This probability was estimated to be low enough

as it shouldn't exceed 0.7%. This estimation was made assuming an average hit rate per unit area of 600 Hz/cm<sup>2</sup> in the iRPCs (see Figure 3.9), a cluster size (average number of strips fired per muon) of 2, a strip active area of 158.4 × 0.87 cm<sup>2</sup> and a safety factor 3 leading to an estimated rate per strip of 380 kHz corresponding to an average time interval of 2600 ns in between 2 consecutive hits. The time for a signal to go through the full strip length is about 10 ns to which can be added 1 ns of dead time and 2 TDC clock cycles of 2.5 ns for a minimal time interval of 16 ns necessary to avoid ambiguities. The probability of having ambiguous double hits in a strip in then the ratio in between this minimal time interval in between 2 consecutive hits and the average time interval estimated from the rate the detectors are subjected to.

The instantaneous luminosity at HL-LHC being very high, the rates at the level of the new chambers needed to be simulated in order to understand the necessary requirements for these detectors. The simulated results for different background components (neutrons, photons, electrons and positrons) are showed in Figure 3.9 assuming known sensitivities to these particles. It is showed that on average over the iRPC areas the rates would be of the order of 600 Hz/cm<sup>2</sup> (600 Hz/cm<sup>2</sup> seen in RE3/1 and 480 Hz/cm<sup>2</sup> in RE4/1) [27]. Thus, taking into account a safety factor of about 3, it was decided that improved RPCs should at least be certified for rates reaching 2 kHz/cm<sup>2</sup> which would be achieved thanks to several improvements on the design and on the electronics. The detectors design will be based on the existing RPC design as they will be double gaps. Similarly to the existing RPC system, the electrode material will be HPL although the thickness of the electrodes and of the gas gap will be reduced to 1.4 mm as a thinner gas gap leads to a decrease of deposited charge per avalanche as showed in Figure 3.10. The smaller the gas gap, the more the detector becomes sensitive to gap non-uniformities across the electrode planes making a gap of 1.4 mm a good compromise in between these two competing factors.

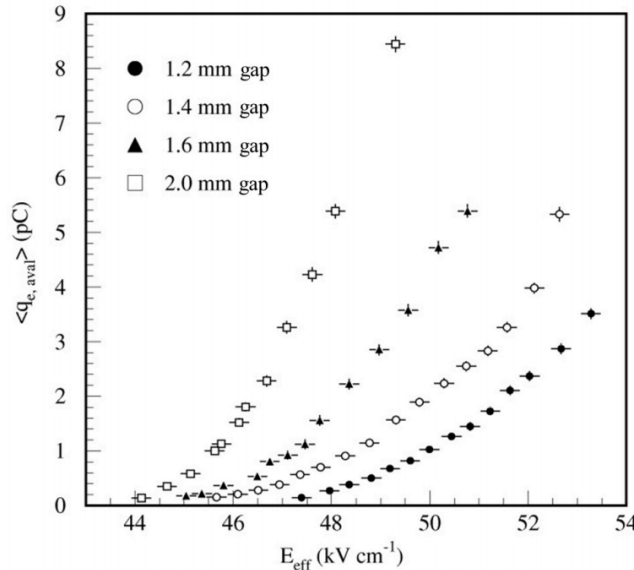


Figure 3.10: Measured average charge per avalanche as a function of the effective electric field for different gas gap thickness in double gap RPCs using HPL electrodes.

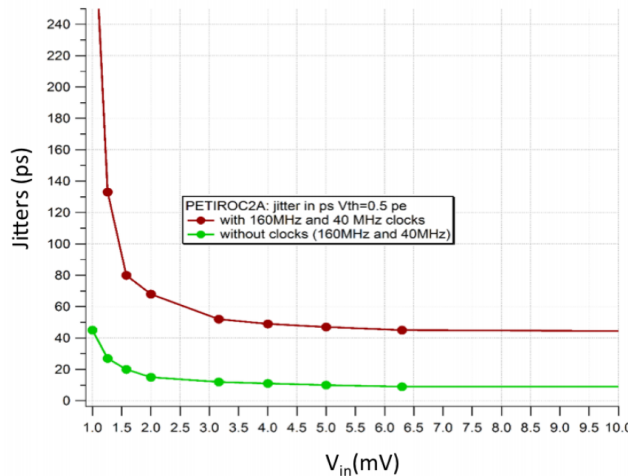


Figure 3.11: The PETIROC time jitter as a function of the input signal amplitude, measured with and without internal clocks.

1696 A lower charge deposition inside of the detector volume means a slower ageing and a longer life-  
 1697 time for detectors subjected to high irradiation. But, in order to take advantage of the lower detector  
 1698 gain, more sensitive electronics are required so that the part of gain that was formerly done in the gas  
 1699 volume can be moved to the electronics. Achieving this with the technology developed more than  
 1700 10 years ago for the present system is not possible as the signal over noise ratio of such electronics  
 1701 doesn't allow to detect charges as low as 10 fC. Moreover, the new front-end electronics will need  
 1702 to be radiation hard to survive to more than 10 years of HL-LHC conditions. The new technology  
 1703 that has been chosen is based on the PETIROC ASIC manufactured by OMEGA and is a 64-channel  
 1704 ASIC called CMS RPCROC on which the original SiGe technology will be replaced by CMOS to  
 1705 increase its radiation hardness while keeping fast pre-amplification and discrimination with a very  
 1706 low jitter that can reach less than 20 ps if no internal clock is used, as can be seen from Figure 3.11.  
 1707 The ASIC is associated with an FPGA which purpose is to measure time thanks to a TDC with a  
 1708 time resolution of 50-100 ps developed by Tsinghua University and that will provide a measurement  
 1709 of the signal position along the strip with a precision of a few cm by measuring the signal timing  
 1710 on both ends of the strips. In order to read-out all 96 strips, 3 ASICs and 3 TDCs, each having 64  
 1711 channels, are hosted on a front-end board attached to the chamber.  
 1712

1713 [Wait for the analysis of 2018 GIF++ data to add interesting information about the time and  
 1714 spatial resolution measured during test beam periods.]  
 1715

### 1716 3.3.2 Gas electron multipliers

1717 In the region closer to the interaction point where the spatial resolution is requested to be better  
 1718 than 1 mm for the new detectors (at least for GE1/1 and ME0, GE2/1 being in the same order of  
 1719 requested spatial resolution than the new iRPCs that will equip the third and fourth endcaps), the  
 1720 choice has been made to use triple GEMs, micro pattern gaseous detectors, in the place of RPCs.  
 1721 The GE1/1 project had been the first to be approved and demonstrators had been installed in CMS

<sup>1722</sup> already during LS1. The rest of the detectors will be installed during LS2 while the GE2/1 and ME0  
<sup>1723</sup> projects are still under development. ME0, GE1/1 and GE2/1 will be installed respectively next to  
<sup>1724</sup> the HCAL endcap, on the first and on the second muon endcap disks as can be seen from Figure 3.3.

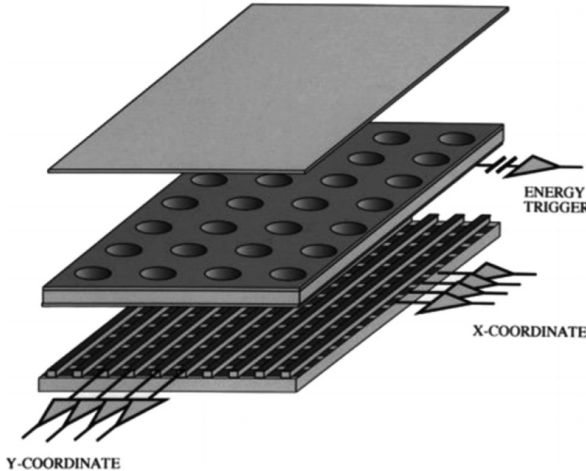


*Figure 3.12: Schematics of a GEM showing the cathode on top, the GEM foil separating the gas volume into the drift region, in between the cathode and foil, and the induction region, in between the GEM foil and the anode, and the anode on which a 2D read-out is installed. A negative voltage is applied on the cathode while the anode is connected to the ground.*

<sup>1725</sup> Gas Electron multipliers are gaseous detectors [28] which gas volume is confined in between  
<sup>1726</sup> 2 planar electrodes, the anode serving as read-out panel. The gas volume is divided in 2 or more  
<sup>1727</sup> regions by a single or multiple *GEM foils* as showed in Figure 3.12. These foils are very thin, of  
<sup>1728</sup> the order of a few tens of  $\mu\text{m}$ , and are pierced with holes as can be seen in Figure 3.13. Both  
<sup>1729</sup> surfaces of the GEM foils are clad with copper in order to apply a strong electric field in between  
<sup>1730</sup> each side that will generate very strong potentials in the holes. The gas region contained in between  
<sup>1731</sup> the cathode and the GEM foil is called the drift region as the electric field is not strong enough to  
<sup>1732</sup> cause avalanches and thus start an amplification. The primary electrons drift toward the foil and are  
<sup>1733</sup> accelerated and amplify by the very high potential within the holes, as showed in Figure 3.13. Then  
<sup>1734</sup> the electrons reach the second drift region in which they will induce signal on the read-out located  
<sup>1735</sup> on the anode. By restraining the amplification process at the level of the holes, the electrons can stay  
<sup>1736</sup> in a very confined space and thus induce a very localized current, providing the GEMs with a very  
<sup>1737</sup> good spatial resolution.

<sup>1738</sup> In order to achieve a stronger amplification, the amplification process can be repeated several  
<sup>1739</sup> times in a row. The GEMs that will be used in CMS are triple GEM detectors operated with a 70/30  
<sup>1740</sup> gas mixture of  $\text{Ar}/\text{CO}_2$ . They contain 3 GEM foils and thus 3 electron amplifications, as can be  
<sup>1741</sup> seen in Figure 3.14. The GEM foils used in CMS are 50  $\mu\text{m}$  foils clad with 5  $\mu\text{m}$  of copper on  
<sup>1742</sup> each side. The foils are pierced with double-canonical holes which inner and outer diameters are  
<sup>1743</sup> respectively 50 and 70  $\mu\text{m}$  which are placed 140  $\mu\text{m}$  from each other in an hexagonal pattern, as  
<sup>1744</sup> showed in Figure 3.13. These detectors have a time resolution better than 10 ns and reach very good  
<sup>1745</sup> spatial resolutions of less than 200  $\mu\text{rad}$  as indeed the position of the hits is not measured along the  
<sup>1746</sup> strips but following the azimuthal angle granularity of the radially organized trapezoidal strips.

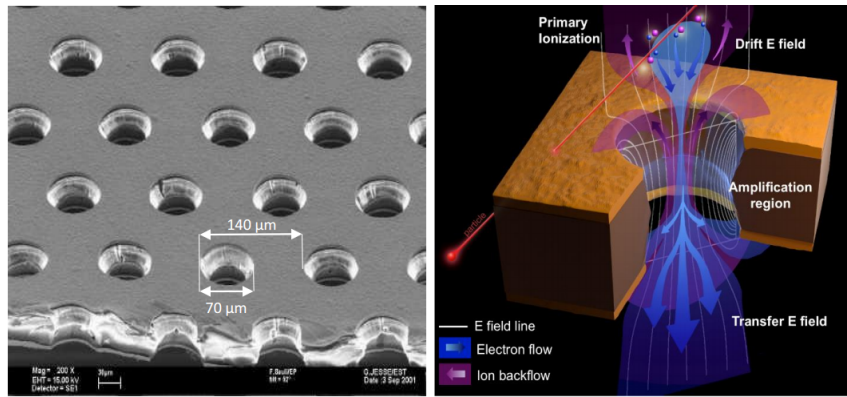


*Figure 3.13: Left: Picture of a CMS GEM foil provided by a scanning electron microscope. Right: Representation of the electric field lines in a GEM hole and of the amplification that electrons and ions undergo in the hole's volume due to the very intense electric field.*

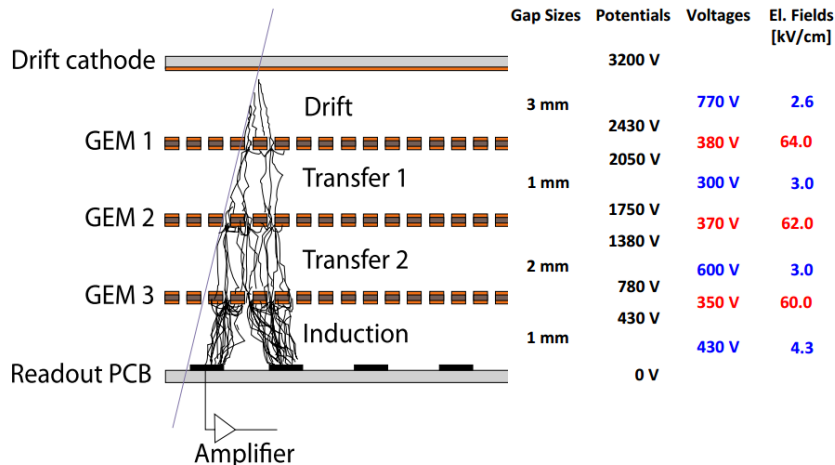


*Figure 3.14: Schematic representation of CMS triple GEMs. The gas volume is divided into 4 areas. The drift area is the region where the primary electrons are created before being amplified a first time while passing through the first GEM foil. Then the process of drift and amplification is repeated twice in following two transfer areas and GEM foils. Finally, the charges have been amplified enough to induce current in the read-out strips while in the last drift area. The dimensions, potentials and electric fields are provided.*

1747 The GEM Upgrade is divided into 3 subsystems as GE1/1 was the first approved project [29]  
 1748 and that the detectors will already be installed during LS2. GE2/1 and ME0, on the other hand,  
 1749 will profit of the R&D knowledge and skills developed for GE1/1 while the requirements for each  
 1750 subsystem are different as they are not placed at the same distance from the interaction point. In this  
 1751 very forward region, a different position with respect to the center of the detector can change dra-  
 1752 matically the conditions in which the detectors will have to be operated. In terms of rate capability,  
 1753 GE2/1, which is the furthest, is required to withstand 2.1 kHz/cm<sup>2</sup> while GE1/1 needs to be better  
 1754 than 10 kHz/cm<sup>2</sup> and ME0, better than 150 kHz/cm<sup>2</sup>. In terms of ageing with respect to charge  
 1755 deposition, ME0 needs to be certified to 840 mC/cm<sup>2</sup>, GE1/1 to 200 mC/cm<sup>2</sup> and GE2/1 only to

1756 9 mC/cm<sup>2</sup>. All 3 detectors need to have a time resolution better than 10 ns and an angular resolution  
 1757 better than 500 µrad.

1758 On each GE1/1 ring, 36 super chambers, consisting of 2 single GEM layers and spanning 10°,  
 1759 will be installed covering the pseudo-rapidity region  $1.6 < |\eta| < 2.2$  together with ME1/1 CSCs and  
 1760 the reach of the muon system will be improved thanks to the GE2/1 that will overlap with the GE1/1  
 1761 and cover a region from  $|\eta| > 1.6$  to  $|\eta| < 2.4$  and complete the redundancy of ME2/1. The super  
 1762 chambers, built with 2 triple GEM layers each consisting of 4 single GEM modules due to the rather  
 1763 large surface of the GE2/1 chambers, that will be installed on the first ring of the second endcap will  
 1764 span 20° each, hence, a total of 72 chambers will be assembled to equip the muon system. Finally,  
 1765 the ME0 installed near the HCAL endcap will cover the region  $2.0 < |\eta| < 2.8$  and this subsystem  
 1766 will consist in super modules of 6 layers of triple GEM detectors covering an azimuthal angle of 20°  
 1767 leading to the construction of 216 single detectors.

1768 All these new GEM detectors will be using a similar internal layout which is described in Figure  
 1769 3.14. The incoming muons will create detectable electron-ion pairs in the 3 mm thick drift  
 1770 volume in which an electric field of 2.6 kV/cm is applied for the electrons to drift to the first GEM  
 1771 foil on which a very intense field of 64 kV/cm is applied over a distance of only 60 µm which allows  
 1772 for an average electronic gain of 20 to 25. After the first amplification stage, the electrons drift over  
 1773 the 1 mm separating the 2 first GEM foils thanks to an electric field of 3.0 kV/cm and are again  
 1774 amplified by a factor 20 to 25 while going through the second GEM foil to which is applied an elec-  
 1775 tric field of 62 kV/cm. The electron drift another 2 mm towards the last GEM foil through a field of  
 1776 3.0 kV/cm and are multiplied one last time from a similar factor passing through the 60 kV/cm  
 1777 of the last GEM foil holes. Finally, they drift along the 1 mm of the induction volume in a field of  
 1778 4.3 kV/cm to reach the trapezoidal strips on the read-out PCB used as anode. The total detector  
 1779 gain is approximately of the order of  $10^4$  and the resulting output signal is both due to the induction  
 1780 of moving charges in the induction volume and of charge pic-up once they read the read-out strips.

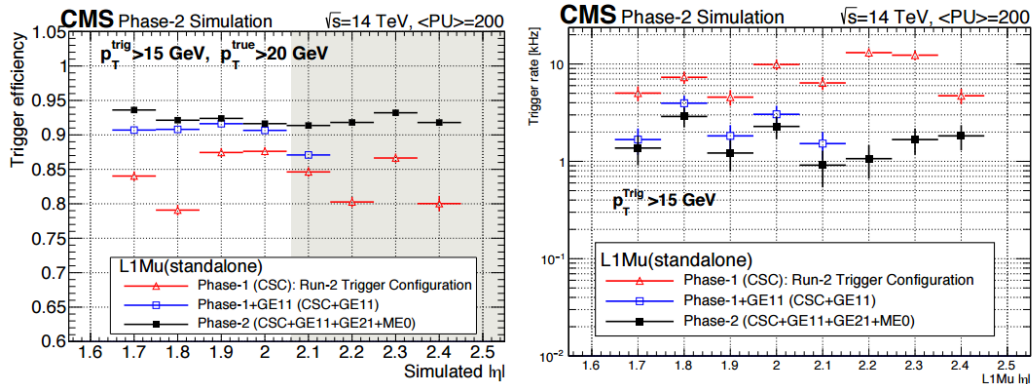


Figure 3.15: Simulated efficiency and rate of the standalone Level-1 muon trigger using tracks reconstructed in CSCs and all GEM stations compared with Phase-I values in the case where only CSCs are used or CSCs+GE1/1. The zones of inefficiency of the CSC subsystem are compensated by the addition of GEMs during Phase-II and the trigger rates is kept from increasing due to the high luminosity.

1781 Adding the GEMs into the forward region of the muon system will allow to strongly enhance  
 1782 the Level-1 Trigger performance by reducing the inefficiency regions and the trigger rate as showed  
 1783 in Figure 3.15. Moreover, benefiting from the good spatial and angular resolution of the GEMs, the

<sup>1784</sup> precision into the muon measurement will also be greatly improved by the addition of GEMs as can  
<sup>1785</sup> be seen from the simulation presented in Figure 3.16.

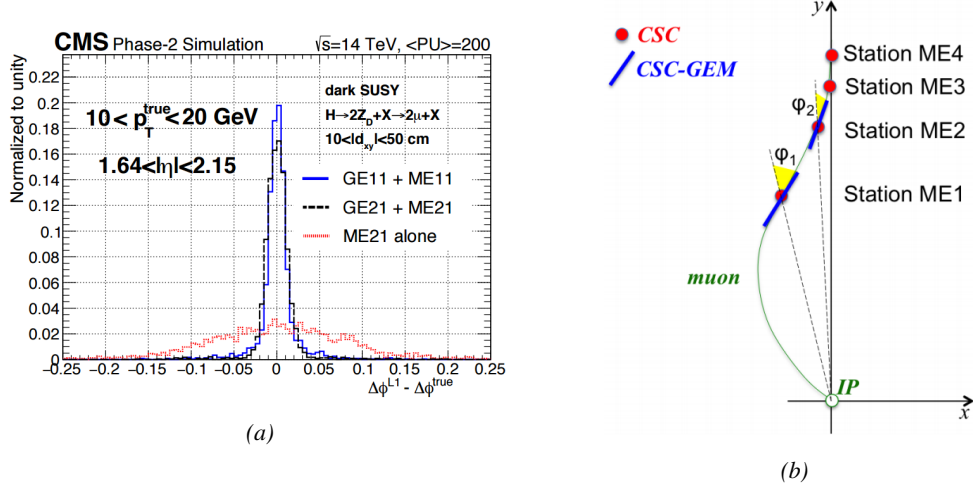


Figure 3.16: Figure 3.16a: Simulated resolution of the muon direction measurement  $\Delta\phi$  with Phase-II conditions. In the second endcap station, the resolution is compared in the case of CSCs (ME2/I) alone and CSCs+GEMs (GE2/I+ME2/I) while a similar resolution measurement is given in the case of the first station (GE1/I+ME1/I). Figure 3.16b: The addition of GEM detectors on stations 1 and 2 (ME0 is considered to contribute to station station 1) as redundant system to CSCs allows to improve the muon momentum improvement through a more accurate measurement of the local bending angles  $\phi_1$  and  $\phi_2$ .

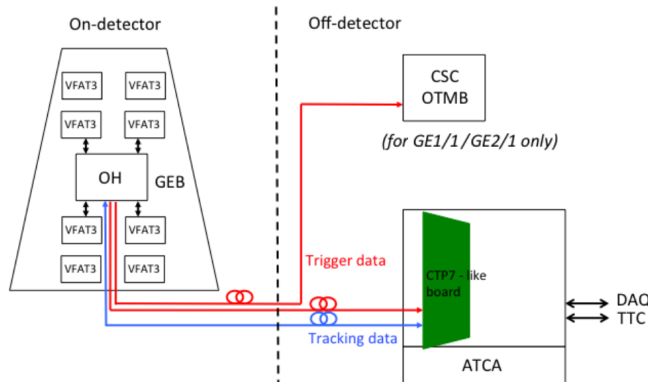


Figure 3.17: Schematics of the data communication chain for DAQ of the GEM subsystems. The sending of trigger data via optical links to the CSC OTMBs is only done for GE1/I and GE2/I to match the data with ME1/I and ME2/I.

<sup>1786</sup> The read-out of GEMs will use the same technology. The anode planes used as read-out PCBs  
<sup>1787</sup> and referred to as GEM Electronics board (GEB) host on their outer surface VFAT3 ASICs that  
<sup>1788</sup> connect to a total of 128 strips for a very fine angular granularity. Along the endcap radius, the strips are  
<sup>1789</sup> divided into 8 pseudo-rapidity partitions. In the case of GE1/I and ME0, each  $\eta$ -partition consist in  
<sup>1790</sup> 384 read-out strips connected into 3 VFAT3 ASICs and offering a while the large GE2/I partitions

1791 contain twice as many channels. Both GE1/1 and GE2/1 strips have an angular pitch of  $474\text{ }\mu\text{m}$   
 1792 while this of ME0 is twice larger due to its proximity with the interaction point. The VFAT3 ASICs  
 1793 allow for a latency better than the  $12.5\text{ }\mu\text{s}$  required by CMS Level-1 Trigger and there frequencies  
 1794 goes up to 1 MHz. They are connected into the Optohybrid Board (OH) and this full ensemble  
 1795 (GEB+VAT3+OH) constitute the on-chamber electronics. The OH is then sending the data to the  
 1796 modules constituting the DAQ of the GEM system via optical fibers. These back-end electronics  
 1797 modules are located in the service cavern of CMS and host CMS communication devices, used to  
 1798 have a common clock, and control and links to the Endcap Muon Track Finder (EMTF) system.  
 1799 Moreover, GE1/1 and GE2/1 also have links with the CSC OTMBs as the OH of these 2 subsystems  
 1800 send data into these boards. This communication chain can be seen in Figure 3.17.

1801

1802 The detectors that will placed in CMS will have to live through Phase-II without significant  
 1803 performance degradation to ensure an efficient data taking and the possibility to investigate more  
 1804 exotic physics. As the 3 GEM subsystems will be using the same detector technology, the choice  
 1805 was made to certify the GEMs in the worst of the 3 environments, i.e. the ME0 station located right  
 1806 behind the HCAL. According to FLUKA simulation, including all the latest foreseen upgrades into  
 1807 the CMS detector geometry, it was shown that the maximal hit rate expected in ME0 would be of  
 1808 the order of  $50\text{ kHz/cm}^2$  with contributions of neutrons ( $6\text{ kHz/cm}^2$ ), photons ( $35\text{ kHz/cm}^2$ ), and  
 1809 electrons and positrons ( $8\text{ kHz/cm}^2$ ) resulting in a charge deposition a little lower than  $300\text{ mC/cm}^2$   
 1810 after 10 years of HL-LHC [23]. It is necessary to understand the classical ageing effects on the GEMs  
 1811 but also premature ageing due to contaminants in the gas mixture leading to polymerization on the  
 1812 surface of the GEM foils during operation and the effect of discharges on the detector operations if  
 1813 they have to happen during their lifetime.

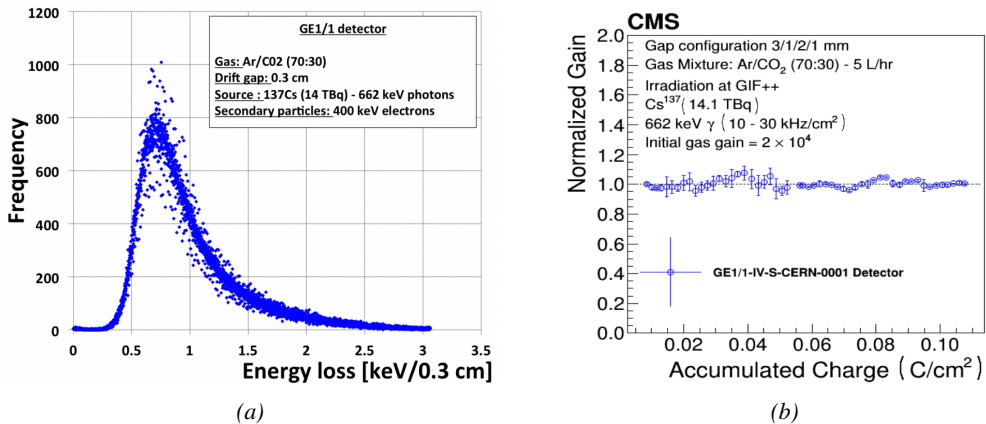


Figure 3.18: Figure 3.18a: Energy spectrum of  $\text{GIF}^{++}$   $^{137}\text{Cs}$  source as measured by the GE1/1 detector installed in  $\text{GIF}^{++}$ . Figure 3.18b: Evolution of the normalized gain of the GE1/1 detector installed at in  $\text{GIF}^{++}$  as a function of the integrated charge per unit area. The first part of the study, up to a charge of  $55\text{ mC/cm}^2$  had been done in the former Gamma Irradiation Facility (GIF) that has now been dismantled following the construction of  $\text{GIF}^{++}$ . No variation of the normalized gain can be observed after an accumulation of  $110\text{ mC/cm}^2$ .

1814

To characterize the classical ageing effects, a campaign is being conducted in the new Gamma Irradiation Facility ( $\text{GIF}^{++}$ ) of CERN where a GE1/1 detector operated at its nominal gain is placed 50 cm from the facility's 14 TBq  $^{137}\text{Cs}$  source which emits gammas at an energy of 662 keV. In

1815

1816

order to spot any ageing of the detector, the effective gain is kept monitored, as can be seen in Figure 3.18b, as its variations gives clues about different aspects of the detector such as the geometry of the holes, the electric field configuration or the gas composition. The monitoring of the gamma energy distribution, showed on Figure 3.18a, can give an idea on the evolution of the performance of the chamber and finally, the evolution of the currents through time also is a good indicator of the appearance of dark current in the detector that would be due to the emission of electrons by thin insulating layers of the detector subjected to a long lasting irradiation known as Malter effect. At the time the Technical Design Report (TDR) for the Phase-II upgrade of the muon system was written [23], the GEM group had reported a total integrated charge of  $110 \text{ mC/cm}^2$  which, if compared with 10 years of HL-LHC operation, represents a safety factor of 18 for the GE1/1 subsystem and a factor 37 for the GE2/1 subsystem but only 39% of the total expected ME0 integrated charge. It is estimated that reaching the total integrated charge necessary to certify the detectors for Phase-II operation will take another 2 to 3 years. Nevertheless, the present status of the longevity study shows no degradation of the performance of the detector installed in GIF++ as can be seen through Figure 3.18.

Aside of the classical ageing tests, outgassing of the different materials composing the GEMs have been conducted by placing the different materials to be tested into an outgassing box that consists in a stainless steel cylinder through which the CMS GEM 70/30 gas mixture of  $\text{Ar}/\text{CO}_2$  with the possible contaminants is flowed while the detector is exposed to the continuous irradiation of a radioactive source and the heat is raised to enhance the outgassing. From the detector that was placed into this outgassing box, only one component was identified to cause loss of performance due to outgassing. This component was the polyurethane *Cell-Pack* used to coat the internal frame of the GEMs and the polymerization on its surface caused a 20% decrease of the gas gain. this polyurethane was replaced with a new one for which no outgassing effect causing a loss of performance was reported.

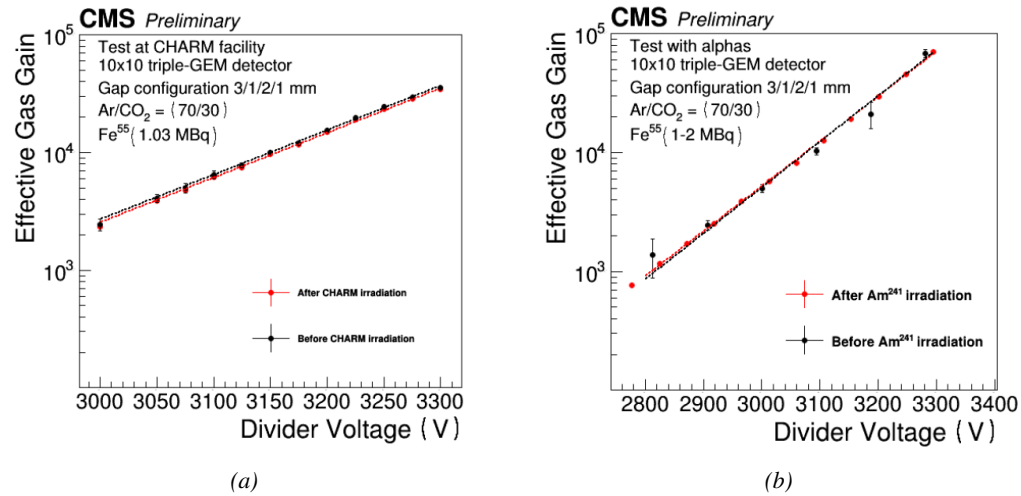


Figure 3.19: Figure 3.19a: Comparison of the gas gain as a function of the divider voltage before and after the irradiation of a triple-GEM by neutrons in CHARM. Figure 3.19b: Comparison of the gas gain as a function of the divider voltage before and after the irradiation of a triple-GEM by alpha particles.

Finally, even though the triple-GEM technology makes the detectors safe of discharges thanks to

its several amplification stages that allow to reach high gas gain using a relatively low electric field applied on the foils and to the distance separating the last foil from the read-out panel that is high enough to prevent discharging from developing all the way to the read-out, and hence, be stopped before it can cause any harm, it is important to have a good understanding of the discharge probability to ensure a safe operation over long periods. In order to further prevent discharges to develop in the detector volume, the GEM foils' power supply have been sectorized and protection resistors have been installed to limit the energy available for the discharge development. To reproduce the high-energy neutron background conditions of CMS, a GE1/1 detector have been placed in the CHARM facility of CERN. This facility allows to irradiate the detectors with a neutron fluence as high as  $2.5 \times 10^8 / \text{cm}^2$ . The detectors were operated with a slightly higher gain of  $3.5 \times 10^4$ . It was measured that the discharge probability for a GEM operated under CMS conditions was of  $2.85 \times 10^{-9}$  per heavily ionizing particle with a 95% confidence level that would correspond to 225 discharges per  $\text{cm}^2$  in ME0, 17 in GE1/1 and 12 in GE2/1 during the full HL-LHC period. According to Figure 3.19a, no degradation of the performance was observed after the irradiation at CHARM were 24 discharges per unit area were reported. Nevertheless, another test were the detector was exposed to a 5.5 MeV alpha source and were 450 discharges per unit area were reported didn't show any drop of performances either, as can be seen in Figure 3.19b.

### 3.3.3 Installation schedule

The previous discussion on the different upgrade projects makes it clear that a lot of work is scheduled for CMS to be ready at the end of LS3 for HL-LHC. Conducting all the upgrades of the muon system together with upgrades of the other subsystems like the replacement of the Tracker and of part of the ECAL, will prove to be very difficult as the opening of CMS to access the Barrel will be done by fully opening the endcaps leaving only the first disk to be accessible. Thus, most subsystems have planned early installation over LS2, and the following YETS until LS3 in order to give more space to LS3 schedule.

First of all, LS2 will see the installation of GE1/1 detectors, all the on-detector schedule of CSCs and the installation of the necessary services for the improved RPCs to be installed later, such as the HV and LV power supply lines, the gas and cooling lines or signal cables. CSCs will have a huge work to do during LS2 as they will need to extract all of their detectors to refurbish them with upgraded DCFEB and ALCT mezzanine boards. The GE1/1 services were installed during LS1 together with a few demonstrator and only the detectors needs to be integrated into the first endcap disk. The detectors are presently being built and tested at the different assembly site to prepare for a smooth LS2 work.

The work of GEMs will be continued during the following YETS during which is planned the installation of the GE2/1 stations to only leave the ME0 to be installed during LS3. The iRPC program will follow a similar path as the new detectors will be installed during the YETS preceding LS3 in preparation of the fact that the endcap disks will not be accessible during LS3. This way, all the subsystems, but DTs, made great effort on planning their installation and integration within CMS only to have to deal with off-detector issues during the LS3 period, such as the replacement of ODMBs and HV system in the case of CSCs or the upgrade of the RPC Link System. Finally, during LS3 are scheduled the replacement of DT minicrates electronics and the installation and integration of ME0 GEMs together with the HGCAL.

### 3.4 Implications of the different upgrades on the Level-1 Trigger. Improvement of physics performance.

The upgrades of the different subsystems will have a subsequent impact on the Level-1 Trigger. Indeed, although its main scheme will not be affected, the efficiency of the trigger in identifying muons and provide the DAQ with good and fast trigger that can cope with HL-LHC instantaneous luminosity is a major improvement. In addition to the upgrade of the muon system in terms of trigger accept rate and latency, the Level-1 Trigger will get extra information in including the Tracker Trigger into its Muon Track Finder logic and combine the L1 Muon Trigger with Tracker and Calorimeter Triggers to generate a Global L1 Trigger with a much better momentum resolution, as showed in Figure 3.20.

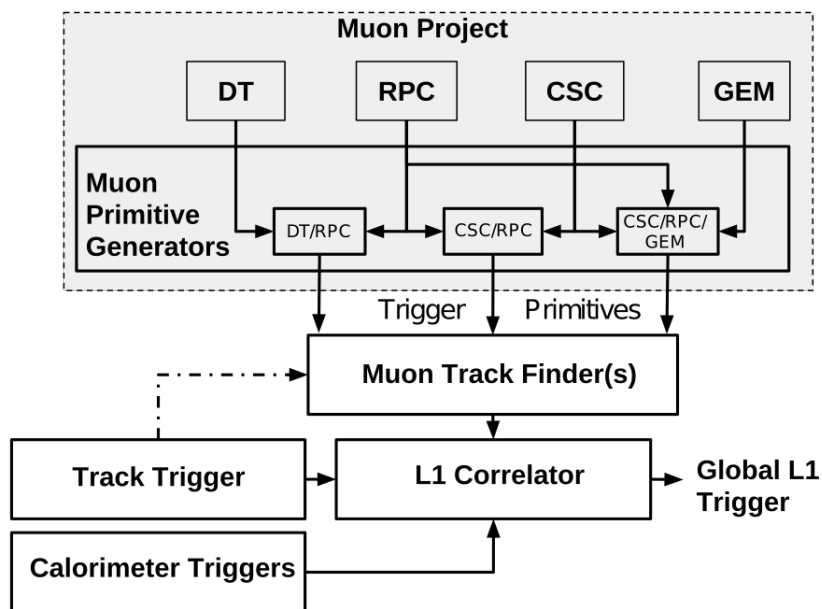
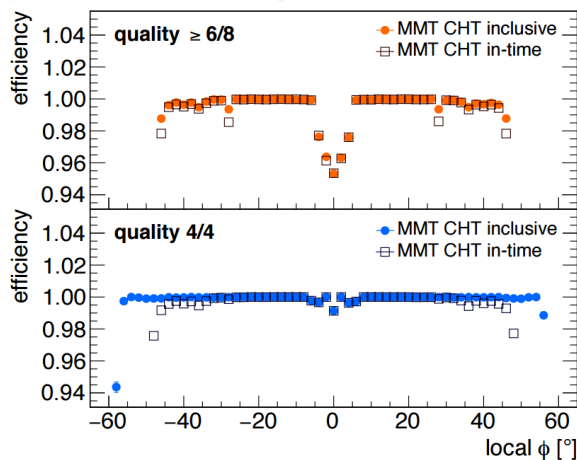


Figure 3.20: Data flow of the Level-1 Trigger during Phase-II operations.

In terms of muon trigger, 3 regions are considered due to their different track finding logic: the Barrel Muon Track Finder (BMTF), the Endcap Muon Track Finder (EMTF) for both the barrel and endcap regions, and finally the Overlap Muon Track Finder (OMTF) which concerns the pseudo-rapidity region in which there is a common coverage by both the barrel and endcap muon systems. This region can be seen in Figure 3.3 for  $0.9 < |\eta| < 1.2$  and requires a specific more complex logic to provide with an efficient reconstruction of the muons due to the different orientation of the detectors and of the more complex magnetic field of this region that needs to be taken into account. The benefits of the upgrade for each of these track finders will be coming from different improvements and will be detailed sector by sector.

The main contribution to the improvement of the BMTF is the time resolution improvement of RPC link systems that will allow to take profit of the full 1.5 ns resolution of the detectors. From the perspective of RPCs only, this improvement will help reducing the neutron induced background and

slightly improve the bunch crossing assignment. The upgrade of DT electronics is also to take into account as the trigger primitive generator will be renewed through the use of TDCs that will send the digitized signals directly to the back-end electronics instead of having an on-detector trigger logic as it will be the case until the end of Phase-I. The front data of both DTs and RPCs will be sent to the same back-end electronics. These upgrades were detailed in section 3.2 and will lead to a more robust operation of the trigger in the barrel region. Indeed, the combination of RPC hits together with DT primitives will bring improvement in the bunch crossing assignment and improve the efficiency of the trigger in between the wheels where the quality of DT primitives is the poorest. Moreover, having a redundant information is important in the case of failure and loss of efficiency of one of either subsystems.



*Figure 3.21: Comparison of Phase-II DT trigger primitives algorithmic efficiency for segments obtained with 2 super-layers ( $\text{quality} \geq 6/8$ ) and 1 super-layer only ( $\text{quality} = 4/4$ ). The simulation was done by generating  $2 \times 10^6$  muons. The candidate tracks with correct time identification is showed with open symbols.*

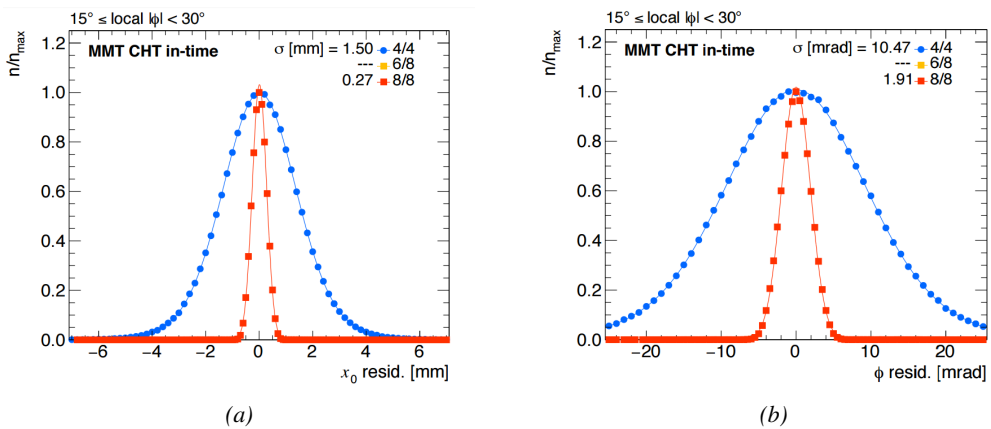


*Figure 3.22: Simulated spatial (3.22a) and angular (3.22b) resolution of the algorithm using 8 aligned hits in both super-layers ( $\text{quality} = 8/8$ ) and 4 aligned hits in only one super-layer ( $\text{quality} = 4/4$ ). The contribution of intermediate quality tracks (6 aligned hits) is negligible in the angular range shown. [Be careful to update this caption as it uses a text to close to the published one.]*

The loss of single hit efficiency of DTs due to ageing will also force the DT to change the algorithm use to identify tracks. So far, the identification was only performed at the level of a single DT super-layer, which is composed of 4 single DT layers. In the perspective the single efficiency drops, this will require to be upgraded to try to combine the data of more than a single super-layer to keep a high muon track identification efficiency. In addition to this change in trigger primitive candidate quality, new algorithms with higher efficiency are being developed. According to Figure 3.21, the efficiency of the new algorithm, both in the cases using 1 or 2 super-layers, is higher than with the current system [30]. Moreover, the overall efficiency of an algorithm requesting at least a muon detected in 6 DT layers out of the 8 composing the 2 super-layers of a DT module would stay comparable to the 4 DT layers out of 4 algorithm within the local bending angle range. On the other hand, despite the slight loss of efficiency in the low angle range, the algorithm using more DT layers achieves both higher spatial and angular resolution according to Figure 3.22.

1931

With new detectors to cover the very forward region and the upgrade of RPC Link System, the EMTF will be greatly improved. The current EMTF already use more sophisticated algorithms by combining together RPC hits and CSC primitives and will also benefit from the improved time resolution of the RPC system. The GEMs, in stations 1 and 2, and the iRPCs, in stations 3 and 4, will be added into the EMTF algorithm. Both these contributions will help increasing the efficiency of the L1 trigger in the endcap region in one hand, and help lowering the L1 trigger rate in the other hand, especially in the most forward region. The improvement of the efficiency will come both from the better time resolution of RPC link boards and from the addition of more hits along the muon tracks and also a contribution from the GEMs to the lever arm of each track thanks to their high angular resolution.

1942

The rate will be partly reduced in the forward region thanks to the better spatial resolution of iRPCs, with respect to the current RPC system, that will reduce the ambiguity brought by multiple local charged tracks in CSCs, as explained through Figure 3.24. Indeed, as the rates will increase, the probability to record more than a single local charged track will greatly increase. This is due to the fact that the trigger algorithm uses information from 3 consecutive bunch crossings to find muon tracks. It is estimated that with iRPCs operated at 95% efficiency the resolution of ambiguous events would be of the order of 99.7%.

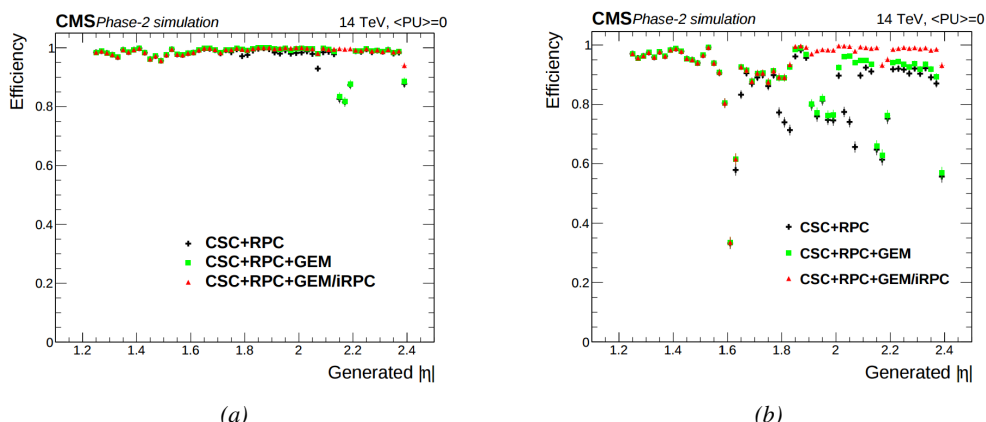


*Figure 3.23: Efficiency of the L1 trigger in the endcap region after Phase-II upgrade in the case CSC/GEM/RPC hits are requested in at least 2 stations out of four (3.23a) and in all four stations (3.23b).*

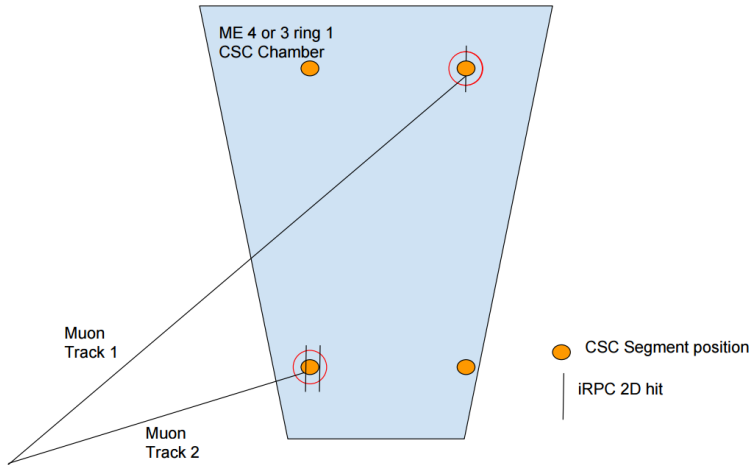


*Figure 3.24: Resolution of the LCT ambiguous events thanks to the combination of CSC and iRPC readout data. Using CSCs only, 2 pairs of hits are possible.*

The addition of GEMs will improve greatly the measured muon momentum resolution by improving the global resolution of the direction of muon tracks, as can be seen in Figure 3.25, which will contribute to lowering the trigger rate and increase the efficiency, as can be seen from Figure 3.26 that focuses especially in the most challenging pseudo-rapidity region. Data from both CSCs and GEMs are combined into the OTMB to build on each station, GEM/CSC primitives matching space and time information from both subsystems.

Finally, the development of a track finder specific to the overlap region was already achieved during the Phase-I upgrade of the L1-Trigger [31]. Nevertheless, the improvements of DT spatial resolution and RPC timing will be carried and implemented into the OMTF.

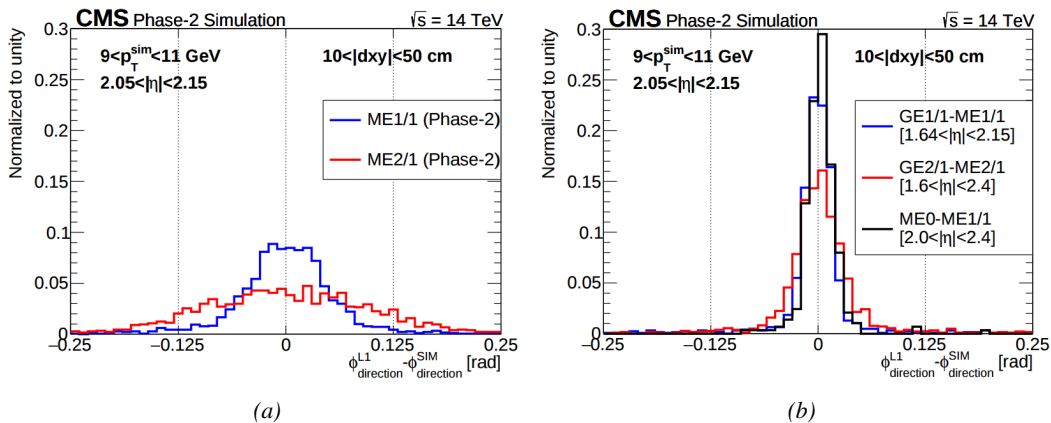


*Figure 3.25: The angular resolution on reconstructed muon tracks in the GEM overlap region  $2.0 < |\eta| < 2.15$  is compared for Phase-II conditions in the case CSC are alone (Figure 3.25a) and in the case the GEMs' data, including ME0, is combined to which of CSCs (Figure 3.25b).*

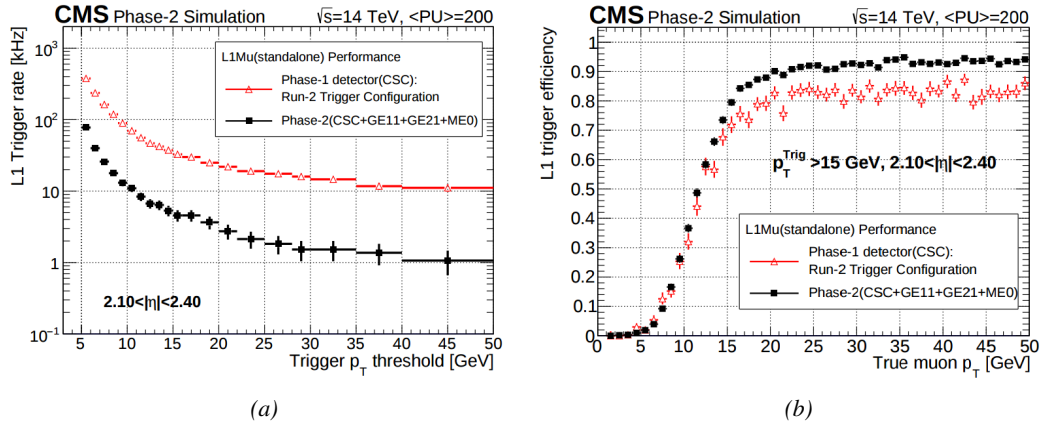


Figure 3.26: Comparison of L1 trigger performances for prompt muons with and without the addition of GEMs in the region  $2.1 < |\eta| < 2.4$  at Phase-II conditions. GEMs would allow a reduction of the trigger accept rate by an order of magnitude (Figure 3.26a) while increasing the trigger efficiency (Figure 3.26b).

### 3.5 Ecofriendly gas studies

Future strict restrictions in the use of certain gases will affect the gaseous detectors of several experiment, including CMS. The European Commission adopted a new "F-gas regulation" in 2014 [32] with the goal to strongly control and reduce the use of fluorinated gases with high Global Warming Potential (GWP). Using  $CF_4$ ,  $C_2H_2F_4$  and  $SF_6$ , both CSC and RPC subsystems will need to address this problem by finding new gas mixture for the operation of their detectors. Finding a replacement for these gas component that were used for very specific reasons will be a great challenge. Indeed, CSCs use  $CF_4$  in order to enhance the longevity of the detectors, increase the drift velocity of electrons and quench photons with a non-flammable gas mixture. RPCs use a mixture mainly composed of  $C_2H_2F_4$ , or  $R134a$ , that features a high effective Townsend coefficient and the great average fast charge allowing for operations with a high threshold, and contains a small fraction of  $SF_6$  that is used for its electronegative properties that prevents the development of delta-rays in the gas volume that might trigger multiple ionization and avalanches.

	CSC	RPC
Greenhouse gases used	$CF_4$	$C_2H_2F_4$ and $SF_6$
Greenhouse gases fraction in the gas mixture	10%	95.2% and 0.3%
Global Warming Potential (relative to $CO_2$ )	6500	1300 and 23900
Gas mixture re-circulation	Yes, 90%	Yes, 85%
Gas mixture replenishing rate (l/hr)	700	1100
F-gas recuperation	Yes, $\approx 40\%$	No
F-gas venting rate (l/hr)	42	1047 and 3.3
$CO_2$ -equivalent rate ( $m^3/h$ )	273	1440
Relative impact (entire muon system = 100%)	16%	84%

Table 3.1: Details of the greenhouse fluorinated gases used in CMS and of their GWP [23].

Nevertheless, all these gases have a very high GWP, as reported in Table 3.1, and only few options are left. The subsystems need to work on strongly decrease the loss of these gases due to leaks in the

gas system or completely change their gas mixture for more ecofriendly ones. Reducing the amount of F-gas released in the atmosphere due to leaks on the current gas system will require installation of a F-gas recuperation system on RPCs side and an upgrade of CSCs existing one in addition to the repair of existing leaks. With such measures, it is expected that the total rate of greenhouses gas vented in the atmosphere would represent only 1.6% of the current levels [23]. In the most critical case the F-gas were to be banned, it would be necessary to have replacement mixtures to operate CMS. CSC is presently investigating replacement for  $CF_4$  such as  $CF_3I$ ,  $C_4F_6$ ,  $IC_3F_6$ ,  $C_3F_8$  or  $CHF_3$  while RPCs, in collaboration with the ATLAS RPC group which uses the same gas mixture and, hence, faces similar restrictions, have identified  $CF_3I$  ( $GWP \leq 1$ ) and  $C_3H_2F_4$  ( $GWP \leq 1$ ), referred to as HFO-1234ze, as potential candidates with mixtures containing  $CO_2$  but more R&D needs to be conducted for both subsystems before concluding on the best alternative. No good alternative to the present mixtures will require very efficient abatement system in CMS to burn and convert the greenhouse gases into less harmful ones. This way, the air pollution would be strongly reduced.

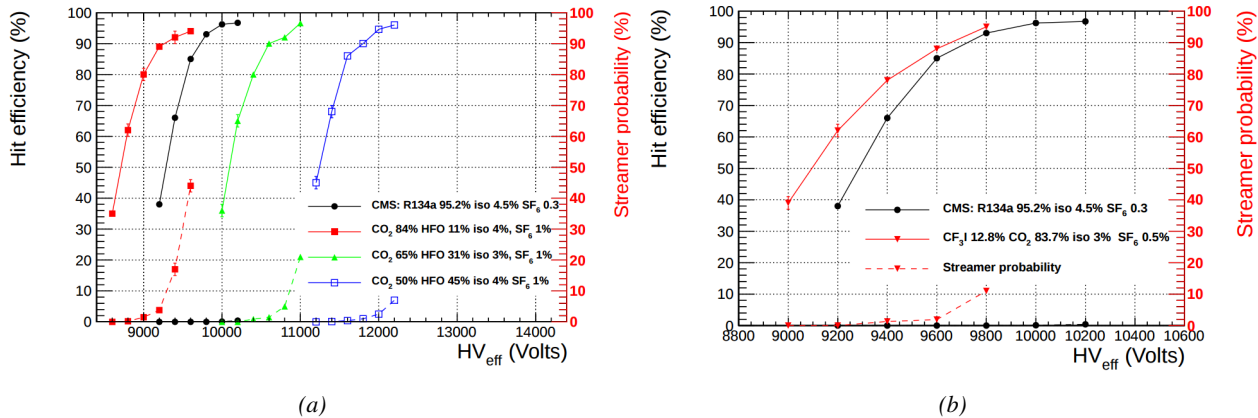


Figure 3.27: The efficiency (solid lines) and streamer probability (dashed lines) of HFO/CO<sub>2</sub> (Figure 3.27a) and CF<sub>3</sub>I/CO<sub>2</sub> (Figure 3.27b) based gas mixtures as a function of the effective high-voltage are compared with the present CMS RPC gas mixture represented in black. The detector used for the study is a single gap RPC with similar properties than CMS RPCs. The streamer probability is defined as the proportion of events with a deposited charge greater than 20 pC.

The status of RPC studies are presented in Figure 3.27 in which the performance (efficiency and streamer probability) of an RPC operated with alternative gas mixtures is compared to the present CMS RPC mixture. Although the efficiency of detectors operated with mixtures containing CO<sub>2</sub>/CF<sub>3</sub>I or CO<sub>2</sub>/HFO as a replacement for C<sub>2</sub>H<sub>2</sub>F<sub>4</sub> seem to reach similar levels than which of the detectors operated with the present mixture, the new gas mixtures feature a streamer probability (probability to have very large avalanches whose induced charge is greater than 20 pC) that far exceeds which of the present fluorinated mixture. The SF<sub>6</sub>, being a component of the mixture added in order to reduce the probability of large avalanches thanks to its electronegativity, doesn't seem to prevent streamers as efficiently even when used at levels more than 3 times higher than with the standard CMS RPC mixture. Nevertheless, it is important to note that these results were obtained with a single gap RPC while the use of a double gap RPC would reduce the operation voltage by 200 to 300 V, lowering the induced charge. A compromise in between good efficiency and acceptable level of streamer probability and the fine tuned composition of potential replacement gas mixtures

<sub>2000</sub> will be studied using a standard double-gap CMS RPC.

# 4

2001

2002

## Physics of Resistive plate chambers

2003 A Resistive Plate Chamber (RPC) is a gaseous detector used in high-energy physics experiments as  
2004 described in Chapter 3. It has been developed in 1981 by Santonico and Cardarelli [33], under the  
2005 name of *Resistive Plate Counter*, as an alternative to the local-discharge spark counters proposed in  
2006 1978 by Pestov and Fedotovich [34, 35]. Working with spark chambers implied using high-pressure  
2007 gas and high mechanical precision which the RPC simplified by formerly using a gas mixture of  
2008 argon and butane flowed at atmospheric pressure and a constant and uniform electric field propagated  
2009 in between two parallel electrode plates. Moreover, a significant increase in rate capability was  
2010 introduced by the use of electrode plate material with high bulk resistivity, preventing the discharge  
2011 from growing throughout the whole gas gap. Indeed, the effect of using resistive electrodes is that  
2012 the constant electric field is locally canceled out by the development of the discharge, limiting its  
2013 growth.

2014 Through its development history, different operating modes [36–38], gas mixtures [33, 38–43]  
2015 and new detector designs [44–46] have been discovered, leading to further improvement of the rate  
2016 capability of such a detector. The low developing costs and easily achievable large detection ar-  
2017 eas offered by RPCs, as well as the wide range of possible designs, made them a natural choice to  
2018 as muon chambers and/or trigger detectors in multipurpose experiments such as CMS [21] or AT-  
2019 LAS [47], time-of-flight detectors in ALICE [48], calorimeter with CALICE [49] or even detectors  
2020 for volcanic muography with ToMuVol [50].

### 2021 4.1 Principle

2022 RPCs are ionisation detectors composed of two parallel resistive plate electrodes in between which  
2023 a constant electric field is set. The space in between the electrodes, referred to as *gap*, is filled with  
2024 a dense gas that is used to generate primary ionization into the gas volume. The free charge carriers  
2025 (electrons and cations) created by the ionization of the gas molecules are then accelerated towards the  
2026 electrodes by the electric field, as shown in Figure 4.1 [51]. RPCs being passive detectors, a current  
2027 on pick-up copper read-out placed outside of the gas volume is induced by the charge accumulation

2028 during the growth of the avalanche resulting from the acceleration of the charge carriers. As a  
 2029 consequence, the time resolution of the detector is substantially increased as the output signal is  
 2030 generated while the electrons are still in movement. The advantage of a constant electric field, over  
 2031 multi-wire proportional chambers, is that the electrons are being fully accelerated from the moment  
 2032 charge carriers are freed and feel the full strength of the electric field that doesn't depend on the  
 2033 distance to the readout and that the output signal doesn't need for the electrons to be physically  
 2034 collected.

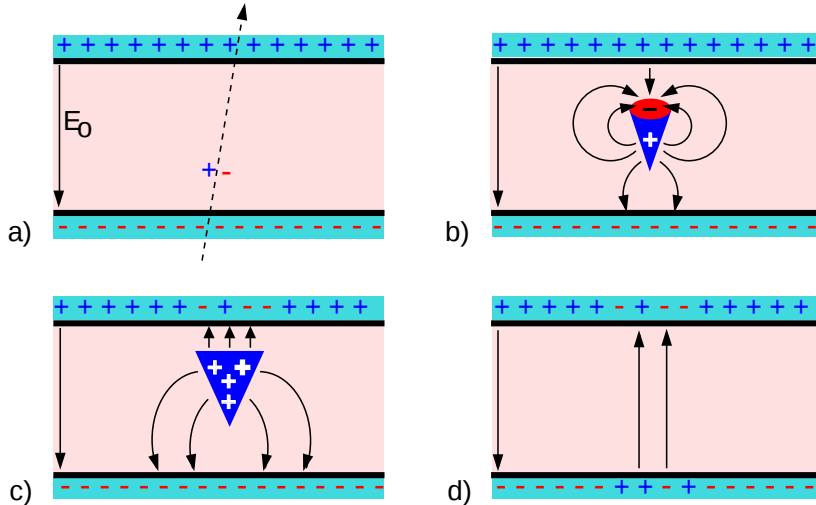


Figure 4.1: Different phases of the avalanche development in the RPC gas volume subjected to a constant electric field  $E_0$ . a) An avalanche is initiated by the primary ionisation caused by the passage of a charged particle through the gas volume. b) Due to its growing size, the avalanche starts to locally influence the electric field. c) The electrons, lighter than the cations reach the anode first. d) The ions reach the cathode. While the charges have not recombined, the electric field in the small region around the avalanche stays affected and locally blinds the detector.

2035 After an avalanche developed in the gas, a time long compared to the development of a discharge  
 2036 is needed to recombine the charge carriers in the electrode material due to their resistivity. This  
 2037 property has the advantage of affecting the local electric field and avoiding sparks in the detector  
 2038 but, on the other hand, the rate capability is intrinsically limited by the time constant  $\tau_{RPC}$  of the  
 2039 detector. Using a quasi-static approximation of Maxwell's equations for weakly conducting media,  
 2040 it can be shown that the time constant  $\tau_{RPC}$  necessary to the charge recombination at the interface  
 2041 in between the electrode and the gas volume is given by the Formula 4.1 [52].

$$\tau_{RPC} = \frac{\epsilon_{electrode} + \epsilon_{gas}}{\sigma_{electrode} + \sigma_{gas}} \quad (4.1)$$

2042 A gas can be assimilated to vacuum, leading to  $\epsilon_{gas} = \epsilon_0$  and  $\sigma_{gas} = 0$ , and the electrodes  
 2043 permittivity and conductivity can be written as  $\epsilon_{electrode} = \epsilon_r \epsilon_0$  and  $\sigma_{electrode} = 1/\rho_{electrode}$ ,  
 2044 showing the strong dependence of the time constant to the electrodes resistivity in Formula 4.2.

$$\tau_{RPC} = (\epsilon_r + 1)\epsilon_0 \times \rho_{electrode} \quad (4.2)$$

2045 Very few materials with a low enough resistivity exist in nature. The resistivity targeted to build

2046 RPCs ranges from  $10^9$  to  $10^{12} \Omega \cdot \text{cm}$ . The most common RPC electrode materials are displayed in  
 2047 Table 4.1. When the doped glass and ceramics can offer short time constants of the order of 1 ms,  
 2048 the developing cost of such materials is quite high due to the very low demand. Thus, High-pressure  
 2049 laminate (HPL) is often the choice for high rate experiments using very large RPC detection areas.  
 2050 Other experiments working at cosmic muon fluxes can safely operate with ordinary float glass.

Material	$\rho_{\text{electrode}} (\Omega \cdot \text{cm})$	$\epsilon_r$	$\tau_{\text{RPC}} (\text{ms})$
Float glass	$10^{12}$	$\sim 7$	$\sim 700$
High-pressure laminate	$10^{10}$ to $10^{12}$	$\sim 6$	$\sim 6$ to 600
Doped glass (LR S)	$10^9$ to $10^{11}$	$\sim 10$	$\sim 1$ to 100
Doped ceramics (SiN/SiC)	$10^9$	$\sim 8.5$	$\sim 1$
Doped ceramics (Ferrite)	$10^8$ to $10^{12}$	$\sim 20$	$\sim 0.2$ to 2000

Table 4.1: Properties of the most used electrode materials for RPCs.

## 2051 4.2 Rate capability and time resolution of Resistive Plate Cham- 2052 bers

2053 The electrode material plays a key role in the maximum intrinsic rate capability of RPCs. R&D is  
 2054 continuously being done to develop at always cheaper costs material with lower resistivity. Never-  
 2055 theless, the amount of charge released, i.e. the size of the discharge, if reduced leads to a smaller  
 2056 blind area in the detector, increasing the rate capability of the detector. On the other hand, the drift  
 2057 velocity of electrons in the gas volume being quite stable with the applied electric field, the design of  
 2058 a detector and the associated read-out and pulse-processing electronics will be a major component of  
 2059 the time resolution of RPCs. Moreover, the sensitivity of the electronics will also help increasing the  
 2060 rate capability by lowering the gain the gas volume needs to be operated at, increasingly lowering  
 2061 the gas volume in which the signals will develop.

### 2062 4.2.1 Operation modes

2063 Being a gaseous detector using an accelerating electric field to amplify the signal of primary charge  
 2064 carriers, the RPC can be operated into different modes as the electric field intensity varies. Each  
 2065 mode offers different performances for such a detector, and it will be showed that the operating mode  
 2066 corresponding to the lowest electric field possible is best suited for high rate detectors working in  
 2067 collider experiments.

2068 RPCs where developed early 1980s. At that time it was using an operating mode now referred to  
 2069 as *streamer mode*. Streamers are large discharges that develop in between the 2 electrodes enough to  
 2070 locally discharge the electrodes. If the electric field inside of the gas volume is strong enough, with  
 2071 electrons being fast compared to ions, a large and dense cloud of positive ions will develop nearby  
 2072 the anode and extend toward the cathode while the electrons are being collected, eventually leading  
 2073 to a streamer discharge due to the increase of field seen at the cathode. The field is then strong  
 2074 enough so that electrons are pulled out of the cathode. Electrodes, though they are a unique volume  
 2075 of resistive material, can be assimilated to capacitors. At the moment an electric field is applied in  
 2076 between their outer surfaces, the charge carriers inside of the volume will start moving leading to  
 2077 a situation where there is no voltage across the electrodes and a higher density of negative charges,  
 2078 i.e. electrons, on the inner surface of the cathode. Finally, when a streamer discharge occurs, these

2079 electrons are partially released in the gas volume contributing to increase the discharge strength until  
 2080 the formation of a conductive plasma, the streamer. This can be understood through Figure 4.2 [36].  
 2081 Streamer signals are very convenient in terms of read-out as no further amplification is required  
 2082 with output pulses amplitudes of the order of a few tens to few hundreds of mV as can be seen on  
 2083 Figure 4.3.

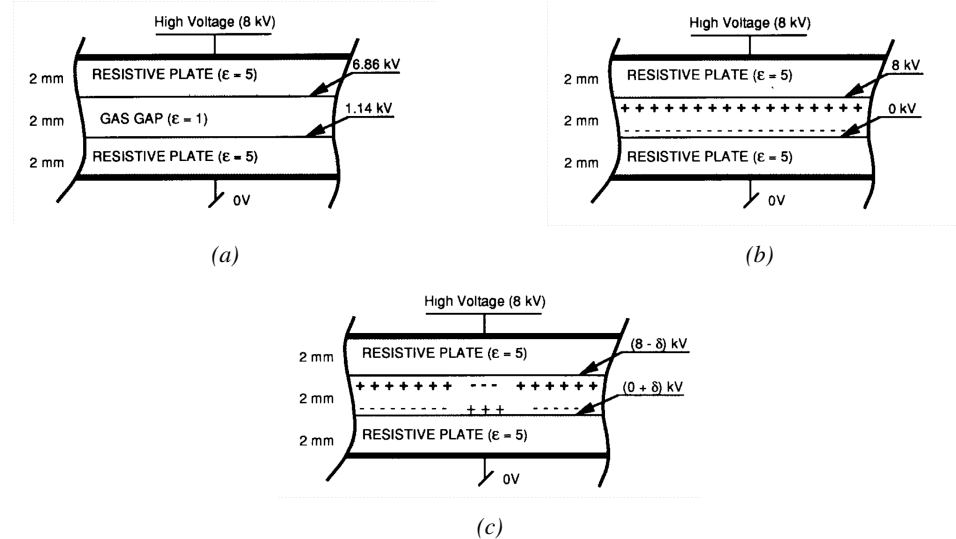


*Figure 4.2: Movement of the charge carriers in an RPC. Figure 4.2a: Voltage across an RPC whose electrode have a relative permittivity of 5 at the moment the tension is applied. Figure 4.2b: After the charge carriers moved, the electrodes are charged and there is no voltage drop over the electrodes anymore. The full potential is applied on the gas gap only. Figure 4.2c: The streamer discharge initiated by a charged particle transports electrons and cations towards the anode and cathode respectively.*

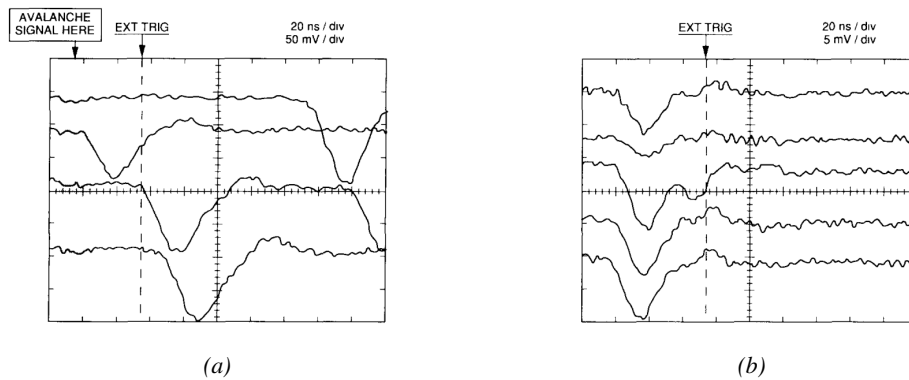


*Figure 4.3: Typical oscilloscope pulses in streamer mode (Figure 4.3a) and avalanche mode (Figure 4.3b). In the case of streamer mode, the very small avalanche signal is visible.*

2084 When the electric field is reduced though, the electronic gain is small until the electrons get close  
 2085 enough to the anode and the positive ion cloud is much smaller. The electric field cannot rise to the  
 2086 point a field emission of electrons on the cathode is possible. The resulting signal is weak, of the

order of a few mv as shown on Figure 4.3, and requires amplification. This is the *avalanche mode* of RPC operation. This mode offers a higher rate capability by providing smaller discharges that don't affect the electrodes charge and are more locally contained in the gas volume as was demonstrated by Crotty with Figure 4.4 [36]. The detector only stays locally blind the time the charge carriers are recombined and there is no need for electrode recharge which is a long process affecting a large portion of the detector. Another advantage of avalanche signals over streamer is the great time consistency. Figure 4.3 shows very clearly that avalanche signals have a very small time jitter. Thus, using such a mode is a natural choice for experiments in which the detectors are required to have a high detection rate.

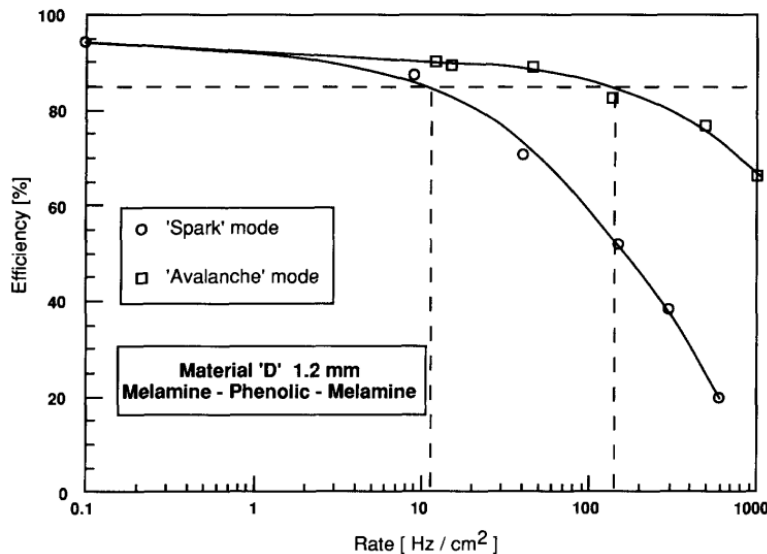
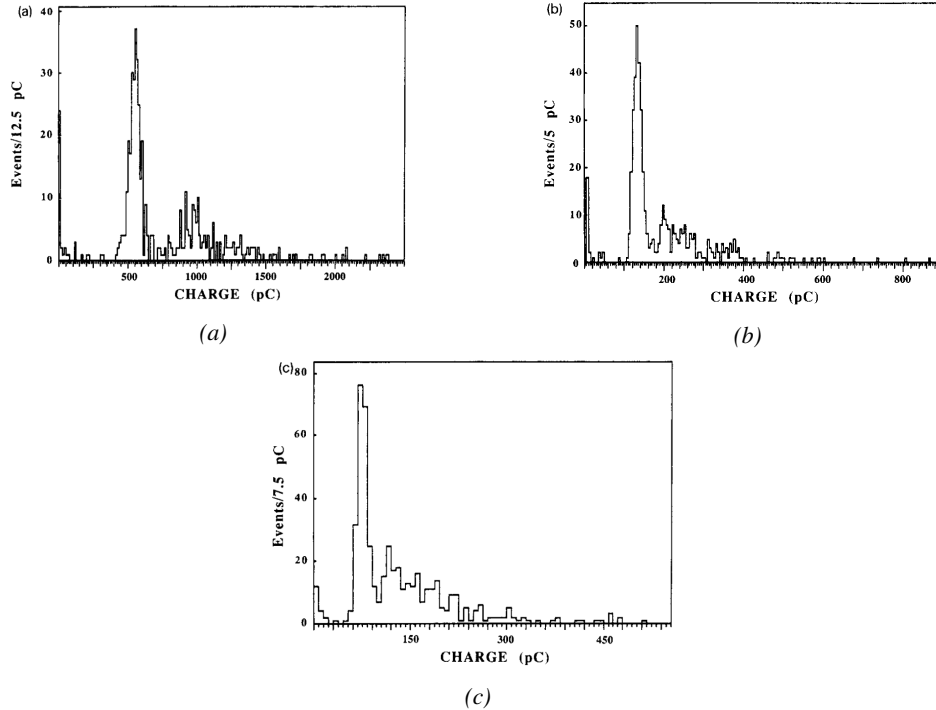


Figure 4.4: Rate capability comparison for the streamer and avalanche mode of operation. An order of magnitude in rate capability for a maximal efficiency drop of 10% is gained by using the avalanche mode over the streamer mode.

#### 4.2.2 Standard gas mixture for RPCs operated in collider experiments

The first RPC working in streamer mode was operated with a 50/50 mixture of argon and butane [33], a standard mixture used at that time in multi-wire proportional chambers, taking profit of the good effective Townsend coefficient of argon to maximize the number of primary charge carriers freed in the gas by ionizing particles and of the quenching properties of butane. Before the discovery of the avalanche mode of RPC operation and concerned about the rate capability of RPCs operated in streamer mode, the performance improvement of the detectors through the increase of fast charge ratio in the signal development ,decreasing the charge induced per avalanche as can be seen through Figure 4.5, was studied by adding Freon based gases, such as  $CF_3Br$ , into the typical  $Ar/C_4H_{10}$  gas mixture was studied and showed that a lower induced charge could lead to an improvement the rate capability [39]. This consideration lead to the discovery of the avalanche mode which confirmed that the smaller the induced charge, the better the rate capability of the RPCs [36]. This discovery could happen thanks to the increased number of lower induced charge events allowed by adding a fraction of strong quencher in the gas mixture.



*Figure 4.5: Comparison of the charge distribution of signals induced by cosmic muons in an RPC operated with a gas mixture of argon, butane and bromotrifluoromethane ( $CF_3Br$ ). The  $Ar/C_4H_{10}$  is kept constant at 60/40 in volume while the total amount of  $CF_3Br$  in the mixture is varied: 0% (Figure 4.5a), 4% (Figure 4.5b) and 8% (Figure 4.5c) [39].*

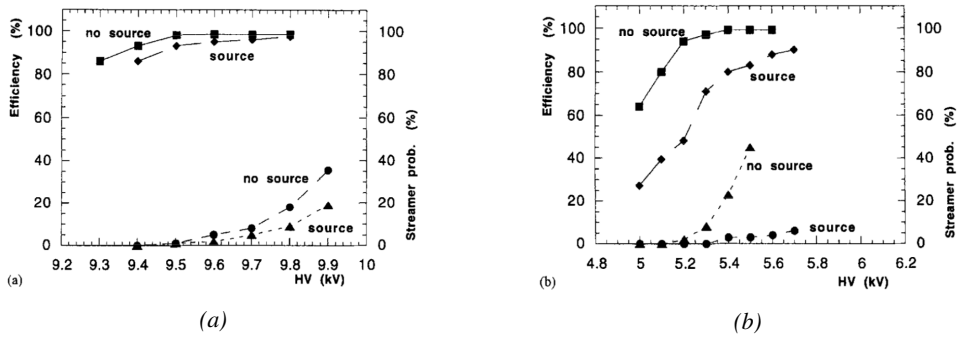


*Figure 4.6: Comparison of the efficiency and streamer probability, defined as the fraction of events with an induced charge 10 times larger than that of the average avalanche, with and without irradiation by a 24 GBq  $^{137}Cs$  source of an RPC successively operated with a 90/10 mixture  $C_2H_2F_4/i-C_4H_{10}$  (Figure 4.6a) and a 70/5/10/15 mixture of  $Ar/i-C_4H_{10}/CO_2/C_2H_2F_4$  (Figure 4.6b) [40].*

From this moment onward, more and more studies were conducted in order to find a gas mixture that would allow for the best suppression of streamers for the benefit of low charge avalanches. Most R&D groups working with narrow gaps started using freon-based gas mixtures while users of wide gap RPCs kept using  $Ar/CO_2$  based mixtures. The differences in between narrow and wide gaps will

be later discussed in Section 4.2.3. The  $CF_3Br$  having a high GWP, tetrafluoroethane ( $C_2H_2F_4$ ) was preferred to it as more suitable ecofriendly gas in the middle of the 90s. An advantage of this new freon component is that it featured a high primary ionization and a low operating voltage, as reported by Cardarelli [38]. Thus, the new gas mixtures used were mainly composed of tetrafluoroethane alone with lower content of isobutane in order to reduce the flammability of the mixtures in the case it were to be used in accelerator experiments for safety reasons. Performance and models about such mixtures were discussed in papers of Abbrescia [40, 41] and showed a better suitability of such a gas mixture, with respect to argon based ones, for operations with high radiation backgrounds leading to a need for high rate capability of the detectors, as can be seen from Figures 4.6 and 4.7. Indeed, although the operating voltage of a tetrafluoroethane based mixture is higher than which of an argon based mixture but the efficiency under irradiation is more stable, the voltage range with negligible streamer probability is much wider, and the fast charge ratio available is much greater, providing with more stable operation of the detector.

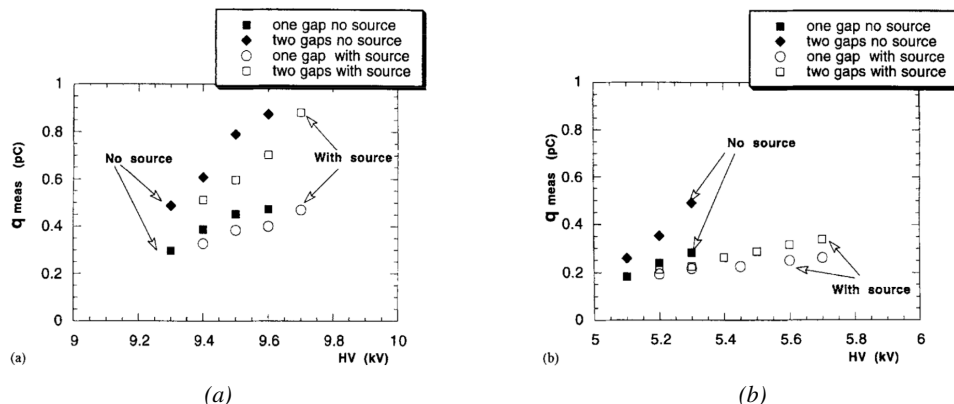


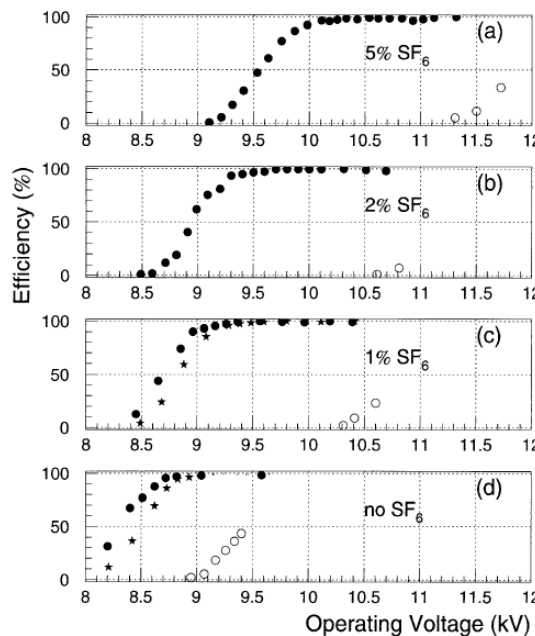
Figure 4.7: Comparison of the fast charge ratio with and without irradiation by a 24 GBq  $^{137}Cs$  source of an RPC successively operated with a 90/10 mixture  $C_2H_2F_4/i-C_4H_{10}$  (Figure 4.7a) and a 70/5/10/15 mixture of  $Ar/i-C_4H_{10}/CO_2/C_2H_2F_4$  (Figure 4.7b). The results are provided for both single gap and double gap operation [40].

Aside of the improvement of the rate capability through linseed oil surface treatment of HPL electrodes, which allowed for a lower intrinsic noise rate and dark current of the detectors by improving the smoothness of the electrodes surface [53], it was later found that the streamers could be further suppressed by adding an electronegative compound into the gas mixture. The benefits of adding  $SF_6$  in order to push the transitions from avalanche to streamers towards high voltages has been discussed in 1998 [42, 43] and eventually the high rate RPC destined to be used in accelerator physics would unanimously start using this compound into RPC gas mixtures. Being able to control the creation of streamers allows for slower ageing of the detector and lower power consumption as the currents driven by the electrodes consecutively to the induced charges would be smaller. In summary, the typical gas mixture RPCs are operated with is generally composed of the following 3 gas compounds, although, as mentioned in Chapter 3.5, research is being conducted into new more ecofriendly gas mixture using gases with a much lower Global Warming Potential:

- Tetrafluoroethane ( $C_2F_4H_2$ ), also referred to as *Freon* or *R134a*, is the principal compound of the RPC gas mixtures, with a typical fraction above 90%. It is used for its high effective

2141 Townsend coefficient and the great average fast charge that allows to operate the detector  
 2142 with a high threshold with respect to argon, for example, that has similar effective Townsend  
 2143 coefficient but suffers from a lower fast charge. To operate with similar conditions, argon  
 2144 would require a higher electric field leading to a higher fraction of streamers, thus limiting the  
 2145 rate capability of the detector [40, 41].

- 2146 • Isobutane ( $i\text{-C}_4\text{H}_{10}$ ), only present in a few percent in the gas mixtures, is used for its UV  
 2147 quenching properties [54] helping to prevent streamers due to UV photon emission during the  
 2148 avalanche growth.
- 2149 • Sulfur hexafluoride, ( $\text{SF}_6$ ), simply referred to as  $\text{SF}_6$ , is used in very little quantities for its  
 2150 high electronegativity. Excess of electrons are being absorbed by the compound and streamers  
 2151 are suppressed [42, 43]. Nevertheless, a fraction of  $\text{SF}_6$  higher than 1% will not bring  
 2152 any extra benefice in terms of streamer cancelation power but will lead to higher operating  
 2153 voltage [42], as can be understood through Figure 4.8.



2154 *Figure 4.8: Efficiency (circles and stars with 30 mV and 100 mV thresholds respectively) and streamer prob-  
 2155 ability (opened circles) as function of the operating voltatge of a 2 mm single gap HPL RPC flushed with a gas  
 2156 mixture containing (a) 5%, (b) 2%, (c) 1% and (d) no  $\text{SF}_6$  [42].*

2157 In the last steps of R&D, the gas mixture of CMS RPCs was foreseen to be a 96.2/3.5/0.3 compo-  
 2158 sition of  $\text{C}_2\text{H}_2\text{F}_4/\text{i-C}_4\text{H}_{10}/\text{SF}_6$  [55] but finally it was slightly changed into a 95.2/4.5/0.3 mixture  
 2159 of the same gases [56]. A summary of the operation performance of the RPCs since the start of LHC  
 and of CMS data taking is given in Figure 4.9 [57]. The performance of the detectors is regularly  
 monitored and the operating voltages updated in order to obtain a very stable performance through  
 time. Nevertheless, the detectors will face new challenges during Phase-II during which they will

exposed to more extreme radiation conditions. Description of the longevity tests with extreme irradiation and the conclusions regarding the operation of the present RPC system will be given in Chapter 5.

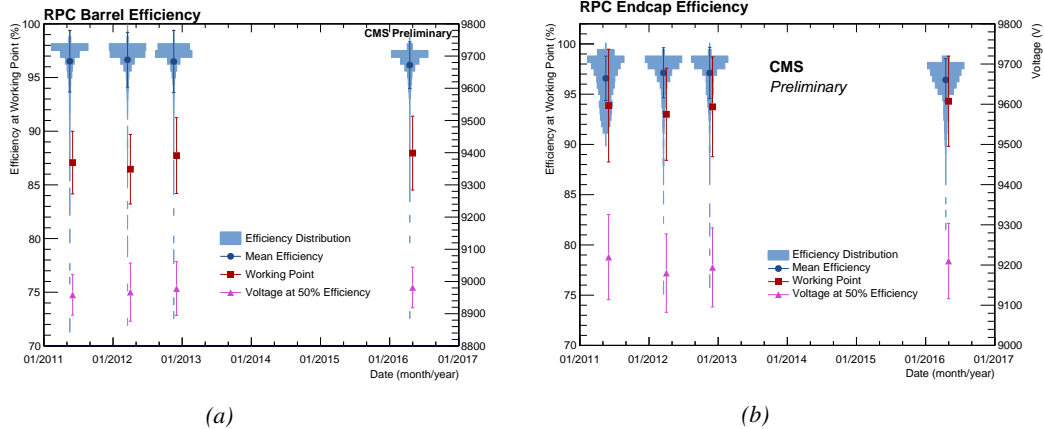


*Figure 4.9: Evolution of the efficiency, working voltage, and voltage at 50% of maximum efficiency for CMS Barrel (Figure 4.9a) and Endcap (Figure 4.9b) RPCs obtained through yearly voltage scans since 2011. The working voltage of each RPC is updated after each voltage scan to ensure optimal operation [57].*

It was already discussed that in the future, it is likely that the use of freon gases could be banned. As potential replacement for tetrafluoroethane was proposed the trifluoriodomethane ( $CF_3I$ ), a molecule with similar properties than  $CF_3Br$  which was replaced by the tetrafluoroethane, and the 1,3,3,3-tetrafluoropropene ( $C_3H_2F_4$  or HFO-1234re), a molecule with similar properties than the actual tetrafluoroethane and proposed as a replacement in refrigerating and air conditioning systems [58]. These 2 gases have stronger quenching properties than  $C_2H_2F_4$  which means a much stronger electric field needs to be applied on the parallel electrodes of the RPCs in order to reach full efficiency. But the power supply system of CMS RPC is limited to 15 kV and so is ATLAS power supply system which is participating in a joined R&D. As can be seen from Figure 3.27, reducing the working voltage was achieved by mixing the potential replacements together with  $CO_2$ . Introducing carbon dioxide into the mixture while keeping similar levels of isobutane and  $SF_6$  increases the streamer probability and the best candidate identified for a compromise in between low enough working voltage and acceptable levels of streamers corresponds to a mixture containing 50% of  $CO_2$ , 45% of HFO, 4% of isobutane and 1% of  $SF_6$  but is not yet considered satisfactory. On the other hand, no good replacement for  $SF_6$  has yet been identified. With its very high Global Warming Potential (23900), even small fraction of this gas in the mixture (it only represents 0.3% of CMS standard mixture but more than 5% of its overall GWP) substantially increase the danger for the environment. Although finding a replacement for this gas is less critical than for the tetrafluoroethane composing more than 90% of usual RPC standard mixtures, the problem will need to be addressed.

### 4.2.3 Detector designs and performance

Different RPC design have been used and each of them present its own advantages. Historically, the first type of RPC to have been developed is what is now referred to as *narrow gap* RPC [33, 59].

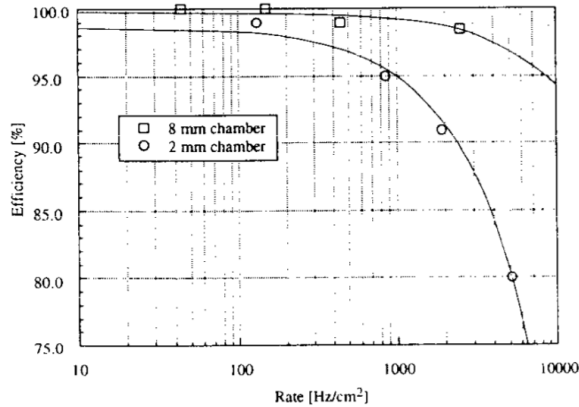


Figure 4.10: Comparison of the rate capability of 8 mm and 2 mm wide RPCs. The lines are linear fits on the data [59].

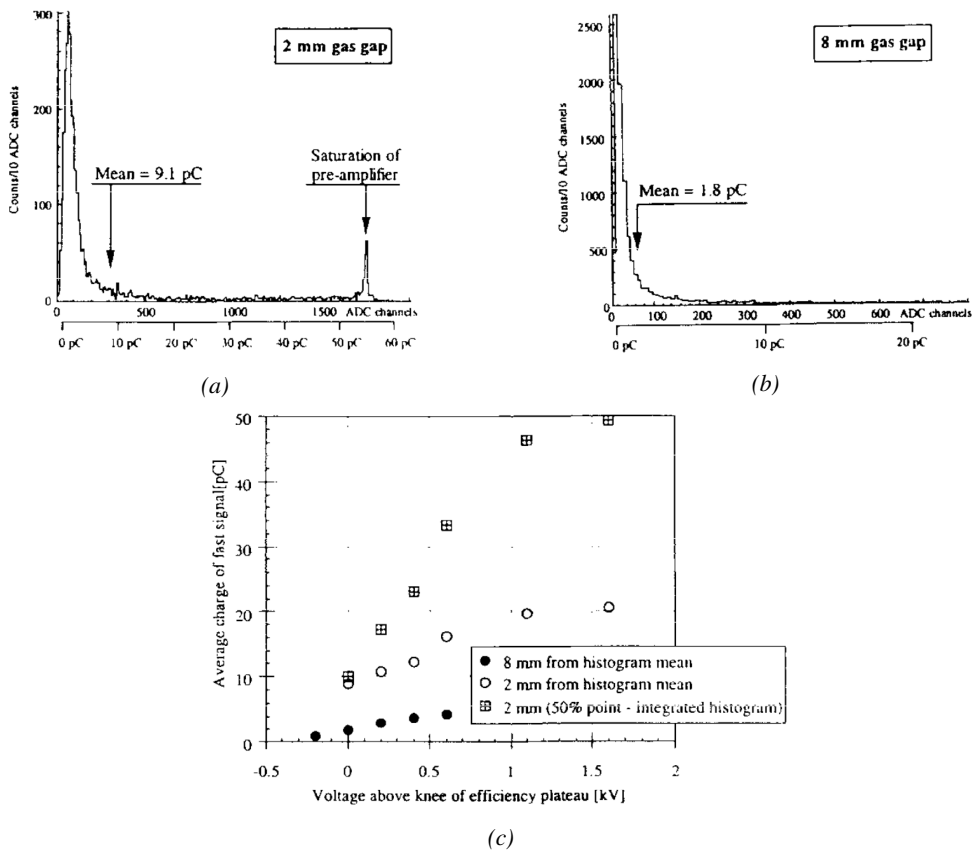


Figure 4.11: Distributions of the induced charge of fast signals on 2 mm (Figure 4.11a) and 8 mm (Figure 4.11b) RPCs exposed to a radiation rate of  $100 \text{ Hz/cm}^2$ . Average induced charge of fast signals as a function of the high voltage applied on 2 mm and 8 mm RPCs (Figure 4.11c). In the case of the 2 mm RPC, a saturation of the pre-amplifier was observed. The average of the distribution is underestimated and the median is showed together with the average to account for this bias [59].

After the avalanche mode has been discovered [36], it has been showed that increasing the width of the gas gap lead to higher rate capability, due to lower charge deposition per avalanche, and lower power dissipation [59], as is showed in Figures 4.10 and 4.11. The distance in between the electrode being greater, a weaker electric field can be applied and a lower gain used as a longer gas volume will contribute to the signal induction on the read-out circuit. Nevertheless, by increasing the gas gap width, the time resolution of the detector decreases. This is a natural result if the increase of active gas volume in the detector is taken into account. Indeed, for a given detection threshold on the induced charge per signal, only the small fraction of gas closest to the cathode will provide enough gain to have a detectable signal. In the case of a wider gas volume, the active region is then larger and a larger time jitter is introduced with the variation of starting position of the avalanche, as discussed in [44] and showed in Figure 4.12.

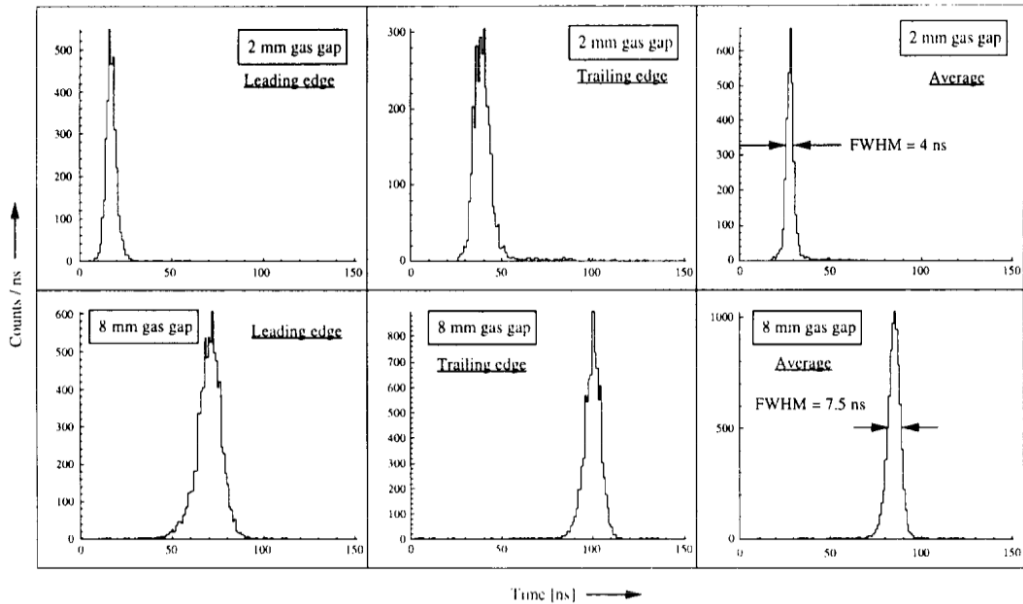


Figure 4.12: Time distributions of the leading, trailing, and average of both leading and trailing edges for 2 mm (top row) and 8 mm (bottom row) RPCs exposed to a 100 Hz/cm<sup>2</sup> radiation rate. The data was collected with RPCs operated at the voltage corresponding to the knee of the efficiency distribution, defined as the point where 95% of the maximum efficiency is obtained [59].

To improve both the time resolution and the rate capability, different methods were used trying to take advantage of both narrow and wide gap RPCs into a single design. Thus, double gap RPCs, combining two narrow gaps into a single detector to increase the effective sensitive volume, and multigap RPCs, which divided the large volume of a wide gap RPC into thinner sub-gaps by adding intermediate electrodes in between the cathode and anode to improve the time resolution by mimicking narrow gap RPCs, were developed starting from the middle of the 90s.

#### 4.2.3.1 Double gap RPC

Made out of 2 narrow RPC detectors stacked on top of each other as shown in Figure 4.13, this detector layout, popularized by the two multipurpose experiments CMS [21] and ATLAS [47] at LHC, can be used as an OR system in which each individual chamber participates in the output signal

and increases the overall sensitive volume of the detector apparatus. Keeping the copper strip read-out system at the ground, CMS and ATLAS, due to different goals, have chosen different designs as CMS RPCs possess a 1D read-out while ATLAS RPCs offer a 2D read-out. The difference comes from placing the read-out in between the gaps, the anodes facing each other, or to have both RPC gaps in between 2 layers of read-out panels, one along the X-axis and one along the Y-axis, the cathodes facing each other.

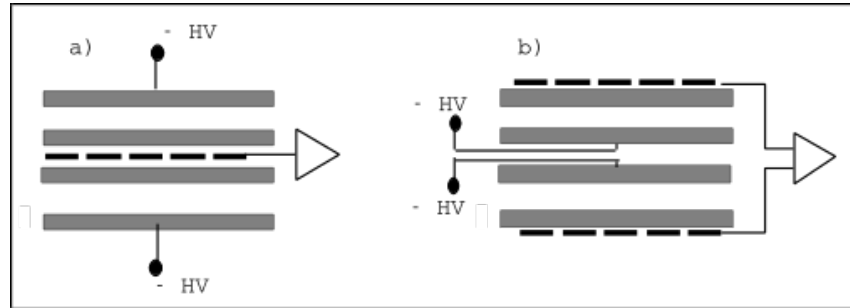


*Figure 4.13: Possible double-gap RPC layouts: a) "standard" 1D double-gap RPC, as used in CMS experiment, where the anodes are facing each other and a 1D read-out plane is sandwiched in between them, b) double read-out double-gap RPC as used in ATLAS experiment, where the cathodes are facing each other and 2 read-out planes are used on the outer surfaces. This last layout can offer the possibility to use a 2D reconstruction by using orthogonal read-out planes.*

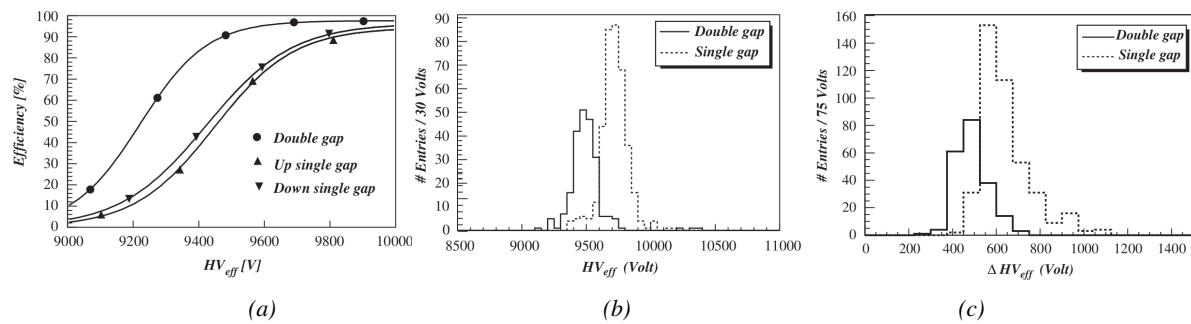


*Figure 4.14: Comparison of performance of CMS double and single gap RPCs using cosmic muons [55]. Figure 4.14a: Comparison of efficiency sigmoids. Figure 4.14b: Voltage distribution at 95% of maximum efficiency. Figure 4.14c:  $\Delta_{10\%}^{90\%}$  distribution.*

The gain of such a detector is reduced by a factor 2 with respect to single-gap RPCs with an efficiency plateau reached at lower voltage, as visible on Figure 4.14, due to the two gas gaps contributing to the signal formation and offering a dynamic range closer to witch of a wide gap RPC. A double gap is then fully efficient while the individual RPC gaps composing it are only 70 to 80% efficient. Naturally, by operating the double gap at a lower voltage, the rate capability is found to be increased as the induced charge per gap is then lower than in the case of a single gap detector also leading to a reduction of the streamer probability and a better extraction of the fast charge of the total signal as could be seen through previously presented Figure 4.7.

2221 **4.2.3.2 Multigap RPC (MRPC)**

2222 MRPCs are layouts in which floating sub electrode plates are placed into a wide gap RPC to divide  
 2223 the gas volume and create a sum of narrow gaps [44, 45]. Similarly to the double gap RPC for which  
 2224 the gain could be reduced by increasing the dynamic range, the multigap reduces the gain while  
 2225 keeping a total dynamic range similar to which of a wide gap RPC by reducing the size of each  
 2226 individual sub-gap composing the detector. The dynamic range, associated to the sensitive volume,  
 2227 and the comparison of each detector layout to the wide gap RPC is showed in Figure 4.15.

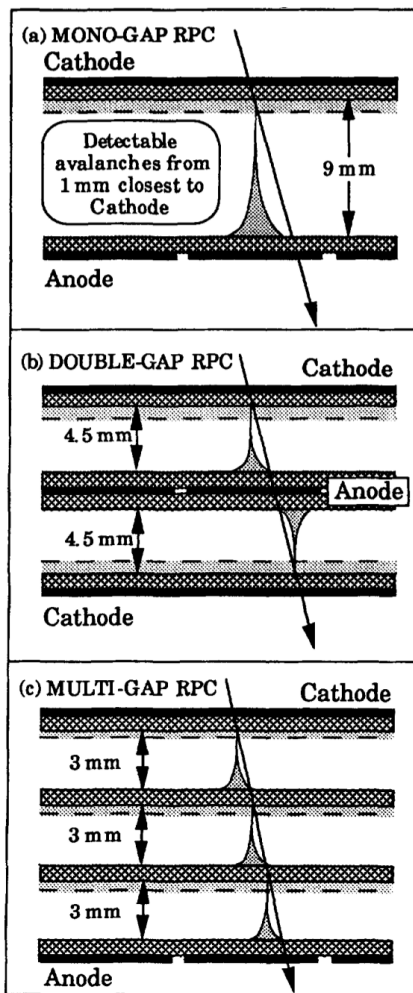


Figure 4.15: Representation of different RPC layouts (wide gap on Figure (a), double gap on Figure (b) and multigap on Figure (c)), of the corresponding sensitive volume in gray, and of the associated avalanche size [45].

2228 By operating the detector with thinner gaps, the time resolution is improved. Comparatively to  
 2229 the time resolution presented in Figure 4.12 for the wide gap RPC of 8 mm, a complementary study  
 2230 was conducted on multigaps using two 4 mm and four 2 mm subgaps and showed, via Figure 4.16,  
 2231 an improvement of the time resolution with the reduction of the gap width and of the number of gaps

while the same sensitive volume was kept [45].

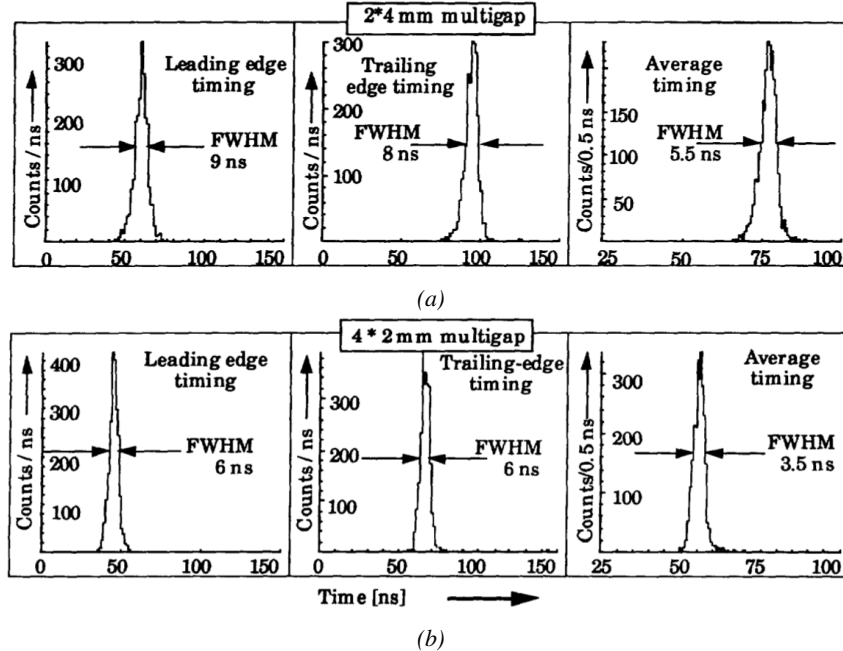


Figure 4.16: Time distributions of the leading, trailing, and average of both leading and trailing edges for multigap RPCs consisting in two 4 mm (Figure 4.16a) and four 2 mm (Figure 4.16b) exposed to a  $100 \text{ Hz/cm}^2$  radiation rate. The data was collected with RPCs operated at the voltage corresponding to the knee of the efficiency distribution, defined as the point where 95% of the maximum efficiency is obtained [45].

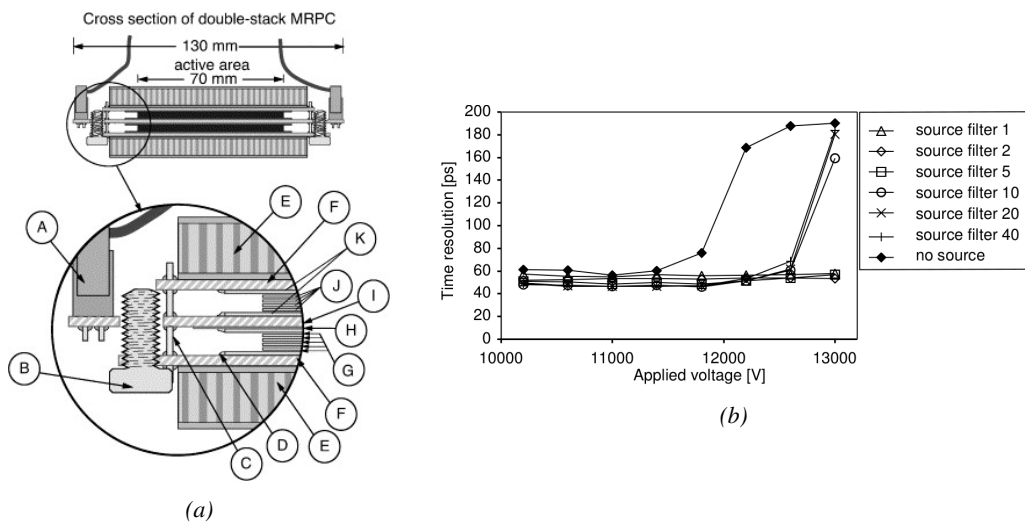


Figure 4.17: Presentation of a study of a possible ALICE MRPC cell using  $250 \mu\text{m}$  gas gaps,  $620 \mu\text{m}$  outer glass electrodes, and  $550 \mu\text{m}$  inner floating electrodes (Figure 4.17a), and of its time resolution performance as a function of the applied high voltage for different radiation levels referred through different filter settings of the  $740 \text{ GBq } ^{137}\text{Cs}$  source the former CERN GIF facility [60].

After the problem of streamers was solved by adding  $SF_6$  into the gas mixture, the size of the MRPCs decreased as the research groups started applying the concept of dividing the gas volume into subvolumes to the narrow gap RPCs leading to the now widely used micro gap MRPCs. The time resolution of such a detector can reach of few tens of ps, with gas gaps of the order of a few hundred  $\mu\text{m}$  as showed in Figure 4.17 representing a single cell of ALICE Time-of-flight (ToF) system consisting of double MRPCs, as it was studied in the early 2000s [60].

Sometimes used as a double multigap RPC, taking advantage of the OR of double gap RPCs to both be able to operate a higher number of gaps while keeping a reasonable high voltage applied in between the cathode and anode and to further reduce the gain, the MRPC is mainly used as ToF detector [60–64] due to its excellent timing properties that allow to perform particle identification as explained by Williams in [65]. The principle of particle identification using ToF is simply the measurement of the velocity of a particle. Indeed, particles are defined by their mass (for the parameter of interest here, their electric charge being measured using the bending angle of the particles traveling through a magnetic field) and this mass can be calculated by measuring the velocity  $\beta$  and momentum of the particle:

$$\beta = \frac{p}{\sqrt{p^2 + m^2}} \quad (4.3)$$

Intuitively, it is trivial to understand that 2 different particles having the same momentum will have a different velocity due to the mass difference and thus a different flight time  $T_1$  and  $T_2$  through the detector and this is used to separate and identify particles. The better the time resolution of the ToF system used, the stronger will the separation be:

$$T = \frac{L}{v} = \frac{L}{c \cdot \beta}, \quad \Delta T = T_1 - T_2 = \frac{L}{c} \left( \sqrt{1 + m_1^2/p^2} - \sqrt{1 + m_2^2/p^2} \right) \cong (m_1^2 - m_2^2) \frac{L}{2cp^2} \quad (4.4)$$

An example of particle identification is given for the case of STAR experiment in Figure 4.18.

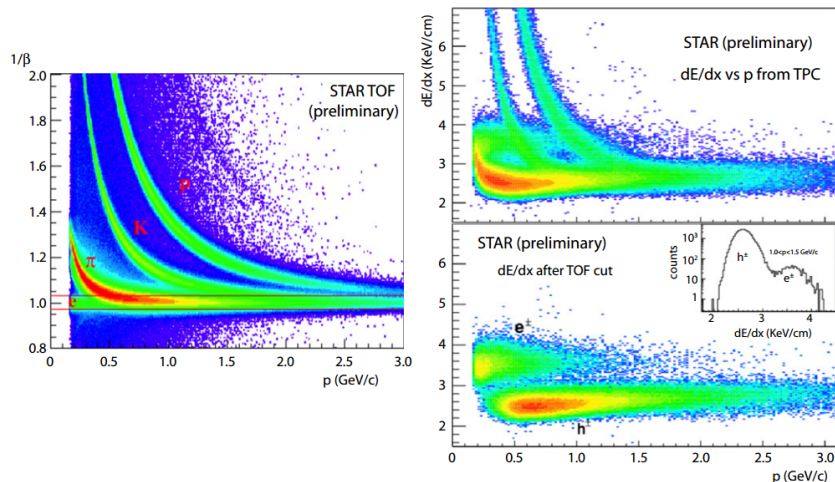


Figure 4.18: Particle identification applied to electrons in the STAR experiment. The identification is performed combining ToF and  $dE/dx$  measurements [65].

2253 Taking into account the distortion effect on the electric field inside of a MRPC built using micro  
 2254 gaps due to the exposition to irradiation, distortion that can be understood by monitoring the current  
 2255 drawn by the detector which should stay constant at constant electric field, another benefice of using  
 2256 such small gas gaps is the strong reduction of the average avalanche volume and thus of the blind  
 2257 spot on MRPCs leading to an improved rate capability. Multigaps can sustain backgrounds of several  
 2258 kHz/cm<sup>2</sup> as demonstrated in Figure 4.19.

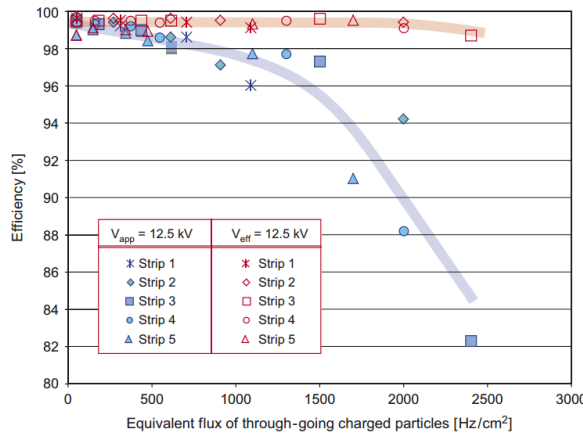


Figure 4.19: Comparison of the detector performance of ALICE ToF MRPC [66] at fixed applied voltage (in blue) and at fixed effective voltage (in red). The effective voltage is kept fixed by increasing the applied voltage accordingly to the current drawn by the detector.

#### 2259 4.2.3.3 Charge distribution and performance limitations

2260 [This part could be moved in the next section of the chapter and deepened using the perspective  
 2261 of the avalanche physics.]

2262 The direct consequence of the different RPC layouts is a variation of intrinsic time resolution of  
 2263 the RPC as the gap size decreases and of the rate capability when the deposited charge per event is  
 2264 spread over a larger number of amplification volumes, allowing for a reduction of the overall gain of  
 2265 the detectors which is replaced by an on-electronics pre-amplification of the signals. in this sense,  
 2266 an advantage is given to multigaps whose design use sub-millimeter gas volumes providing very  
 2267 consistent signals.

2268 From the charge spectrum point of view, each layout has its own advantages. When the double-  
 2269 gap has the highest induced over drifting charge ratio, as seen in Figure 4.20, the multigap has a  
 2270 charge spectrum strongly detached from the origin, as visible in Figure 4.21. A high induced over  
 2271 drifting charge ratio means that the double gap can be safely operated at high threshold or that at  
 2272 similar threshold it can be operated with a twice smaller drifting charge, meaning a higher rate  
 2273 capability if operated with sensitive enough electronics. On the other hand, the strong detachment  
 2274 of the charge spectrum from the origin in the MRPC case allows to reach a higher efficiency with  
 2275 increasing threshold as most of the induced charge is not low due to the convolution of several  
 2276 single gap spectra. The range of stable efficiency increases with the number of gap, as presented in  
 2277 Figure 4.22.

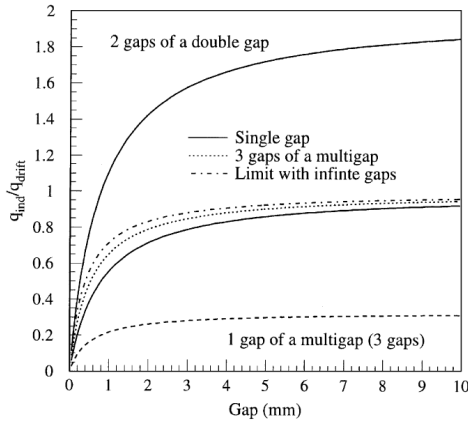


Figure 4.20: Ratio between total induced and drifting charge have been simulated for single gap, double-gap and multigap layouts [67]. The total induced charge for a double-gap RPC is a factor 2 higher than for a multigap.

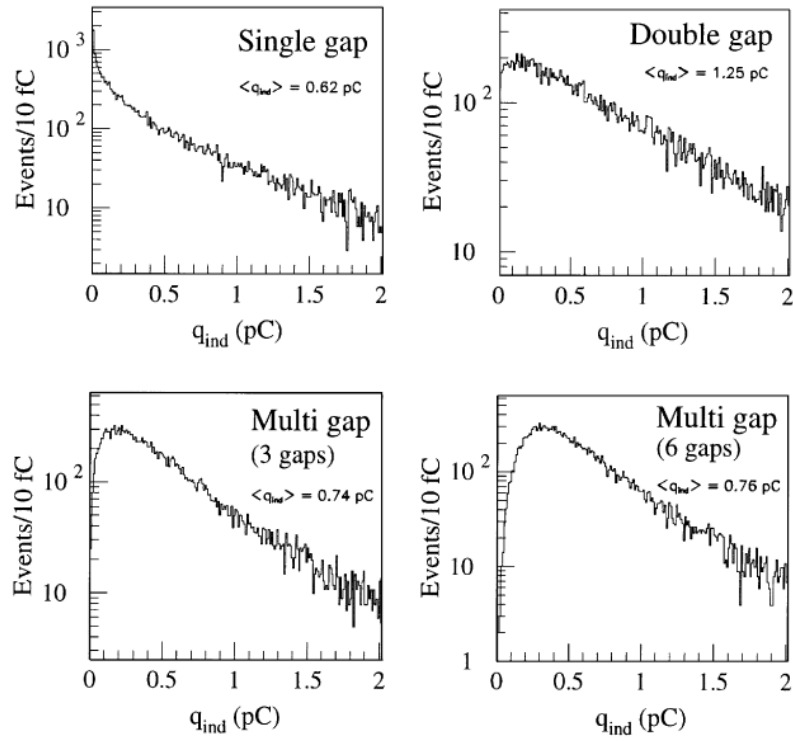
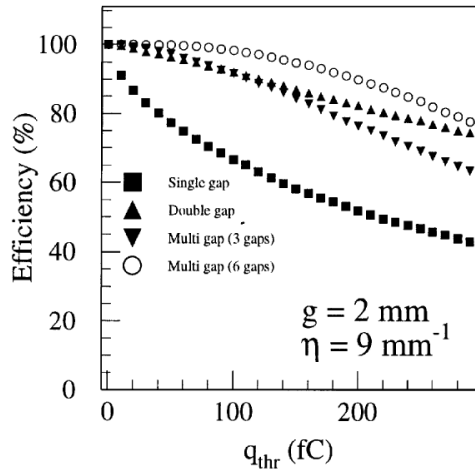
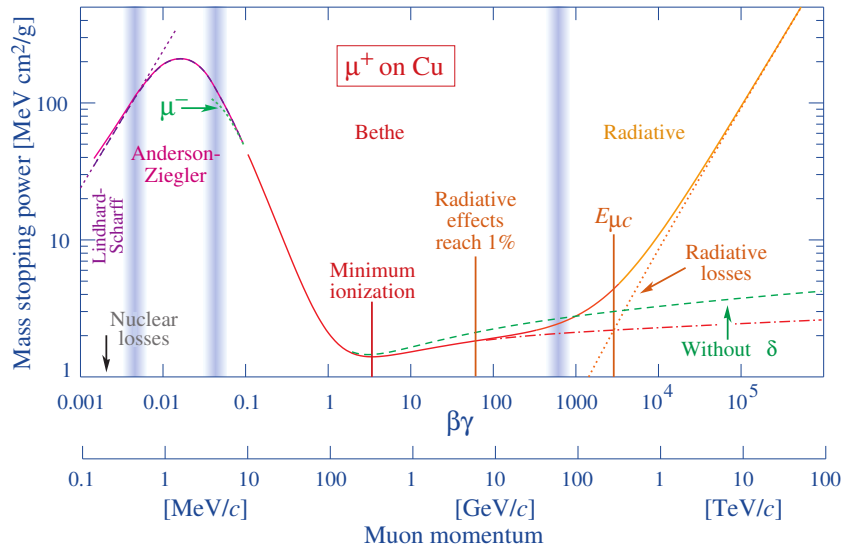


Figure 4.21: Charge spectra have been simulated for single gap, double-gap and multigap layouts [67]. It appears that when single gap shows a decreasing spectrum, double and multigap layouts exhibit a spectrum whose peak is detached from the origin. The detachment gets stronger as the number of gaps increases.



*Figure 4.22:* The maximal theoretical efficiency is simulated for single gap, double-gap and multigap layouts [67] at a constant gap thickness of 2 mm and using an effective Townsend coefficient of  $9 \text{ mm}^{-1}$ .

### 4.3 Signal formation



*Figure 4.23:* Mass stopping power as a function of  $\beta\gamma = p/Mc$  for positive muons in copper [68]. The total stopping power is indicated with solid line and local components with dashed lines. The vertical bands are used to indicate boundaries between different approximations used at different energy range.

The physics of Resistive Plate Chambers still is far from being fully understood and work is regularly being accomplished in trying to model these detectors the best way possible by phenomenological models using well-defined physics [51, 69, 70]. These theoretical works have nevertheless lead to a better understanding of the key principles that account for RPCs signal formation. As previously

discussed, the typical mixture of such a detector is in great majority composed by a ionizing gas with some quenching properties and a low ionization potential to easily produce electrons, with the addition of UV quencher and electronegative compounds. The electronic avalanche formation will be triggered by a charged particle passing through the gas, typically a muon in the case of most uses of RPCs. The production of electrons in the gas of a detector is related to the energy lost by the incoming particle traveling through a material medium. The example of the mass stopping power of copper on muons is given in Figure 4.23 on which the different energy loss mechanisms at different energy ranges are visible. Once primary electrons have been freed in the gas volume, the electric field applied in between the electrodes of the RPC will make the charges move and there will be a competition in the gas in between the Townsend and attachment coefficient which describe the evolution of the number of electrons in an avalanche. While drifting through the gas, the electrons are also subjected to diffusion that will affect the evolution of the avalanches. Finally, when the avalanche is big enough, the accumulation of negative (electrons) and positive (ions) charges in the gas volume will start affecting the local electric field. This effect is known as space charge effect.

### 4.3.1 Energy loss at intermediate energies

Intuitively, a particle traveling through a medium will interact with its components, losing energy. When a muon travels through the gas of a gaseous detector, at the energy range usually observed, it interacts with the molecules of the gas leading to dissipation of the transferred energy in the form of inelastic diffusion or ionization. The photons and electron-ion pairs resulting from these interaction can trigger avalanches in the gas which will contribute to feed the avalanche growth thanks to the strong electric field applied in between the 2 electrodes of a RPC.

The mass stopping power of moderately relativistic ( $0.1 \lesssim \beta\gamma \lesssim 1000$ ) heavy particles ( $M \gg m_e$ ) traveling through a medium via excitation and ionization processes was studied by Bethe in 1930 [71] and is well described by the so called the Bethe Formula given in Equation 4.5.

$$\left\langle -\frac{dE}{dx} \right\rangle = K z^2 \frac{Z}{A} \frac{1}{\beta^2} \left( \frac{1}{2} \ln \frac{2m_e c^2 \beta^2 \gamma^2 W_{max}}{I^2} - \beta^2 - \delta(\beta\gamma) \right) \quad (4.5)$$

The different parameters used in this equation are

$E$	- incident particle energy $\gamma Mc^2$	MeV
$x$	- mass per unit area	$\text{g cm}^{-2}$
$N_A$	- Avogadro's number	$6.022\ 140\ 857(74) \times 10^{23} \text{ mol}^{-1}$
$c$	- speed of light in vacuum	$299\ 792\ 458 \text{ m s}^{-1}$
$\mu_0$	- permeability of free space	$4\pi \times 10^{-7} \text{ N A}^{-2}$
$\epsilon_0$	- permittivity of free space $\epsilon_0 = 1/\mu_0 c^2$	$8.854\ 187\ 817 \dots \times 10^{-12} \text{ F m}^{-1}$
$\alpha$	- fine structure constant $\alpha = e^2/4\pi\epsilon_0\hbar c$	$1/137.035\ 999\ 139(31)$
$r_e$	- classical electron radius $r_e = e^2/4\pi\epsilon_0 m_e c^2$	$2.817\ 940\ 3227(19) \text{ fm}$
$e$	- elementary charge of the electron	$-1.6021766208(98) \times 10^{-19} \text{ C}$
$m_e c^2$	- electron mass $\times c^2$	$0.510\ 998\ 9461(31) \text{ MeV}$
$K$	- constant defined as $K = 4\pi N_A r_e^2 m_e c^2$	$0.307\ 075 \text{ MeV mol}^{-1} \text{ cm}^2$
$z$	- charge number of incident particle	
$Z$	- atomic number of absorbing medium	
$A$	- atomic mass of absorbing medium	$\text{g mol}^{-1}$
$\beta$	- velocity of particle $\beta = v/c$	
$\gamma$	- Lorentz factor $\gamma = (1 - \beta^2)^{-1/2}$	
$W_{max}$	- maximum energy transfer through a single collision	MeV

$I$  - mean excitation energy of absorbing medium eV  
 $\delta(\beta\gamma)$  - density effect correction to ionization energy loss

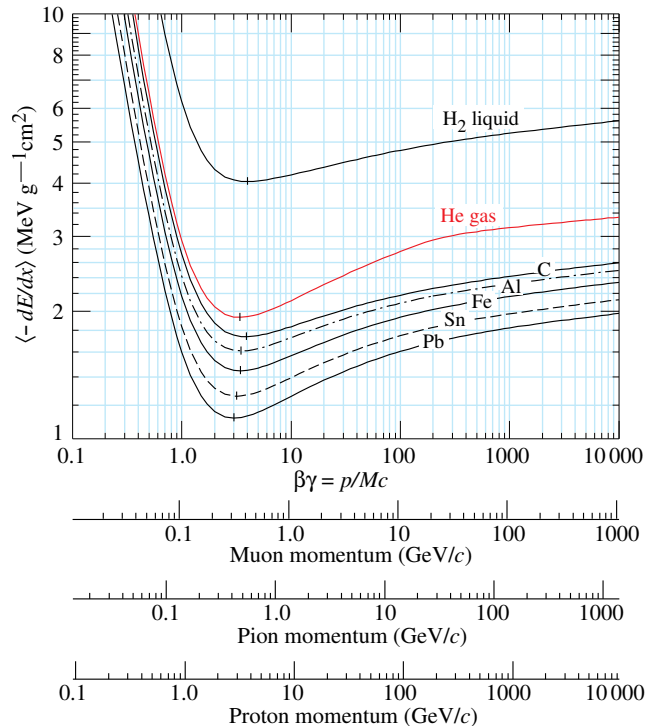


Figure 4.24: Mean mass stopping power for liquid hydrogen, as used in bubble chambers, gaseous helium, carbon, aluminum, iron, tin, and lead without the inclusion of radiative effect at higher  $\beta\gamma$  necessary for pions and muons in denser materials [68].

2308 In this equation, the maximum energy transfer  $W_{max}$  is defined as function of the incident par-  
 2309 ticle mass  $M$ , expressed in  $\text{MeV}/c^2$

$$W_{max} = \frac{2m_e c^2 \beta^2 \gamma^2}{1 + 2\gamma m_e/M + (m_e/M)^2} \quad (4.6)$$

2310 and the mean excitation energy  $I$  depends on the absorber and its determination is non-trivial but  
 2311 recommendation are given by the International Commission on Radiation Units & Measurements  
 2312 (ICRU) based on experimental measurements and interpolations as showed in Figure 4.25.

2313 For the case of copper, the mean stopping power is visible in Figure 4.23. The mean stopping  
 2314 power corresponding only to the Bethe range for other materials is given in Figure 4.24 and shows  
 2315 that  $\langle -dE/dx \rangle$  is similar for each material with a slow decrease with  $Z$ . The factor affecting the  
 2316 equation the most is  $\beta$  as the dependence on  $M$  is introduced at higher energies in the logarithm via  
 2317 the max transfer energy per single collision but in most practice cases, only the dependence on  $\beta$  is  
 2318 considered as most of the relativistic particles are closed to the lowest mean energy loss rate and are  
 2319 referred to as minimum ionizing particles (mip's). The almost logarithmic relation in between the  
 2320 mean energy loss rate for minimum ionizing particles and  $Z$  is showed in Figure 4.26.

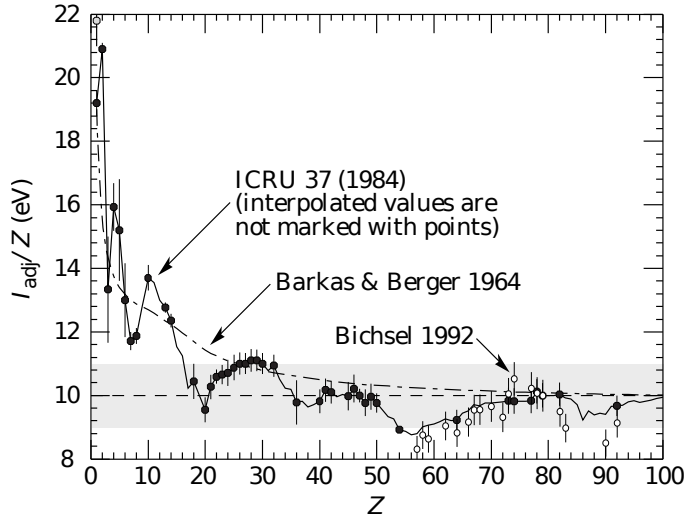


Figure 4.25: Mean excitation energies normalized to the atomic number as adopted by the ICRU [68, 72, 73].

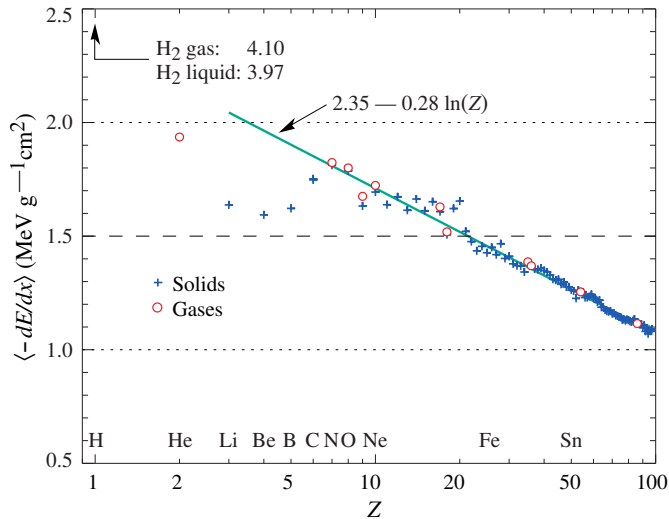


Figure 4.26: Mean mass stopping power at minimum ionization as a function of the atomic number [68].

Finally, the term  $\delta(\beta\gamma)/2$  corresponds to the density effect correction introduced to account for the polarization of a real media that limits the spatial extension of the electric field of relativistic particles. Indeed, as the energy of a particle increases, the associated electric field will flatten and extend. Due to this effect, the distant collision contribution to Equation 4.5 will increase as  $\ln(\beta\gamma)$  but the polarization of the media trunc this rise. At high energies, the correction is given by Equation 4.7

$$\delta/2 \longrightarrow \ln(\hbar\omega_p/I) + \ln(\beta\gamma) - 1/2 \quad (4.7)$$

where  $\hbar\omega_p$  represents the plasma energy that depends on the electron density of the media and

the electron mass and can be calculated as  $\sqrt{\rho \langle Z/A \rangle} \times 28.816$  eV. The introduction of this correction term reduces the increase of the mean stopping power at higher energies as can be seen in Figure 4.23. Moreover, due to poorer electron density, the effect is less visible on gases than on liquids and solids has van be seen from Figure 4.24.

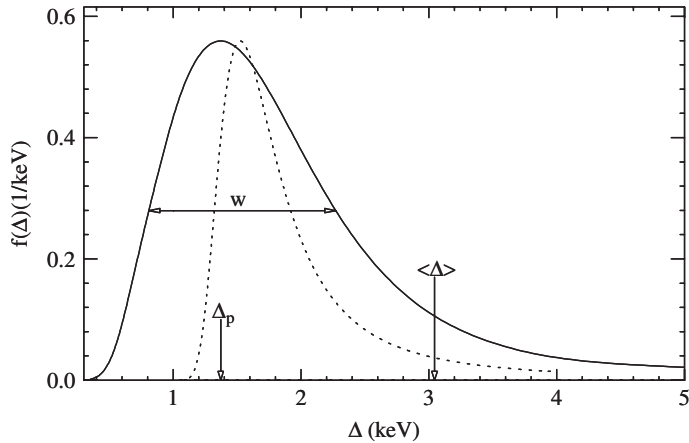


Figure 4.27: Example of straggling function  $f(\Delta)$  of particles passing through 1.2 cm of Argon gas with a  $\beta\gamma$  of 3.6 and represented with a solid line. The original Landau distribution is showed with a dashed line [74].

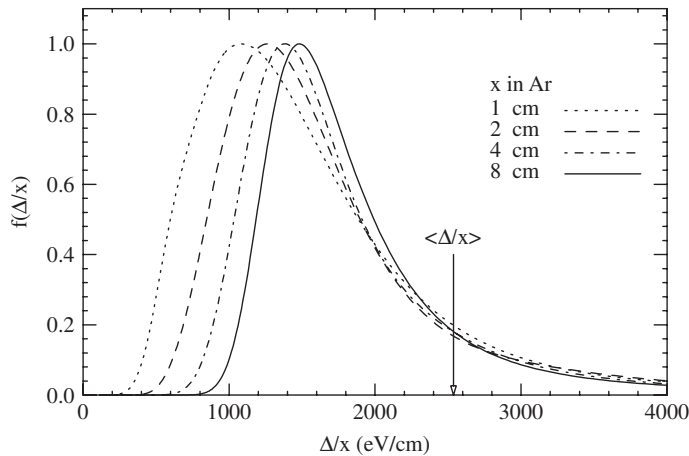


Figure 4.28: Evolution of straggling functions  $f(\Delta)$  of particles passing through a volume of Argon gas with a  $\beta\gamma$  of 3.6 with increasing thickness  $x$  [74].

The mean energy loss per collision can be difficult to measure for low data samples and is not always representative of the energy loss distribution for a given incident particle energy. Hence, it is easier to access the most probable energy loss which is a lower value than than the average loss due to the distribution of the energy transfer. This value is well described by a highly skewed Landau distribution for detectors with "moderate" thickness  $x$ , expressed in g mol<sup>-1</sup>. But for gas volumes, a Landau distribution greatly underestimates the width  $w$  of the distribution and only succeeds to provide with a correct value for the most probable energy loss, as showed in Figure 4.27. Thus, the energy loss distribution is better represented by its most probable energy loss  $\Delta_p$  and its full-

width-at-half-maximum (FWHM)  $w$ . As showed by Figure 4.28, the distribution is affected by the thickness of the gas volume and the most probable energy loss normalized to the thickness is increased and the width decreased, converging towards the Landau distribution, whereas the mean energy loss is unchanged. Correction are brought to the original Landau equation in order to account better for the number of collisions leading to an increased width of the energy loss distribution [74].

In the case of gas mixtures, composed of several elements, using Bragg additivity it can be understood that the mean energy loss of the mixture is the sum of the mean energy losses in each individual element  $j$  layer of weight  $w_j$ .

$$\left\langle \frac{dE}{dx} \right\rangle = \sum w_j \left\langle \frac{dE}{dx} \right\rangle_j \quad (4.8)$$

### 4.3.2 Primary ionization

Using Bethe formula to understand the mean energy transfer of charged particle when traveling through a gas volume give an intuition of the physics that affect the particle but doesn't provide a detailed enough information about the individual ionizations along its tracks at a microscopic level. In order to simulate efficiently an RPC and hence understand the processes governing avalanches creation and growth, knowledge on the ionization process is necessary.

To convert the energy loss rate into a number of primary ionizations was developed in 1980 the Photo-Absorption Ionisation (PAI) model [75] based on the cross section of ionization of gas atoms to real photons and the dielectric constant of the medium through which the charged particles are going. Indeed, the interaction of charged particles with the gas molecules being of electromagnetic nature, it is mediated by quasi-real photons and, hence, the cross section to photon ionization is important to understand. This approach is nevertheless semi-classical as it relies on classical electrodynamics and it only gives access to the energy transfer to the gas atoms and no information on the energy dissipation and secondary emissions is available on the output of the model. The energy transferred to the medium is not all used for ionization. For an energy deposition  $\Delta$ , the number of electron-ion pairs produced is:

$$\Delta = n_i W \quad (4.9)$$

$W$  corresponds to the mean work per pair production that depends on the medium and is greater than the ionization potential leading to the conclusion that part of the transferred energy is dissipated through other processes [70, 76]. In order to understand the energy dissipation and the secondary emissions, the fine structure of each atom is taken into account. Through the PAI model, the incident charged particle interacts is assumed to interact with the full atom rather than with a single electron.

Although, considering that the particle interacts with a single electron, leads to the possibility to study the excited state of the atom once the photo-electron has been emitted with an energy corresponding to the transferred energy minus the binding energy of the electronic shell. The resulting vacancies in the electronic shell will be filled through emission of photons or Auger electrons and can contribute to further ionization or excitation in the gas volume. Fluorescence photons are usually not considered as they only constitute a very small fraction of secondary emissions [77]. Assuming that the transferred energy is absorbed in its totality by a single electronic shell, the PAI model was modified to include relaxations and constitute the new Photo-Absorption Ionisation with Relaxation (PAIR) model [77]. In this model, the cross section corresponding to the whole atom is re-expressed using a sum of partial cross sections corresponding to the different electronic shells. When one or

more electrons are knocked out of the atom, the vacancies are filled by electrons of the shell above with relaxation by Auger electron emission. These processes happen in cascade from the inner shell to the outer one until all the vacancies are filled and the energy has been released.

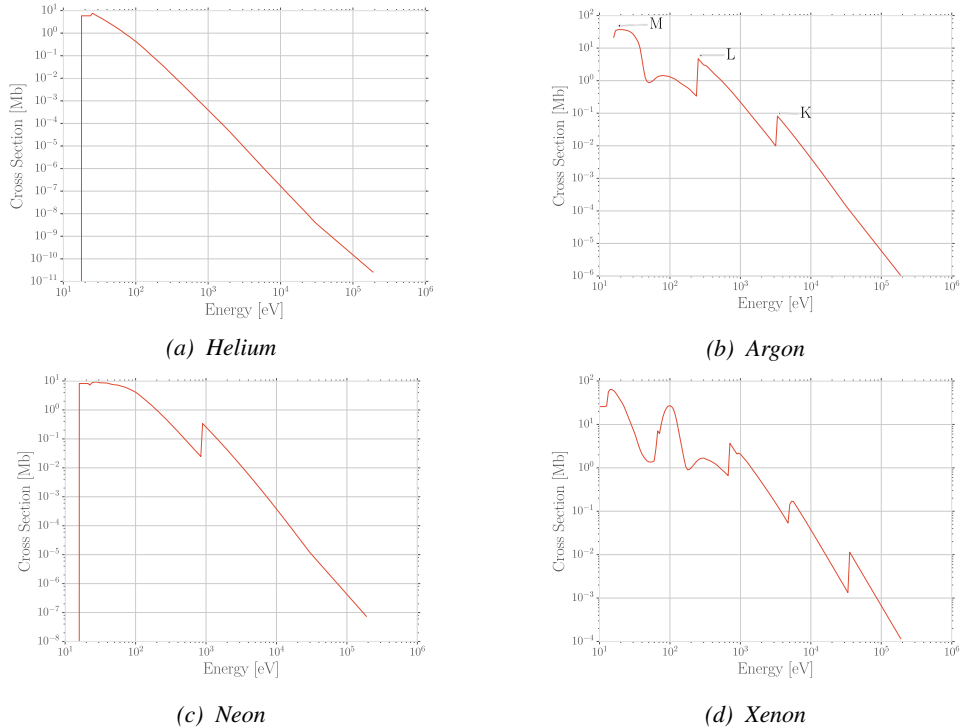


Figure 4.29: Photo-absorption cross section as computed by HEED for noble gases with different electric shell numbers [70].

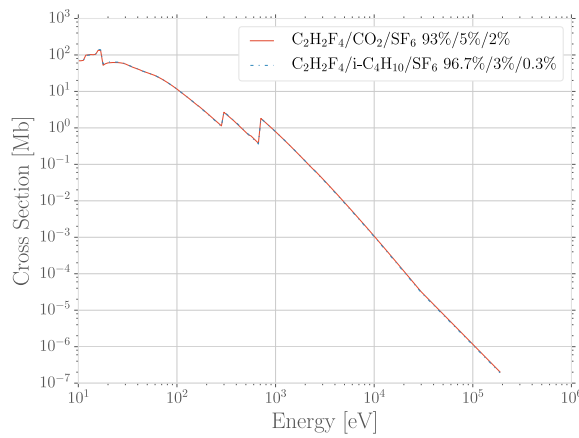


Figure 4.30: Photo-absorption cross section as computed by HEED for typical RPC gas mixtures [70]. The RPC mixture with  $\text{CO}_2$  corresponds to the mixture used by CALICE SDHCAL [78] while the other one was foreseen for the experiment ATLAS [79] but has been changed since then.

This model is included in the program HEED developed at CERN [80] and called by Garfield, a program developed for the simulation of gaseous detectors. The results for the cross section for a few noble gases are given in Figure 4.29. It can be seen that for each shell, the cross section is increased. More complex patterns are seen with bigger atoms such as Xenon on Figure 4.29d. For gas mixtures, like the typical RPC mixtures, the cross section is showed in Figure 4.30. Both mixtures being mainly composed of  $C_2H_2F_4$ , the variations in between the 2 cross section profiles are very subtle and depends on the concentration of the other compounds.

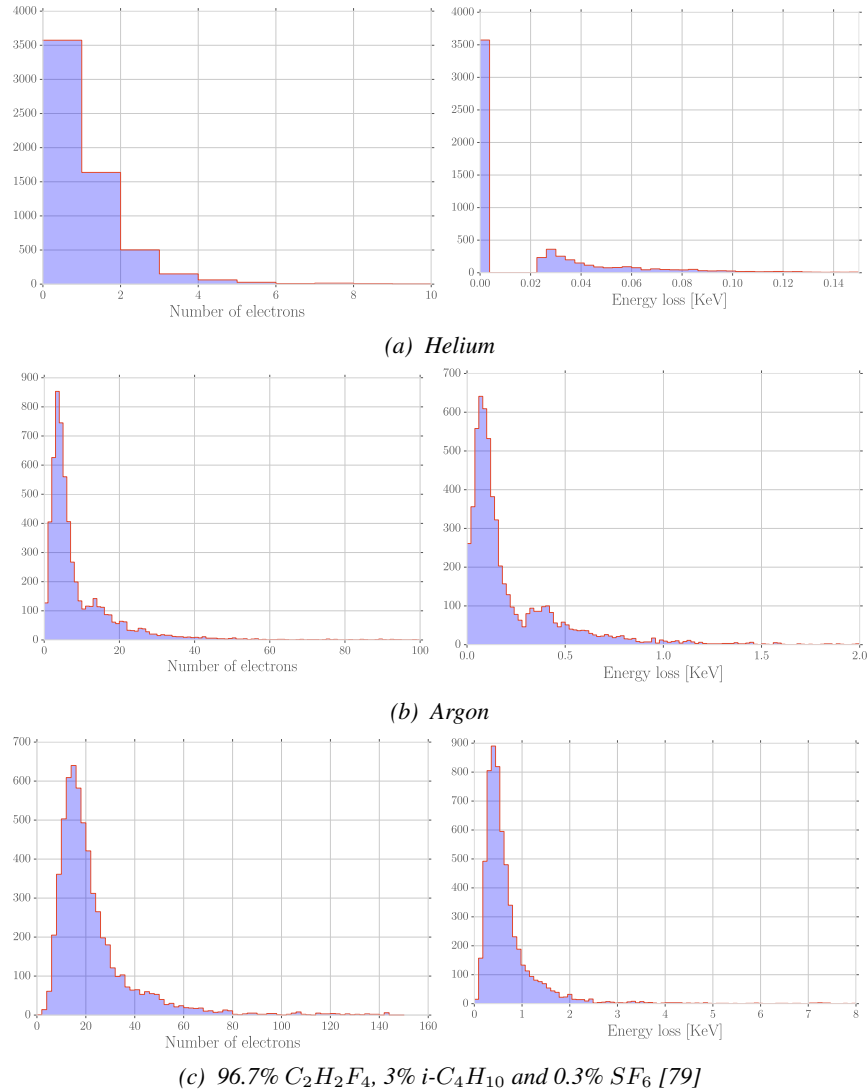


Figure 4.31: Distributions of number of electrons (left) and energy loss (right) for a 5 GeV/c muon passing through 1.2 mm of Helium (Figure 4.31a), Argon (Figure 4.31b) or a typical RPC gas mixture (Figure 4.31c) [70].

Once the cross section of interaction is known, it is possible to extract the distribution of energy loss and of the number of electron produced, as showed in Figure 4.31 for Helium, Argon, which is

used in gaseous detectors, and for a typical RPC mixture [70]. The distributions are computed using HEED and show typical straggling function profiles with some complex structures that can be related to interaction of the incoming particle with the different electronic shells. Helium does not have a great photo-absorption cross-section according to Figure 4.29a and a muon will not be likely to lose a lot of energy and to create a lot of electrons whereas in a more complex atom like Argon, the cross-section is greater and will lead to a greater energy loss of muons and more electron produced. Finally, a complex gas mixture used in RPCs will offer an even greater cross-section, a wider energy loss distribution and will be able to produce more electrons. The same information is seen by looking at the evolution of the mean number of cluster as a function of the lorentz factor associated to muons showed in Figure 4.32a. Indeed, the greater photo-absorption cross-section of RPC mixtures allow for a much greater amount of clusters to be created by charged particles. The size of these clusters is studied through Figure 4.32b which shows that, in most of the cases ( $\approx 80\%$ ), the clusters only are composed of a single electron which is consistent with minimum ionizing particles.

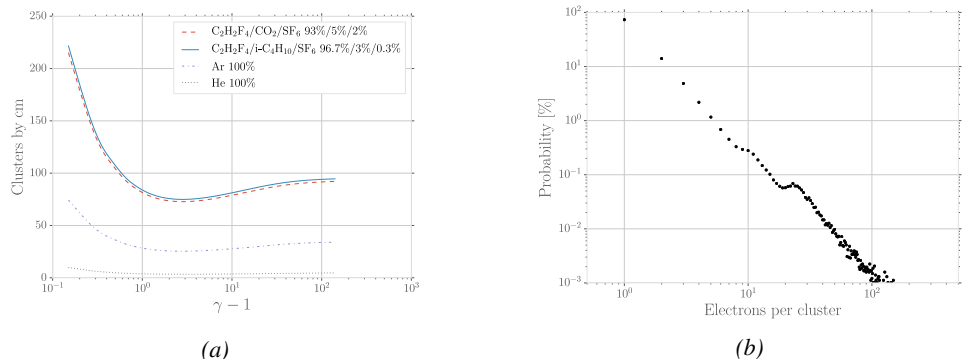


Figure 4.32: Figure 4.32a: Mean cluster density for muons through different gas volumes [70]. Figure 4.32b: Distribution of the number of electrons per cluster for a 5 GeV/c muon traveling through a mixture of 96.7%  $C_2H_2F_4$ , 3%  $i-C_4H_{10}$  and 0.3%  $SF_6$  [70, 79].

### 4.3.3 Development and propagation of avalanches

From the clusters released in the gas volume by the charged particles, free electrons will start drifting due to the electric applied in between the electrodes of the RPC. Gaining velocity and energy, these electrons in their turn will be able to ionize the gas. This process being repeated by all the produced electrons will trigger an avalanche to develop.

The growth of the avalanche can be intuitively understood as a competition between 2 effects. Due to their increasing energy, electrons have a probability to trigger new ionizations by interacting with gas molecules. On the other hand, before the minimal amount of energy is reached, the electrons can get attached to a gas molecule instead. These two effects can be described using a simple model in which the multiplication and attachment processes are given by the Townsend coefficient  $\alpha$  and the attachment coefficient  $\eta$ , assuming that the history of previous interactions in the gas does not influence new interactions. This model simply takes into account probabilities to have at the gas depth  $z$  for a given number  $n$  of free electrons in the gas  $n+1$  or  $n-1$  electrons at the depth  $z+dz$  (respectively  $n\alpha dz$  and  $n\eta dz$ ). Then, the mean number of electrons  $\bar{n}$  and cations  $\bar{p}$  can be written

<sup>2418</sup> for single compound gases as

$$\frac{d\bar{n}}{dz} = (\alpha - \eta)\bar{n}, \quad \frac{d\bar{p}}{dz} = \alpha\bar{n} \quad (4.10)$$

<sup>2419</sup> which, assuming the initial conditions  $\bar{n}(0) = 1$  and  $\bar{p}(0) = 0$ , lead to the mean number of  
<sup>2420</sup> electrons and cations at a depth  $z$

$$\bar{n}(z) = e^{(\alpha-\eta)z}, \quad \bar{p}(z) = \frac{\alpha}{\alpha-\eta} \left( e^{(\alpha-\eta)z} - 1 \right) \quad (4.11)$$

<sup>2421</sup> The Townsend and attachment coefficient as a function of the applied electric field are given in  
<sup>2422</sup> Figure 4.33 for a standard RPC gas mixture using Magboltz [81].

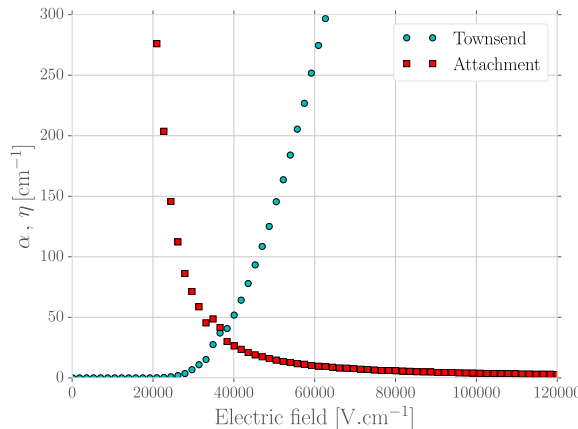


Figure 4.33: Townsend and attachment coefficient for a typical 96.7/3/0.3 mixture of  $C_2H_2F_4/i-C_4H_{10}/SF_6$ , at a temperature  $T = 296.15$  K and a pressure  $P = 1013$  hPa [70, 79].

<sup>2423</sup> Nevertheless, there are more to the avalanche growth than simply these two factors. Throughout  
<sup>2424</sup> the 20<sup>th</sup> century, models have been developed to better understand the physics of discharges in gas.  
<sup>2425</sup> In 1937, Furry developed a model to describe electromagnetic cascades [82] that would be used for  
<sup>2426</sup> electron avalanches in gas during the 1950s. Furry realized that the use of a Poisson law to describe  
<sup>2427</sup> the distribution of shower sizes could not be accurate as he understood that the events occurring in  
<sup>2428</sup> the development of a cascade are not independent from each other, as a Poisson law would suggest.  
<sup>2429</sup> Indeed, part of the particles produce others and this process depends on both their original energy  
<sup>2430</sup> and energy lost. Experimental results showed excess of small showers and an under estimate of very  
<sup>2431</sup> large ones. To solve this problem, Furry proposed a distribution of sizes of following the likelihood  
<sup>2432</sup> described in Equation 4.12, in which  $\bar{n} = e^{\alpha z}$ , compared with a Poisson law in Figure 4.34.

$$P(n, \bar{n}) = \bar{n}^{-1} (1 - \bar{n}^{-1})^{n-1} \quad (4.12)$$

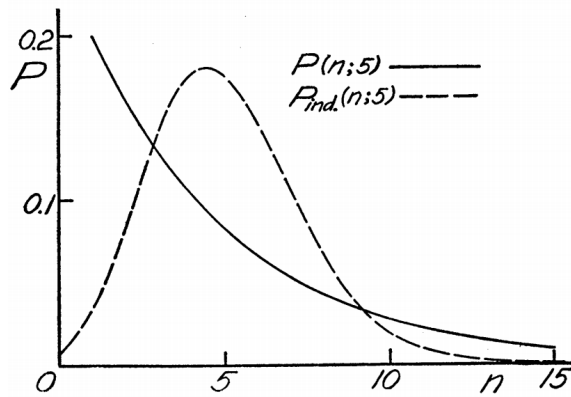


Figure 4.34: Comparison of the distribution law of Furry and the Poisson law for  $\bar{n} = 5$  [82].

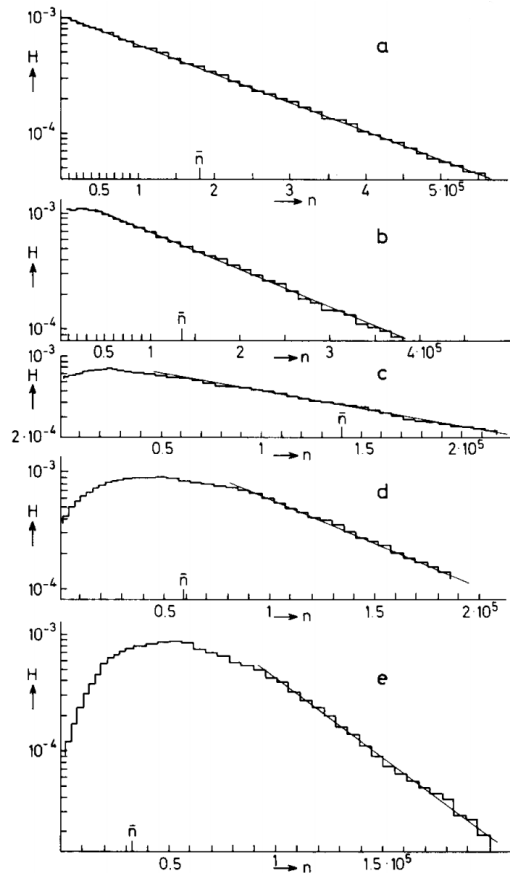


Figure 4.35: Single-electron avalanche size distribution in a proportional counter filled with methylal at different  $E/p$  values. (a) 70, (b) 76.5, (c) 105, (d) 186.5, (e) 426V/cm torr [83].

<sup>2433</sup> In this model, no extra energy is brought to the electrons in the showers, contrary to the case of  
<sup>2434</sup> a gaseous detector such as a RPC where an electric field accelerates them. Using the Furry model,

2435 Genz studied the fluctuations in electron avalanches in gaseous detectors [83]. Collisions leading to  
 2436 ionizations leave electrons with an energy much smaller than the ionization energy  $eU_i$ , where  $U_i$  is  
 2437 the ionization potential of a gas molecule. Hence, the electrons need to travel a distance  $s = U_i/E$   
 2438 along the electric field  $E$  to acquire a high enough energy to trigger a new ionization. For the  
 2439 probability of a new ionization to be independent from the path followed by the electrons since the  
 2440 previous ionization, the mean free path  $1/\alpha$  of electrons in the gas has to be large compared to  $s$  and  
 2441 thus  $E/\alpha \gg U_i$ . The Townsend coefficient is related to the gas pressure leading to conditions on the  
 2442 value of  $E/p$ . Avalanches in gas are large compared to the showers Furry has studied in his original  
 2443 paper. For very large avalanche sizes, Equation 4.12 can be written as an exponential, as showed in  
 2444 Equation 4.13.

$$P(n, \bar{n}) = \bar{n}^{-1} e^{-n/\bar{n}} \quad (4.13)$$

2445 This exponential behaviour is showed through Figure 4.35. In practice, to fully understand the  
 2446 avalanche growth, taking into account the path followed by electrons from one ionization to another  
 2447 will become necessary. In the same paper, Genz then discusses models using Polya distributions  
 2448 to estimate the multiplication by looking at the size of the avalanche it self. Indeed, the number of  
 2449 charge carriers in the avalanche might become important enough to have an effect on the multipli-  
 2450 cation process. To account for this, it was proposed to use a varying Townsend coefficient such as  
 2451 described by Equation 4.14 depending on the position  $x$  in which  $\theta$  is an empirical parameter leading  
 2452 to the probability distribution of Equation 4.15. In the limit case where  $\theta$  goes to 0, the formula  
 2453 describes again the Furry model. But the data deviates from this model as well at large  $n$  values.  
 2454 Moreover, the introduction of an empirical parameters makes the model hard to interpret physically.

$$\alpha(n, x) = \alpha(x) \left(1 + \frac{\theta}{n}\right), \quad n > 0 \quad (4.14)$$

$$P(n, x) = \frac{1 + \theta}{\bar{n}} \frac{1}{\theta!} \left(\frac{n(1 + \theta)}{\bar{n}}\right)^{\theta} e^{-\frac{n(1 + \theta)}{\bar{n}}} \quad (4.15)$$

2455 In order to have a model that describes reality better, the introduction of the attachment into the  
 2456 model is an important step. Despite its limitations, the Furry model had the advantage to describe  
 2457 well avalanches occurring when the attachment could be ignored. This is only natural that this model  
 2458 was then extended to included attachment. This was done by Riegler, Lippmann and Veenhof [79]  
 2459 which showed that was important was to consider both the Townsend coefficient describing the  
 2460 multiplication *and* the attachment coefficient, not only the effective multiplication coefficient  $\bar{\alpha} =$   
 2461  $\alpha - \eta$ . The probability to see an avalanche started by a single electron grow to a size  $n$  after having  
 2462 traveled a distance  $z$  through the gas is given by Equation 4.16.

$$\begin{aligned} P(n, z) = & P(n - 1, z) (n - 1) \alpha dz (1 - (n - 1) \eta dz) \\ & + P(n, z) (1 - n \alpha dz) (1 - n \eta dz) \\ & + P(n, z) n \alpha dz n \eta dz \\ & + P(n + 1, z) (1 - (n + 1) \alpha dz) (n + 1) \eta dz \end{aligned} \quad (4.16)$$

2463 The first term of this probability that from a state with  $n - 1$  electrons, only 1 multiplies while  
 2464 the others don't get attached. Both the second and third terms describes the probability that from  
 2465 a state with already  $n$  electrons the total number of electrons stay the same. On the second term,  
 2466 no electron gets attached nor multiplies while on the third term, 1 electron gets multiplied and 1

2467 gets attached to compensate. Finally, the fourth term describes the probability to fall from a state  
 2468 with  $n + 1$  to a state with  $n$  electrons due to the attachment of a single electron. At the first order,  
 2469 the evaluation of the previous expression leads to Equation 4.17 which general solution is given in  
 2470 Equation 4.18 in which are introduced the variables  $\bar{n}(z)$ , defined as in Equation 4.11, and  $k = \eta/\alpha$   
 2471 making explicit the fact that the distribution not only depends on the effective Townsend coefficient.

$$\frac{dP(n, z)}{dz} = -P(n, z)n(\alpha + \eta) + P(n - 1, z)(n - 1)\alpha + P(n + 1, z)(n + 1)\eta \quad (4.17)$$

$$P(n, z) = \begin{cases} k \frac{\bar{n}(z)-1}{\bar{n}(z)-k}, & n = 0 \\ \bar{n}(z) \left( \frac{1-k}{\bar{n}(z)-k} \right)^2 \left( \frac{\bar{n}(z)-1}{\bar{n}(z)-k} \right)^{n-1}, & n > 0 \end{cases} \quad (4.18)$$

2472 The example given through Figure 4.36 shows the importance of each individual process in  
 2473 the growth of avalanches and the fluctuation of their size. The values of  $\alpha$  and  $\eta$  will influence  
 2474 the probability distribution, as can be seen from Figure 4.36a. Then, Figure 4.36b shows that the  
 2475 fluctuation really takes place within the very first interactions. Indeed, when the avalanche contains  
 2476 a large enough amount of charge carriers (a few hundreds), its size then increases like  $e^{z(\alpha-\eta)}$ .

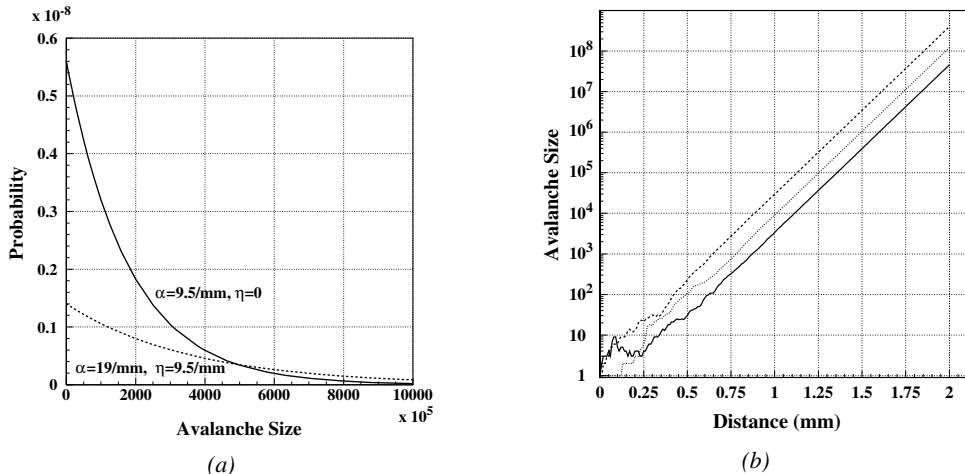


Figure 4.36: Figure 4.36a: Comparison of avalanche size distributions for different values of Townsend and attachment coefficients. The effective Townsend coefficient is the same for both distributions. Figure 4.36b: Fluctuation in avalanche size for avalanche started by a single electron with  $\alpha = 13 \text{ mm}^{-1}$  and  $\eta = 3.5 \text{ mm}^{-1}$  [79].

#### 2477 4.3.4 Drift and diffusion of the electron cloud

2478 During the growth of avalanches, an electron cloud drifting along the electric field through the gas  
 2479 will undergo thermal diffusion due to random collisions with the gas molecules. This phenomenon  
 2480 can be studied using Maxwell-Boltzmann distribution whose mean is defined by the thermal energy  
 2481 of the cloud  $\langle E \rangle = 3/2kT$  with an extra component coming from the constant drift motion. The  
 2482 drift of electrons along the field lines is usually observed on a macroscopic scale through which the  
 2483 speed can be assimilated to a constant  $v_D$  which corresponds to the mean drift speed over a large  
 2484 number of collisions in the gas.

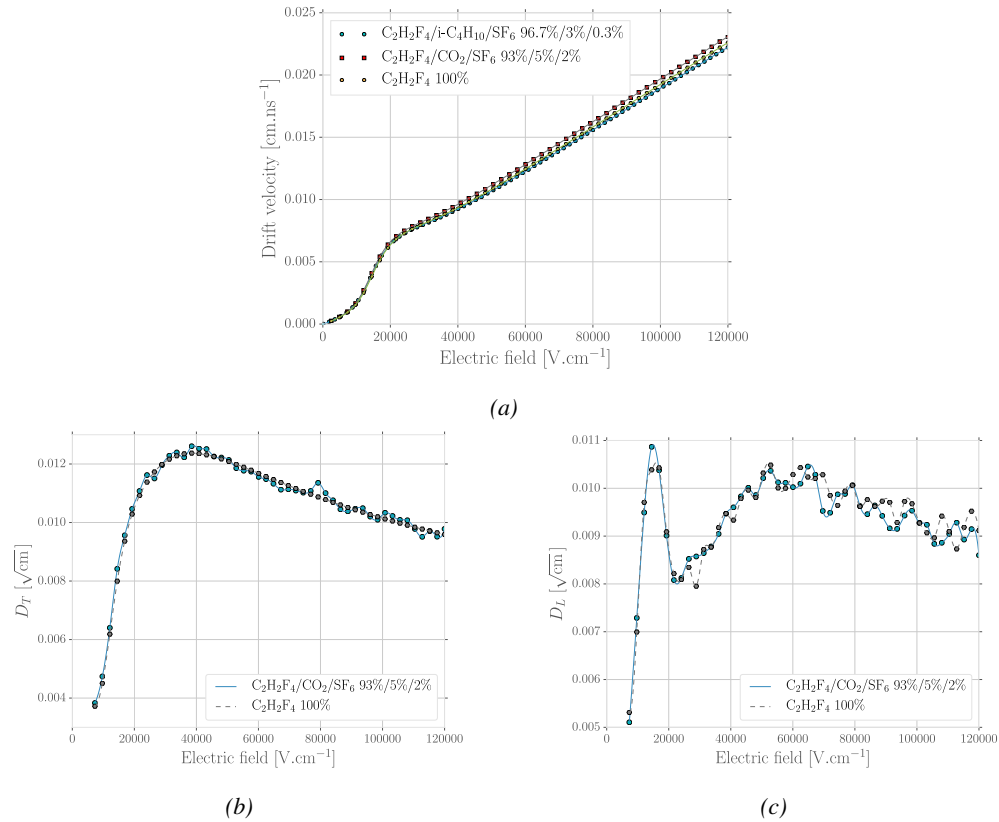


Figure 4.37: Figure 4.37a: Electron mean drift velocity  $v_D$  in pure  $C_2H_2F_4$  and typical RPC gas mixtures. Figure 4.37b: Transverse diffusion coefficient in pure  $C_2H_2F_4$  and a typical RPC gas mixture. Figure 4.37c: Longitudinal diffusion coefficient in pure  $C_2H_2F_4$  and a typical RPC gas mixture. All results are given with a pressure  $P = 760$  Torr and a temperature  $T = 296.15$  K [70].

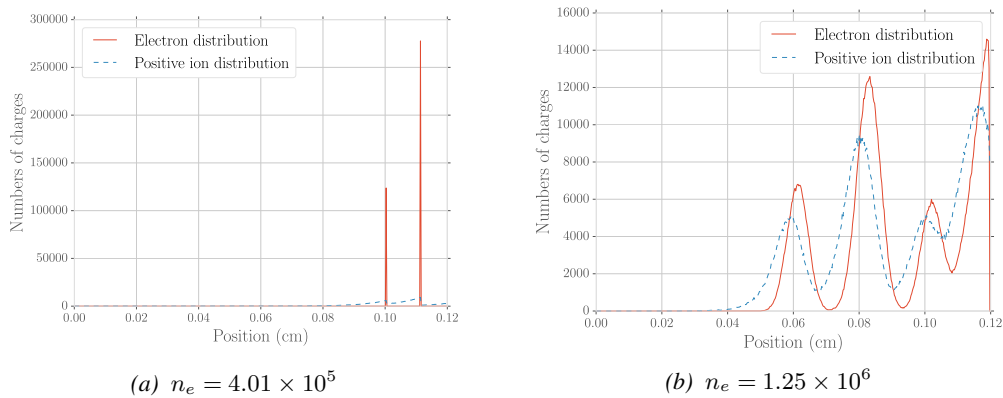


Figure 4.38: Comparison of the free charge carriers in the gas after a time  $t = 7.90$  ns in the case where no diffusion is taken into account to simulate the avalanche (Figure 4.38a) and in the case where the diffusion is implemented (Figure 4.38b) [70].

Indeed, at the microscopic scale, the electrons are drifting over a distance  $\delta z$  while acquiring the corresponding kinetic energy  $T = e_0 |\vec{E}| \delta z$  until they are slowed down by a collision in which they lose part of their energy. This process is repeated as long as electrons are free carriers. Starting from a point-like electron cloud, the Gaussian density distribution at  $\vec{r}_0$  will be described by Formula 4.19 in which the width of the isotropic distribution is  $\sigma = 2\bar{D}t$ , with  $\bar{D}$  being a diffusion coefficient expressed in  $\text{m}^2/\text{s}$  [51].

$$\varphi(\vec{r}, t) = \frac{1}{(\sqrt{2\pi}\sigma(t))^3} \exp\left(-\frac{(\vec{r} - \vec{r}_0)^2}{2\sigma^2(t)}\right) \quad (4.19)$$

Now, if the constant drifting motion is added, the distribution is anisotropic and can be divided onto transversal (Formula 4.20) and longitudinal (Formula 4.21) terms,  $\varphi(r, z, t) = \varphi_T(r, t)\varphi_L(z, t)$ , with a cylindrical symmetry around the field axis [51]. The variables  $t$  and  $\sigma_{T,L}(t)$  can be hidden to the profit of the diffusion coefficients by using the relations  $v_D = l/t$  and  $\sigma_{T,L}^2(t) = 2\bar{D}_{T,L}l/v_D$  and introducing new diffusion coefficients  $D_{T,L} = \sqrt{2\bar{D}_{T,L}/v_D}$  in order to explicitly show the dependence of the Gaussian width in drifted distance  $l$ .

$$\varphi_T(r, t) = \frac{1}{D_T^2 l} \exp\left(-\frac{(r - r_0)^2}{2D_T^2 l}\right) \quad (4.20)$$

$$\varphi_L(z, t) = \frac{1}{\sqrt{2\pi l} D_L} \exp\left(-\frac{(z - z_0)^2}{2D_L^2 l}\right) \quad (4.21)$$

These coefficients, as well as the drift velocity of the electrons, can be calculated thanks to Magboltz as showed in Figure 4.37. The influence of the diffusion on the distribution of charge carriers throughout the gas volume is depicted in Figure 4.38. From very localised electron clusters in the gas in Figure 4.38a, a Gaussian diffusion is then visible in Figure 4.38b. Due to the interactions with gas molecules during the drift, diffusions can occur in the forward and backward direction. Electrons diffused backward will effectively drift over a longer distance and multiply more than electrons diffused forward that will see a shorter drift length. As an effect, the avalanche develops over a longer time and extends over a greater gas volume than in the case the electron cloud is considered as point like and without diffusion. Moreover, as a side effect to the longer growth of the avalanche due to backward longitudinal diffusion, the total production of electrons is increased.

### 4.3.5 Space charge effect

Now that have been considered the basic processes that influence the development of avalanches in a gaseous detector in the previous sections, it is now important to consider the influence of the charge carriers present in the avalanche on the electric field seen by the avalanche. Indeed, each charged particle induces an electric field and it is only natural that the increasing density of electrons and ions in the detector volume will affect the electric field. Thus, parameters such as the Townsend and attachment coefficients, drift velocity or diffusion coefficients will find themselves to be modified along the gas gap length due to this effect referred to as *space charge effect*. Figure 4.39 is a more detailed version of Figure 4.1 (b) in which three electric regions are distinguished [51]. When compared to the linear electric field of strength  $E_0$  that is developed in between the detector's electrodes, the accumulation of negative charges (electrons) on the front of the avalanche will reinforce the effective electric field in between the anode of the avalanche front. Deeper in the gas volume, the positive charges (cations) slowly drift towards the cathode and can induce together with the avalanche front

opposite electric field loops. Finally, due to the density of positive charges, the electric field seen in between the ions tails and the cathode charged with negative charges is on average stronger than  $E_0$  and compensate for the locally reversed field  $E_2$ . Lippmann roughly estimated by considering that  $10^6$  charges were contained in a sphere of radius  $r_d = 0.1$  mm that the space charge effect could change the electric field by 3% and the Townsend and attachment coefficient up to 14% [51, 70].

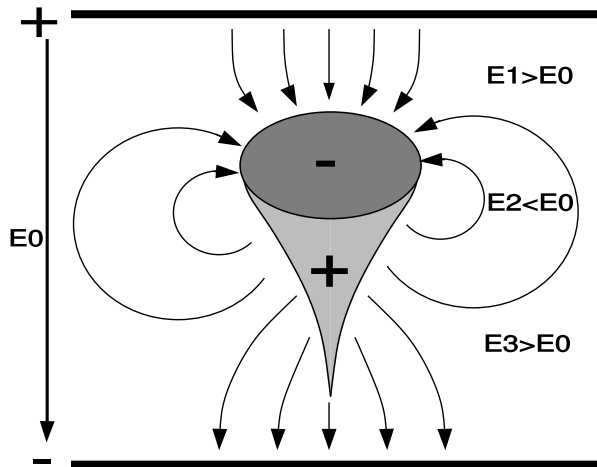


*Figure 4.39: Schematic representation of an avalanche and of the electric field deformation it causes due to the local concentration of charge carriers [51].*

To account for the space charge effect, the electric potential and field of free charges are solved and applied to each charges in the avalanche [51, 70]. As discussed by Fran ais who has been working on simulating RPCs similar to that used by the SDHCAL project of ILC, the computation of these equations for each individual charge carrier to dynamically know the space charge field at every stage of an avalanche development is a difficult task and would require far too much computation time and a solution is to pre-compute an interpolation table keeping an adequately large number of values of the space charge field for each positions in space thanks to which the values stored in the interpolation table become very close to the analytic solution and allow for a much faster simulation.

The study of space charge effect through simulation shows that it can lead to a saturation of the avalanche growth due to the deformation of the electric field, as showed through Figure 4.40. Additionnally, a more precise understanding of the space charge effect is given through Figure 4.41 which looks at the distribution of charges and the distortion of the electric field at different steps of the evolution of an avalanche in a RPC. At the moment a 5 GeV muon ionizes the gas, electron-ion pairs are created in the gas in different clusters (Figure 4.41a). Later, the first clusters have reached the anode while the clusters that where created the closest to the cathode are now big enough to start influencing the electric field in the gap (Figure 4.41b). When a cluster is big enough, the electric field in front of it locally increases a lot and contributes to a stronger but very localised multiplication. At the same moment, the positive ions right behind the cluster avalanche front decrease the electric field, saturating the electron multiplication on the tail of the electron cloud (Figure 4.41c). Finally, when all the electrons have reached the anode and are relaxing, the electric field still is very deformed by the distribution of both positive and negative ions in the the gas volume closest to the anode (Figure 4.41d).

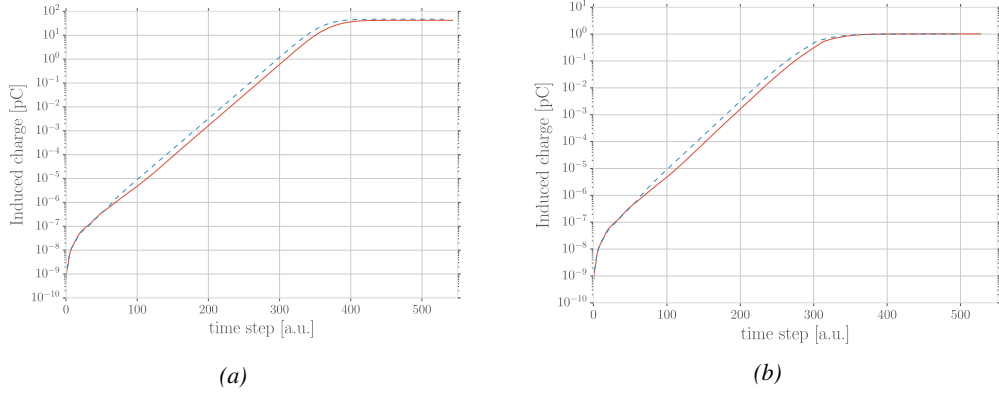


**Figure 4.40:** Evolution of the charge induced by an avalanche started by a single electron in a 1.2 mm thick RPC with an applied electric field of 54 kV/cm in the case space charge is not taken into account (Figure 4.40a) and in the case it is implemented into the simulation (Figure 4.40b). The total induced charge is correlated to the size of the avalanche [70].

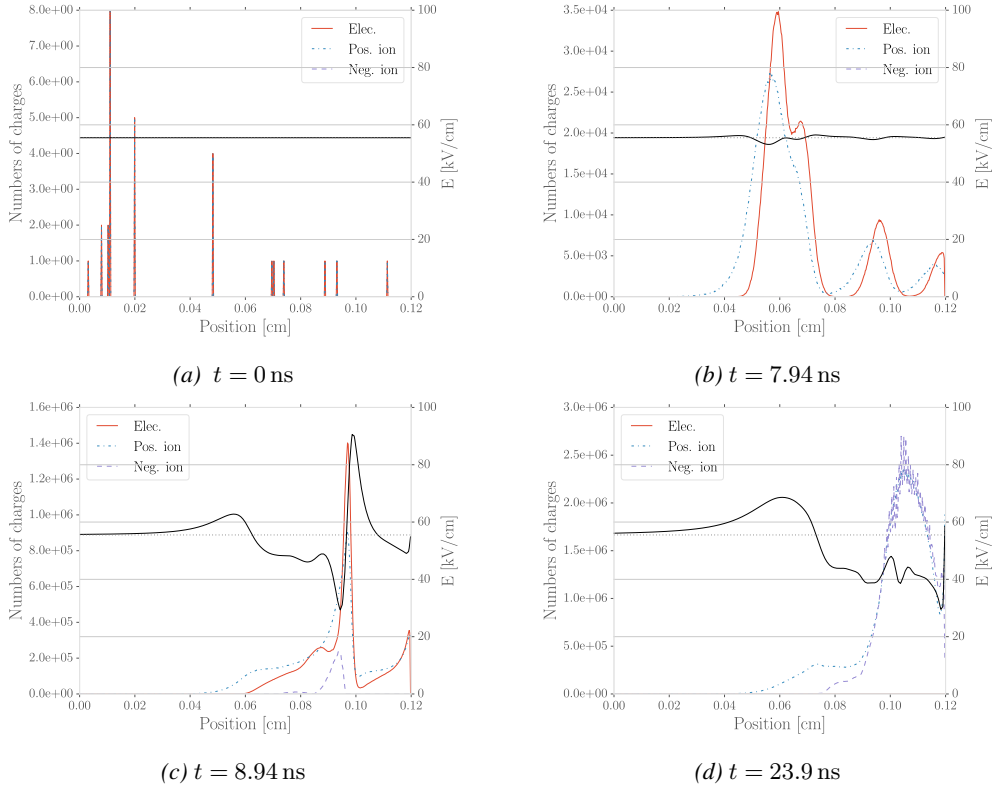


**Figure 4.41:** Distributions of charge carriers within the gas volume of a 1.2 mm thick RPC and the corresponding deformation of the electric field at different time steps with an applied electric field of 55.5 kV/cm [70].

2548     The electric field following the development of an avalanche can stay perturbed for a long time  
2549     with respect to the avalanche development due to the slow drift of the much heavier ions. This

2550 can result in secondary avalanches triggered by the fluctuation of the electric field close enough to  
2551 the cathode leading to emission of electrons at the surface of the electrode. this phenomenon is  
2552 frequently observed experimentally after a strong avalanche.



# 5

2553

2554

2555

## Longevity studies and Consolidation of the present CMS RPC subsystem

### 2556 5.1 Resistive Plate Chambers at CMS

#### 2557 5.1.1 Overview

2558 The Resistive Plate Chambers (RPC) system, located in both barrel and endcap regions, provides a  
2559 fast, independent muon trigger with a looser  $p_T$  threshold over a large portion of the pseudorapidity  
2560 range ( $|\eta| < 1.6$ ) [add reconstruction].

2561

2562 During High-Luminosity LHC (HL-LHC) operations the expected conditions in terms of back-  
2563 ground and pile-up will make the identification and correct  $P_T$  assignment a challenge for the Muon  
2564 system. The goal of RPC upgrade is to provide additional hits to the Muon system with precise tim-  
2565 ing. All these informations will be elaborated by the trigger system in a global way enhancing the  
2566 performance of the trigger in terms of efficiency and rate control. The RPC Upgrade is based on two  
2567 projects: an improved Link Board System and the extension of the RPC coverage up to  $|\eta| = 2.4$ .  
2568 [FIXME 2.4 or 2.5?]

2569 The Link Board system, that will be described in section xxx, is responsible to process, syn-  
2570 chronize and zero-suppress the signals coming from the RPC front end boards. The Link Board  
2571 components have been produced between 2006 and 2007 and will be subjected to aging and failure  
2572 in the long term. The upgraded Link Board system will overcome the aging problems described in  
2573 section xxx and will allow for a more precise timing information to the RPC hits from 25 to 1 ns [ref  
2574 section xxx].

2575 The extension of the RPC system up to  $|\eta| = 2.1$  was already planned in the CMS TDR [ref  
2576 cmstdr] and staged because of budget limitations and expected background rates higher than the rate  
2577 capability of the present CMS RPCs in that region. An extensive R&D program has been done in  
2578 order to develop an improved RPC that fulfills the CMS requirements. Two new RPC layers in the  
2579 innermost ring of stations 3 and 4 will be added with benefits to the neutron-induced background

2580 reduction and efficiency improvement for both trigger and offline reconstruction.

### 2581 5.1.2 The present RPC system

2582 The RPC system is organized in 4 stations called RB1 to RB4 in the barrel region, and RE1 to RE4  
 2583 in the endcap region. The innermost barrel stations, RB1 and RB2, are instrumented with 2 layers  
 2584 of RPCs facing the innermost (RB1in and RB2in) and outermost (RB1out and RB2out) sides of the  
 2585 DT chambers. Every chamber is then divided from the read-out point of view into 2 or 3  $\eta$  partitions  
 2586 called “rolls”. The RPC system consist of 480 barrel chambers and 576 endcap chambers. Details  
 2587 on the geometry are discussed in the paper [ref to geo paper].

2588 The CMS RPC chamber is a double-gap, operated in avalanche mode to ensure reliable operation  
 2589 at high rates. Each RPC gap consists of two 2-mm-thick resistive High-Pressure Laminate (HPL)  
 2590 plates separated by a 2-mm-thick gas gap. The outer surface of the HPL plates is coated with a thin  
 2591 conductive graphite layer, and a voltage is applied. The RPCs are operated with a 3-component,  
 2592 non-flammable gas mixture consisting of 95.2% freon ( $C_2H_2F_4$ , known as R134a), 4.5% isobutane  
 2593 ( $i-C_4H_{10}$ ), and 0.3% sulphur hexafluoride ( $SF_6$ ) with a relative humidity of 40% - 50%. Readout  
 2594 strips are aligned in  $\eta$  between the 2 gas gaps. [\[Add a sentence on FEBs.\]](#)

2595 The discriminated signals coming from the Front End boards feed via twisted cables (10 to 20 m  
 2596 long) the Link Board System located in UXC on the balconies around the detector. The Link System  
 2597 consist of the 1376 Link Boards (LBs) and the 216 Control Boards (CBs), placed in 108 Link Boxes.  
 2598 The Link Box is a custom crate (6U high) with 20 slots (for two CBs and eighteen LBs). The Link  
 2599 Box contains custom backplane to which the cables from the chambers are connected, as well as the  
 2600 cables providing the LBs and CBs power supply and the cables for the RPC FEBs control with use  
 2601 of the I2C protocol (trough the CB). The backplane itself contains only connectors (and no any other  
 2602 electronic devices).

2603 The Link Board has 96 input channels (one channel corresponds to one RPC strip). The input  
 2604 signals are the  $\sim 100$  ns binary pulses which are synchronous to the RPC hits, but not to the LHC  
 2605 clock (which drives the entire CMS electronics). Thus the first step of the FEB signals processing  
 2606 is synchronization, i.e. assignment of the signals to the BXes (25 ns periods). Then the data are  
 2607 compressed with a simple zero-suppressing algorithm (the input channels are grouped into 8 bit  
 2608 partitions, only the partitions with at least one nonzero bit are selected for each BX). Next, the non-  
 2609 empty partitions are time-multiplexed i.e. if there are more than one such partition in a given BX,  
 2610 they are sent one-by-one in consecutive BXes. The data from 3 neighbouring LBs are concentrated  
 2611 by the middle LB which contains the optical transmitter for sending them to the USC over a fiber at  
 2612 1.6 Gbps.

2613 The Control Boards provide the communication of the control software with the LBs via the  
 2614 FEC/CCU system. The CBs are connected into token rings, each ring consists of 12 CBs of one  
 2615 detector tower and a FEC mezzanine board placed on the CCS board located in the VME crate in  
 2616 the USC. In total, there are 18 rings in the entire Link System. The CBs also perform automatic  
 2617 reloading of the LB's firmware which is needed in order to avoid accumulation of the radiation  
 2618 induced SEUs in the LBs firmware.

2619 Both LBs and CB are based on the Xilinx Spartan III FPGAs, the CB additionally contains  
 2620 radiation-tolerant (FLASH based) FPGA Actel ProAsicPlus.

2621 The High Voltage power system is located in USC, not exposed to radiation and easily accessible  
 2622 for any reparation. A single HV channel powers 2 RPC chambers both in the barrel and endcap  
 2623 regions. The Low Voltage boards are located in UXC on the balconies and provide the voltage to the

2624 front end electronics.

### 2625 5.1.3 Pulse processing of CMS RPCs

2626 Signals induced by cosmic particle in the RPC strips are shaped by standard CMS RPC Front-End  
 2627 Electronics (FEE) following the scheme of Figure 5.1. On a first stage, analogic signals are amplified  
 2628 and then sent to the Constant Fraction Discriminator (CFD) described in Figure 5.2. At the end of  
 2629 the chain, 100 ns long pulses are sent in the LVDS output. These output signal are sent on one side to  
 2630 a V1190A Time-to-Digital Converter (TDC) module from CAEN and on the other to an OR module  
 2631 to count the number of detected signals. Trigger and hit coïncidences are monitored using scalers.  
 2632 The TDC is used to store the data into ROOT files. These files are thus analysed to understand the  
 2633 detectors performance.

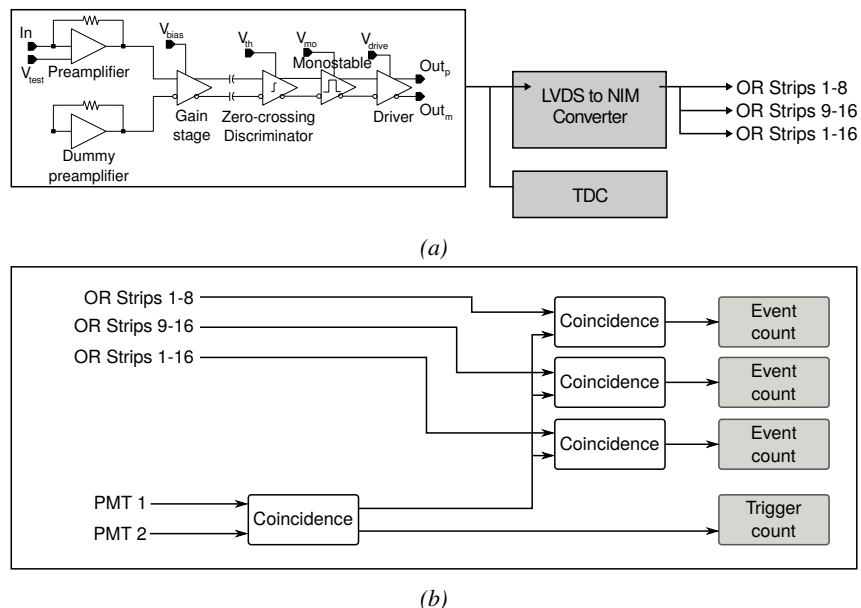
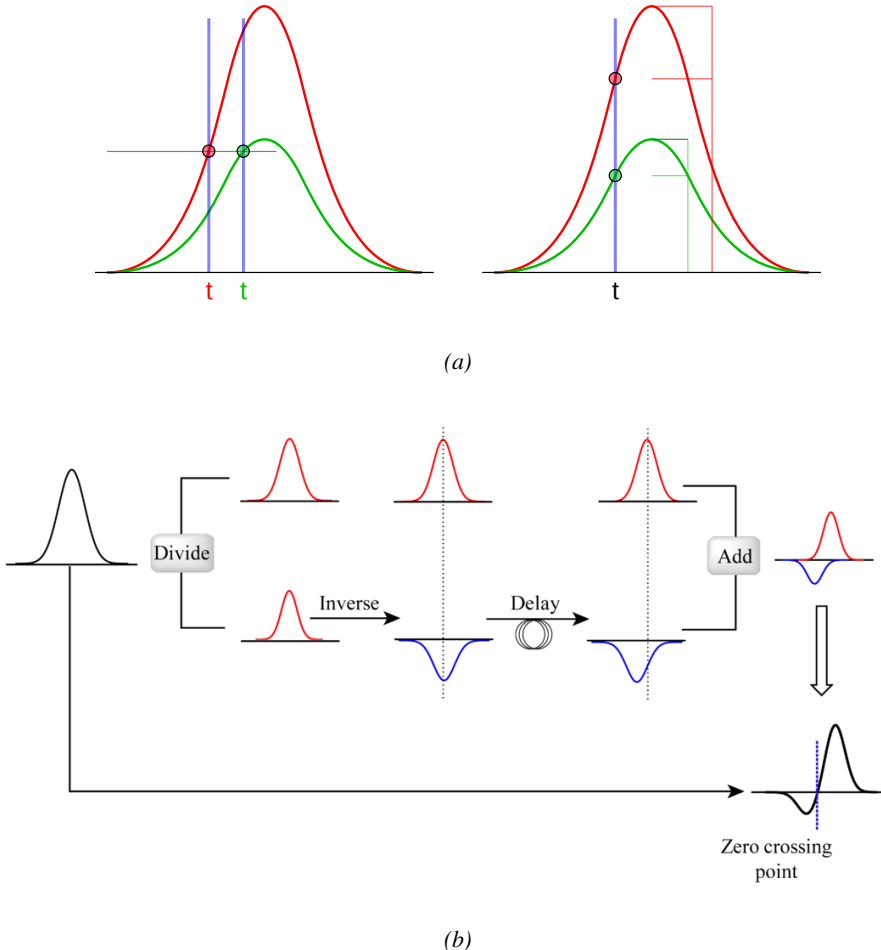


Figure 5.1: Signals from the RPC strips are shaped by the FEE described on Figure 5.1a. Output LVDS signals are then read-out by a TDC module connected to a computer or converted into NIM and sent to scalers. Figure 5.1b describes how these converted signals are put in coincidence with the trigger.



*Figure 5.2: Description of the principle of a CFD. A comparison of threshold triggering (left) and constant fraction triggering (right) is shown in Figure 5.2a. Constant fraction triggering is obtained thanks to zero-crossing technique as explained in Figure 5.2b. The signal arriving at the input of the CFD is split into three components. A first one is delayed and connected to the inverting input of a first comparator. A second component is connected to the noninverting input of this first comparator. A third component is connected to the noninverting input of another comparator along with a threshold value connected to the inverting input. Finally, the output of both comparators is fed through an AND gate.*

## 5.2 Testing detectors under extreme conditions

The upgrade from LHC to HL-LHC will increase the peak luminosity from  $10^{34} \text{ cm}^{-2} \text{ s}^{-1}$  to reach  $5 \times 10^{34} \text{ cm}^{-2} \text{ s}^{-1}$ , increasing in the same way the total expected background to which the RPC system will be subjected to. Composed of low energy gammas and neutrons from  $p\text{-}p$  collisions, low momentum primary and secondary muons, puch-through hadrons from calorimeters, and particles produced in the interaction of the beams with collimators, the background will mostly affect the regions of CMS that are the closest to the beam line, i.e. the RPC detectors located in the endcaps. [To update.]

2642

2643     The 2016 data allowed to study the values of the background rate in all RPC system. In Figure 5.3, the distribution of the chamber background hit rate per unit area is shown at a luminosity  
 2644     of  $5 \times 10^{34} \text{ cm}^{-2} \cdot \text{s}^{-1}$  linearly extrapolating from data collected in 2016 [ref mentioning the linear  
 2645     dependency of rate vs lumi]. The maximum rate per unit area at HL-LHC conditions is expected to  
 2646     be of the order of  $600 \text{ Hz/cm}^2$  (including a safety factor 3). Nevertheless, Fluka simulations have  
 2647     conducted in order to understand the background at HL-LHC conditions. The comparison to the  
 2648     data has shown, in Figure 5.4, a discrepancy of a factor 2 even though the order of magnitude is  
 2649     consistent. [Understand mismatch.]  
 2650

2651

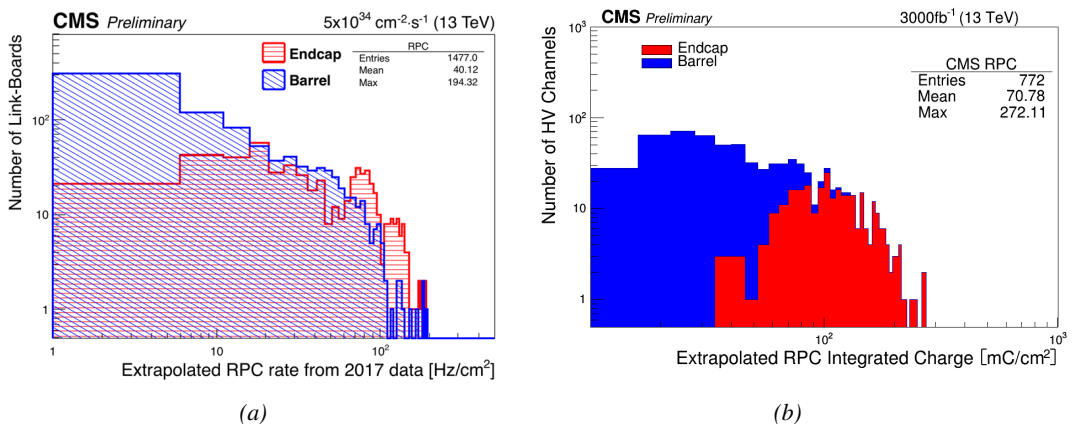


Figure 5.3: Figure 5.3a: The integrated charge per region (Barrel, Endcap) is extrapolated to HL-LHC integrated luminosity ( $3000 \text{ fb}^{-1}$ ) using the data accumulated in 2016 in every HV channels. Figure 5.3b: The hit rate per region (Barrel, Endcap) is linearly extrapolated to HL-LHC highest instantaneous luminosity ( $5 \times 10^{34} \text{ cm}^{-2} \text{s}^{-1}$ ) using the rate as a function of instantaneous luminosity recorded by RPCs in 2017 showing a linear dependence.

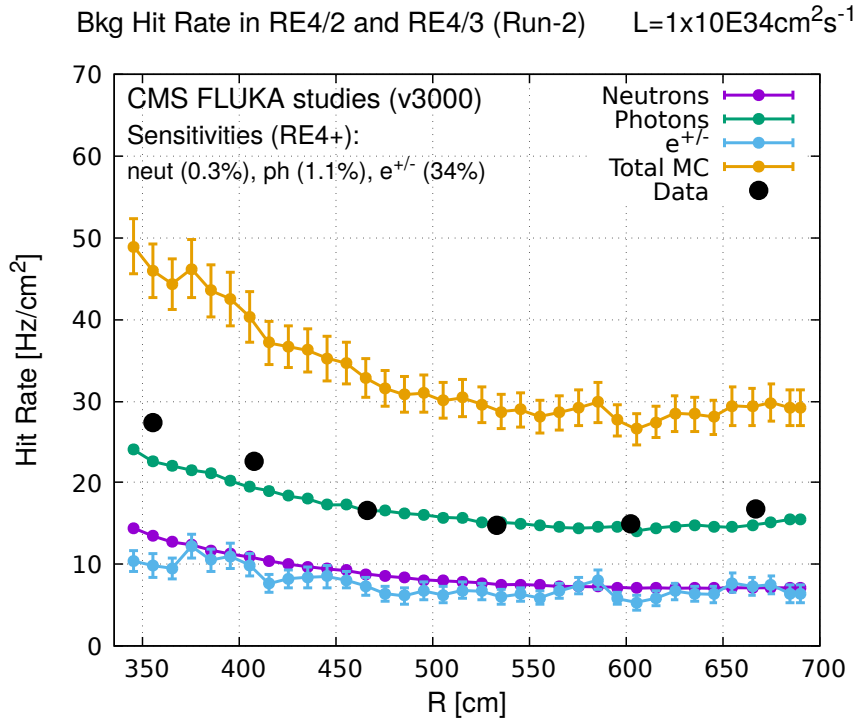


Figure 5.4: Background Fluka simulation compared to 2016 Data at  $L = 10^{34} \text{ cm}^{-2} \cdot \text{s}^{-1}$  in the fourth endcap disk region. A mismatch in between simulation and data can be observed. [\[To be understood.\]](#)

In the past, extensive long-term tests were carried out at several gamma and neutron facilities certifying the detector performance. Both full size and small prototype RPCs have been irradiated with photons up to an integrated charge of  $\sim 0.05 \text{ C/cm}^2$  and  $\sim 0.4 \text{ C/cm}^2$ , respectively [84, 85]. During Run-I, the RPC system provided stable operation and excellent performance and did not show any aging effects for integrated charge of the order of  $0.01 \text{ C/cm}^2$ . Projections on currents from 2016 Data, has allowed to determine that the total integrated charge, by the end of HL-LHC, would be of the order of  $1 \text{ C/cm}^2$  (including a safety factor 3). [\[Corresponding figure needed.\]](#)

2659

## 2660 5.2.1 The Gamma Irradiation Facilities

### 2661 5.2.1.1 GIF

2662 Located in the SPS West Area at the downstream end of the X5 test beam, the Gamma Irradiation  
 2663 Facility (GIF) was a test area in which particle detectors were exposed to a particle beam in presence  
 2664 of an adjustable gamma background [86]. Its goal was to reproduce background conditions these  
 2665 detectors would suffer in their operating environment at LHC. GIF layout is shown in Figure 5.5.  
 2666 Gamma photons are produced by a strong  $^{137}\text{Cs}$  source installed in the upstream part of the zone  
 2667 inside a lead container. The source container includes a collimator, designed to irradiate a  $6 \times 6 \text{ m}^2$   
 2668 area at 5 m maximum to the source. A thin lens-shaped lead filter helps providing with a uniform  
 2669 outcoming flux in a vertical plane, orthogonal to the beam direction. The principal collimator hole  
 2670 provides a pyramidal aperture of  $74^\circ \times 74^\circ$  solid angle and provides a photon flux in a pyramidal vol-

2671   ume along the beam axis. The photon rate is controled by further lead filters allowing the maximum  
 2672   rate to be limited and to vary within a range of four orders of magnitude. Particle detectors under test  
 2673   are then placed within the pyramidal volume in front of the source, perpendicularly to the beam line  
 2674   in order to profit from the homogeneous photon flux. Adjusting the background flux of photons can  
 2675   then be done by using the filters and choosing the position of the detectors with respect to the source.

2676

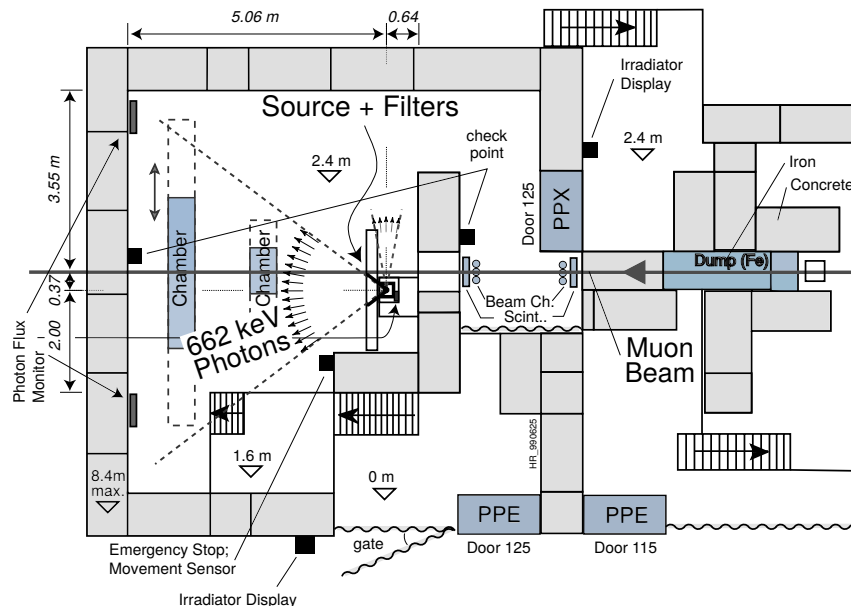


Figure 5.5: Layout of the test beam zone called X5c GIF at CERN. Photons from the radioactive source produce a sustained high rate of random hits over the whole area. The zone is surrounded by 8 m high and 80 cm thick concrete walls. Access is possible through three entry points. Two access doors for personnel and one large gate for material. A crane allows installation of heavy equipment in the area.

2677   As described on Figure 5.6, the  $^{137}\text{Cs}$  source emits a 662 keV photon in 85% of the decays. An  
 2678   activity of 740 GBq was measured on the 5<sup>th</sup> March 1997. To estimate the strength of the flux in  
 2679   2014, it is necessary to consider the nuclear decay through time assiciated to the Cesium source  
 2680   whose half-life is well known ( $t_{1/2} = (30.05 \pm 0.08)$  y). The GIF tests where done in between the  
 2681   20<sup>th</sup> and the 31<sup>st</sup> of August 2014, i.e. at a time  $t = (17.47 \pm 0.02)$  y resulting in an attenuation of  
 2682   the activity from 740 GBq in 1997 to 494 GBq in 2014.

2683

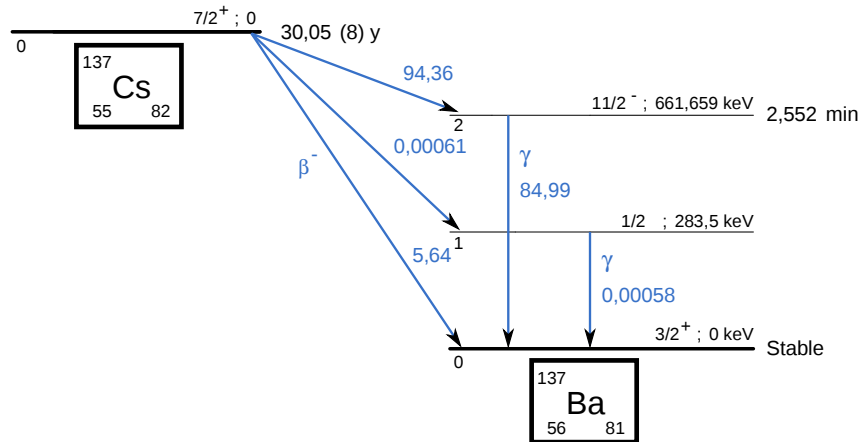


Figure 5.6:  $^{137}\text{Cs}$  decays by  $\beta^-$  emission to the ground state of  $^{137}\text{Ba}$  ( $BR = 5.64\%$ ) and via the 662 keV isomeric level of  $^{137}\text{Ba}$  ( $BR = 94.36\%$ ) whose half-life is 2.55 min.

### 5.2.1.2 GIF++

The new Gamma Irradiation Facility (GIF++), located in the SPS North Area at the downstream end of the H4 test beam, has replaced its predecessor during LS1 and has been operational since spring 2015 [87]. Like GIF, GIF++ features a  $^{137}\text{Cs}$  source of 662 keV gamma photons, their fluence being controlled with a set of filters of various attenuation factors. The source provides two separated large irradiation areas for testing several full-size muon detectors with continuous homogeneous irradiation, as presented in Figure 5.7.

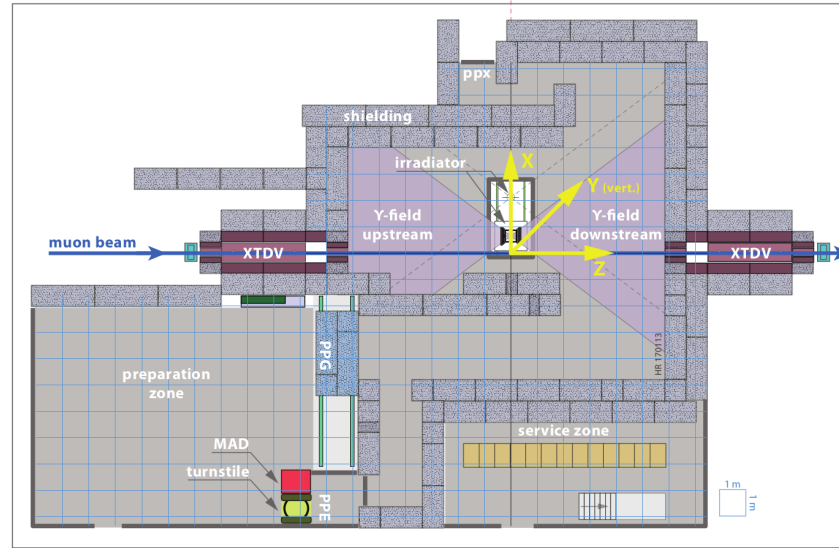
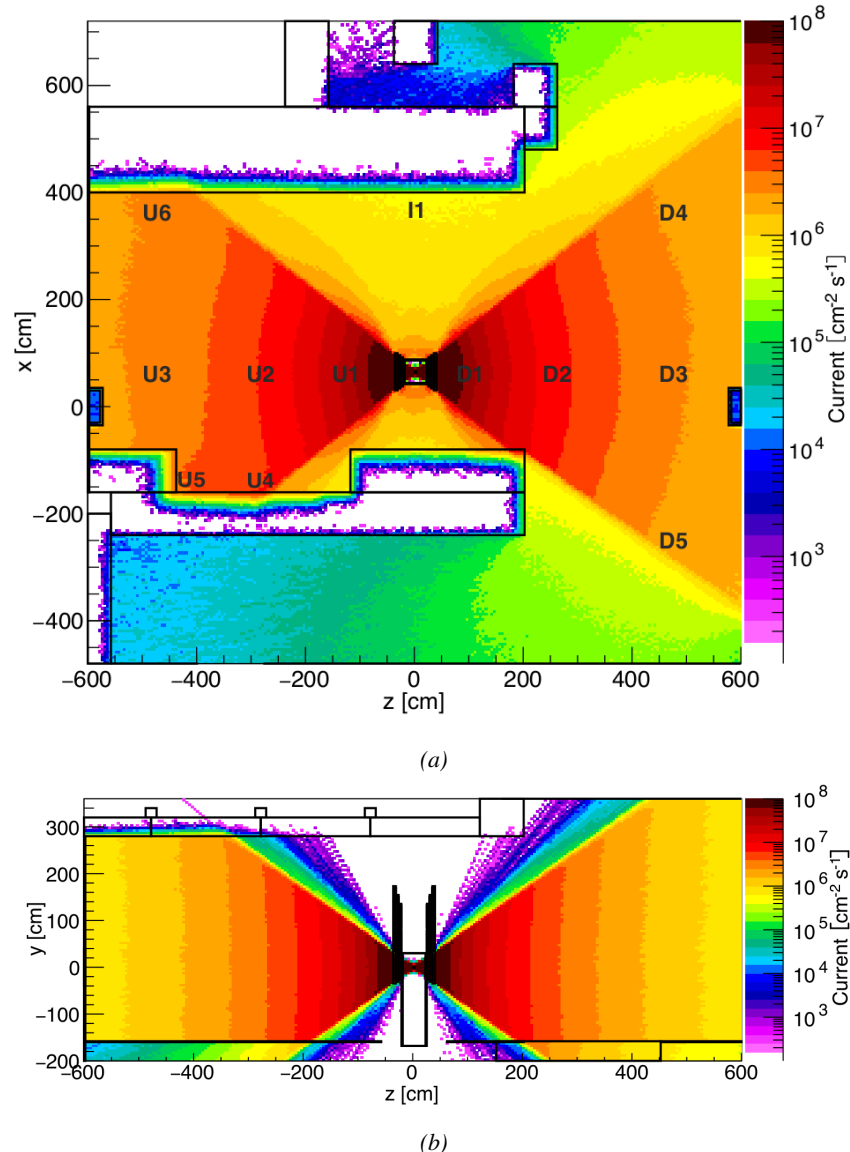


Figure 5.7: Floor plan of the GIF++ facility. When the facility downstream of the GIF++ takes electron beam, a beam pipe is installed along the beam line (z-axis). The irradiator can be displaced laterally (its center moves from  $x = 0.65 \text{ m}$  to  $2.15 \text{ m}$ ), to increase the distance to the beam pipe.

The source activity was measured to be about 13.5 TBq in March 2016. The photon flux being far greater than HL-LHC expectations, GIF++ provides an excellent facility for accelerated aging tests of muon detectors.

2695



*Figure 5.8: Simulated unattenuated current of photons in the xz plane (Figure 5.8a) and yz plane (Figure 5.8b) through the source at  $x = 0.65$  m and  $y = 0$  m. With angular correction filters, the current of 662 keV photons is made uniform in xy planes.*

2696

The source is situated in the muon beam line with the muon beam being available a few times a year. The H4 beam, composed of muons with a momentum of about 150 GeV/c, passes through the GIF++ zone and is used to study the performance of the detectors. Its flux is of 104 particles/s/cm<sup>2</sup>

2697

2698

2699 focused in an area similar to  $10 \times 10 \text{ cm}^2$ . Therefore, with properly adjusted filters, one can imitate  
 2700 the HL-LHC background and study the performance of muon detectors with their trigger/readout  
 2701 electronics in HL-LHC environment.

2702

## 2703 5.3 Preliminary tests at GIF

### 2704 5.3.1 Resistive Plate Chamber test setup

2705 During summer 2014, preliminary tests have been conducted in the GIF area on a newly produced  
 2706 RE4/2 chamber labelled RE-4-2-BARC-161. This chamber has been placed into a trolley covered  
 2707 with a tent. The position of the RPC inside the tent and of the tent related to the source is described  
 2708 in Figure 5.9. To test this CMS RPC, three different absorber settings were used. First of all,  
 2709 measurements were done with fully opened source. Then, to complete this preliminary study, the  
 2710 gamma flux has been attenuated from a factor 2 and a factor 5. The expected gamma flux at the level  
 2711 of our detector will be discussed in subsection ??.

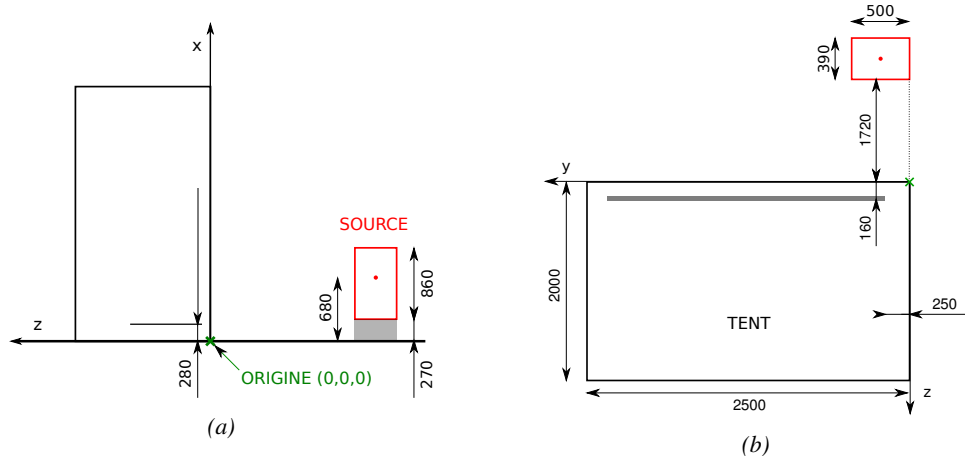
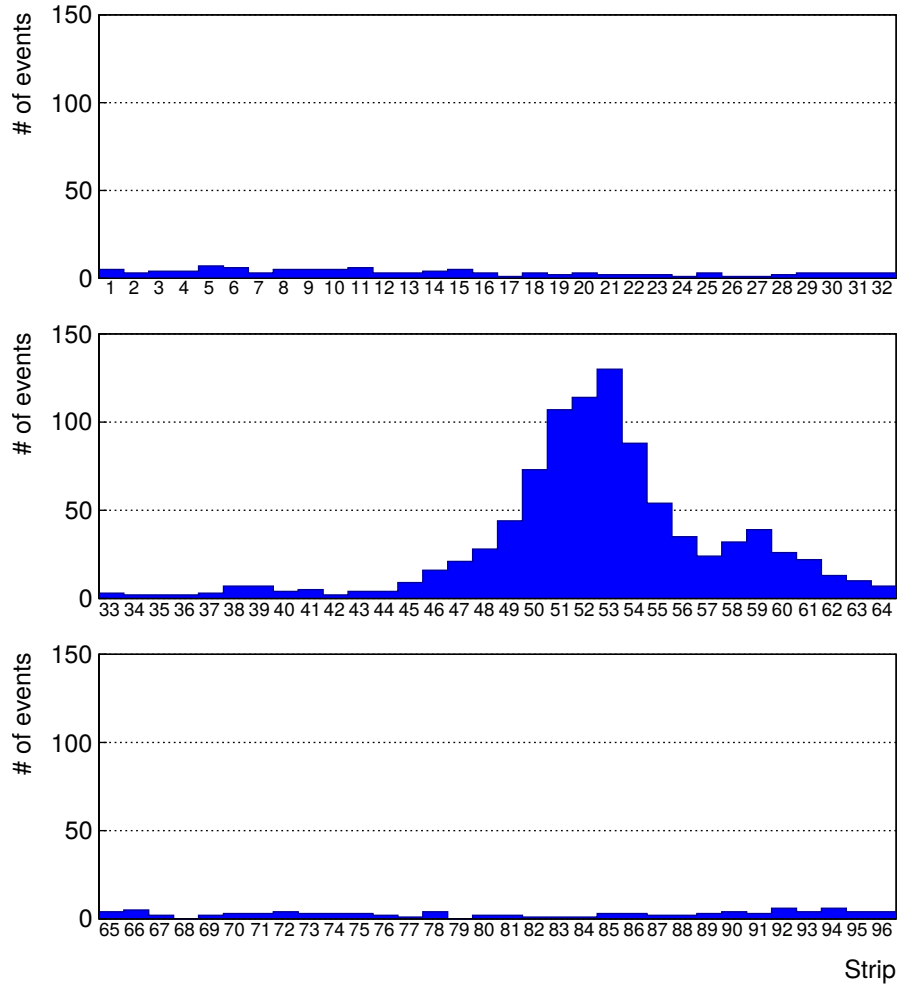


Figure 5.9: Description of the RPC setup. Dimensions are given in mm. A tent containing RPCs is placed at 1720 mm from the source container. The source is situated in the center of the container. RE-4-2-BARC-161 chamber is 160 mm inside the tent. This way, the distance between the source and the chambers plan is 2060 mm. Figure 5.9a provides a side view of the setup in the xz plane while Figure 5.9b shows a top view in the yz plane.



*Figure 5.10: RE-4-2-BARC-I61 chamber is inside the tent as described in Figure 5.9. In the top right, the two scintillators used as trigger can be seen. This trigger system has an inclination of 10° relative to horizontal and is placed above half-partition B2 of the RPCs. PMT electronics are shielded thanks to lead blocks placed in order to protect them without stopping photons from going through the scintillators and the chamber.*

2712 At the time of the tests, the beam not being operationnal anymore, a trigger composed of 2 plastic  
 2713 scintillators has been placed in front of the setup with an inclination of 10 deg with respect to the  
 2714 detector plane in order to look at cosmic muons. Using this particular trigger layout, shown on Fig-  
 2715 ure 5.10, leads to a cosmic muon hit distribution into the chamber similar to the one in Figure 5.11.  
 2716 Measured without gamma irradiation, two peaks can be seen on the profil of partition B, centered  
 2717 on strips 52 and 59. Section ?? will help us understand that these two peaks are due respectively to  
 2718 forward and backward coming cosmic particles where forward coming particles are first detected by  
 2719 the scintillators and then the RPC while the backward coming muons are first detected in the RPC.



*Figure 5.11: Hit distributions over all 3 partitions of RE-4-2-BARC-161 chamber is showed on these plots. Top, middle and bottom figures respectively correspond to partitions A, B, and C. These plots show that some events still occur in other half-partitions than B2, which corresponds to strips 49 to 64, in front of which the trigger is placed, contributing to the inefficiency of detection of cosmic muons. In the case of partitions A and C, the very low amount of data can be interpreted as noise. On the other hand, it is clear that a little portion of muons reach the half-partition B1, corresponding to strips 33 to 48.*

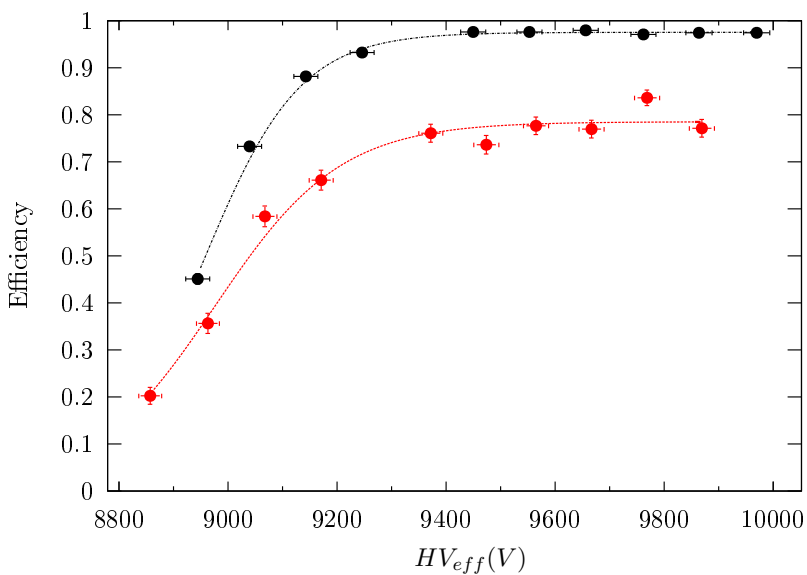
### 2720 5.3.2 Data Acquisition

### 2721 5.3.3 Geometrical acceptance of the setup layout to cosmic muons

2722 In order to profit from a constant gamma irradiation, the detectors inside of the GIF bunker need  
 2723 to be placed in a plane orthogonal to the beam line. The muon beam that used to be available was  
 2724 meant to test the performance of detectors under test. This beam not being active anymore, another  
 2725 solution to test detector performance had to be used. Thus, it has been decided to use cosmic muons  
 2726 detected through a telescope composed of two scintillators. Lead blocks were used as shielding to

2727 protect the photomultipliers from gammas as can be seen from Figure 5.10.

2728 An inclination has been given to the cosmic telescope to maximize the muon flux. A good com-  
 2729 promise had to be found between good enough muon flux and narrow enough hit distribution to  
 2730 be sure to contain all the events into only one half partitions as required from the limited available  
 2731 readout hardware. Nevertheless, a consequence of the misplaced trigger, that can be seen as a loss  
 2732 of events in half-partition B1 in Figure 5.11, is an inefficiency. Nevertheless, the inefficiency of ap-  
 2733 proximately 20 % highlighted in Figure 5.12 by comparing the performance of chamber BARC-161  
 2734 in 904 and at GIF without irradiation seems too important to be explained only by the geometri-  
 2735 cal acceptance of the setup itself. Simulations have been conducted to show how the setup brings  
 2736 inefficiency.



2737 *Figure 5.12: Results are derived from data taken on half-partition B2 only. On the 18<sup>th</sup> of June 2014, data  
 2738 has been taken on chamber RE-2-BARC-161 at building 904 (Prevessin Site) with cosmic muons providing us a  
 2739 reference efficiency plateau of  $(97.54 \pm 0.15)\%$  represented by a black curve. A similar measurement has been  
 2740 done at GIF on the 21<sup>st</sup> of July with the same chamber giving a plateau of  $(78.52 \pm 0.94)\%$  represented by a  
 2741 red curve.*

### 2737 5.3.3.1 Description of the simulation layout

2738 The layout of GIF setup has been reproduced and incorporated into a Monte Carlo (MC) simulation  
 2739 to study the influence of the disposition of the telescope on the final distribution measured by the  
 2740 RPC. A 3D view of the simulated layout is given into Figure 5.13. Muons are generated randomly  
 2741 in a horizontal plane located at a height corresponding to the lowest point of the PMTs. This way,  
 2742 the needed size of the plane in order to simulate events happening at very big azimuthal angles (i.e.  
 2743  $\theta \approx \pi$ ) can be kept relatively small. The muon flux is designed to follow the usual  $\cos^2\theta$  distribution  
 2744 for cosmic particle. The goal of the simulation is to look at muons that pass through the muon  
 2745 telescope composed of the two scintillators and define their distribution onto the RPC plane. During  
 2746 the reconstruction, the RPC plane is then divided into its strips and each muon track is assigned to a  
 2747 strip.

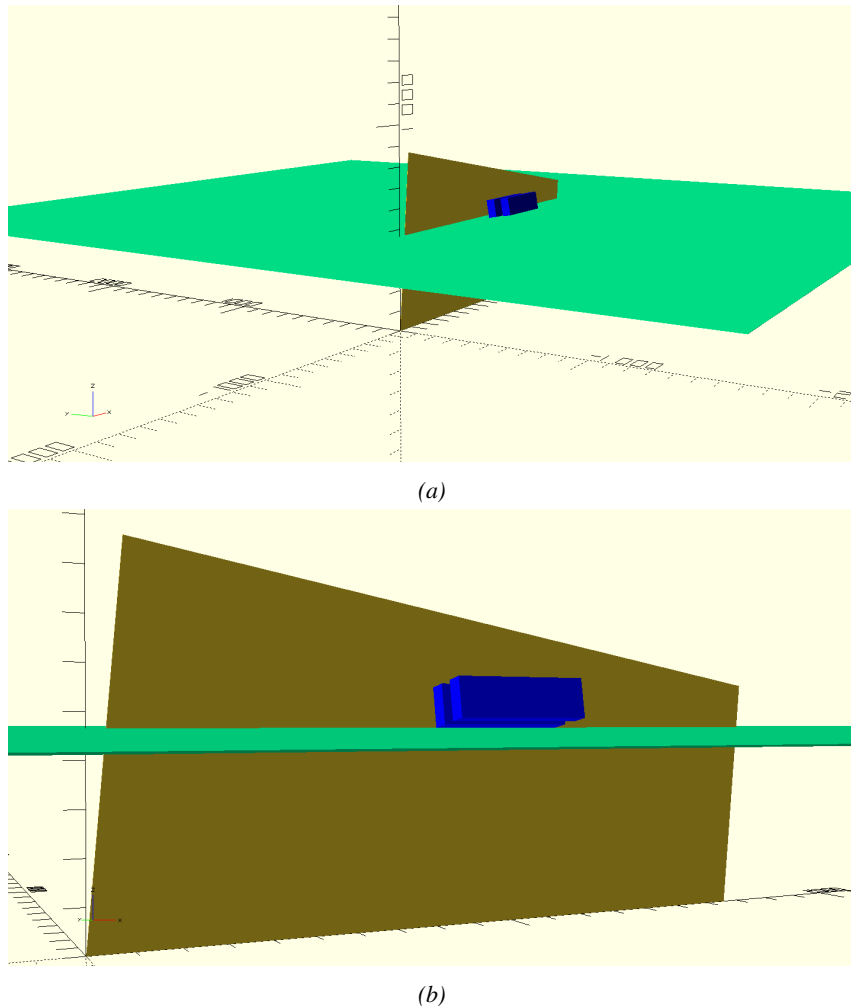


*Figure 5.13: Representation of the layout used for the simulations of the test setup. The RPC is represented as a yellow trapezoid while the two scintillators as blue cuboids looking at the sky. A green plane corresponds to the muon generation plane within the simulation. Figure 5.9a shows a global view of the simulated setup. Figure 5.9b shows a zoomed view that allows to see the 2 scintillators as well as the full RPC plane.*

2748 In order to further refine the quality of the simulation and understand deeper the results the  
 2749 dependance of the distribution has been studied for a range of telescope inclinations. Moreover,  
 2750 the threshold applied on the PMT signals has been included into the simulation in the form of a  
 2751 cut. In the approximation of uniform scintillators, it has been considered that the threshold can be  
 2752 understood as the minimum distance particles need to travel through the scintillating material to give  
 2753 a strong enough signal. Particles that travel a distance smaller than the set "threshold" are thus not  
 2754 detected by the telescope and cannot trigger the data taking. Finally, the FEE threshold also has  
 2755 been considered in a similar way. The mean momentum of horizontal cosmic rays is higher than  
 2756 those of vertical ones but the stopping power of matter for momenta ranging from 1 GeV to 1 TeV  
 2757 stays comparable. It is then possible to assume that the mean number of primary  $e^-$ /ion pairs per  
 2758 unit length will stay similar and thus, depending on the applied discriminator threshold, muons with

2759 the shortest path through the gas volume will deposit less charge and induce a smaller signal on the  
 2760 pick-up strips that could eventually not be detected. These two thresholds also restrain the overall  
 2761 geometrical acceptance of the system.

### 2762 5.3.3.2 Simulation procedure

2763 The simulation software has been designed using C++ and the output data is saved into ROOT  
 2764 histograms. Simulations start for a threshold  $T_{scint}$  varying in a range from 0 to 45 mm in steps  
 2765 of 5 mm, where  $T_{scint} = 0$  mm corresponds to the case where there isn't any threshold apply on  
 2766 the input signal while  $T_{scint} = 45$  mm, which is the scintillator thickness, is the case where muons  
 2767 cannot arrive orthogonally onto the scintillator surface. For a given  $T_{scint}$ , a set of RPC thresholds  
 2768 are considered. The RPC threshold,  $T_{RPC}$  varies from 2 mm, the thickness of the gas volume, to  
 2769 3 mm in steps of 0.25 mm. For each  $(T_{scint}; T_{RPC})$  pair,  $N_\mu = 10^8$  muons are randomly generated  
 2770 inside the muon plane described in the previous paragraph with an azimuthal angle  $\theta$  chosen to follow  
 2771 a  $\cos^2\theta$  distribution.

2772 Planes are associated to each surface of the scintillators. Knowing muon position into the muon  
 2773 plane and its direction allows us, by assuming that muons travel in a straight line, to compute the  
 2774 intersection of the muon track with these planes. Applying conditions to the limits of the surfaces  
 2775 of the scintillator faces then gives us an answer to whether or not the muon passed through the  
 2776 scintillators. In the case the muon has indeed passed through the telescope, the path through each  
 2777 scintillator is computed and muons whose path was shorter than  $T_{scint}$  are rejected and are thus  
 2778 considered as having not interacted with the setup.

2779 On the contrary, if the muon is labeled as good, its position within the RPC plane is computed  
 2780 and the corresponding strip, determined by geometrical tests in the case the distance through the  
 2781 gas volume was enough not to be rejected because of  $T_{RPC}$ , gets a hit and several histograms  
 2782 are filled in order to keep track of the generation point on the muon plane, the intersection points  
 2783 of the reconstructed muons within the telescope, or on the RPC plane, the path traveled through  
 2784 each individual scintillator or the gas volume, as well as other histograms. Moreover, muons fill  
 2785 different histograms whether they are forward or backward coming muons. They are discriminated  
 2786 according to their direction components. When a muon is generated, an  $(x, y, z)$  position is assigned  
 2787 into the muon plane as well as a  $(\theta; \phi)$  pair that gives us the direction it's coming from. This way,  
 2788 muons satisfying the condition  $0 \leq \phi < \pi$  are designated as backward coming muons while muons  
 2789 satisfying  $\pi \leq \phi < 2\pi$  as forward coming muons.

2790 This simulation is then repeated for different telescope inclinations ranging in between 4 and 20°  
 2791 and varying in steps of 2°. Due to this inclination and to the vertical position of the detector under  
 2792 test, the muon distribution reconstructed in the detector plane is asymmetrical. The choice as been  
 2793 made to chose a skew distribution formula to fit the data built as the multiplication of gaussian and  
 2794 sigmoidal curves together. A typical gaussian formula is given as 5.1 and has three free parameters  
 2795 as  $A_g$ , its amplitude,  $\bar{x}$ , its mean value and  $\sigma$ , its root mean square. Sigmoidal curves as given by  
 2796 formula 5.2 are functions converging to 0 and  $A_s$  as  $x$  diverges. The inflection point is given as  $x_i$   
 2797 and  $\lambda$  is proportional to the slope at  $x = x_i$ . In the limit where  $\lambda \rightarrow \infty$ , the sigmoid becomes a  
 2798 step function.

$$g(x) = A_g e^{-\frac{(x-\bar{x})^2}{2\sigma^2}} \quad (5.1)$$

$$s(x) = \frac{A_s}{1 + e^{-\lambda(x-x_i)}} \quad (5.2)$$

Finally, a possible representation of a skew distribution is given by formula 5.3 and is the product of 5.1 and 5.2. Naturally, here  $A_{sk} = A_g \times A_s$  and represents the theoretical maximum in the limit where the skew tends to a gaussian function.

$$sk(x) = g(x) \times s(x) = A_{sk} \frac{e^{\frac{-(x-\bar{x})^2}{2\sigma^2}}}{1 + e^{-\lambda(x-x_i)}} \quad (5.3)$$

### 5.3.3.3 Results

#### Influence of $T_{scint}$ on the muon distribution

#### Influence of $T_{RPC}$ on the muon distribution

#### Influence of the telescope inclination on the muon distribution

#### Comparison to data taken at GIF without irradiation

### 5.3.4 Photon flux at GIF

#### 5.3.4.1 Expectations from simulations

In order to understand and evaluate the  $\gamma$  flux in the GIF area, simulations had been conducted in 1999 and published by S. Agosteo et al [86]. Table 5.1 presented in this article gives us the  $\gamma$  flux for different distances  $D$  to the source. This simulation was done using GEANT and a Monte Carlo N-Particle (MCNP) transport code, and the flux  $F$  is given in number of  $\gamma$  per unit area and unit time along with the estimated error from these packages expressed in %.

Nominal ABS	Photon flux $F$ [ $s^{-1}cm^{-2}$ ]			
	at $D = 50$ cm	at $D = 155$ cm	at $D = 300$ cm	at $D = 400$ cm
1	$0.12 \cdot 10^8 \pm 0.2\%$	$0.14 \cdot 10^7 \pm 0.5\%$	$0.45 \cdot 10^6 \pm 0.5\%$	$0.28 \cdot 10^6 \pm 0.5\%$
2	$0.68 \cdot 10^7 \pm 0.3\%$	$0.80 \cdot 10^6 \pm 0.8\%$	$0.25 \cdot 10^6 \pm 0.8\%$	$0.16 \cdot 10^6 \pm 0.6\%$
5	$0.31 \cdot 10^7 \pm 0.4\%$	$0.36 \cdot 10^6 \pm 1.2\%$	$0.11 \cdot 10^6 \pm 1.2\%$	$0.70 \cdot 10^5 \pm 0.9\%$

Table 5.1: Total photon flux ( $E\gamma \leq 662$  keV) with statistical error predicted considering a  $^{137}Cs$  activity of 740 GBq at different values of the distance  $D$  to the source along the  $x$ -axis of irradiation field [86].

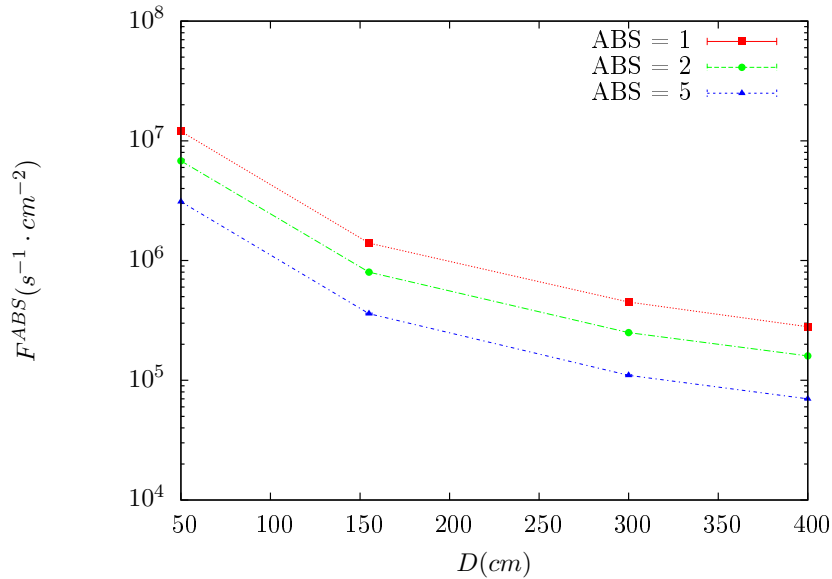


Figure 5.14:  $\gamma$  flux  $F(D)$  is plot using values from table 5.1. As expected, the plot shows similar attenuation behaviours with increasing distance for each absorption factors.

The simulation doesn't directly provides us with an estimated flux at the level of our RPC. First of all, it is needed to extract the value of the flux from the available data contained in the original paper and then to estimate the flux in 2014 at the time the experimentation took place. Figure 5.14 that contains the data from Table 5.1. In the case of a pointlike source emitting isotropic and homogeneous gamma radiations, the gamma flux  $F$  at a distance  $D$  to the source with respect to a reference point situated at  $D_0$  where a known flux  $F_0$  is measured will be expressed like in Equation 5.4, assuming that the flux decreases as  $1/D^2$ , where  $c$  is a fitting factor.

$$F^{ABS} = F_0^{ABS} \times \left( \frac{cD_0}{D} \right)^2 \quad (5.4)$$

By rewriting Equation 5.4, it comes that :

$$c = \frac{D}{D_0} \sqrt{\frac{F^{ABS}}{F_0^{ABS}}} \quad (5.5)$$

$$\Delta c = \frac{c}{2} \left( \frac{\Delta F^{ABS}}{F^{ABS}} + \frac{\Delta F_0^{ABS}}{F_0^{ABS}} \right) \quad (5.6)$$

Finally, using Equation 5.5 and the data in Table 5.1 with  $D_0 = 50$  cm as reference point, we can build Table 5.2. It is interesting to note that  $c$  for each value of  $D$  doesn't depend on the absorption factor.

Nominal ABS	Correction factor $c$		
	at $D = 155$ cm	at $D = 300$ cm	at $D = 400$ cm
1	$1.059 \pm 0.70\%$	$1.162 \pm 0.70\%$	$1.222 \pm 0.70\%$
2	$1.063 \pm 1.10\%$	$1.150 \pm 1.10\%$	$1.227 \pm 0.90\%$
5	$1.056 \pm 1.60\%$	$1.130 \pm 1.60\%$	$1.202 \pm 1.30\%$

Table 5.2: Correction factor  $c$  is computed thanks to formulae 5.5 taking as reference  $D_0 = 50$  cm and the associated flux  $F_0^{ABS}$  for each absorption factor available in table 5.1.

2825 For the range of  $D/D_0$  values available, it is possible to use a simple linear fit to get the evolution  
 2826 of  $c$ . The linear fit will then use only 2 free parameters,  $a$  and  $b$ , as written in Equation 5.7. This gives  
 2827 us the results showed in Figure 5.15. Figure 5.15b confirms that using only a linear fit to extract  $c$  is  
 2828 enough as the evolution of the rate that can be obtained superimposes well on the simulation points.

$$c \left( \frac{D}{D_0} \right) = a \frac{D}{D_0} + b \quad (5.7)$$

$$F^{ABS} = F_0^{ABS} \left( a + \frac{bD_0}{D} \right)^2 \quad (5.8)$$

$$\Delta F^{ABS} = F^{ABS} \left[ \frac{\Delta F_0^{ABS}}{F_0^{ABS}} + 2 \frac{\Delta a + \Delta b \frac{D_0}{D}}{a + \frac{bD_0}{D}} \right] \quad (5.9)$$

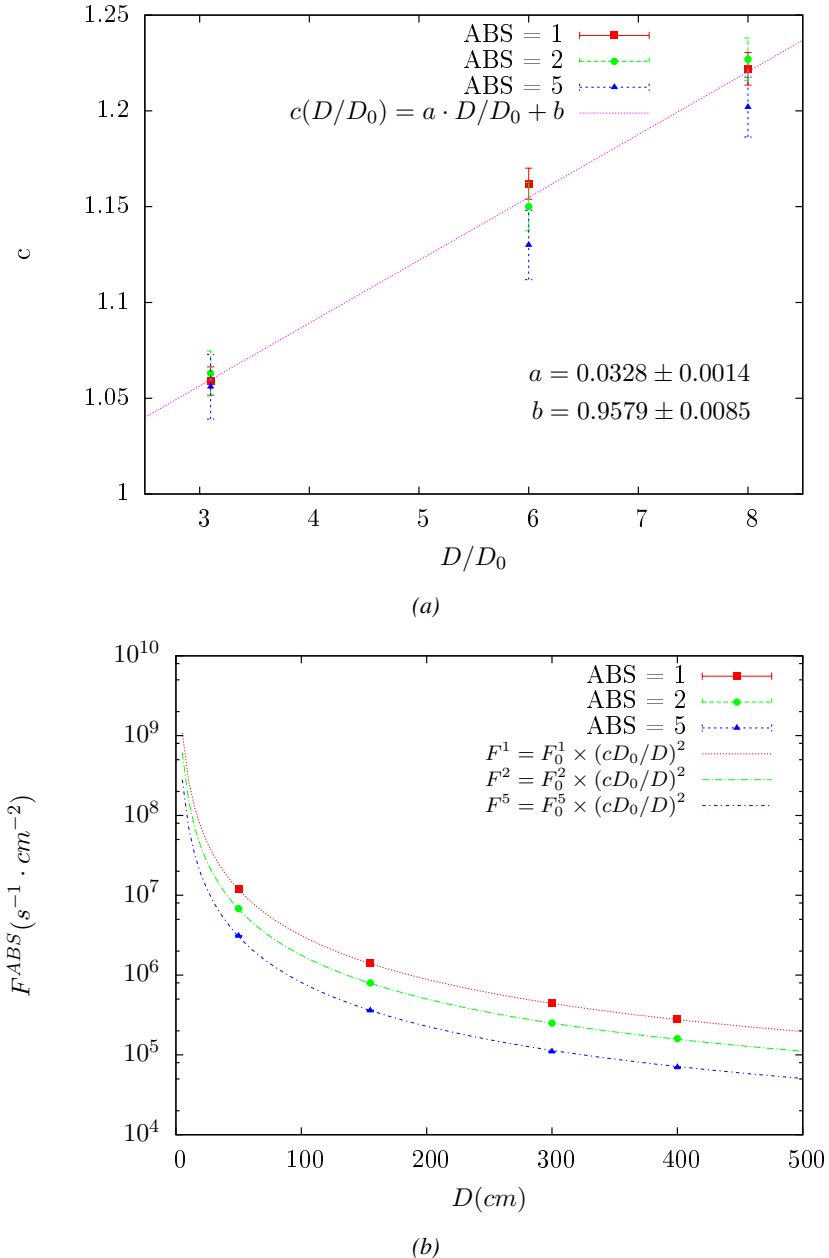


Figure 5.15: Figure 5.15a shows the linear approximation fit done via formulae 5.7 on data from table 5.2. Figure 5.15b shows a comparison of this model with the simulated flux using  $a$  and  $b$  given in figure 5.15a in formulae 5.4 and the reference value  $D_0 = 50\text{cm}$  and the associated flux for each absorption factor  $F_0^{ABS}$  from table 5.1

In the case of the 2014 GIF tests, the RPC plane is located at a distance  $D = 206\text{ cm}$  to the source. Moreover, to estimate the strength of the flux in 2014, it is necessary to consider the nuclear decay through time associated to the Cesium source whose half-life is well known ( $t_{1/2} = (30.05 \pm 0.08)\text{ y}$ ). The very first source activity measurement has been done on the 5<sup>th</sup> of March 1997 while the GIF

2833 tests were done in between the 20<sup>th</sup> and the 31<sup>st</sup> of August 2014, i.e. at a time  $t = (17.47 \pm 0.02)$  y  
 2834 resulting in an attenuation of the activity from 740 GBq in 1997 to 494 GBq in 2014. All the needed  
 2835 information to extrapolate the flux through our detector in 2014 has now been assembled, leading  
 2836 to the Table 5.3. It is interesting to note that for a common RPC sensitivity to  $\gamma$  of  $2 \cdot 10^{-3}$ , the  
 2837 order of magnitude of the estimated hit rate per unit area is of the order of the kHz for the fully  
 2838 opened source. Moreover, taking profit of the two working absorbers, it will be possible to scan  
 2839 background rates at 0 Hz,  $\sim 300$  Hz as well as  $\sim 600$  Hz. Without source, a good estimate of the  
 2840 intrinsic performance will be available. Then at 300 Hz, the goal will be to show that the detectors  
 2841 fulfill the performance certification of CMS RPCs. Then a first idea of the performance of the  
 2842 detectors at higher background will be provided with absorption factors 2 ( $\sim 600$  Hz) and 1 (no  
 2843 absorption). *[Here I will also put a reference to the plot showing the estimated background rate at  
 2844 the level of RE3/1 in the case of HL-LHC but this one being in another chapter, I will do it later.]*

Nominal ABS	Photon flux $F$ [ $s^{-1}cm^{-2}$ ]			Hit rate/unit area [ $Hz cm^{-2}$ ] at $D^{2014} = 206$ cm
	at $D_0^{1997} = 50$ cm	at $D^{1997} = 206$ cm	at $D^{2014} = 206$ cm	
1	$0.12 \cdot 10^8 \pm 0.2\%$	$0.84 \cdot 10^6 \pm 0.3\%$	$0.56 \cdot 10^6 \pm 0.3\%$	$1129 \pm 32$
2	$0.68 \cdot 10^7 \pm 0.3\%$	$0.48 \cdot 10^6 \pm 0.3\%$	$0.32 \cdot 10^6 \pm 0.3\%$	$640 \pm 19$
5	$0.31 \cdot 10^7 \pm 0.4\%$	$0.22 \cdot 10^6 \pm 0.3\%$	$0.15 \cdot 10^6 \pm 0.3\%$	$292 \pm 9$

Table 5.3: The data at  $D_0$  in 1997 is taken from [86]. In a second step, using Equations 5.8 and 5.9, the flux at  $D$  can be estimated in 1997. Then, taking into account the attenuation of the source activity, the flux at  $D$  can be estimated at the time of the tests in GIF in 2014. Finally, assuming a sensitivity of the RPC to  $\gamma$   $s = 2 \cdot 10^{-3}$ , an estimation of the hit rate per unit area is obtained.

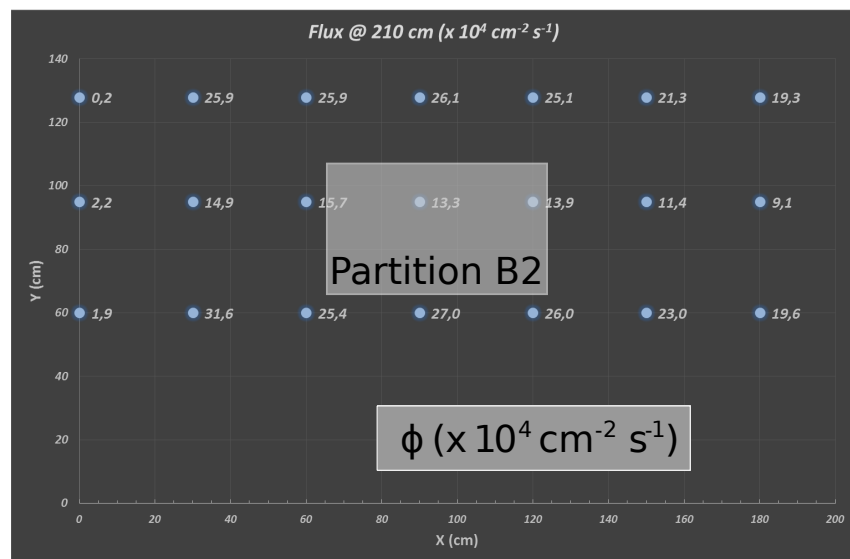
2845 **5.3.4.2 Dose measurements**

Figure 5.16: Dose measurements has been done in a plane corresponding to the tents front side. This plan is 1900 mm away from the source. As explained in the first chapter, a lens-shaped lead filter provides a uniform photon flux in the vertical plan orthogonal to the beam direction. If the second line of measured fluxes is not taken into account because of lower values due to experimental equipments in the way between the source and the tent, the uniformity of the flux is well showed by the results.

<sup>2846</sup> **5.3.5 Results and discussions**

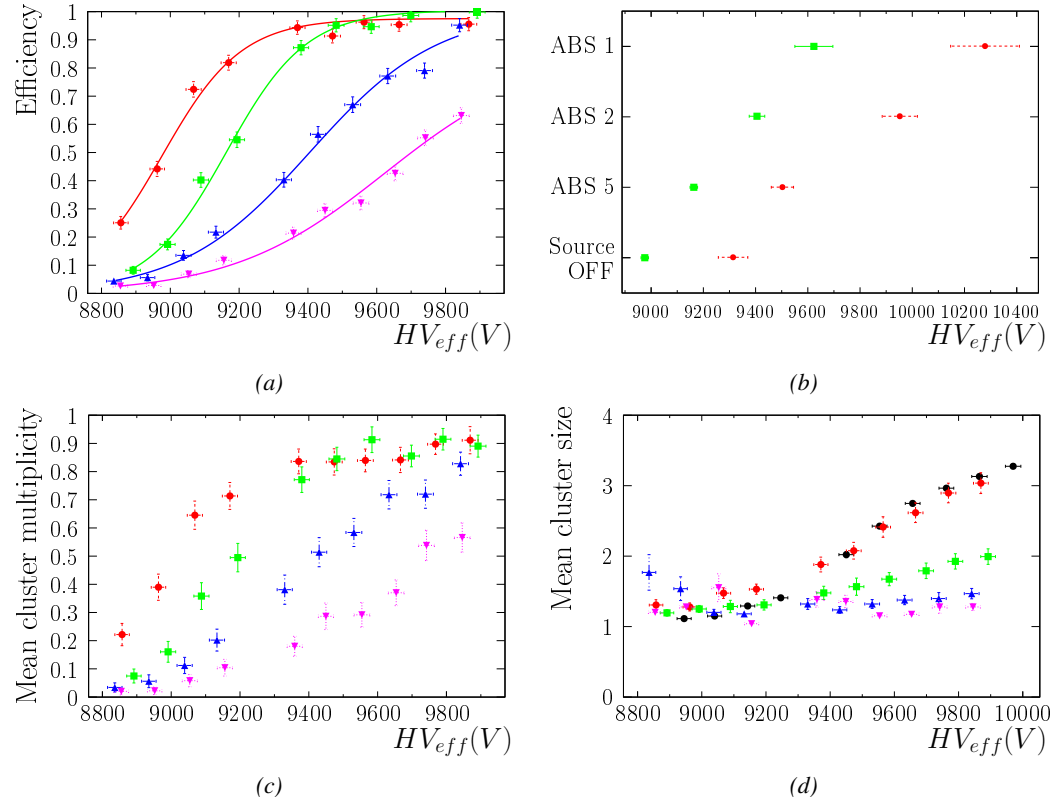


Figure 5.17

## 2847 5.4 Longevity tests at GIF++

2848 Longevity studies imply a monitoring of the performance of the detectors probed using a high inten-  
2849 sity muon beam in a irradiated environment by periodically measuring their rate capability, the dark  
2850 current running through them and the bulk resistivity of the Bakelite composing their electrodes.  
2851 GIF++, with its very intense  $^{137}\text{Cs}$  source, provides the perfect environment to perform such kind  
2852 of tests. Assuming a maximum acceleration factor of 3, it is expected to accumulate the equivalent  
2853 charge in 1.7 years.

2854 As the maximum background is found in the endcap, the choice naturally was made to focus the  
2855 GIF++ longevity studies on endcap chambers. Most of the RPC system was installed in 2007. Nev-  
2856 ertheless, the large chambers in the fourth endcap (RE4/2 and RE4/3) have been installed during  
2857 LS1 in 2014. The Bakelite of these two different productions having different properties, four spare  
2858 chambers of the present system were selected, two RE2,3/2 spares and two RE4/2 spares. Having  
2859 two chambers of each type allows to always keep one of them non irradiated as reference, the per-  
2860 formance evolution of the irradiated chamber being then compared through time to the performance  
2861 of the non irradiated one.

2862 The performance of the detectors under different level of irradiation is measured periodically dur-  
2863 ing dedicated test beam periods using the H4 muon beam. In between these test beam periods, the  
2864 two RE2,3/2 and RE4/2 chambers selected for this study are irradiated by the  $^{137}\text{Cs}$  source in order  
2865 to accumulate charge and the gamma background is monitored, as well as the currents. The two  
2866 remaining chambers are kept non-irradiated as reference detectors. Due to the limited gas flow in  
2867 GIF++, the RE4 chamber remained non-irradiated until end of November 2016 where a new mass  
2868 flow controller has been installed allowing for bigger volumes of gas to flow in the system.

2869 Figures 5.18 and 5.19 give us for different test beam periods, and thus for increasing integrated  
2870 charge through time, a comparison of the maximum efficiency, obtained using a sigmoid-like func-  
2871 tion, and of the working point of both irradiated and non irradiated chambers [55]. No aging is yet  
2872 to see from this data, the shifts in  $\gamma$  rate per unit area in between irradiated and non irradiated detec-  
2873 tors and RE2 and RE4 types being easily explained by a difference of sensitivity due to the various  
2874 Bakelite resistivities of the HPL electrodes used for the electrode production.

2875 Collecting performance data at each test beam period allows us to extrapolate the maximum effi-  
2876 ciency for a background hit rate of  $300\text{ Hz}/\text{cm}^2$  corresponding to the expected HL-LHC conditions.  
2877 Aging effects could emerge from a loss of efficiency with increasing integrated charge over time,  
2878 thus Figure 5.20 helps us understand such degradation of the performance of irradiated detectors in  
2879 comparison with non irradiated ones. The final answer for an eventual loss of efficiency is given in  
2880 Figure 5.21 by comparing for both irradiated and non irradiated detectors the efficiency sigmoids  
2881 before and after the longevity study. Moreover, to complete the performance information, the Bake-  
2882 lite resistivity is regularly measured thanks to  $Ag$  scans (Figure 5.22) and the noise rate is monitored  
2883 weekly during irradiation periods (Figure 5.23). At the end of 2016, no signs of aging were observed  
2884 and further investigation is needed to get closer to the final integrated charge requirements proposed  
2885 for the longevity study of the present CMS RPC sub-system.

2886

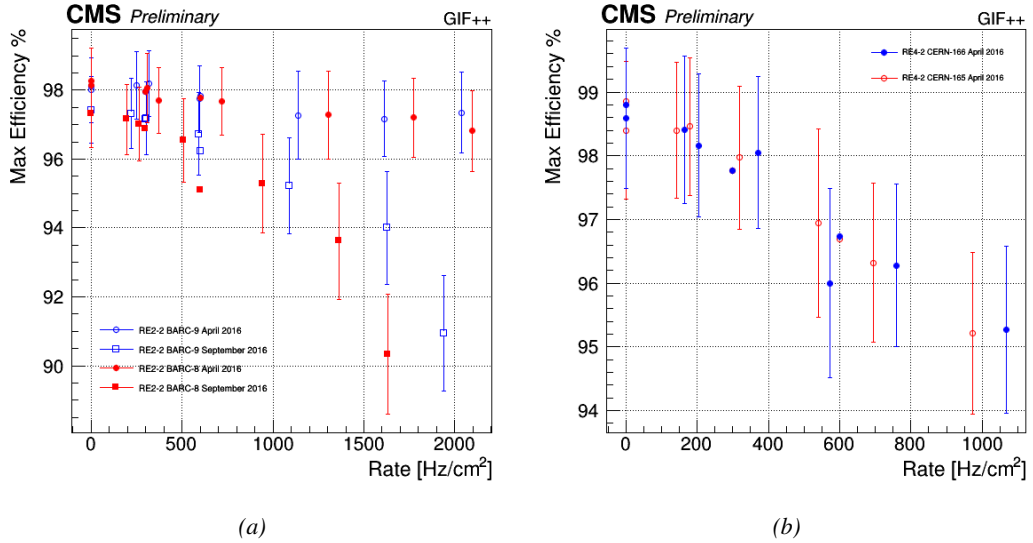


Figure 5.18: Evolution of the maximum efficiency for RE2 (5.18a) and RE4 (5.18b) chambers with increasing extrapolated  $\gamma$  rate per unit area at working point. Both irradiated (blue) and non irradiated (red) chambers are shown.

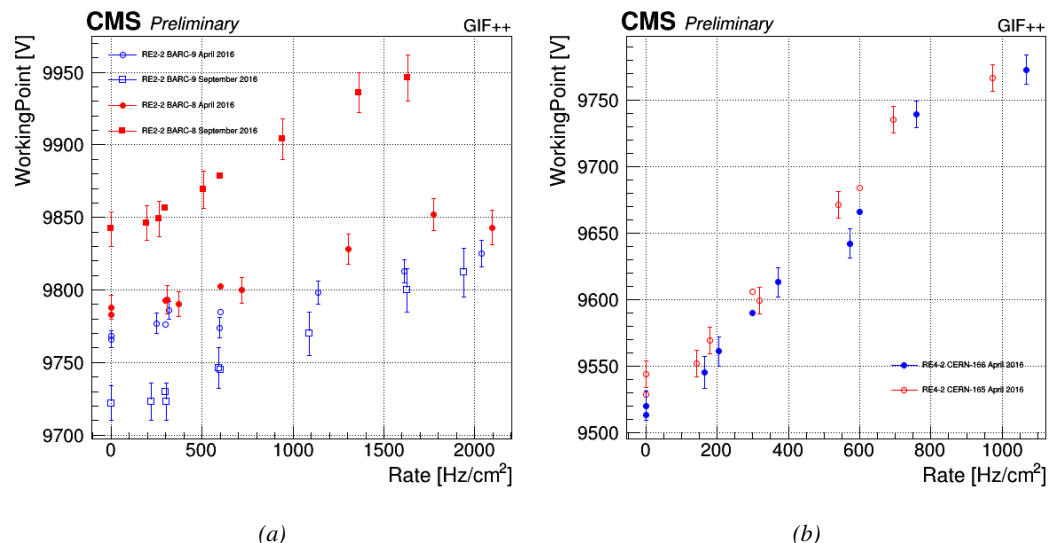
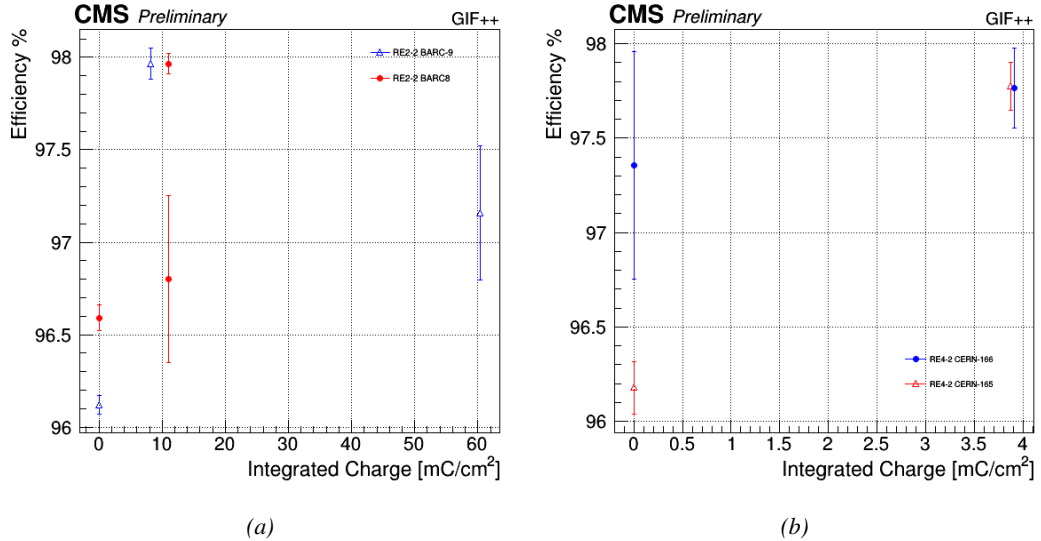
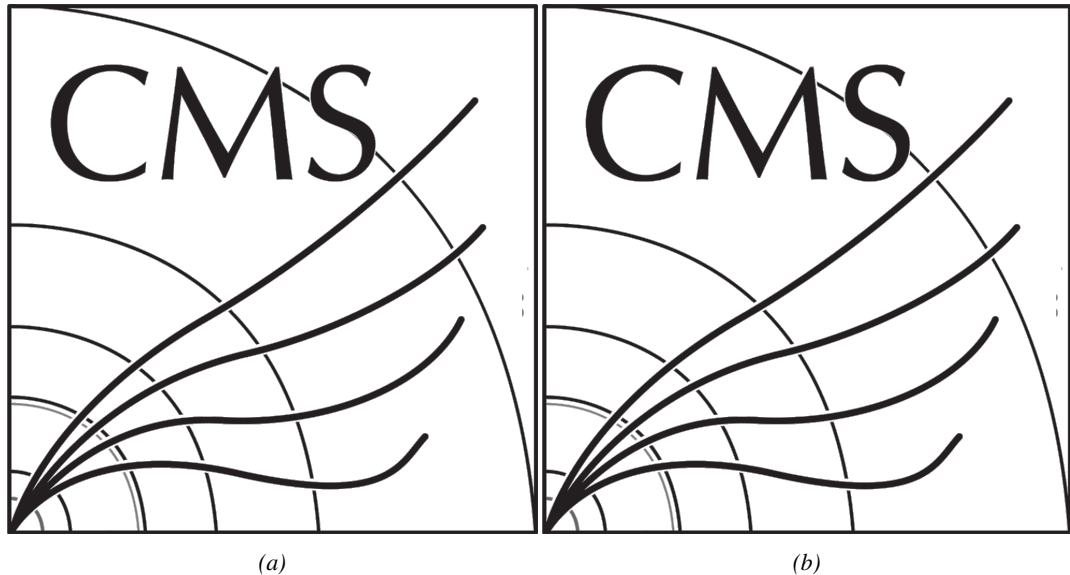


Figure 5.19: Evolution of the working point for RE2 (5.19a) and RE4 (5.19b) with increasing extrapolated  $\gamma$  rate per unit area at working point. Both irradiated (blue) and non irradiated (red) chambers are shown.



*Figure 5.20: Evolution of the maximum efficiency at HL-LHC conditions, i.e. a background hit rate per unit area of 300 Hz/cm<sup>2</sup>, with increasing integrated charge for RE2 (5.20a) and RE4 (5.20b) detectors. Both irradiated (blue) and non irradiated (red) chambers are shown. The integrated charge for non irradiated detectors is recorded during test beam periods and stays small with respect to the charge accumulated in irradiated chambers.*



*Figure 5.21: Comparison of the efficiency sigmoid before (triangles) and after (circles) irradiation for RE2 (5.21a) and RE4 (5.21b) detectors. Both irradiated (blue) and non irradiated (red) chambers are shown.*

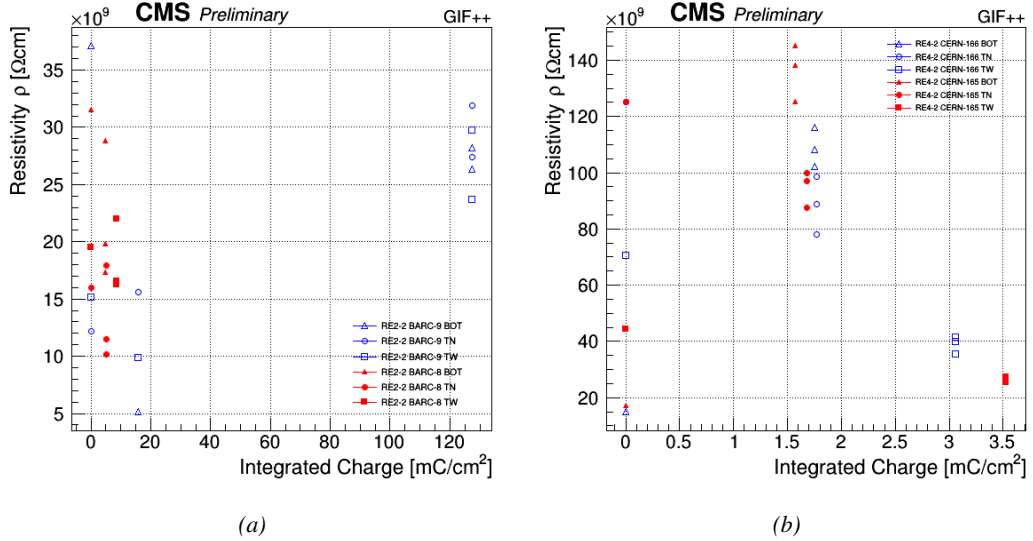


Figure 5.22: Evolution of the Bakelite resistivity for RE2 (5.22a) and RE4 (5.22b) detectors. Both irradiated (blue) and non-irradiated (red) chambers are shown.

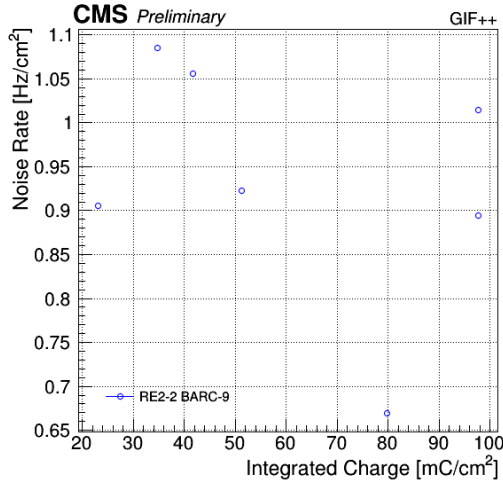


Figure 5.23: Evolution of the noise rate per unit area for the irradiated chamber RE2-2-BARC-9 only.

#### 5.4.1 Description of the Data Acquisition

For the longevity studies, four spare chambers of the present system are used. Two spare RPCs of the RE2,3 stations as well as two spare RPCs from the new RE4 stations have been mounted in a Trolley. Six RE4 gaps are also placed in the trolley. The trolley is placed inside the GIFT++ in the upstream region of the bunker, taking the cesium source as a reference. The trolley is oriented for the detection surface of the chambers to be orthogonal to the beam line. The system can be moved along the orthogonal plane in order to have the beam in all  $\eta$ -partitions. For the aging the trolley is

2894 moved outside the beam line and is placed in a distance of 5.2 m to the source, which irradiates the  
 2895 bunker using an attenuation filter of 2.2 which corresponds to a fluence of  $10^7 \text{ gamma/cm}^2$ .

2896 During GIF++ operation, the data collected can be divided into different categories as several  
 2897 parameters are monitored in addition to the usual RPC performance data. On one hand, to know  
 2898 the performance of a chamber, it is need to measure its efficiency and to know the background  
 2899 conditions in which it is operated. To do this, the hit signals from the chamber are recorded and  
 2900 stored in a ROOT file via a Data Acquisition (DAQ) software. On the other hand, it is also very  
 2901 important to monitor parameters such as environmental pressure and temperature, gas temperature  
 2902 and humidity, RPC HV, LV, and currents, or even source and beam status. This is done through the  
 2903 GIF++ web Detector Control Software (DCS) that stores this information in a database.

2904 Two different types of tests are conducted on RPCs via the DAQ. Indeed, the performance of the  
 2905 detectors is measured periodically during dedicated test beam periods using the H4 muon beam. In  
 2906 between these test beam periods, when the beam is not available, the chambers are irradiated by the  
 2907  $^{137}\text{Cs}$  in order to accumulate deposited charge and the gamma background is measured.

2908 RPCs under test are connected through LVDS cables to V1190A Time-to-Digital Converter  
 2909 (TDC) modules manufactured by CAEN. These modules, located in the rack area outside of the  
 2910 bunker, get the logic signals sent by the chambers and save them into their buffers. Due to the  
 2911 limited size of the buffers, the collected data is regularly erased and replaced. A trigger signal is  
 2912 needed for the TDC modules to send the useful data to the DAQ computer via a V1718 CAEN USB  
 2913 communication module.

2914 In the case of performance test, the trigger signal used for data acquisition is generated by the  
 2915 coincidence of three scintillators. A first one is placed upstream outside of the bunker, a second one  
 2916 is placed downstream outside of the bunker, while a third one is placed in front of the trolley, close by  
 2917 the chambers. Every time a trigger is sent to the TDCs, i.e. every time a muon is detected, knowing  
 2918 the time delay in between the trigger and the RPC signals, signals located in the right time window  
 2919 are extracted from the buffers and saved for later analysis. Signals are taken in a time window of  
 2920 400 ns centered on the muon peak (here we could show a time spectrum). On the other hand, in the  
 2921 case of background rate measurement, the trigger signal needs to be "random" not to measure muons  
 2922 but to look at gamma background. A trigger pulse is continuously generated at a rate of 300 Hz using  
 2923 a dual timer. To integrate an as great as possible time, all signals contained within a time window of  
 2924 10us prior to the random trigger signal are extracted form the buffers and saved for further analysis  
 2925 (here another time spectrum to illustrate could be useful, maybe even place both spectrum together  
 2926 as a single Figure).

2927 The signals sent to the TDCs correspond to hit collections in the RPCs. When a particle hits  
 2928 a RPC, it induce a signal in the pickup strips of the RPC readout. If this signal is higher than the  
 2929 detection threshold, a LVDS signal is sent to the TDCs. The data is then organised into 4 branches  
 2930 keeping track of the event number, the hit multiplicity for the whole setup, and the time and channel  
 2931 profile of the hits in the TDCs.

#### 2932 **5.4.2 RPC current, environmental and operation parameter monitoring**

2933 In order to take into account the variation of pressure and temperature between different data taking  
 2934 periods the applied voltage is corrected following the relationship :

$$2935 \quad HV_{eff} = HV_{app} \times \left( 0.2 + 0.8 \cdot \frac{P_0}{P} \times \frac{T}{T_0} \right) \quad (5.10)$$

2935 where  $T_0$  (=293 K) and  $P_0$  (=990 mbar) are the reference values.

2936 **5.4.3 Measurement procedure**

2937 Insert a short description of the online tools (DAQ, DCS, DQM).

2938 Insert a short description of the offline tools : tracking and efficiency algorithm.

2939 Identify long term aging effects we are monitoring the rates per strip.

2940 **5.4.4 Longevity studies results**

# 6

2941

2942

## Investigation on high rate RPCs

2943 **6.1 Rate limitations and ageing of RPCs**

2944 **6.1.1 Low resistivity electrodes**

2945 **6.1.2 Low noise front-end electronics**

2946 **6.2 Construction of prototypes**

2947 **6.3 Results and discussions**



# 7

2948

2949

## Conclusions and outlooks

2950 **7.1 Conclusions**

2951 **7.2 Outlooks**



# A

2952

2953

## A data acquisition software for CAEN VME TDCs

2954

2955 Certifying detectors in the perspective of HL-LHC required to develop tools for the GIF++ experiment.  
2956 Among them was the C++ Data Acquisition (DAQ) software that allows to make the communications  
2957 in between a computer and TDC modules in order to retrieve the RPC data [88]. In this  
2958 appendix, details about this software, as of how the software was written, how it functions and how  
2959 it can be exported to another similar setup, will be given.

### 2960 A.1 GIF++ DAQ file tree

2961 GIF++ DAQ source code is fully available on github at [https://github.com/afagot/GIF\\_DAQ](https://github.com/afagot/GIF_DAQ). The software requires 3 non-optional dependencies:

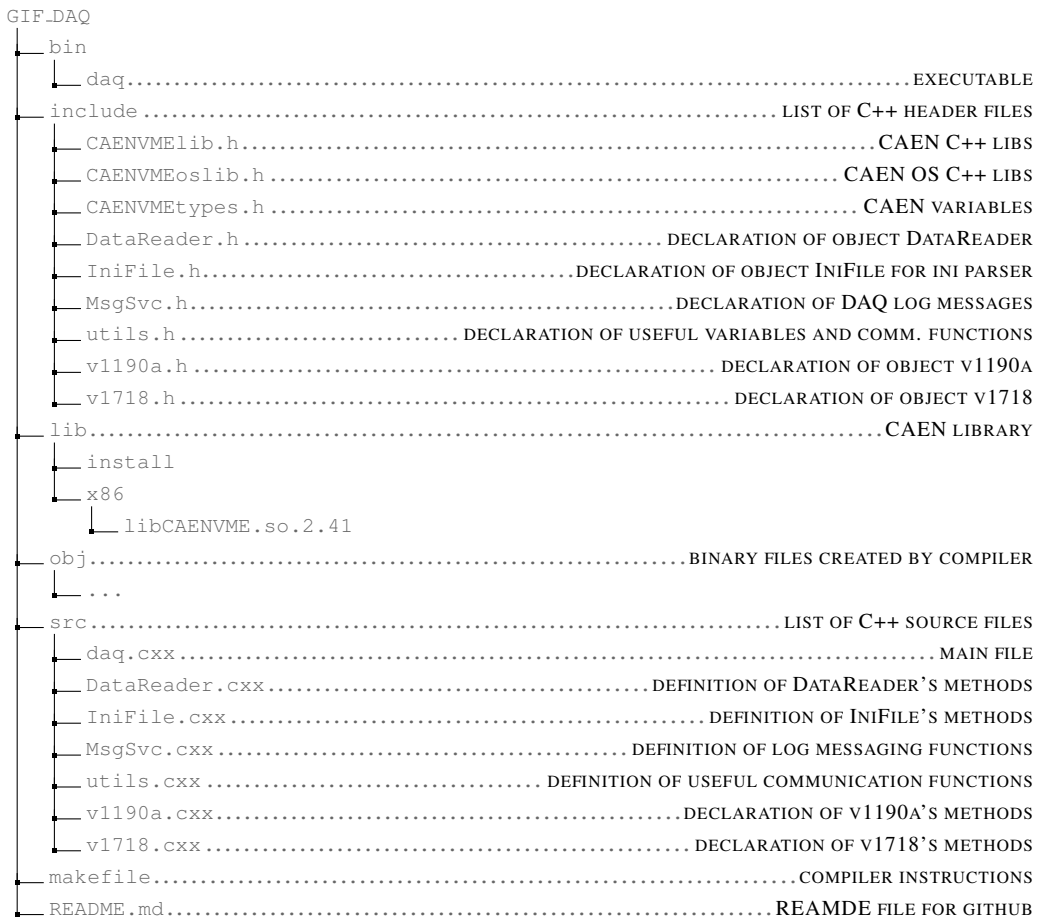
- 2963 • CAEN USB Driver, to mount the VME hardware,  
2964 • CAEN VME Library, to communicate with the VME hardware, and  
2965 • ROOT, to organize the collected data into a TTree.

2966 The CAEN VME library will not be packaged by distributions and will need to be installed man-  
2967 ually. To compile the GIF++ DAQ project via a terminal, from the DAQ folder use the command:

2968     make

2970 The source code tree is provided below along with comments to give an overview of the files' con-  
2971 tent. The different objects created for this project (`v1718`, `v1190a`, `IniFile` & `DataReader`) will be  
2972 described in details in the following sections.

2973



## 2974 A.2 Usage of the DAQ

2975     GIF++ DAQ, as used in GIF++, is not a standalone software. Indeed, the system being more com-  
 2976     plex, the DAQ only is a sub-layer of the software architecture developed to control and monitor  
 2977     the RPCs that are placed into the bunker for performance study in an irradiated environment. The top  
 2978     layer of GIF++ is a Web Detector Control System (webDCS) application. The DAQ is only called  
 2979     by the webDCS when data needs to be acquired. The webDCS operates the DAQ through command  
 2980     line. To start the DAQ, the webDCS calls:

2981  
 2982        bin/daq /path/to/the/log/file/in/the/output/data/folder

2983     where /path/to/the/log/file/in/the/output/data/folder is the only argument required. This  
 2984     log file is important for the webDCS as this file contains all the content of the communication of the  
 2985     webDCS and the different systems monitored by the webDCS. Its content is constantly displayed  
 2986     during data taking for the users to be able to follow the operations. The communication messages  
 2987     are normally sent to the webDCS log file via the functions declared in file `MsgSvc.h`, typically  
 2988     `MSG_INFO(string message)`.

2989

### 2990 A.3 Description of the readout setup

2991 The CMS RPC setup at GIF++ counts 5 V1190A Time-to-Digital Converter (TDC) manufactured  
 2992 by CAEN [89]. V1190A are VME units accepting 128 independent Multi-Hit/Multi-Event TDC  
 2993 channels whose signals are treated by 4 100 ps high performance TDC chips developed by CERN  
 2994 / ECP-MIC Division. The communication between the computer and the TDCs to transfer data is  
 2995 done via a V1718 VME master module also manufactured by CAEN and operated from a USB  
 2996 port [90]. These VME modules are all hosted into a 6U VME 6021 powered crate manufactured by  
 2997 W-Ie-Ne-R than can accommodate up to 21 VME bus cards [91]. These 3 components of the DAQ  
 2998 setup are shown in Figure A.1.

2999

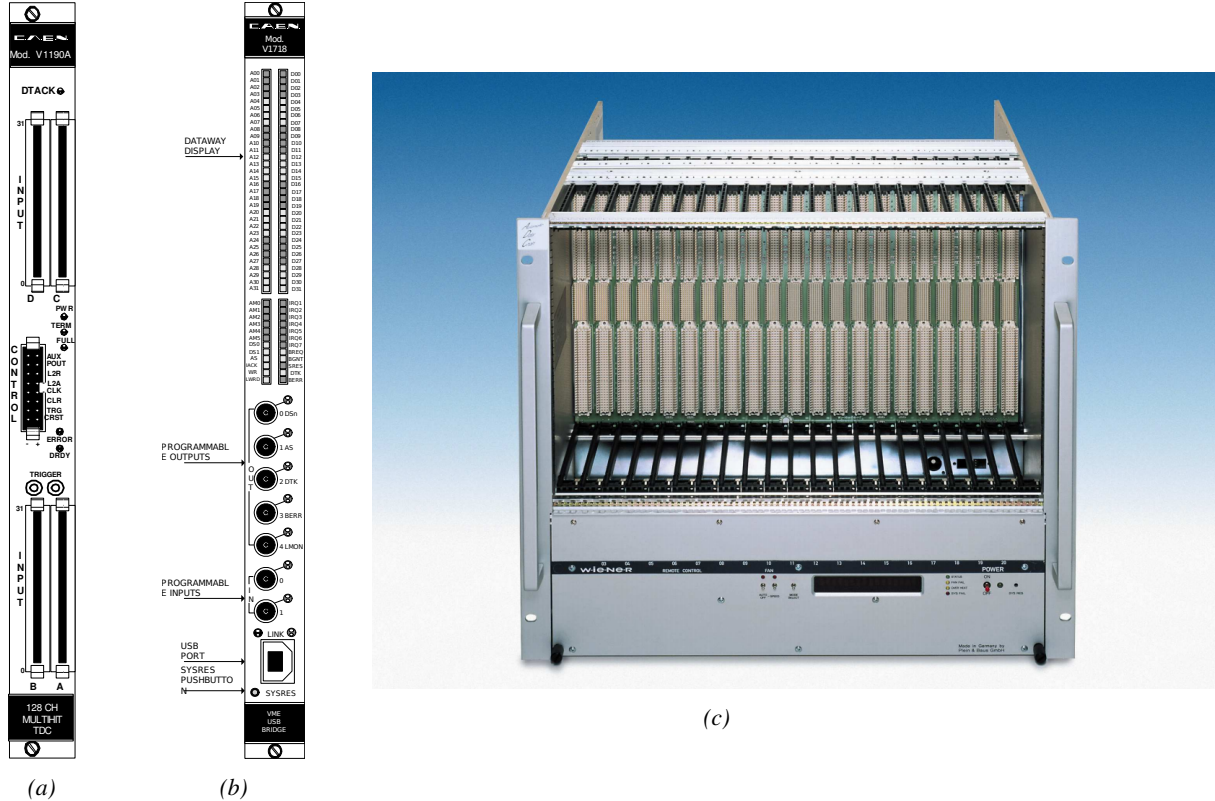


Figure A.1: (A.1a) View of the front panel of a V1190A TDC module [89]. (A.1b) View of the front panel of a V1718 Bridge module [90]. (A.1c) View of the front panel of a 6U 6021 VME crate [91].

3000

### A.4 Data read-out

3001 To efficiently perform a data readout algorithm, C++ objects to handle the VME modules (TDCs  
 3002 and VME bridge) have been created along with objects to store data and read the configuration file

3003 that comes as an input of the DAQ software.

3004

### 3005 A.4.1 V1190A TDCs

3006 The DAQ used at GIF takes profit of the *Trigger Matching Mode* offered by V1190A modules.  
 3007 This setting is enabled through the method `v1190a::SetTrigMatching (int ntdcs)` where `ntdcs`  
 3008 is the total number of TDCs in the setup this setting needs to be enabled for (Source Code A.1). A  
 3009 trigger matching is performed in between a trigger time tag, a trigger signal sent into the TRIGGER  
 3010 input of the TDC visible on Figure A.1a, and the channel time measurements, signals recorded from  
 3011 the detectors under test in our case. Control over this data acquisition mode, explained through  
 3012 Figure A.2, is offered via 4 programmable parameters:

- 3013 • **match window:** the matching between a trigger and a hit is done within a programmable time  
 3014 window. This is set via the method  
`void v1190a::SetTrigWindowWidth(Uint windowHeight, int ntdcs)`
- 3016 • **window offset:** temporal distance between the trigger tag and the start of the trigger matching  
 3017 window. This is set via the method  
`void v1190a::SetTrigWindowWidth(Uint windowHeight, int ntdcs)`
- 3019 • **extra search margin:** an extended time window is used to ensure that all matching hits are  
 3020 found. This is set via the method  
`void v1190a::SetTrigSearchMargin(Uint searchMargin, int ntdcs)`
- 3022 • **reject margin:** older hits are automatically rejected to prevent buffer overflows and to speed  
 3023 up the search time. This is set via the method  
`void v1190a::SetTrigRejectionMargin(Uint rejectMargin, int ntdcs)`

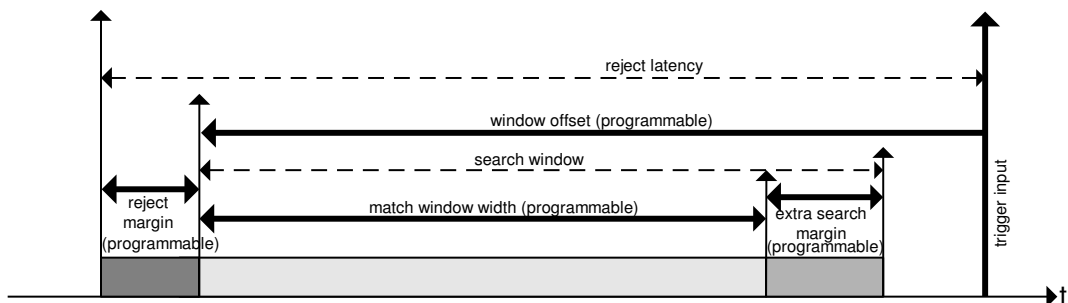


Figure A.2: Module V1190A Trigger Matching Mode timing diagram [89].

3025 Each of these 4 parameters are given in number of clocks, 1 clock being 25 ns long. It is easy to  
 3026 understand at this level that there are 3 possible functioning settings:

- 3027 • **1:** the match window is entirely contained after the trigger signal,
- 3028 • **2:** the match window overlaps the trigger signal, or
- 3029 • **3:** the match window is entirely contained before the trigger signal as displayed on Figure A.2.

3030 In both the first and second cases, the sum of the window width and of the offset can be set to  
3031 a maximum of 40 clocks, which corresponds to 1  $\mu$ s. Evidently, the offset can be negative, allowing  
3032 for a longer match window, with the constraint of having the window ending at most 1  $\mu$ s after the  
3033 trigger signal. In the third case, the maximum negative offset allowed is of 2048 clocks (12 bit) cor-  
3034 responding to 51.2  $\mu$ s, the match window being strictly smaller than the offset. In the case of GIF++,  
3035 the choice has been made to use this last setting by delaying the trigger signal. During the studies  
3036 performed in GIF++, both the efficiency of the RPCs, probed using a muon beam, and the noise or  
3037 gamma background rate are monitored. The extra search and reject margins are left unused.  
3038 To probe the efficiency of RPC detectors, the trigger time tag is provided by the coïncidence of  
3039 scintillators when a bunch of muons passes through GIF++ area is used to trigger the data acquisi-  
3040 tion. For this measurement, it is useful to reduce the match window width only to contain the muon  
3041 information. Indeed, the delay in between a trigger signal and the detection of the corresponding  
3042 muon in the RPC being very contant (typically a few tens of ns due to jitter and cable length), the  
3043 muon signals are very localised in time. Thus, due to a delay of approximalety 325 ns in between  
3044 the muons and the trigger, the settings where chosen to have a window width of 24 clocks (600 ns)  
3045 centered on the muon peak thanks to a negative offset of 29 clocks (725 ns).  
3046 On the otherhand, monitoring the rates don't require for the DAQ to look at a specific time window.  
3047 It is important to integrate enough time to have a robust measurement of the rate as the number of  
3048 hits per time unit. The triggerring signal is provided by a pulse generator at a frequency of 300 Hz  
3049 to ensure that the data taking occurs in a random way, with respect to beam physics, to probe only  
3050 the irradiation spectrum on the detectors. The match window is set to 400 clocks (10  $\mu$ s) and the  
3051 negative offset to 401 clocks as it needs to exceed the value of the match window.

```

3052
class v1190a
{
    private :
        long Handle;
        vector<Data32> Address;
        CVDataWidth DataWidth;
        CVAddressModifier AddressModifier;

    public:

        v1190a(long handle, IniFile *inifile, int ntdcs);
        ~v1190a();
        Data16 write_op_reg(Data32 address, int code, string error);
        Data16 read_op_reg(Data32 address, string error);
        void Reset(int ntdcs);
        void Clear(int ntdcs);
        void TestWR(Data16 value,int ntdcs);
        void CheckTDCStatus(int ntdcs);
        void CheckCommunication(int ntdcs);
        void SetTDCTestMode(Data16 mode,int ntdcs);
        void SetTrigMatching(int ntdcs);
        void SetTrigTimeSubtraction(Data16 mode,int ntdcs);
        void SetTrigWindowWidth(Uint windowHeight,int ntdcs);
        void SetTrigWindowOffset(Uint windowOffset,int ntdcs);
        void SetTrigSearchMargin(Uint searchMargin,int ntdcs);
        void SetTrigRejectionMargin(Uint rejectMargin,int ntdcs);
        void GetTrigConfiguration(int ntdcs);
        void SetTrigConfiguration(IniFile *inifile,int ntdcs);
        void SetTDCDetectionMode(Data16 mode,int ntdcs);
        void SetTDCResolution(Data16 lsb,int ntdcs);
        void SetTDCDeadTime(Data16 time,int ntdcs);
        void SetTDCHeadTrailer(Data16 mode,int ntdcs);
        void SetTDCEventSize(Data16 size,int ntdcs);
        void SwitchChannels(IniFile *inifile,int ntdcs);
        void SetIRQ(Data32 level, Data32 count,int ntdcs);
        void SetBlockTransferMode(Data16 mode,int ntdcs);
        void Set(IniFile *inifile,int ntdcs);
        void CheckStatus(CVErrorCodes status) const;
        int ReadBlockD32(Uint tdc, const Data16 address,
                           Data32 *data, const Uint words, bool ignore_berr);
        Uint Read(RAWData *DataList,int ntdcs);
};

3053

```

3054       *Source Code A.1: Description of C++ object v1190a.*

3055       The v1190a object, defined in the DAQ software as in Source Code A.1, offers the possibility to  
 3056       concatenate all TDCs in the readout setup into a single object containing a list of hardware addresses  
 3057       (addresses to access the TDCs' buffer through the VME crate) and each constructor and method acts  
 3058       on the list of TDCs.

3059

#### 3060     A.4.2 DataReader

3061       Enabled thanks to v1190a::SetBlockTransferMode(Data16 mode, **int** ntdcs), the data transfer  
 3062       is done via Block Transfer (BLT). Using BLT allows to tranfer a fixed number of events called a  
 3063       *block*. This is used together with an Almost Full Level (AFL) of the TDCs' output buffers, defined

3064 through `v1190a::SetIRQ(Data32 level, Data32 count, int ntdcs)`. This AFL gives the maximum amount of 32735 words (16 bits, corresponding to the depth of a TDC output buffer) that can  
 3065 written in a buffer before an Interrupt Request (IRQ) is generated and seen by the VME Bridge,  
 3066 stopping the data acquisition to transfer the content of each TDC buffers before resuming. For each  
 3067 trigger, 6 words or more are written into the TDC buffer:

- 3069     • a **global header** providing information of the event number since the beginning of the data  
       acquisition,
- 3071     • a **TDC header**,
- 3072     • the **TDC data** (*if any*), 1 for each hit recorded during the event, providing the channel and the  
       time stamp associated to the hit,
- 3074     • a **TDC error** providing error flags,
- 3075     • a **TDC trailer**,
- 3076     • a **global trigger time tag** that provides the absolute trigger time relatively to the last reset,  
       and
- 3078     • a **global trailer** providing the total word count in the event.

3079     As previously described in Section ??, CMS RPC FEEs provide us with 100 ns long LVDS out-  
 3080     put signals that are injected into the TDCs' input. Any avalanche signal that gives a signal above the  
 3081     FEEs threshold is thus recorded by the TDCs as a hit within the match window. Each hit is assigned  
 3082     to a specific TDC channel with a time stamp, with a precision of 100 ps. The reference time,  $t_0 = 0$ ,  
 3083     is provided by the beginning of the match window. Thus for each trigger, coming from a scintillator  
 3084     coincidence or the pulse generator, a list of hits is stored into the TDCs' buffers and will then be  
 3085     transferred into a ROOT Tree.

3086     When the BLT is used, it is easy to understand that the maximum number of words that have  
 3087     been set as ALF will not be a finite number of events or, at least, the number of events that would  
 3088     be recorded into the TDC buffers will not be a multiple of the block size. In the last BLT cycle to  
 3089     transfer data, the number of events to transfer will most probably be lower than the block size. In that  
 3090     case, the TDC can add fillers at the end of the block but this option requires to send more data to the  
 3091     computer and is thus a little slower. Another solution is to finish the transfer after the last event by  
 3092     sending a bus error that states that the BLT reached the last event in the pile. This method has been  
 3093     chosen in GIF++.

3095  
 3096     Due to irradiation, an event in GIF++ can count up to 300 words per TDC. A limit of 4096 words  
 3097     (12 bits) has been set to generate IRQ which represent from 14 to almost 700 events depending on  
 3098     the average of hits collected per event. Then the block size has been set to 100 events with enabled  
 3099     bus errors. When an AFL is reached for one of the TDCs, the VME bridge stops the acquisition by  
 3100     sending a BUSY signal.

3101

3102     The data is then transferred one TDC at a time into a structure called `RAWData` (Source Code A.2).

```
3103
3104   struct RAWData{
3105     vector<int>           *EventList;
3106     vector<int>           *NHitsList;
3107     vector<int>           *QFlagList;
3108     vector<vector<int>>    *Channellist;
3109     vector<vector<float>>  *TimeStampList;
3110   };
```

3105                     *Source Code A.2: Description of data holding C++ structure `RAWData`.*

3106     In order to organize the data transfer and the data storage, an object called `DataReader` was  
 3107     created (Source Code A.3). On one hand, it has `v1718` and `v1190a` objects as private members for  
 3108     communication purposes, such as VME modules settings via the configuration file `*iniFile` or data  
 3109     read-out through `v1190a::Read()` and on the other hand, it contains the structure `RAWData` that allows  
 3110     to organise the data in vectors reproducing the tree structure of a ROOT file.

```
3111
3112   class DataReader
3113   {
3114     private:
3115       bool      StopFlag;
3116       IniFile  *iniFile;
3117       Data32    MaxTriggers;
3118       v1718    *VME;
3119       int      nTDCs;
3120       v1190a   *TDCs;
3121       RAWData  TDCData;
3122
3123     public:
3124       DataReader();
3125       virtual ~DataReader();
3126       void      SetIniFile(string inifilename);
3127       void      SetMaxTriggers();
3128       Data32    GetMaxTriggers();
3129       void      SetVME();
3130       void      SetTDC();
3131       int      GetQFlag(Uint it);
3132       void      Init(string inifilename);
3133       void      FlushBuffer();
3134       void      Update();
3135       string   GetFileName();
3136       void      WriteRunRegistry(string filename);
3137       void      Run();
3138   };
```

3113                     *Source Code A.3: Description of C++ object `DataReader`.*

3114     Each event is transferred from `TDCData` and saved into branches of a ROOT `TTree` as 3 integers  
 3115     that represent the event ID (`EventCount`), the number of hits read from the TDCs (`nHits`), and the  
 3116     quality flag that provides information for any problem in the data transfer (`qflag`), and 2 lists of  
 3117     `nHits` elements containing the fired TDC channels (`TDCCh`) and their respective time stamps (`TDCTS`),  
 3118     as presented in Source Code A.4. The ROOT file file is named using information contained into  
 3119     the configuration file, presented in section A.5.2. The needed information is extracted using method  
 3120     `DataReader::GetFileName()` and allow to build the output filename format `ScanXXXXXX_HVX_DAQ.root`

3121 where ScanXXXXXX is a 6 digit number representing the scan number into GIFT++ database and HVX  
 3122 the HV step within the scan that can be more than a single digit. An example of ROOT data file is  
 3123 provided with Figure A.3.

```
3124
RAWData TDCData;
TFile *outputFile = new TFile(outputFileName.c_str(),"recreate");
TTree *RAWDataTree = new TTree("RAWData","RAWData");

int EventCount = -9;
int nHits = -8;
int qflag = -7;
vector<int> TDCCh;
vector<float> TDCTS;

RAWDataTree->Branch("EventNumber",&EventCount, "EventNumber/I");
RAWDataTree->Branch("number_of_hits",&nHits,"number_of_hits/I");
RAWDataTree->Branch("Quality_flag",&qflag,"Quality_flag/I");
RAWDataTree->Branch("TDC_channel",&TDCCh);
RAWDataTree->Branch("TDC_TimeStamp",&TDCTS);

3125
//...
//Here read the TDC data using v1190a::Read() and place it into
//TDCData for as long as you didn't collect the requested amount
//of data.
//...

for(Uint i=0; i<TDCData.EventList->size(); i++){
    EventCount = TDCData.EventList->at(i);
    nHits = TDCData.NHitsList->at(i);
    qflag = TDCData.QFlagList->at(i);
    TDCCh = TDCData.ChannelList->at(i);
    TDCTS = TDCData.TimeStampList->at(i);
    RAWDataTree->Fill();
}
```

3126 *Source Code A.4: Highlight of the data transfer and organisation within DataReader::Run() after the data has been collected into TDCData.*

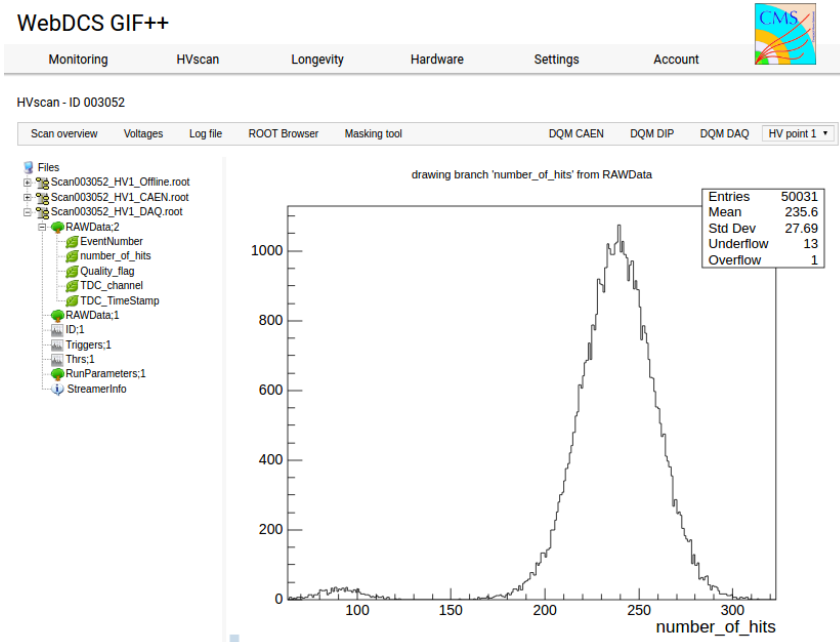


*Figure A.3: Structure of the ROOT output file generated by the DAQ. The 5 branches (EventNumber, number\_of\_hits, Quality\_flag, TDC\_channel and TDC\_TimeStamp) are visible on the left panel of the ROOT browser. On the right panel is visible the histogram corresponding to the variable nHits. In this specific example, there were approximately 50k events recorded to measure the gamma irradiation rate on the detectors. Each event is stored as a single entry in the TTree.*

#### 3127    A.4.3 Data quality flag

3128    Among the parameters that are recorded for each event, the quality flag, defined in Source Code A.5,  
 3129    is determined on the fly by checking the data recorded by every single TDC. From method `v1190a::Read()`,  
 3130    it can be understood that the content of each TDC buffer is readout one TDC at a time. Entries are  
 3131    created in the data list for the first TDC and then, when the second buffer is readout, events corre-  
 3132    sponding to entries that have already been created to store data for the previous TDC are added to  
 3133    the existing list element. On the contrary, when an event entry has not been yet created in the data  
 3134    list, a new entry is created.

```
3135    typedef enum _QualityFlag {
  3136     GOOD      = 1,
    CORRUPTED = 0
 } QualityFlag;
```

3137    *Source Code A.5: Definition of the quality flag `enum`.*

3138    It is possible that each TDC buffer contains a different number of events. In cases where the first  
 3139    element in the buffer list is an event for corresponds to a new entry, the difference in between the  
 3140    entry from the buffer and the last entry in the data list is recorded and checked. If it is greater than 1,  
 3141    what should never be the case, the quality flag is set to CORRUPTED for this TDC and an empty entry  
 3142    is created in the place of the missing ones. Missing entries are believe to be the result of a bad hold

3143 on the TDC buffers at the moment of the readout. Indeed, the software hold is effective only on 1  
 3144 TDC at a time and no solution as been found yet to completely block the writting in the buffers when  
 3145 an IRQ is received.

3146 At the end of each BLT cycle, the ID of the last entry stored for each TDC buffer is not recorded.  
 3147 When starting the next cycle, if the first entry in the pile corresponds to an event already existing  
 3148 in the list, the readout will start from this list element and will not be able to check the difference  
 3149 in between this entry's ID and the one of the last entry that was recorded for this TDC buffer in  
 3150 the previous cycle. In the case events were missing, the flag stays at its initial value of 0, which is  
 3151 similar to CORRUPTED and it is assumed that then this TDC will not contribute to `number_of_hits`,  
 3152 `TDC_channel` or `TDC_TimeStamp`.

3153 Finally, since there will be 1 `RAWData` entry per TDC for each event (meaning `nTDCs` entries,  
 3154 referring to `DataReader` private attribute), the individual flags of each TDC will be added together.  
 3155 The final format is an integer composed `nTDCs` digits where each digit is the flag of a specific TDC.  
 3156 This is constructed using powers of 10 like follows:

```
3157     TDC 0: QFlag = 100 × _QualityFlag
3158     TDC 1: QFlag = 101 × _QualityFlag
3159     ...
3160     TDC N: QFlag = 10N × _QualityFlag
```

3161 and the final flag to be with N digits:

```
3162     QFlag = n....3210
```

3163 each digit being 1 or 0. Below is given an example with a 4 TDCs setup.

3164 If all TDCs were good : `QFlag = 1111`,

3165 but if TDC 2 was corrupted : `QFlag = 1011`.

3166 When data taking is over and the data contained in the dynamical `RAWData` structure is transferred  
 3167 to the ROOT file, all the 0s are changed into 2s by calling the method `DataReader::GetQFlag()`.  
 3168 This will help translating the flag without knowing the number of TDCs beforehand. Indeed, a flag  
 3169 111 could be due to a 3 TDC setup with 3 good individual TDC flags or to a more than 3 TDC setup  
 3170 with TDCs those ID is greater than 2 being CORRUPTED, thus giving a 0.

3171 The quality flag has been introduced quite late, in October 2017 only, to the list of GIFT++ DAQ  
 3172 parameters to be recorded into the output ROOT file. Before this addition, the missing data, corrupting  
 3173 the quality for the offline analysis, was contributing to artificially fill data with lower multiplicity.  
 3174 Looking at `TBranch number_of_hits` provides an information about the data of the full GIFT++  
 3175 setup. When a TDC is not able to transfer data for a specific event, the effect is a reduction of the  
 3176 total number of hits recorded in the full setup, this is what can be seen from Figure A.4. After offline  
 3177 reconstruction detector by detector, the effect of missing events can be seen in the artificially filled  
 3178 bin at multiplicity 0 shown in Figure A.5. Nonetheless, for data with high irradiation levels, as it is  
 3179 the case for Figure A.5a, discarding the fake multiplicity 0 data can be done easily during the offline  
 3180 analysis. At lower radiation, the missing events contribution becomes more problematic as the multi-  
 3181 tiplicity distribution overlaps the multiplicity 0 and that in the same time the proportion of missing

3182 events decreases. Attempts to fit the distribution with a Poisson or skew distribution function were  
 3183 not conclusive and this very problem has been at the origin of the quality flag that allows to give a  
 3184 non ambiguous information about each event quality.

3185

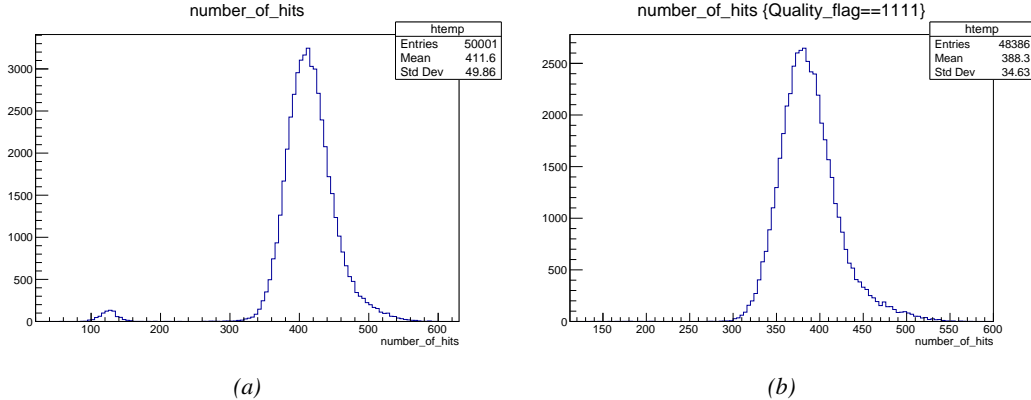


Figure A.4: The effect of the quality flag is explained by presenting the content of `TBranch` `number_of_hits` of a data file without `Quality_flag` in Figure A.4a and the content of the same `TBranch` for data corresponding to a `Quality_flag` where all TDCs were labelled as `GOOD` in Figure A.4b taken with similar conditions. It can be noted that the number of entries in Figure A.4b is slightly lower than in Figure A.4a due to the excluded events.

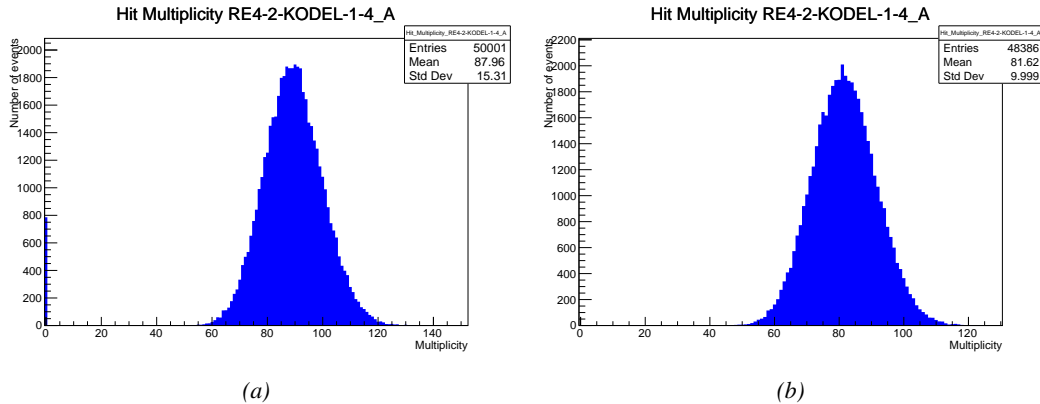


Figure A.5: Using the same data as previously showed in Figure A.4, the effect of the quality flag is explained by presenting the reconstructed hit multiplicity of a data file without `Quality_flag` in Figure A.5a and the reconstructed content of the same RPC partition for data corresponding to a `Quality_flag` where all TDCs were labelled as `GOOD` in Figure A.5b taken with similar conditions. The artificial high content of bin 0 is completely suppressed.

## A.5 Communications

3186 To ensure data readout and dialog in between the machine and the TDCs or in between the webDCS  
 3187 and the DAQ, different communication solutions were used. First of all, it is important to have a

3189 module to allow the communication in between the TDCs and the computer from which the DAQ  
 3190 operates. When this communication is effective, shifters using the webDCS to control data taking  
 3191 can thus send instructions to the DAQ.

3192

### 3193 A.5.1 V1718 USB Bridge

3194 In the previous section, the data transfer has been discussed. The importance of the `v1718` object  
 3195 (Source Code A.6), used as private member of `DataReader`, was not explicated. VME master  
 3196 modules are used for communication purposes as they host the USB port that connects the pow-  
 3197 ered crate buffer to the computer where the DAQ is installed. From the source code point of view,  
 3198 this object is used to control the communication status, by reading the returned error codes with  
 3199 `v1718::CheckStatus()`, or to check for IRQs coming from the TDCs through `v1718::CheckIRQ()`.  
 3200 Finally, to ensure that triggers are blocked at the hardware level, a NIM pulse is sent out of one of the  
 3201 5 programmable outputs (`v1718::SendBUSY()`) to the VETO of the coincidence module where the  
 3202 trigger signals originate from. As long as this signal is ON, no trigger can reach the TDCs anymore.  
 3203

```
3204 class v1718{
3205     private:
3206         int Handle;
3207         Data32 Data;           // Data
3208         CVIRQLevels Level;    // Interrupt level
3209         CVAddressModifier AM;   // Addressing Mode
3210         CVDataWidth dataSize; // Data Format
3211         Data32 BaseAddress;   // Base Address
3212
3213     public:
3214         v1718(IniFile *inifile);
3215         ~v1718();
3216         long GetHandle(void) const;
3217         int GetData(Data16 data);
3218         Data16 GetData(void);
3219         int SetData(void);
3220         CVIRQLevels GetLevel(void);
3221         int SetLevel(CVIRQLevels level);
3222         CVAddressModifier GetAM(void);
3223         int SetAM(CVAddressModifier am);
3224         CVAddressModifier GetAM(void);
3225         int SetDataSize(CVDataWidth datasize);
3226         CVDataWidth GetDataSize(void);
3227         int SetBaseAddress(Data16 baseaddress);
3228         Data16 GetBaseAddress(void);
3229         void CheckStatus(CVErrorCodes status) const;
3230         bool CheckIRQ();
3231         void SetPulsers();
3232         void SendBUSY(BusyLevel level);
3233     };

```

3205

*Source Code A.6: Description of C++ object v1718.*

### 3206 A.5.2 Configuration file

3207 The DAQ software takes as input a configuration file written using INI standard [92]. This file is  
 3208 partly filled with the information provided by the shifters when starting data acquisition using the  
 3209 webDCS, as shown by Figure A.6. This information is written in section [`General`] and will later

3210 be stored in the ROOT file that contains the DAQ data as can be seen from Figure A.3. Indeed,  
 3211 another `TTree` called `RunParameters` as well as the 2 histograms `ID`, containing the scan number,  
 3212 start and stop time stamps, and `Triggers`, containing the number of triggers requested by the shifter,  
 3213 are available in the data files. Moreover, `ScanID` and `HV` are then used to construct the file name  
 3214 thanks to the method `DataReader::GetFileName()`.

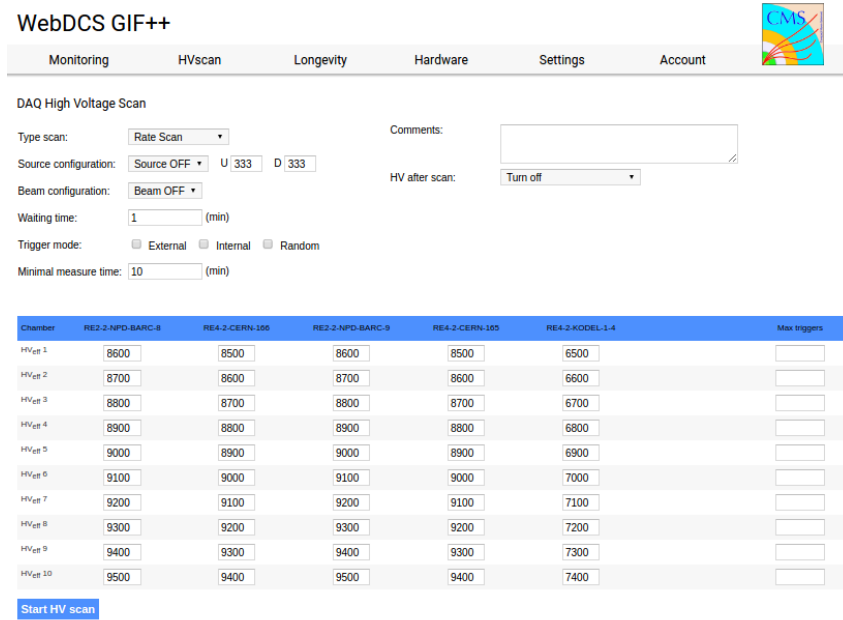


Figure A.6: WebDCS DAQ scan page. On this page, shifters need to choose the type of scan (Rate, Efficiency or Noise Reference scan), the gamma source configuration at the moment of data taking, the beam configuration, and the trigger mode. These information will be stored in the DAQ ROOT output. Are also given the minimal measurement time and waiting time after ramping up of the detectors is over before starting the data acquisition. Then, the list of HV points to scan and the number of triggers for each run of the scan are given in the table underneath.

3215 The rest of the information is written beforehand in the configuration file template, as explicated  
 3216 in Source Code A.7, and contains the hardware addresses to the different VME modules in the  
 3217 setup as well as settings for the TDCs. As the TDC settings available in the configuration file are not  
 3218 supposed to be modified, an improvement would be to remove them from the configuration file and  
 3219 to hardcode them inside of the DAQ code itself or to place them into a different INI file that would  
 3220 host only the TDC settings to lower the probability for a bad manipulation of the configuration file  
 3221 that can be modified from one of webDCS' menus.

3222

```

[General]
TdcS=4
ScanID=$scanid
HV=$HV
RunType=$runtype
MaxTriggers=$maxtriggers
Beam=$beam
[VMEInterface]
Type=V1718
BaseAddress=0xFF0000
Name=VmeInterface
[TDC0]
Type=V1190A
BaseAddress=0x00000000
Name=Tdc0
StatusA00-15=1
StatusA16-31=1
StatusB00-15=1
StatusB16-31=1
StatusC00-15=1
StatusC16-31=1
StatusD00-15=1
StatusD16-31=1
[TDC1]
Type=V1190A
BaseAddress=0x11110000
Name=Tdc1
StatusA00-15=1
StatusA16-31=1
StatusB00-15=1
StatusB16-31=1
StatusC00-15=1
StatusC16-31=1
StatusD00-15=1
StatusD16-31=1
[TDC2]
Type=V1190A
BaseAddress=0x22220000
Name=Tdc2
StatusA00-15=1
StatusA16-31=1
StatusB00-15=1
StatusB16-31=1
StatusC00-15=1
StatusC16-31=1
StatusD00-15=1
StatusD16-31=1
[TDC3]
Type=V1190A
BaseAddress=0x44440000
Name=Tdc3
StatusA00-15=1
StatusA16-31=1
StatusB00-15=1
StatusB16-31=1
StatusC00-15=1
StatusC16-31=1
StatusD00-15=1
StatusD16-31=1
[TDCSettings]
TriggerExtraSearchMargin=0
TriggerRejectMargin=0
TriggerTimeSubtraction=0b1
TdcDetectionMode=0b01
TdcResolution=0b10
TdcDeadTime=0b00
TdcHeadTrailer=0b1
TdcEventSize=0b1001
TdcTestMode=0b0
BLTMode=1

```

3223

*Source Code A.7: INI configuration file template for 4 TDCs. In section [General], the number of TDCs is explicitated and information about the ongoing run is given. Then, there are sections for each and every VME modules. There buffer addresses are given and for the TDCs, the list of channels to enable is given. Finally, in section [TDCSettings], a part of the TDC settings are given.*

3225     In order to retrieve the information of the configuration file, the object `IniFile` has been developed  
 3226     to provide an INI parser, presented in Source Code A.8. It contains private methods returning a  
 3227     boolean to check the type of line written in the file, whether a comment, a group header or a key line  
 3228     (`IniFile::CheckIfComment()`, `IniFile::CheckIfGroup()` and `IniFile::CheckIfToken()`). The  
 3229     key may sometimes be referred to as *token* in the source code. Moreover, the private element  
 3230     `FileData` is a map of `const string` to `string` that allows to store the data contained inside the  
 3231     configuration file via the public method `IniFile::GetFileData()` following the formatting (see  
 3232     method `IniFile::Read()`):

```
3233
  string group, token, value;
  // Get the field values for the 3 strings.
  // Then concatenate group and token together as a single string
  // with a dot separation.
  token = group + "." + token;
  FileData[token] = value;
```

3235     More methods have been written to translate the different keys into the right variable format  
 3236     when used by the DAQ. For example, to get a `float` value out of the configuration file data, knowing  
 3237     the group and the key needed, the method `IniFile::floatType()` can be used. It takes 3 arguments  
 3238     being the group name and key name (both `string`), and a default `float` value used as exception in  
 3239     the case the expected combination of group and key cannot be found in the configuration file. This  
 3240     default value is then used and the DAQ continues on working after sending an alert in the log file for  
 3241     further debugging.

```

3242 typedef map< const string, string > IniFileData;
3243
class IniFile{
    private:
        bool          CheckIfComment (string line);
        bool          CheckIfGroup(string line, string& group);
        bool          CheckIfToken(string line, string& key, string& value);
        string         FileName;
        IniFileData   FileData;
        int           Error;

    public:
        IniFile();
        IniFile(string filename);
        virtual      ~IniFile();

        // Basic file operations
        void          SetFileName(string filename);
        int           Read();
        int           Write();
        IniFileData GetFileData();

        // Data readout methods
        Data32         addressType (string groupname, string keyname, Data32
→     defaultvalue);
        long          intType     (string groupname, string keyname, long
→     defaultvalue);
        long long    longType    (string groupname, string keyname, long long
→     defaultvalue );
        string         stringType  (string groupname, string keyname, string
→     defaultvalue );
        float         floatType   (string groupname, string keyname, float
→     defaultvalue );

        // Error methods
        string         GetErrorMsg();
    };

```

3244       *Source Code A.8: Description of C++ object `IniFile` used as a parser for INI file format.*

### 3245   A.5.3 WebDCS/DAQ intercommunication

3246 When shifters send instructions to the DAQ via the configuration file, it is the webDCS itself that  
 3247 gives the start command to the DAQ and then the 2 softwares use inter-process communication  
 3248 through file to synchronise themselves. This communication file is represented by the variable **const**  
 3249 **string** \_\_runstatuspath.

3250 On one side, the webDCS sends commands or status that are readout by the DAQ:

- 3251     ● INIT, status sent when launching a scan and read via function `CtrlRunStatus(...)`,
- 3252     ● START, command to start data taking and read via function `CheckSTART()`,
- 3253     ● STOP, command to stop data taking at the end of the scan and read via function `CheckSTOP()`,  
 3254       and
- 3255     ● KILL, command to kill data taking sent by user and read via function `CheckKILL()`

3256 and on the other, the DAQ sends status that are controled by the webDCS:

- 3257     ● `DAQ_RDY`, sent with `SendDAQReady()` to signify that the DAQ is ready to receive commands  
3258       from the webDCS,
- 3259     ● `RUNNING`, sent with `SendDAQRunning()` to signify that the DAQ is taking data,
- 3260     ● `DAQ_ERR`, sent with `SendDAQError()` to signify that the DAQ didn't receive the expected com-  
3261       mand from the webDCS or that the launch command didn't have the right number of argu-  
3262       ments,
- 3263     ● `RD_ERR`, sent when the DAQ wasn't able to read the communication file, and
- 3264     ● `WR_ERR`, sent when the DAQ wasn't able to write into the communication file.

#### 3265     **A.5.4 Example of inter-process communication cycle**

3266 Under normal conditions, the webDCS and the DAQ processes exchange commands and status via  
3267 the file hosted at the address `__runstatuspath`, as explained in subsection A.5.3. An example of  
3268 cycle is given in Table A.1. In this example, the steps 3 to 5 are repeated as long as the webDCS tells  
3269 the DAQ to take data. A data taking cycle is the equivalent as what is called a *Scan* in GIFT++ jargon,  
3270 referring to a set a runs with several HV steps. Each repetition of steps 3 to 5 is then equivalent to a  
3271 single *Run*.

3272 At any moment during the data taking, for any reason, the shifter can decide that the data taking  
3273 needs to be stopped before it reached the end of the scheduled cycle. Thus at any moment on the  
3274 cycle, the content of the inter-process communication file will be changed to `KILL` and the DAQ will  
3275 shut down right away. The DAQ checks for `KILL` signals every 5s after the TDCs configuration is  
3276 over. So far, the function `CheckKILL()` has been used only inside of the data taking loop of method  
3277 `DataReader::Run()` and thus, if the shifter decides to KILL the data taking during the TDC con-  
3278 figuration phase or the HV ramping in between 2 HV steps, the DAQ will not be stopped smoothly  
3279 and a *force kill* command will be sent to stop the DAQ process that is still awake on the computer.  
3280 Improvements can be brought on this part of the software to make sure that the DAQ can safely  
3281 shutdown at any moment.

#### 3284     **A.6 Software export**

3285 In section A.2 was discussed the fact that the DAQ as written in its last version is not a standalone  
3286 software. It is possible to make it a standalone program that could be adapted to any VME setup  
3287 using V1190A and V1718 modules by creating a GUI for the software or by printing the log mes-  
3288 sages that are normally printed in the webDCS through the log file, directly into the terminal. This  
3289 method was used by the DAQ up to version 3.0 moment where the webDCS was completed. Also, it  
3290 is possible to check branches of DAQ v2.X to have example of communication through a terminal.

3291  
3292     DAQ v2.X is nonetheless limited in it's possibilities and requires a lot of offline manual interven-  
3293       tions from the users. Indeed, there is no communication of the software with the detectors' power  
3294       supply system that would allow for a user a predefine a list of voltages to operate the detectors at

step	actions of webDCS	status of DAQ	<code>__runstatuspath</code>
1	launch DAQ ramp voltages ramping over wait for currents stabilization	readout of IniFile configuration of TDCs	INIT
2		configuration done send DAQ ready wait for START signal	DAQ_RDY
3	waiting time over send START		START
4	wait for run to end monitor DAQ run status	data taking ongoing check for KILL signal	RUNNING
5		run over send DAQ_RDY wait for next DCS signal	DAQ_RDY
6	ramp voltages ramping over wait for currents stabilization		DAQ_RDY
3	waiting time over send START		START
4	wait for run to end monitor DAQ run status	update IniFile information data taking ongoing check for KILL signal	RUNNING
5		run over send DAQ_RDY wait for next DCS signal	DAQ_RDY
7	send command STOP	DAQ shuts down	STOP

Table A.1: Inter-process communication cycles in between the webDCS and the DAQ through file string signals.

3295 and loop over to take data without any further manual intervention. In v2.X, the data is taken for a  
3296 single detector setting and at the end of each run, the softwares asks the user if he intends on taking  
3297 more runs. If so, the software invites the user to set the operating voltages accordingly to what is  
3298 necessary and to manual update the configuration file in consequence. This working mode can be a  
3299 very first approach before an evolution and has been successfully used by colleagues from different  
3300 collaborations.

3301  
3302 For a more robust operation, it is recommended to develop a GUI or a web application to inter-  
3303 face the DAQ. Moreover, to limit the amount of manual interventions, and thus the probability to  
3304 make mistakes, it is also recommended to add an extra feature into the DAQ by installing the HV  
3305 Wrapper library provided by CAEN of which an example of use in a similar DAQ software devel-  
3306 opped by a master student of UGent, and called TinyDAQ, is provided on UGent's github. Then, this  
3307 HV Wrapper will help you communicating with and give instructions to a CAEN HV powered crate  
3308 and can be added into the DAQ at the same level where the communication with the user was made  
3309 in DAQ v2.X. In case you are using another kind of power system for your detectors, it is stringly  
3310 adviced to use HV modules or crates that can be remotely controled via a using C++ libraries.

3311

# B

3312

3313

## Details on the offline analysis package

3314 The data collected in GIF++ thanks to the DAQ described in Appendix A is difficult to interpret by  
3315 a human user that doesn't have a clear idea of the raw data architecture of the ROOT data files. In  
3316 order to render the data human readable, a C++ offline analysis tool was designed to provide users  
3317 with detector by detector histograms that give a clear overview of the parameters monitored during  
3318 the data acquisition [93]. In this appendix, details about this software in the context of GIF++, as of  
3319 how the software was written and how it functions will be given.

### 3320 B.1 GIF++ Offline Analysis file tree

3321 GIF++ Offline Analysis source code is fully available on github at [https://github.com/aafagot/GIF\\_OfflineAnalysis](https://github.com/aafagot/GIF_OfflineAnalysis). The software requires ROOT as non-optionnal dependency  
3322 as it takes ROOT files in input and write an output ROOT file containing histograms. To compile the  
3324 GIF++ Offline Analysis project is compiled with cmake. To compile, first a build/ directory must  
3325 be created to compile from there:

```
3326 mkdir build
3327 cd build
3328 cmake ..
3329 make
3330 make install
```

3328 To clean the directory and create a new build directory, the bash script cleandir.sh can be used:

```
3329
3330 ./cleandir.sh
```

3331 The source code tree is provided below along with comments to give an overview of the files' con-  
3332 tent. The different objects created for this project (`Infrastructure`, `Trolley`, `RPC`, `Mapping`, `RPCHit`,  
3333 `RPCCluster` and `Inifile`) will be described in details in the following sections.

3334

```

GIF_OfflineAnalysis
├── bin
│   └── offlineanalysis ..... EXECUTABLE
├── build..... CMAKE COMPILATION DIRECTORY
└── ...
    ├── include..... LIST OF C++ HEADER FILES
    │   ├── Cluster.h..... DECLARATION OF OBJECT RPCCLUSTER
    │   ├── Current.h..... DECLARATION OF GETCURRENT ANALYSIS MACRO
    │   ├── GIFTrolley.h..... DECLARATION OF OBJECT TROLLEY
    │   ├── Infrastructure.h..... DECLARATION OF OBJECT INFRASTRUCTURE
    │   ├── IniFile.h..... DECLARATION OF OBJECT INI FILE FORINI PARSER
    │   ├── Mapping.h..... DECLARATION OF OBJECT MAPPING
    │   ├── MsgSvc.h..... DECLARATION OF OFFLINE LOG MESSAGES
    │   ├── OfflineAnalysis.h..... DECLARATION OF DATA ANALYSIS MACRO
    │   ├── RPCTracker.h..... DECLARATION OF OBJECT RPC
    │   ├── RPCHit.h..... DECLARATION OF OBJECT RPCHIT
    │   ├── types.h..... DEFINITION OF USEFUL VARIABLE TYPES
    │   └── utils.h..... DECLARATION OF USEFUL FUNCTIONS
    ├── obj..... BINARY FILES CREATED BY COMPILER
    └── ...
        ├── src..... LIST OF C++ SOURCE FILES
        │   ├── Cluster.cc..... DEFINITION OF OBJECT RPCCLUSTER
        │   ├── Current.cc..... DEFINITION OF GETCURRENT ANALYSIS MACRO
        │   ├── GIFTrolley.cc..... DEFINITION OF OBJECT TROLLEY
        │   ├── Infrastructure.cc..... DEFINITION OF OBJECT INFRASTRUCTURE
        │   ├── IniFile.cc..... DEFINITION OF OBJECT INI FILE FORINI PARSER
        │   ├── main.cc..... MAIN FILE
        │   ├── Mapping.cc..... DEFINITION OF OBJECT MAPPING
        │   ├── MsgSvc.cc..... DEFINITION OF OFFLINE LOG MESSAGES
        │   ├── OfflineAnalysis.cc..... DEFINITION OF DATA ANALYSIS MACRO
        │   ├── RPCTracker.cc..... DEFINITION OF OBJECT RPC
        │   ├── RPCHit.cc..... DEFINITION OF OBJECT RPCHIT
        │   └── utils.cc..... DEFINITION OF USEFUL FUNCTIONS
        ├── cleandir.sh..... BASH SCRIPT TO CLEAN BUILD DIRECTORY
        ├── CMakeLists.txt..... SET OF INSTRUCTIONS FOR CMAKE
        ├── config.h.in..... DEFINITION OF VERSION NUMBER
        └── README.md..... README FILE FOR GITHUB

```

3335

## B.2 Usage of the Offline Analysis

3336 In order to use the Offline Analysis tool, it is necessary to know the Scan number and the HV Step  
 3337 of the run that needs to be analysed. This information needs to be written in the following format:

3338

3339     Scan00XXXX\_HVY

3340 where XXXX is the scan ID and Y is the high voltage step (in case of a high voltage scan, data will be  
 3341 taken for several HV steps). This format corresponds to the base name of data files in the database

3342 of the GIF++ webDCS. Usually, the offline analysis tool is automatically called by the webDCS at  
 3343 the end of data taking or by a user from the webDCS panel if an update of the tool was brought.  
 3344 Nonetheless, an expert can locally launch the analysis for tests on the GIF++ computer, or a user can  
 3345 get the code on its local machine from github and download data from the webDCS for its own anal-  
 3346 ysis. To launch the code, the following command can be used from the `GIF_OfflineAnalysis` folder:

3347

```
3348 bin/offlineanalysis /path/to/Scan00XXXX_HVY
```

3349 where, `/path/to/Scan00XXXX_HVY` refers to the local data files. Then, the offline tool will by itself  
 3350 take care of finding all available ROOT data files present in the folder, as listed below:

3351

- `Scan00XXXX_HVY_DAQ.root` containing the TDC data as described in Appendix ?? (events, hit  
 3352 and timestamp lists), and
- `Scan00XXXX_HVY_CAEN.root` containing the CAEN mainframe data recorded by the monitor-  
 3354 ing tool webDCS during data taking (HVs and currents of every HV channels). This file is  
 3355 created independently of the DAQ.

3356 **B.2.1 Output of the offline tool**

3357 **B.2.1.1 ROOT file**

3358 The analysis gives in output ROOT datafiles that are saved into the data folder and called using the  
 3359 naming convention `Scan00XXXX_HVY_Offline.root`. Inside those, a list of `TH1` histograms can be  
 3360 found. Its size will vary as a function of the number of detectors in the setup as each set of histograms  
 3361 is produced detector by detector. For each partition of each chamber, can be found:

3362

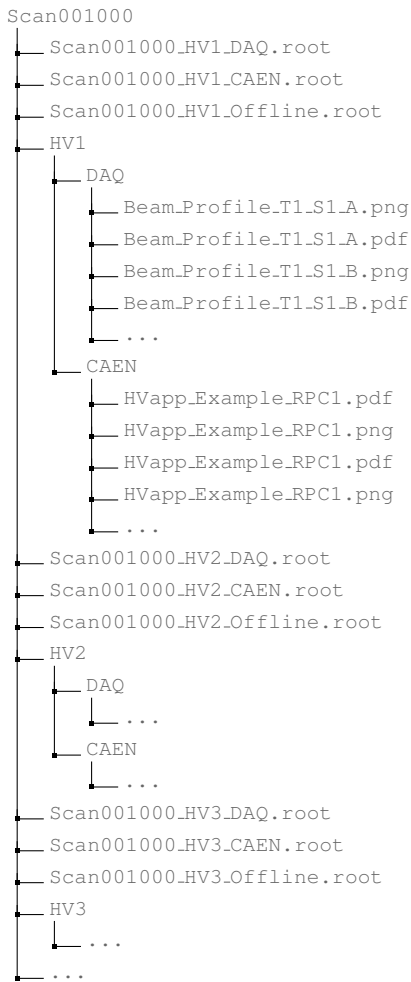
- `Time_Profile_Tt_Sc_p` shows the time profile of all recorded events (number of events per  
 3363 time bin),
- `Hit_Profile_Tt_Sc_p` shows the hit profile of all recorded events (number of events per chan-  
 3365 nel),
- `Hit_Multiplicity_Tt_Sc_p` shows the hit multiplicity (number of hits per event) of all recorded  
 3366 events (number of occurrences per multiplicity bin),
- `Strip_Mean_Noise_Tt_Sc_p` shows noise/gamma rate per unit area for each strip in a se-  
 3369 lected time range. After filters are applied on `Time_Profile_Tt_Sc_p`, the filtered version  
 3370 of `Hit_Profile_Tt_Sc_p` is normalised to the total integrated time and active detection area  
 3371 of a single channel,
- `Strip_Activity_Tt_Sc_p` shows noise/gamma activity for each strip (normalised version of  
 3373 previous histogram - strip activity = strip rate / average partition rate),
- `Strip_Homogeneity_Tt_Sc_p` shows the *homogeneity* of a given partition ( $\text{homogeneity} = \exp(-\text{strip rates standard deviation(strip rates in partition/average partition rate)})$ ),
- `mask_Strip_Mean_Noise_Tt_Sc_p` shows noise/gamma rate per unit area for each masked  
 3377 strip in a selected time range. Offline, the user can control the noise/gamma rate and decide to  
 3378 mask the strips that are judged to be noisy or dead. This is done via the *Masking Tool* provided  
 3379 by the webDCS,

- 3380     ● `mask_Strip_Activity_Tt_Sc_p` shows noise/gamma activity per unit area for each masked  
3381       strip with respect to the average rate of active strips,
- 3382     ● `NoiseCSize_H_Tt_Sc_p` shows noise/gamma cluster size, a cluster being constructed out of  
3383       adjacent strips giving a signal at the *same time* (hits within a time window of 25 ns),
- 3384     ● `NoiseCMult_H_Tt_Sc_p` shows noise/gamma cluster multiplicity (number of reconstructed  
3385       clusters per event),
- 3386     ● `Chip_Mean_Noise_Tt_Sc_p` shows the same information than `Strip_Mean_Noise_Tt_Scp` us-  
3387       ing a different binning (1 chip corresponds to 8 strips),
- 3388     ● `Chip_Activity_Tt_Sc_p` shows the same information than `Strip_Activity_Tt_Scp` using  
3389       chip binning,
- 3390     ● `Chip_Homogeneity_Tt_Sc_p` shows the homogeneity of a given partition using chip binning,
- 3391     ● `Beam_Profile_Tt_Sc_p` shows the estimated beam profile when taking efficiency scan. This  
3392       is obtained by filtering `Time_Profile_Tt_Sc_p` to only consider the muon peak where the  
3393       noise/gamma background has been subtracted. The resulting hit profile corresponds to the  
3394       beam profile on the detector channels,
- 3395     ● `L0_Efficiency_Tt_Sc_p` shows the level 0 efficiency that was estimated **without** muon track-  
3396       ing,
- 3397     ● `MuonCSize_H_Tt_Sc_p` shows the level 0 muon cluster size that was estimated **without** muon  
3398       tracking, and
- 3399     ● `MuonCMult_H_Tt_Sc_p` shows the level 0 muon cluster multiplicity that was estimated **without**  
3400       muon tracking.

3401     In the histogram labels,  $t$  stands for the trolley number (1 or 3),  $c$  for the chamber slot label in  
3402       trolley  $t$  and  $p$  for the partition label (A, B, C or D depending on the chamber layout) as explained  
3403       in Chapter 5.4.

3404     In the context of GIF++, an extra script called by the webDCS is called to extract the histograms  
3405       from the ROOT files. The histograms are then stored in PNG and PDF formats into the correspond-  
3406       ing folder (a single folder per HV step, so per ROOT file). the goal is to then display the histograms  
3407       on the Data Quality Monitoring (DQM) page of the webDCS in order for the users to control the  
3408       quality of the data taking at the end of data taking. An example of histogram organisation is given  
3409       below:

3411



3412     *Here can put some screens from the webDCS to show the DQM and the plots available to users.*  
 3413

### 3414     **B.2.1.2 CSV files**

3415     Moreover, up to 3 CSV files can be created depending on which ones of the 3 input files were in the  
 3416     data folder:

- 3417       • `Offline-Corrupted.csv` , is used to keep track of the amount of data that was corrupted and  
 3418       removed from old data format files that don't contain any data quality flag.
- 3419       • `Offline-Current.csv` , contains the summary of the currents and voltages applied on each  
 3420       RPC HV channel.
- 3421       • `Offline-L0-EffC1.csv` , is used to write the efficiencies, cluster size and cluster multiplicity  
 3422       of efficiency runs. Note that `L0` refers here to *Level 0* and means that the results of efficiency and  
 3423       clusterization are a first approximation calculated without performing any muon tracking in

3424 between the different detectors. This offline tool provides the user with a preliminar calculation  
 3425 of the efficiency and of the muon event parameters. Another analysis software especially  
 3426 dedicated to muon tracking is called on selected data to retrieve the results of efficiency and  
 3427 muon clusterization using a tracking algorithm to discriminate noise or gamma from muons  
 3428 as muons are the only particles that pass through the full setup, leaving hits than can be used  
 3429 to reconstruct their tracks.

- 3430 • `Offline-Rate.csv`, is used to write the noise or gamma rates measured in the detector readout  
 3431 partitions.

3432 Note that these 4 CSV files are created along with their *headers* (`Offline-[...]-Header.csv`  
 3433 containing the names of each data columns) and are automatically merged together when the offline  
 3434 analysis tool is called from the webDCS, contrary to the case where the tool is runned locally from  
 3435 the terminal as the merging bash script is then not called. Thus, the resulting files, used to make  
 3436 official plots, are:

- 3437 • `Corrupted.csv`,  
 3438 • `Current.csv`,  
 3439 • `L0-EffCl.csv`.  
 3440 • `Rate.csv`.

### 3441 B.3 Analysis inputs and information handling

3442 The usage of the Offline Analysis tool as well as its output have been presented in the previous section.  
 3443 It is now important to dig further and start looking at the source code and the inputs necessary  
 3444 for the tool to work. Indeed, other than the raw ROOT data files that are analysed, more information  
 3445 needs to be imported inside of the program to perform the analysis such as the description of the  
 3446 setup inside of GIFT++ at the time of data taking (number of trolleys, of RPCs, dimensions of the  
 3447 detectors, etc...) or the mapping that links the TDC channels to the coresponding RPC channels in  
 3448 order to translate the TDC information into human readable data. 2 files are used to transmit all this  
 3449 information:  
 3450

- 3451 • `Dimensions.ini`, that provides the necessary setup and RPC information, and  
 3452 • `ChannelsMapping.csv`, that gives the link between the TDC and RPC channels as well as the  
 3453 *mask* for each channel (masked or not?).

#### 3454 B.3.1 Dimensions file and InFile parser

3455 This input file, present in every data folder, allows the analysis tool to know of the number of active  
 3456 trolleys, the number of active RPCs in those trolleys, and the details about each RPCs such as  
 3457 the number of RPC gaps, the number of pseudo-rapidity partitions (for CMS-like prototypes), the  
 3458 number of strips per partion or the dimensions. To do so, there are 3 types of groups in the INI file  
 3459 architecture. A first general group, appearing only once at the head of the document, gives information  
 3460 about the number of active trolleys as well as their IDs, as presented in Source Code B.1. For

3461 each active trolley, a group similar to Source Code B.2 can be found containing information about  
 3462 the number of active detectors in the trolley and their IDs. Each trolley group as a `Tt` name format,  
 3463 where `t` is the trolley ID. Finally, for each detector stored in slots of an active trolley, there is a group  
 3464 providing information about their names and dimensions, as shown in Source Code B.3. Each slot  
 3465 group as a `TtSs` name format, where `s` is the slot ID of trolley `t` where the active RPC is hosted.

```
3466 [General]
3467 nTrolleys=2
  TrolleysID=13
```

3468 *Source Code B.1: Example of `[General]` group as might be found in `Dimensions.ini`. In Gif++, only 2 trolleys are available to hold RPCs and place them inside of the bunker for irradiation. The IDs of the trolleys are written in a single string as "13" and then read character by character by the program.*

```
3469 [T1]
  nSlots=4
  SlotsID=1234
```

3470 *Source Code B.2: Example of trolley group as might be found in `Dimensions.ini`. In this example, the file tells that there are 4 detectors placed in the holding slots of the trolley `T1` and that their IDs, written as a single string variable, are 1, 2, 3 and 4.*

```
3471 [T1S1]
  Name=RE2-2-NPD-BARC-8
  Partitions=3
  Gaps=3
  Gap1=BOT
  Gap2=TN
  Gap3=TW
  AreaGap1=11694.25
  AreaGap2=6432
  AreaGap3=4582.82
  Strips=32
  ActiveArea-A=157.8
  ActiveArea-B=121.69
  ActiveArea-C=93.03
```

3472 *Source Code B.3: Example of slot group as might be found in `Dimensions.ini`. In this example, the file provides information about a detector named `RE2-2-NPD-BARC-8`, having 3 pseudo-rapidity readout partitions and stored in slot `S1` of trolley `T1`. This is a CMS RE2-2 type of detector. This information will then be used for example to compute the rate per unit area calculation.*

3473 This information is readout and stored in a C++ object called `IniFile`, that parses the information  
 3474 in the INI input file and stores it into a local buffer for later use. This INI parser is the exact same  
 3475 one that was previously developed for the Gif++ DAQ and described in Appendix A.5.2.

### 3476 B.3.2 TDC to RPC link file and Mapping

3477 The same way the INI dimension file information is stored using `map`, the channel mapping and mask  
 3478 information is stored and accessed through `map`. First of all, the mapping CSV file is organised into  
 3479 3 columns separated by tabulations (and not by commas, as expected for CSV files as it is easier using  
 3480 streams to read tab or space separated data using C++):

3481

3482	RPC_channel	TDC_channel	mask
------	-------------	-------------	------

3483 using as formatting for each field:

3484	TSCCC	TCCC	M
------	-------	------	---

3486 TSCCC is a 5-digit integer where  $\tau$  is the trolley ID,  $s$  the slot ID in which the RPC is held insite  
 3487 the trolley  $\tau$  and ccc is the RPC channel number, or *strip* number, that can take values up to  
 3488 3-digits depending on the detector,

3489 TCCC is a 4 digit integer where  $\tau$  is the TDC ID, ccc is the TDC channel number that can take values  
 3490 in between 0 and 127, and

3491 M is a 1-digit integer indicating if the channel should be considered ( $M = 1$ ) or discarded ( $M = 0$ )  
 3492 during analysis.

3493 This mapping and masking information is readout and stored thanks to the object `Mapping`, pre-  
 3494 sented in Source Code B.4. Similarly to `IniFile` objects, this class has private methods. The first  
 3495 one, `Mapping::CheckIfNewLine()` is used to find the newline character '`\n`' or return character  
 3496 '`\r`' (depending on which kind of operating system interacted with the file). This is used for the  
 3497 simple reason that the masking information has been introduced only during the year 2017 but the  
 3498 channel mapping files exist since 2015 and the very beginning of data taking at GIF++. This means  
 3499 that in the older data folders, before the upgrade, the channel mapping file only had 2 columns, the  
 3500 RPC channel and the TDC channel. For compatibility reasons, this method helps controling the  
 3501 character following the readout of the 2 first fields of a line. In case any end of line character is  
 3502 found, no mask information is present in the file and the default  $M = 1$  is used. On the contrary, if  
 3503 the next character was a tabulation or a space, the mask information is present.

3504 Once the 3 fields have been readout, the second private method `Mapping::CheckIfTDCCh()` is  
 3505 used to control that the TDC channel is an existing TDC channel. Finally, the information is stored  
 3506 into 3 different maps (`Link`, `ReverseLink` and `Mask`) thanks to the public method `Mapping::Read()`.  
 3507 `Link` allows to get the RPC channel by knowing the TDC channel while `ReverseLink` does the op-  
 3508 posite by returning the TDC channel by knowing the RPC channel. Finally, `Mask` returns the mask  
 3509 associated to a given RPC channel.

```

3510 typedef map<Uint,Uint> MappingData;

3511 class Mapping {
3512     private:
3513         bool          CheckIfNewLine(char next);
3514         bool          CheckIfTDCCh(Uint channel);
3515         string        FileName;
3516         MappingData  Link;
3517         MappingData  ReverseLink;
3518         MappingData  Mask;
3519         int           Error;
3520
3521     public:
3522         Mapping();
3523         Mapping(string baseName);
3524         ~Mapping();
3525
3526         void SetFileName(const string filename);
3527         int  Read();
3528         Uint GetLink(Uint tdcchannel);
3529         Uint GetReverse(Uint rpcchannel);
3530         Uint GetMask(Uint rpcchannel);
3531     };

```

3512 *Source Code B.4: Description of C++ object Mapping used as a parser for the channel mapping and mask file.*

## 3513 B.4 Description of GIF++ setup within the Offline Analysis tool

3514 In the previous section, the tool input files have been discussed. The dimension file information is  
 3515 stored in a map hosted by the `IniFile` object. But this information is then used to create a series of  
 3516 new objects that helps defining the GIF++ infrastructure directly into the Offline Analysis. Indeed,  
 3517 from the `RPC`, to the more general `Infrastructure`, every element of the GIF++ infrastrucutre is  
 3518 recreated for each data analysis based on the information provided in input. All this information  
 3519 about the infrastructure will be used to assign each hit signal to a specific strip channel of a specific  
 3520 detector, and having a specific active area. This way, rate per unit area calculation is possible.  
 3521

### 3522 B.4.1 RPC objects

3523 `RPC` objects have been developped to represent physical active detectors in GIF++ at the moment  
 3524 of data taking. Thus, there are as many `RPC` objects created during the analysis than there were  
 3525 active RPCs tested during a run. Each `RPC` hosts the information present in the corresponding INI  
 3526 slot group, as shown in B.3, and organises it using a similar architecture. This can be seen from  
 3527 Source Code B.5.

3528 To make the object more compact, the lists of gap labels, of gap active areas and strip active  
 3529 areas are stored into `vector` dynamical containers. `RPC` objects are always contructed thanks to the  
 3530 dimension file information stored into the `IniFILE` and their ID, using the format `TtSs`. Using the  
 3531 `RPC` ID, the constructor calls the methods of `IniFILE` to initialise the `RPC`. The other constructors  
 3532 are not used but exist in case of need. Finally, some getters have been written to access the different  
 3533 private parameters storing the detector information.

```

3534 class RPC{
3535     private:
3536         string          name;           //RPC name as in webDCS database
3537         Uint            nGaps;          //Number of gaps in the RPC
3538         Uint            nPartitions;    //Number of partitions in the RPC
3539         Uint            nStrips;        //Number of strips per partition
3540         vector<string> gaps;          //List of gap labels (BOT, TOP, etc...)
3541         vector<float> gapGeo;        //List of gap active areas
3542         vector<float> stripGeo;      //List of strip active areas
3543
3544     public:
3545         RPC();
3546         RPC(string ID, IniFile* geofile);
3547         RPC(const RPC& other);
3548         ~RPC();
3549         RPC& operator=(const RPC& other);
3550
3551         string GetName();
3552         Uint GetNGaps();
3553         Uint GetNPartitions();
3554         Uint GetNStrips();
3555         string GetGap(Uint g);
3556         float GetGapGeo(Uint g);
3557         float GetStripGeo(Uint p);
3558     };

```

3536 *Source Code B.5: Description of C++ objects RPC that describe each active detectors used during data taking.*

## 3537 B.4.2 Trolley objects

3538 Trolley objects have been developped to represent physical active trolleys in GIFT++ at the moment  
 3539 of data taking. Thus, there are as many trolley objects created during the analysis than there were  
 3540 active trolleys hosting tested RPCs during a run. Each Trolley hosts the information present in the  
 3541 corresponding INI trolley group, as shown in B.2, and organises it using a similar architecture. In  
 3542 addition to the information hosted in the INI file, these object have a dynamical container of RPC  
 3543 objects, representing the active detectors the active trolley was hosting at the time of data taking.  
 3544 This can been seen from Source Code B.6.

3545 Trolley objects are always contructed thanks to the dimension file information stored into the  
 3546 IniFILE and their ID, using the format Tt. Using the Trolley ID, the constructor calls the methods  
 3547 of IniFILE to initialise the Trolley. Retrieving the information of the RPC IDs via SlotsID, a new  
 3548 RPC is constructed and added to the container RPCs for each character in the ID string. The other  
 3549 constructors are not used but exist in case of need. Finally, some getters have been written to access  
 3550 the different private parameters storing the trolley and detectors information.

```

3551
class Trolley{
    private:
        Uint          nSlots; //Number of active RPCs in the considered trolley
        string        SlotsID; //Active RPC IDs written into a string
        vector<RPC*> RPCs;   //List of active RPCs

    public:
        //Constructors, destructor and operator =
        Trolley();
        Trolley(string ID, IniFile* geofile);
        Trolley(const Trolley& other);
        ~Trolley();
        Trolley& operator=(const Trolley& other);

        //Get GIFTrolley members
        Uint  GetNSlots();
        string GetSlotsID();
        Uint   GetSlotID(Uint s);

        //Manage RPC list
        RPC*  GetRPC(Uint r);
        void  DeleteRPC(Uint r);

        //Methods to get members of RPC objects stored in RPCs
        string GetName(Uint r);
        Uint   GetNGaps(Uint r);
        Uint   GetNPartitions(Uint r);
        Uint   GetNStrips(Uint r);
        string GetGap(Uint r, Uint g);
        float  GetGapGeo(Uint r, Uint g);
        float  GetStripGeo(Uint r, Uint p);
    };

```

*Source Code B.6: Description of C++ objects `Trolley` that describe each active trolley used during data taking.*

### 3554    B.4.3 Infrastructure object

3555 The `Infrastructure` object has been developped to represent the GIFT++ bunker area dedicated to  
 3556 CMS RPC experiments. With this very specific object, all the information about the CMS RPC  
 3557 setup within GIFT++ at the moment of data taking is stored. It hosts the information present in the  
 3558 corresponding INI general group, as shown in B.1, and organises it using a similar architecture. In  
 3559 addition to the information hosted in the INI file, this object have a dynamical container of `Trolley`  
 3560 objects, representing the active tolleys in GIFT++ area. This can be seen from Source Code B.7.

3561 The `Infrastructure` object is always contructed thanks to the dimension file information stored  
 3562 into the `IniFILE`. Retrieving the information of the trolley IDs via `TrolleysID`, a new `Trolley` is  
 3563 constructed and added to the container `Trolleys` for each character in the ID `string`. By extension,  
 3564 it is easy to understand that the process described in Section B.4.2 for the construction of RPCs  
 3565 takes place when a trolley is constructed. The other constructors are not used but exist in case of  
 3566 need. Finally, some getters have been written to access the different private parameters storing the  
 3567 infrastructure, tolleys and detectors information.

```

3568
class Infrastructure {
    private:
        Uint             nTrolleys;   //Number of active Trolleys in the run
        string          TrolleysID; //Active trolley IDs written into a string
        vector<Trolley*> Trolleys; //List of active Trolleys (struct)

    public:
        //Constructors and destructor
        Infrastructure();
        Infrastructure(IniFile* geofile);
        Infrastructure(const Infrastructure& other);
        ~Infrastructure();
        Infrastructure& operator=(const Infrastructure& other);

        //Get Infrastructure members
        Uint  GetNTrolleys();
        string GetTrolleysID();
        Uint  GetTrolleyID(Uint t);

3569
        //Manage Trolleys
        Trolley* GetTrolley(Uint t);
        void     DeleteTrolley(Uint t);

        //Methods to get members of GIFTrolley objects stored in Trolleys
        Uint  GetNSlots(Uint t);
        string GetSlotsID(Uint t);
        Uint  GetSlotID(Uint t, Uint s);
        RPC*  GetRPC(Uint t, Uint r);

        //Methods to get members of RPC objects stored in RPCs
        string GetName(Uint t, Uint r);
        Uint  GetNGaps(Uint t, Uint r);
        Uint  GetNPartitions(Uint t, Uint r);
        Uint  GetNStrips(Uint t, Uint r);
        string GetGap(Uint t, Uint r, Uint g);
        float  GetGapGeo(Uint t, Uint r, Uint g);
        float  GetStripGeo(Uint t, Uint r, Uint p);
    };

```

Source Code B.7: Description of C++ object *Infrastructure* that contains the full information about CMS RPC experiment in GIF++.

## 3571 B.5 Handeling of data

3572 As discussed in Appendix A.4.2, the raw data as a `TTree` architecture where every entry is related to  
 3573 a trigger signal provided by a muon or a random pulse, whether the goal of the data taking was to  
 3574 measure the performance of the detector or the noise/gamma background respectively. Each of these  
 3575 entries, referred also as events, contain a more or less full list of hits in the TDC channels to which  
 3576 the detectors are connected. To this list of hits corresponds a list of time stamps, marking the arrival  
 3577 of the hits within the TDC channel.

3578 The infrastructure of the CMS RPC experiment within GIF++ being defined, combining the  
 3579 information about the raw data with the information provided by both the mapping/mask file and the  
 3580 dimension file allows to build new physical objects that will help in computing efficiency or rates.

### 3581 B.5.1 RPC hits

3582 The raw data stored in the ROOT file as output of the GIFT++ DAQ, is readout by the analysis tool  
 3583 using the structure `RAWData` presented in Source Code B.9 that differs from the structure presented  
 3584 in Appendix A.4.2 as it is not meant to hold all of the data contained in the ROOT file. In this sense,  
 3585 this structure is in the case of the offline analysis tool not a dynamical object and will only be storing  
 3586 a single event contained in a single entry of the `TTree`.

```
3587
3588 class RPCHit {
    private:
        Uint Channel;      //RPC channel according to mapping (5 digits)
        Uint Trolley;     //0, 1 or 3 (1st digit of the RPC channel)
        Uint Station;     //Slot where is held the RPC in Trolley (2nd digit)
        Uint Strip;       //Physical RPC strip where the hit occurred (last 3
    →   digits)
        Uint Partition;   //Readout partition along eta segmentation
        float TimeStamp; //Time stamp of the arrival in TDC

    public:
        //Constructors, destructor & operator =
        RPCHit();
        RPCHit(Uint channel, float time, Infrastructure* Infra);
        RPCHit(const RPCHit& other);
        ~RPCHit();
        RPCHit& operator=(const RPCHit& other);

        //Get RPCHit members
        Uint GetChannel();
        Uint GetTrolley();
        Uint GetStation();
        Uint GetStrip();
        Uint GetPartition();
        float GetTime();
    };

    typedef vector<RPCHit> HitList;
    typedef struct GIFHitList { HitList rpc[NTROLLEYS][NSLOTS][NPARTITIONS]; } → GIFHitList;

    bool SortHitbyStrip(RPCHit h1, RPCHit h2);
    bool SortHitbyTime(RPCHit h1, RPCHit h2);
}
```

3589 *Source Code B.8: Description of C++ object RPCHit.*

```
3590
3591 struct RAWData{
    int          iEvent;    //Event i
    int          TDCNHits; //Number of hits in event i
    int          QFlag;    //Quality flag list (1 flag digit per TDC)
    vector<Uint> *TDCCh;   //List of channels giving hits per event
    vector<float> *TDCTS;   //List of the corresponding time stamps
};
```

3591 *Source Code B.9: Description of C++ structure RAWData.*

3592 Each member of the structure is then linked to the corresponding branch of the ROOT data tree,  
 3593 as shown in the example of Source Code B.10, and using the method `GetEntry(int i)` of the ROOT  
 3594 class `TTree` will update the state of the members of `RAWData`.

```

3595     TTree* dataTree = (TTree*)dataFile.Get("RAWData");
3596     RAWData data;
3597
3598     dataTree->SetBranchAddress("EventNumber", &data.iEvent);
3599     dataTree->SetBranchAddress("number_of_hits", &data.TDCNHits);
3600     dataTree->SetBranchAddress("Quality_flag", &data.QFlag);
3601     dataTree->SetBranchAddress("TDC_channel", &data.TDCCh);
3602     dataTree->SetBranchAddress("TDC_TimeStamp", &data.TDCTS);

```

3597       *Source Code B.10: Example of link in between RAWData and TTree.*

3598       The data is then analysed entry by entry and to each element of the TDC channel list, a `RPCHit` is  
 3599       constructed by linking each TDC channel to the corresponding RPC channel thanks to the `Mapping`  
 3600       object. The information carried by the RPC channel format allows to easily retrieve the trolley and  
 3601       slot from which the hit was recorded (see section B.3.2). Using these 2 values, the readout partition  
 3602       can be found by knowing the strip channel and comparing it with the number of partitions and strips  
 3603       per partition stored into the `Infrastructure` object.

3604       Thus `RPCHit` objects are then stored into 3D dynamical list called `GIFHitList` (Source Code B.9)  
 3605       where the 3 dimensions refer to the 3 layers of the readout in `GIF++` : in the bunker there are *trolleys*  
 3606       ( $\tau$ ) holding detectors in *slots* ( $s$ ) and each detector readout is divided into 1 or more pseudo-rapidity  
 3607       *partitions* ( $p$ ). Using these 3 information allows to assign an address to each readout partition and  
 3608       this address will point to a specific hit list.

3609

## 3610      B.5.2 Clusters of hits

3611      All the hits contained in the ROOT file have been sorted into the different hit lists through the  
 3612      `GIFHitList`. At this point, it is possible to start looking for clusters. A cluster is a group of adjacent  
 3613      strips getting hits within a time window of 25 ns. These strips are then assumed to be part of the same  
 3614      physical avalanche signal generated by a muon passing through the chamber or by the interaction of  
 3615      a gamma stopping into the electrodes of the RPCs.

3616      To keep the cluster information, `RPCCluster` objects have been defined as shown in Source  
 3617      Code B.11. Using the information of each individual `RPCHit` taken out of the hit list, it stores  
 3618      the cluster size (number of adjacent strips composing the cluster), the first and last hit, the center for  
 3619      spatial reconstruction and finally the start and stop time stamps as well as te time spread in between  
 3620      the first and last hit.

```

3621
class RPCCluster{
    private:
        Uint ClusterSize; //Size of cluster #ID
        Uint FirstStrip; //First strip of cluster #ID
        Uint LastStrip; //Last strip of cluster #ID
        float Center; //Center of cluster #ID ((first+last)/2)
        float StartStamp; //Time stamp of the earliest hit of cluster #ID
        float StopStamp; //Time stamp of the latest hit of cluster #ID
        float TimeSpread; //Time difference between earliest and latest hits
                           //of cluster #ID
    public:
        //Constructors, destructor & operator =
        RPCCluster();
        RPCCluster(HitList List, Uint cID, Uint cSize, Uint first, Uint firstID);
        RPCCluster(const RPCCluster& other);
        ~RPCCluster();
        RPCCluster& operator=(const RPCCluster& other);

        //Get Cluster members
        Uint GetID();
        Uint GetSize();
        Uint GetFirstStrip();
        Uint GetLastStrip();
        float GetCenter();
        float GetStart();
        float GetStop();
        float GetSpread();
    };

    typedef vector<RPCCluster> ClusterList;

    //Other functions to build cluster lists out of hit lists
    void BuildClusters(HitList &cluster, ClusterList &clusterList);
    void Clusterization(HitList &hits, TH1 *hcSize, TH1 *hcMult);
}

```

3623                   *Source Code B.11: Description of C++ object Cluster.*

3624       To investigate the hit list of a given detector partition, the function `Clusterization()` defined  
 3625       in `include/Cluster.h` needs the hits in the list to be time sorted. This is achieved by calling func-  
 3626       tion `sort()` of library `<algorithm>` using the comparator `SortHitbyTime(RPCHit h1, RPCHit h2)`  
 3627       defined in `include/RPCHit.h` that returns `true` if the time stamp of hit `h1` is lower than that of `h2`.  
 3628       A first isolation of strips is made only based on time information. All the hits within the 25 ns win-  
 3629       dow are taken separately from the rest. Then, this sub-list of hits is sorted this time by ascending  
 3630       strip number, using this time the comparator `SortHitbyStrip(RPCHit h1, RPCHit h2)`. Finally, the  
 3631       groups of adjacent strips are used to construct `RPCCluster` objects that are then stored in a temporary  
 3632       list of clusters that is at the end of the process used to know how many clusters were reconstructed  
 3633       and to fill their sizes into an histogram that will allows to know the mean size of muon or gamma  
 3634       clusters.

3635

## 3636       **B.6 DAQ data Analysis**

3637       All the ingredients to analyse GIF++ data have been defined. This section will focus on the different  
 3638       part of the analysis performed on the data, from determining the type of data the tool is dealing with

3639 to calculating the rate in each detector or reconstructing muon or gamma clusters.

### 3640 B.6.1 Determination of the run type

3641 In GIF++, both the performance of the detectors in detecting muons in an irradiated environment and  
 3642 the gamma background can be independantly measured. These corresponds to different run types  
 3643 and thus, to different TDC settings giving different data to look at.

3644  
 3645 In the case of performance measurements, the trigger for data taking is provided by the coïncidence  
 3646 of several scintillators when muons from the beam passing through the area are detected. Data  
 3647 is collected in a 600 ns wide window around the arrival of muons in the RPCs. The expected time  
 3648 distribution of hits is shown in Figure B.1a. The muon peak is clearly visible in the center of the  
 3649 distribution and is to be extracted from the gamma background that composes the flat part of the  
 3650 distribution.

3651 On the other hand, gamma background or noise measurements are focussed on the non muon  
 3652 related physics and the trigger needs to be independant from the muons to give a good measurement  
 3653 of the gamma/noise distribution as seen by the detectors. The trigger is then provided by a pulse  
 3654 generator at a frequency of 300 Hz whose pulse is not likely to be on time with a muon. In order  
 3655 to increase the integrated time without increasing the acquisition time too much, the width of the  
 3656 acquisition windows are increased to 10  $\mu$ s. The time distribution of the hits is expected to be flat, as  
 3657 shown by Figure B.1b.

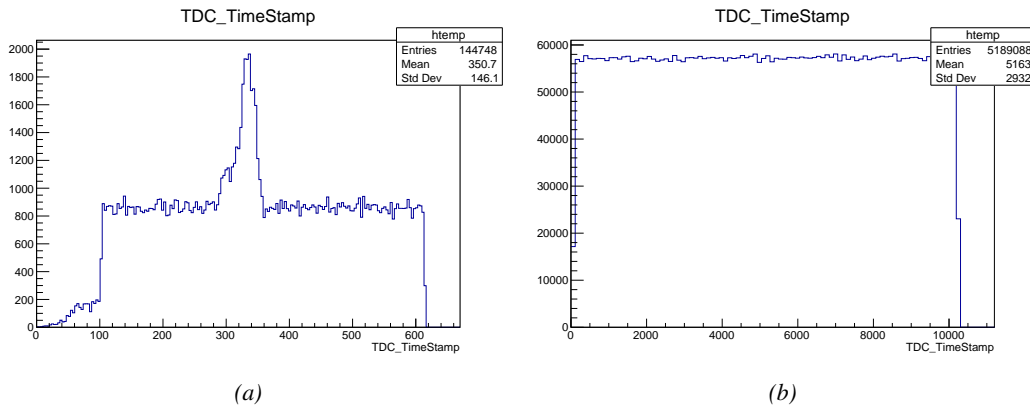


Figure B.1: Example of expected hit time distributions in the cases of efficiency (Figure B.1a) and noise/gamma rate per unit area (Figure B.1b) measurements as extracted from the raw ROOT files. The unit along the x-axis corresponds to ns. The fact that "the" muon peak is not well defined in Figure B.1a is due to the contribution of all the RPCs being tested at the same time that don't necessarily have the same signal arrival time. Each individual peak can have an offset with the ones of other detectors. The inconsistency in the first 100 ns of both time distributions is an artefact of the TDCs and are systematically rejected during the analysis.

3658 The ROOT files include a TTree called RunParameters containing, among other things, the in-  
 3659 formation related to the type of run. The run type can then be accessed as described by Source  
 3660 Code B.12 and the function IsEfficiencyRun() is then used to determine if the run file is an effi-  
 3661 ciency run or, on the contrary, another type of run (noise or gamma measurement).

```

3662     TTree* RunParameters = (TTree*)dataFile.Get("RunParameters");
3663     TString* RunType = new TString();
3664     RunParameters->SetBranchAddress("RunType", &RunType);
3665     RunParameters->GetEntry(0);

```

3664       *Source Code B.12: Access to the run type contained in TTree\* RunParameters.*

3665       Finally, the data files will have a slightly different content whether it was collected before or after  
 3666       October 2017 and the upgrade of the DAQ software that brought a new information into the ROOT  
 3667       output. This is discussed in Appendix A.4.3 and implies that the analysis will differ a little depending  
 3668       on the data format. Indeed, as no information on the data quality is stored, in older data files, the cor-  
 3669       rections for missing events has to be done at the end of the analysis. The information about the type  
 3670       of data format is stored in the variable **bool** `isNewFormat` by checking the list of branches contained  
 3671       in the data tree via the methods `TTree::GetListOfBranches()` and `TCollection::Contains()`.

## 3672       **B.6.2 Beam time window calculation for efficiency runs**

3673       Knowing the run type is important first of all to know the width of the acquisition window to be used  
 3674       for the rate calculation and finally to be able to seek for muons. Indeed, the peak that appears in the  
 3675       time distribution for each detectors is then fitted to extract the most probable time window in which  
 3676       the tool should look for muon hits. The data outside of this time window is then used to evaluate the  
 3677       noise or gamma background the detector was subjected to during the data taking. Computing the  
 3678       position of the peak is done calling the function `SetBeamWindow()` defined in file `src/RPCHit.cc` that  
 3679       loops a first time on the data. The data is first sorted in a 3D array of 1D histograms (`GIFH1Array`, see  
 3680       include/types.h). Then the location of the highest bin is determined using `TH1::GetMaximumBin()`  
 3681       and is used to define a window in which a gaussian fit will be applied to compute the peak width.  
 3682       This window is a 80 ns defined by Formula B.1 around the central bin.

$$t_{center}(ns) = bin \times width_{bin}(ns) \quad (\text{B.1a})$$

$$[t_{low}; t_{high}] = [t_{center} - 40; t_{center} + 40] \quad (\text{B.1b})$$

3683       Before the fit is performed, the average number of noise/gamma hits per bin is evaluated using  
 3684       the data outside of the fit window. Excluding the first 100 ns, the average number of hits per bin  
 3685       due to the noise or gamma is defined by Formula B.2 after extracting the amount of hits in the time  
 3686       windows  $[100; t_{low}]$  and  $[t_{high}; 600]$  thanks to the method `TH1::Integral()`. This average number  
 3687       of hits is then subtracted to every bin of the 1D histogram, in order to *clean* it from the noise or  
 3688       gamma contribution as much as possible to improve the fit quality. Bins where  $\langle n_{hits} \rangle$  is greater  
 3689       than the actual bin content are set to 0.

$$\Delta t_{noise}(ns) = 600 \overbrace{-t_{high} + t_{low}}^{-80ns} - 100 = 420ns \quad (\text{B.2a})$$

$$\langle n_{hits} \rangle = width_{bin}(ns) \times \frac{\sum_{t=100}^{t_{low}} + \sum_{t=t_{high}}^{600}}{\Delta t_{noise}(ns)} \quad (\text{B.2b})$$

3690       Finally, the fit parameters are extracted and saved for each detector in 3D arrays of **float**  
 3691       (`muonPeak`, see include/types.h), a first one for the mean arrival time of the muons, `PeakTime`,

3692 and a second one for the width of the peak, `PeakWidth`. The width is defined as  $6\sigma$  of the gaussian  
 3693 fit. The same settings are applied to every partitions of the same detector. To determine which one  
 3694 of the detector's partitions is directly illuminated by the beam, the peak height of each partition is  
 3695 compared and the highest one is then used to define the peak settings.

### 3696 **B.6.3 Data loop and histogram filling**

3697 3D arrays of histogram are created to store the data and display it on the DQM of G4F++ webDCS  
 3698 for the use of shifters. These histograms, presented in section B.2.1.1, are filled while looping on  
 3699 the data. Before starting the analysis loop, it is necessary to control the entry quality for the new  
 3700 file formats featuring `QFlag`. If the `QFlag` value for this entry shows that 1 TDC or more have a  
 3701 `CORRUPTED` flag, then this event is discarded. The loss of statistics is low enough to be neglected.  
 3702 `QFlag` is controlled using the function `IsCorruptedEvent()` defined in `src/utils.cc`. As explained  
 3703 in Appendix A.4.3, each digit of this integer represents a TDC flag that can be 1 or 2. Each 2 is  
 3704 the sign of a `CORRUPTED` state. Then, the data is accessed entry by entry in the ROOT `TTree` using  
 3705 `RAWData` and each hit in the hit list is assigned to a detector channel and saved in the corresponding  
 3706 histograms. In the first part of the analysis, in which the loop over the ROOT file's content is  
 3707 performed, the different steps are:

3708 **1- RPC channel assignment and control:** a check is done on the RPC channel extracted thanks  
 3709 to the mapping via the method `Mapping::GetLink()`. If the channel is not initialised and is 0, or if  
 3710 the TDC channel was greater than 5127, the hit is discarded. This means there was a problem in the  
 3711 mapping. Often a mapping problem leads to the crash of the offline tool.

3712 **2- Creation of a `RPCHit` object:** to easily get the trolley, slot and partition in which the hit has  
 3713 been assigned, this object is particularly helpful.

3714 **3- General histograms are filled:** the hit is filled into the time distribution and the general hit  
 3715 distribution histograms, and if the arrival time is within the first 100 ns, it is discarded and nothing  
 3716 else happens and the loop proceeds with the next hit in the list.

3717 **4- Multiplicity counter:** the hit multiplicity counter of the corresponding detectors incremented.

3718 **5-a- Efficiency runs - Is the hit within the peak window? :** if the peak is contained in the peak  
 3719 window previously defined in section B.6.2, the hit is filled into the beam hit profile histogram of  
 3720 the corresponding chamber, added into the list of muon hits and increments the counter of *in time*  
 3721 hits. The term *in time* here refers to the hits that are likely to be muons by arriving in the expected  
 3722 time window. If the hit is outside of the peak window, it is filled into the noise profile histogram  
 3723 of the corresponding detector, added into the list of noise/gamma hits and increments the counter of  
 3724 noise/gamma hits.

3725 **5-b- Noise/gamma rate runs - Noise histograms are filled:** the hit is filled into the noise profile  
 3726 histogram of the corresponding detector, added into the list of noise/gamma hits and increments the  
 3727 counter of noise/gamma hits.

3728

3729 After the loop on the hit list of the entry is over, the next step is to clusterize the 3D lists filled  
 3730 in the previous steps. A 3D loop is then started over the active trolley, slot and RPC partitions to  
 3731 access these objects. Each `NoiseHitList` and `MuonHitList`, in case of efficiency run, are clusterized  
 3732 as described in section B.5.2. There corresponding cluster size and multiplicity histograms are filled  
 3733 at the end of the clustering process. Then, the efficiency histogram is filled in case of efficiency run.  
 3734 The selection is simply made by checking whether the RPC detected signals in the peak window  
 3735 during this event. Nevertheless, it is useful to highlight that at this level, it is not possible yet to  
 3736 discriminate in between a muon hit and noise or gamma hit. Thus, `MuonCSize_H`, `MuonCMult_H`  
 3737 and `Efficiency0_H` are subjected to noise and gamma contamination. This contamination will be  
 3738 estimated and corrected at the moment the results will be written into output CSV files. Finally, the  
 3739 loop ends on the filling of the general hit multiplicity histogram.

#### 3740 **B.6.4 Results calculation**

3741 As mentioned in section B.2.1, the analysis of DAQ data provides the user with 3 CSV files and  
 3742 a ROOT file associated to each and every ROOT data file. The fourth CSV file is provided by the  
 3743 extraction of the CEAN main frame data monitored during data taking and will be discussed later.  
 3744 After looping on the data in the previous part of the analysis macro, the output files are created and a  
 3745 3D loop on each RPC readout partitions is started to extract the histograms parameters and compute  
 3746 the final results.

3747

##### 3748 **B.6.4.1 Rate normalisation**

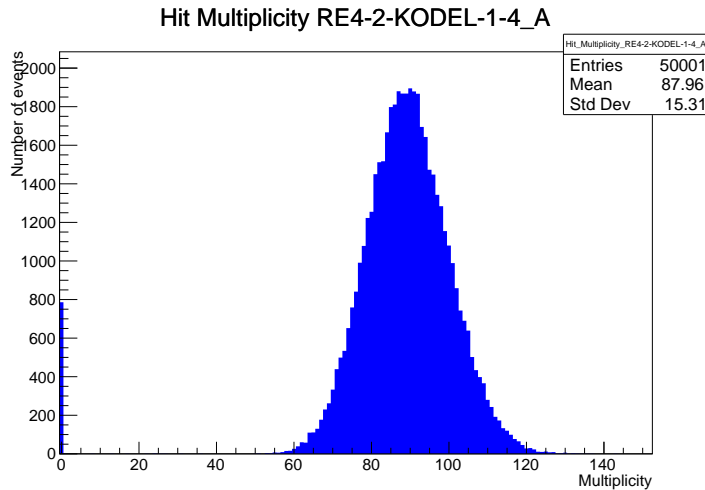


Figure B.2: The effect of the quality flag is explained by presenting the reconstructed hit multiplicity of a data file without `Quality_flag`. The artificial high content of bin 0 is the effect of corrupted data.

3749 To analyse old data format files, not containing any quality flag, it is needed to estimate the amount  
 3750 of corrupted data via a fit as the corrupted data will always fill events with a fake "0 multiplicity".  
 3751 Indeed, as no hits were stored in the DAQ ROOT files, these events artificially contribute to fill  
 3752 the bin corresponding to a null multiplicity, as shown in Figure B.2. In the case the mean of the

3753 hit multiplicity distribution is high, the contribution of the corrupted data can easily be evaluated  
 3754 for later correction by comparing the level of the bin at multiplicity 0 and of a skew fit curve that  
 3755 should indicate a value consistent with 0. A skew fit has been chosen over a Poisson fit as it was  
 3756 giving better results for lower mean multiplicity values. Nevertheless, for low irradiation cases,  
 3757 as explained in Appendix A.4.3, the hit multiplicity distribution mean is, on the contrary, rather  
 3758 small and the probability to record events without hits can't be considered small anymore, leading  
 3759 to a difficult and non-reliable estimation of the corruption. As can be seen in Source Code B.13,  
 3760 conditions have been applied to prevent bad fits and wrong corruption estimation in cases where :

- 3761 • The difference in between the data for multiplicity 1 and the corresponding fit value should be  
 3762 lower than 1% of the total amount of data :  $\frac{|n_{m=1} - sk(1)|}{N_{tot}} < 0.01$  where  $n_{m=1}$  is the number  
 3763 of entries with multiplicity 1,  $sk(1)$  the value of the skew fit, as defined by Formula 5.3, for  
 3764 multiplicity 1 and  $N_{tot}$  the total number of entries.
- 3765 • The amount of data contained in the multiplicity 0 bin should not exceed 40% :  $\frac{n_{m=0}}{N_{tot}} \leq 0.4$   
 3766 where  $n_{m=0}$  is the number of entries with multiplicity 0. This number has been determined  
 3767 to be the maximum to be able to separate the excess of data due to corruption from the hit  
 3768 multiplicity distribution.

3769 Those 2 conditions need to be fulfilled to estimate the corruption of old data format files. If the  
 3770 fit was successful, the level of corruption is written in `Offline-Corrupted.csv` and the number of  
 3771 corrupted entries, refered as the integer `nEmptyEvent`, is subtracted from the total number of entries  
 3772 when the rate normalisation factor is computed as explicit in Source Code B.13. Note that for new  
 3773 data format files, the number of corrupted entries being set to 0, the definition of `rate_norm` stays  
 3774 valid.

```

3775   if(!isNewFormat){
      TF1* GaussFit = new TF1("gaussfit","[0]*exp(-0.5*((x-[1])/[2])**2)",0,Xmax);
      GaussFit->SetParameter(0,100);
      GaussFit->SetParameter(1,10);
      GaussFit->SetParameter(2,1);
      HitMultiplicity_H.rpc[T][S][p]->Fit(GaussFit,"LIQR","");
      HitMultiplicity_H.rpc[T][S][p]->Fit(GaussFit,"LIQR","");
      TF1* SkewFit = new TF1("skewfit","[0]*exp(-0.5*((x-[1])/[2])**2) / (1 +
→      exp(-[3]*(x-[4])))",0,Xmax);
      SkewFit->SetParameter(0,GaussFit->GetParameter(0));
      SkewFit->SetParameter(1,GaussFit->GetParameter(1));
      SkewFit->SetParameter(2,GaussFit->GetParameter(2));
      SkewFit->SetParameter(3,1);
      SkewFit->SetParameter(4,1);
      HitMultiplicity_H.rpc[T][S][p]->Fit(SkewFit,"LIQR","");
      HitMultiplicity_H.rpc[T][S][p]->Fit(SkewFit,"LIQR","");
      double fitValue = SkewFit->Eval(1,0,0,0);
      double dataValue = (double)HitMultiplicity_H.rpc[T][S][p]->GetBinContent(2);
      double difference = TMath::Abs(dataValue - fitValue);
      double fitTOdataVSentries_ratio = difference / (double)nEntries;
      bool isFitGOOD = fitTOdataVSentries_ratio < 0.01;

3776      double nSinglehit = (double)HitMultiplicity_H.rpc[T][S][p]->GetBinContent(1);
      double lowMultRatio = nSinglehit / (double)nEntries;
      bool isMultLOW = lowMultRatio > 0.4;

      if(isFitGOOD && !isMultLOW){
          nEmptyEvent = HitMultiplicity_H.rpc[T][S][p]->GetBinContent(1);
          nPhysics = (int)SkewFit->Eval(0,0,0,0);
          if(nPhysics < nEmptyEvent)
              nEmptyEvent = nEmptyEvent-nPhysics;
      }
}

double corrupt_ratio = 100.*(double)nEmptyEvent / (double)nEntries;
outputCorrCSV << corrupt_ratio << '\t';

float rate_norm = 0.;
float stripArea = GIFIInfra->GetStripGeo(tr,sl,p);

if(IsEfficiencyRun(RunType)){
    float noiseWindow = BMTDCWINDOW - TIMEREJECT - 2*PeakWidth.rpc[T][S][p];
    rate_norm = (nEntries-nEmptyEvent)*noiseWindow*1e-9*stripArea;
} else
    rate_norm = (nEntries-nEmptyEvent)*RDMNOISEWDW*1e-9*stripArea;

```

*Source Code B.13: Definition of the rate normalisation variable. It takes into account the number of non corrupted entries and the time window used for noise calculation, to estimate the total integrated time, and the strip active area to express the result as rate per unit area.*

#### 3778 B.6.4.2 Rate and activity

3779 At this point, the strip rate histograms, StripNoiseProfile\_H.rpc[T][S][p], only contain an in-  
 3780 formation about the total number of noise or rate hits each channel received during the data taking.  
 3781 As described in Source Code B.14, a loop on the strip channels will be used to normalise the content  
 3782 of the rate distribution histogram for each detector partitions. The initial number of hits recorded for  
 3783 a given bin will be extracted and 2 values will be computed:

- 3784     ● the strip rate, defined as the number of hits recorded in the bin normalised like described in  
 3785       the previous section, using the variable `rate_norm`, and

- 3786     ● the strip activity, defined as the number of hits recorded in the bin normalised to the average  
 3787       number of hits per bin contained in the partition histogram, using the variable `averageNhit`.  
 3788       This value provides an information on the homogeneity of the detector response to the gamma  
 3789       background or of the detector noise. An activity of 1 corresponds to an average response.  
 3790       Above 1, the channel is more active than the average and bellow 1, the channel is less active.

```

int nNoise = StripNoiseProfile_H.rpc[T][S][p]->GetEntries();
float averageNhit = (nNoise>0) ? (float)(nNoise/nStripsPart) : 1.;

for(Uint st = 1; st <= nStripsPart; st++) {
    float stripRate =
        StripNoiseProfile_H.rpc[T][S][p]->GetBinContent(st)/rate_norm;
    float stripAct =
        StripNoiseProfile_H.rpc[T][S][p]->GetBinContent(st)/averageNhit;

    StripNoiseProfile_H.rpc[T][S][p]->SetBinContent(st,stripRate);
    StripActivity_H.rpc[T][S][p]->SetBinContent(st,stripAct);
}

```

3792     *Source Code B.14: Description of the loop that allows to set the content of each strip rate and strip activity  
 channel for each detector partition.*

3793     On each detector partitions, which are readout by a single FEE, all the channels are not processed  
 3794       by the same chip. Each chip can give a different noise response and thus, histograms using a chip  
 3795       binning are used to investigate chip related noise behaviours. The average values of the strip rate  
 3796       or activity grouped into a given chip are extracted using the using the function `GetChipBin()` and  
 3797       stored in dedicated histograms as described in Source Codes B.15 and B.16 respectively.

```

float GetChipBin(TH1* H, Uint chip){
    Uint start = 1 + chip*NSTRIPSCHIP;
    int nActive = NSTRIPSCHIP;
    float mean = 0.;

    for(Uint b = start; b <= (chip+1)*NSTRIPSCHIP; b++) {
        float value = H->GetBinContent(b);
        mean += value;
        if(value == 0.) nActive--;
    }

    if(nActive != 0) mean /= (float)nActive;
    else mean = 0.;

    return mean;
}

```

3800     *Source Code B.15: Function used to compute the content of a bin for an histogram using chip binning.*

```

3801   for(UInt ch = 0; ch < (nStripsPart/NSTRIPSCHIP); ch++) {
3802     ChipMeanNoiseProf_H.rpc[T][S][p]->
3803       SetBinContent(ch+1,GetChipBin(StripNoiseProfile_H.rpc[T][S][p],ch));
3804     ChipActivity_H.rpc[T][S][p]->
3805       SetBinContent(ch+1,GetChipBin(StripActivity_H.rpc[T][S][p],ch));
3806   }

```

*Source Code B.16: Description of the loop that allows to set the content of each chip rate and chip activity bins for each detector partition knowing the information contained in the corresponding strip distribution histograms.*

The activity variable is used to evaluate the homogeneity of the detector response to background or of the detector noise. The homogeneity  $h_p$  of each detector partition can be evaluated using the formula  $h_p = \exp(-\sigma_p^R / \langle R \rangle_p)$ , where  $\langle R \rangle_p$  is the partition mean rate and  $\sigma_p^R$  is the rate standard deviation calculated over the partition channels. The more homogeneously the rates are distributed and the smaller will  $\sigma_p^R$  be, and the closer to 1 will  $h_p$  get. On the contrary, if the standard deviation of the channel's rates is large,  $h_p$  will rapidly get to 0. This value is saved into histograms as shown in Source Code B.17 and could in the future be used to monitor through time, once extracted, the evolution of every partition homogeneity. This could be of great help to understand the apparition of eventual hot spots due to ageing of the chambers subjected to high radiation levels. The monitored homogeneity information could then be combined with a monitoring of the activity of each individual channel in order to have a finer information. Monitoring tools have been suggested and need to be developed for this purpose.

```

3815   float MeanPartSDev = GetTH1StdDev(StripNoiseProfile_H.rpc[T][S][p]);
3816   float strip_homog = (MeanPartRate==0)
3817     ? 0.
3818     : exp(-MeanPartSDev/MeanPartRate);
3819   StripHomogeneity_H.rpc[T][S][p]->Fill("exp -#left(#frac{\#sigma_{Strip}
3820     \rightarrow Rate}{\#mu_{Strip Rate}}\#right)",strip_homog);
3821   StripHomogeneity_H.rpc[T][S][p]->GetYaxis()->SetRangeUser(0.,1.);

3822   float ChipStDevMean = GetTH1StdDev(ChipMeanNoiseProf_H.rpc[T][S][p]);
3823   float chip_homog = (MeanPartRate==0)
3824     ? 0.
3825     : exp(-ChipStDevMean/MeanPartRate);
3826   ChipHomogeneity_H.rpc[T][S][p]->Fill("exp -#left(#frac{\#sigma_{Chip}
3827     \rightarrow Rate}{\#mu_{Chip Rate}}\#right)",chip_homog);
3828   ChipHomogeneity_H.rpc[T][S][p]->GetYaxis()->SetRangeUser(0.,1.);

```

*Source Code B.17: Storage of the homogeneity into dedicated histograms.*

### 3818 B.6.4.3 Strip masking tool

The offline tool is automatically called at the end of each data taking to analyse the data and offer the shifter DQM histograms to control the data quality. After the histograms have been published online in the DQM page, the shifter can decide to mask noisy or dead channels that will contribute to bias the final rate calculation by editing the mask column of `ChannelsMapping.csv` as can be seen in Figure B.3.

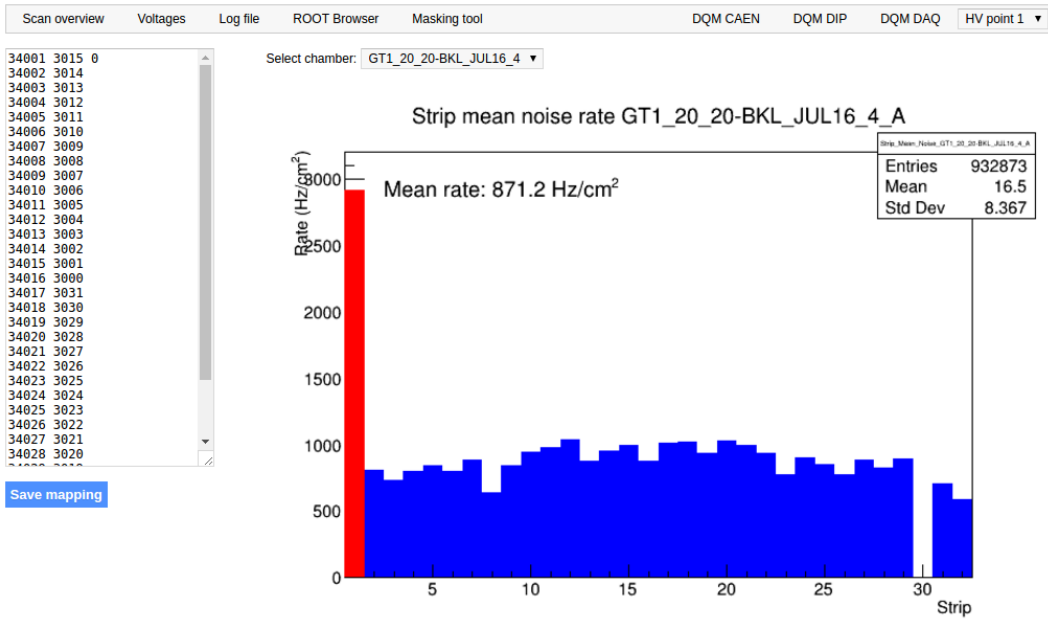


*Figure B.3: Display of the masking tool page on the webDCS. The window on the left allows the shifter to edit ChannelsMapping.csv. To mask a channel, it only is needed to set the 3rd field corresponding to the strip to mask to 0. It is not necessary for older mapping file formats to add a 1 for each strip that is not masked as the code is versatile and the default behaviour is to consider missing mask fields as active strips. The effect of the mask is directly visible for noisy channels as the corresponding bin turns red. The global effect of masking strips will be an update of the rate value showed on the histogram that will take into consideration the rejected channels.*

3824 From the code point of view, the function `GetTH1Mean()` is used to retrieve the mean rate par-  
 3825 tition by partition after the rates have been calculated strip by strip and filled into the histograms  
 3826 `StripNoiseProfile_H.rpc[T][S][p]`, as described through Source Code B.18.

3827 Once the mask for each rejected channel has been updated, the shifter can manually run the of-  
 3828 fline tool again to update the DQM plots, now including the masked strips, as well the rate results  
 3829 written in the output CSV file `Offline-Rate.csv`. If not done during the shifts, the strip masking  
 3830 procedure needs to be carefully done by the person in charge of data analysis on the scans that were  
 3831 selected to produce the final results.

```

3832   float GetTH1Mean(TH1* H) {
3833     int nBins = H->GetNbinsX();
3834     int nActive = nBins;
3835     float mean = 0.;

      for(int b = 1; b <= nBins; b++) {
        float value = H->GetBinContent(b);
        mean += value;
        if(value == 0.) nActive--;
      }

      if(nActive != 0) mean /= (float)nActive;
      else mean = 0.;

      return mean;
    }

```

*Source Code B.18: The function `GetTH1Mean()` is used to return the mean along the y-axis of `TH1` histograms containing rate information. In order to take into account masked strips whose rate is set to 0, the function looks for masked channels and decrement the number of active channels for each null value found.*

#### 3835    B.6.4.4 Output CSV files filling

3836 All the histograms have been filled. Parameters will then be extracted from them to compute the  
 3837 final results that will later be used to produce plots. Once the results have been computed, the very  
 3838 last step of the offline macro is to write these values into the corresponding CSV outputs. Aside of  
 3839 the file `Offline-Corrupted.csv`, 2 CSV files are being written by the macro `offlineAnalysis()`,  
 3840 `Offline-Rates.csv` and `Offline-L0-EffCl.csv` that respectively contain information about noise  
 3841 or gamma rates, cluster size and multiplicity, and about level 0 reconstruction of the detector effi-  
 3842 ciency, muon cluster size and multiplicity. Details on the computation and file writing are respec-  
 3843 tively given in Sources Codes B.19 and B.20.

3844 **Noise/gamma background variables** are computed and written in the output file for each detector  
 3845 partitions. A detector average of the hit and cluster rate is also provided, as shown through Sources  
 3846 Code B.19. The variables that are written for each partition are:

- 3847    • The mean partition hit rate per unit area, `MeanPartRate`, that is extracted from the histogram  
     `StripNoiseProfile_H` as the mean value along the y-axis, as described in section B.6.4.3. No  
     error is recorded for the hit rate as this is considered a single measurement. No statistical error  
     can be associated to it and the systematics are unknown.
- 3851    • The mean cluster size, `cSizePart`, is extracted from the histogram `NoiseCSize_H` and it's  
     statistical error, `cSizePartErr`, is taken to be  $2\sigma$  of the total distribution.
- 3853    • The mean cluster multiplicity per trigger, `cMultPart`, is extracted from the histogram `NoiseCMult_H`  
     and it's statistical error, `cMultPartErr`, is taken to be  $2\sigma$  of the total distribution. It is impor-  
     tant to point to the fact that this variable gives an information that is dependent on the buffer  
     window width used for each trigger for the calculation.
- 3855    • The mean cluster rate per unit area, `ClustPartRate`, is defined as the mean hit rate normalised

3858 to the mean cluster size and it's statistical error, `ClustPartRateErr`, is then obtained using the  
 3859 relative statistical error on the mean cluster size.

```

for (UInt tr = 0; tr < GIFInfra->GetNTrolleys(); tr++) {
  UInt T = GIFInfra->GetTrolleyID(tr);

  for (UInt sl = 0; sl < GIFInfra->GetNSlots(tr); sl++) {
    UInt S = GIFInfra->GetSlotID(tr,sl) - 1;

    float MeanNoiseRate = 0.;
    float ClusterRate = 0.;
    float ClusterSDev = 0.;

    for (UInt p = 0; p < GIFInfra->GetNPartitions(tr,sl); p++) {
      float MeanPartRate = GetTH1Mean(StripNoiseProfile_H.rpc[T][S][p]);
      float cSizePart = NoiseCSIZE_H.rpc[T][S][p]->GetMean();
      float cSizePartErr = (NoiseCSIZE_H.rpc[T][S][p]->GetEntries()==0)
        ? 0.
        : 2*NoiseCSIZE_H.rpc[T][S][p]->GetStdDev() /
          sqrt(NoiseCSIZE_H.rpc[T][S][p]->GetEntries());
      float cMultPart = NoiseCMult_H.rpc[T][S][p]->GetMean();
      float cMultPartErr = (NoiseCMult_H.rpc[T][S][p]->GetEntries()==0)
        ? 0.
        : 2*NoiseCMult_H.rpc[T][S][p]->GetStdDev() /
          sqrt(NoiseCMult_H.rpc[T][S][p]->GetEntries());
      float ClustPartRate = (cSizePart==0) ? 0.
        : MeanPartRate/cSizePart;
      float ClustPartRateErr = (cSizePart==0) ? 0.
        : ClustPartRate * cSizePartErr/cSizePart;

      outputRateCSV << MeanPartRate << '\t'
        << cSizePart << '\t' << cSizePartErr << '\t'
        << cMultPart << '\t' << cMultPartErr << '\t'
        << ClustPartRate << '\t' << ClustPartRateErr << '\t';

      RPCarea += stripArea * nStripsPart;
      MeanNoiseRate += MeanPartRate * stripArea * nStripsPart;
      ClusterRate += ClustPartRate * stripArea * nStripsPart;
      ClusterSDev += (cSizePart==0)
        ? 0.
        : ClusterRate*cSizePartErr/cSizePart;
    }

    MeanNoiseRate /= RPCarea;
    ClusterRate /= RPCarea;
    ClusterSDev /= RPCarea;

    outputRateCSV << MeanNoiseRate << '\t'
      << ClusterRate << '\t' << ClusterSDev << '\t';
  }
}

```

3861 *Source Code B.19: Description of rate result calculation and writing into the CSV output Offline-Rate.csv. Are saved into the file for each detector, the mean partition rate, cluster size and cluster mutiplicity, along with their errors, for each partition and as well as a detector average.*

3862 **Muon performance variables** are computed and written in the output file for each detector parti-  
 3863 tions as shown through Sources Code B.20. The variables that are written for each partition are:

- 3864     ● The muon efficiency, `eff`, extracted from the histogram `Efficiency0_H`. It is reminded that  
3865       this offline tool doesn't include any tracking algorithm to identify muons from the beam and  
3866       only relies on the hits arriving in the time window corresponding to the beam time. The con-  
3867       tent of the efficiency histogram is thus biased by the noise/gamma background contribution  
3868       into this window and is thus corrected by estimating the muon data content in the peak re-  
3869       gion knowing the noise/gamma content in the rate calculation region. Both time windows  
3870       being different, the choice was made to normalise the noise/gamma background calculation  
3871       window to it's equivalent beam window in order to have comparable values using the variable  
3872       `windowRatio`. Finally, to estimate the data ratio in the peak region, the variable `DataRatio`  
3873       is defined as the ratio in between the estimated mean cluster multiplicity of the muons in the  
3874       peak region, `MuonCM`, and of the total mean cluster multiplicity in the peak region, `PeakCM`.  
3875       `MuonCM` is itself defined as the difference in between the total mean cluster multiplicity in the  
3876       peak region and the normalised mean noise/gamma cluster multiplicity calculated outside of  
3877       the peak region. The statistical error related to the efficiency, `eff_err`, is computed using a  
3878       binomial distribution, as the efficiency measure the probability of "success" and "failure" to  
3879       detect muons.
- 3880     ● The mean muon cluster size, `MuonCS`, is calculated using the total mean cluster size and multi-  
3881       plicity in the peak region, respectively extracted from histograms `MuonCSize_H` and `MuonCMult_H`,  
3882       the noise/gamma background mean cluster size and normalised multiplicity, extracted from  
3883       `NoiseCSize_H` and `NoiseCMult_H`, and of the estimated muon cluster multiplicity `MuonCM` pre-  
3884       viously explicated. The associated statistical error, `MuonCM_err`, is calculated using the propa-  
3885       gation of errors of the mentioned variables.
- 3886     ● The mean muon cluster multiplicity in the peak region, `MuonCM`, explicated above whose sta-  
3887       tistical error, `MuonCM_err`, is the sum of statistical error associated to the total mean clus-  
3888       ter multiplicity in the peak reagion, `PeakCM_err`, and of the mean noise/gamma cluster size,  
3889       `NoiseCM_err`.

3890       In addition to these 2 CSV files, the histograms are saved in ROOT file `Scan00XXXX_HVY_Offline.root`  
3891       as explained in section B.2.1.1.

3892

```

for (UInt tr = 0; tr < GIFInfra->GetNTrolleys(); tr++) {
    UInt T = GIFInfra->GetTrolleyID(tr);
    for (UInt sl = 0; sl < GIFInfra->GetNSlots(tr); sl++) {
        UInt S = GIFInfra->GetSlotID(tr,sl) - 1;
        for (UInt p = 0; p < GIFInfra->GetNPartitions(tr,sl); p++) {
            float noiseWindow =
                BMTDCWINDOW - TIMEREJECT - 2*PeakWidth.rpc[T][S][p];
            float peakWindow = 2*PeakWidth.rpc[T][S][p];
            float windowRatio = peakWindow/noiseWindow;

            float PeakCM = MuonCMult_H.rpc[T][S][p]->GetMean();
            float PeakCS = MuonCSize_H.rpc[T][S][p]->GetMean();
            float NoiseCM = NoiseCMult_H.rpc[T][S][p]->GetMean() *windowRatio;
            float NoiseCS = NoiseCSize_H.rpc[T][S][p]->GetMean();
            float MuonCM = (PeakCM<NoiseCM) ? 0. : PeakCM-NoiseCM;
            float MuonCS = (MuonCM==0 || PeakCM*PeakCS<NoiseCM*NoiseCS)
                ? 0.
                : (PeakCM*PeakCS-NoiseCM*NoiseCS) / MuonCM;
            float PeakCM_err = (MuonCMult_H.rpc[T][S][p]->GetEntries()==0.)
                ? 0.
                : 2*MuonCMult_H.rpc[T][S][p]->GetStdDev() /
                    sqrt(MuonCMult_H.rpc[T][S][p]->GetEntries());
            float PeakCS_err = (MuonCSize_H.rpc[T][S][p]->GetEntries()==0.)
                ? 0.
                : 2*MuonCSize_H.rpc[T][S][p]->GetStdDev() /
                    sqrt(MuonCSize_H.rpc[T][S][p]->GetEntries());
            float NoiseCM_err = (NoiseCMult_H.rpc[T][S][p]->GetEntries()==0.)
                ? 0.
                : windowRatio*2*NoiseCMult_H.rpc[T][S][p]->GetStdDev() /
                    sqrt(NoiseCMult_H.rpc[T][S][p]->GetEntries());
            float NoiseCS_err = (NoiseCSize_H.rpc[T][S][p]->GetEntries()==0.)
                ? 0.
                : 2*NoiseCSize_H.rpc[T][S][p]->GetStdDev() /
                    sqrt(NoiseCSize_H.rpc[T][S][p]->GetEntries());
            float MuonCM_err = (MuonCM==0) ? 0. : PeakCM_err+NoiseCM_err;
            float MuonCS_err = (MuonCS==0 || MuonCM==0) ? 0.
                : (PeakCS*PeakCM_err + PeakCM*PeakCS_err +
                    NoiseCS*NoiseCM_err + NoiseCM*NoiseCS_err +
                    MuonCS*MuonCM_err) / MuonCM;

            float DataRatio = MuonCM/PeakCM;
            float DataRatio_err = (MuonCM==0) ? 0.
                : DataRatio*(MuonCM_err/MuonCM + PeakCM_err/PeakCM);
            float eff = DataRatio*Efficiency0_H.rpc[T][S][p]->GetMean();
            float eff_err = DataRatio*2*Efficiency0_H.rpc[T][S][p]->GetStdDev() /
                sqrt(Efficiency0_H.rpc[T][S][p]->GetEntries()) +
                Efficiency0_H.rpc[T][S][p]->GetMean()*DataRatio_err;

            outputEffCSV << eff << '\t' << eff_err << '\t'
                << MuonCS << '\t' << MuonCS_err << '\t'
                << MuonCM << '\t' << MuonCM_err << '\t';
        }
    }
}

```

3893

*Source Code B.20: Description of efficiency result calculation and writing into the CSV output Offline-L0-EffCl.csv. Are saved into the file for each detector, the efficiency, corrected taking into account the background in the peak window of the time profile, muon cluster size and muon cluster multiplicity, along with their errors, for each partition and as well as a detector average.*

3894

## 3895    B.7 Current data Analysis

3896 Detectors under test at GIF++ are connected both to a CAEN HV power supply and to a CAEN  
3897 ADC that reads the currents inside of the RPC gaps bypassing the supply cable. During data tak-  
3898 ing, the webDCS records into a ROOT file called `Scan00XXXX_HVY_CAEN.root` histograms with the  
3899 monitored parameters of both CAEN devices. Are recorded for each RPC channels (in most cases,  
3900 a channel corresponds to an RPC gap):

- 3901    • the effective voltage,  $HV_{eff}$ , set by the webDCS using the PT correction on the CAEN power  
3902    supply,
- 3903    • the applied voltage,  $HV_{app}$ , monitored by the CAEN power supply, and the statistical error  
3904    related to the variations of this value through time to follow the variation of the environmental  
3905    parameters defined as the RMS of the histogram divided by the square root of the number of  
3906    recorded points,
- 3907    • the monitored current,  $I_{mon}$ , monitored by the CAEN power supply, and the statistical error  
3908    related to the variations of this value through time to follow the variation of the environmental  
3909    parameters defined as the RMS of the histogram divided by the square root of the number of  
3910    recorded points,
- 3911    • the corresponding current density,  $J_{mon}$ , defined as the monitored current per unit area,  
3912     $J_{mon} = I_{mon}/A$ , where  $A$  is the active area of the corresponding gap,
- 3913    • the ADC current,  $I_{ADC}$ , recorded through the CAEN ADC module that monitors the dark  
3914    current in the gap itself. First of all, the resolution of such a module is better than that of  
3915    CAEN power supplies and moreover, the current is not read-out through the HV supply line  
3916    but directly at the chamber level giving the real current inside of the detector. The statistical  
3917    error is defined as the RMS of the histogram distribution divided by the square root of the  
3918    number of recorded points.

3919    Once extracted through a loop over the element of GIF++ infrastructure via the C++ macro  
3920    `GetCurrent()`, these parameters, organised in 9 columns per detector HV supply line, are written in  
3921    the output CSV file `Offline-Current.csv`. The macro can be found in the file `Current.cc`.

## References

3922

- 3923 [1] T. Massam et al. “Experimental observation of antideuteron production”. In: *Il Nuovo Cimento A* 63 (1965), pp. 10–14.
- 3924
- 3925 [2] UA1 Collaboration. “Experimental observation of isolated large transverse energy electrons with associated missing energy at  $s = 540 \text{ GeV}$ ”. In: *Physics Letters B* 122 (1983), pp. 103–116.
- 3926
- 3927
- 3928 [3] UA2 Collaboration. “Observation of single isolated electrons of high transverse momentum in events with missing transverse energy at the CERN pp collider”. In: *Physics Letters B* 122 (1983), pp. 476–485.
- 3929
- 3930
- 3931 [4] UA1 Collaboration. “Experimental observation of lepton pairs of invariant mass around  $95 \text{ GeV}/c^2$  at the CERN SPS collider”. In: *Physics Letters B* 126 (1983), pp. 398–410.
- 3932
- 3933 [5] UA2 Collaboration. “Evidence for  $Z_0 \rightarrow e^+e^-$  at the CERN pp collider”. In: *Physics Letters B* 129 (1983), pp. 130–140.
- 3934
- 3935 [6] ALEPH Collaboration. “Determination of the number of light neutrino species”. In: *Physics Letters B* 231 (1989), pp. 519–529.
- 3936
- 3937 [7] CERN, ed. (1985).
- 3938 [8] CERN, ed. (1986).
- 3939 [9] CERN, ed. (1994).
- 3940 [10] CERN, ed. (1998).
- 3941 [11] CERN, ed. (1999).
- 3942 [12] CERN. Geneva. LHC Experiments Committee. *Letter of Intent for A Large Ion Collider Experiment [ALICE]*, note = CERN-LHCC-93-016. Tech. rep. ALICE Collaboration, 1993.
- 3943
- 3944 [13] CERN. Geneva. LHC Experiments Committee. *ATLAS : technical proposal for a general-purpose pp experiment at the Large Hadron Collider at CERN*, note = CERN-LHCC-94-43. Tech. rep. ATLAS Collaboration, 1994.
- 3945
- 3946
- 3947 [14] CERN. Geneva. LHC Experiments Committee. *CMS : letter of intent by the CMS Collaboration for a general purpose detector at LHC*, note = CERN-LHCC-92-003. Tech. rep. CMS Collaboration, 1992.
- 3948
- 3949
- 3950 [15] CERN. Geneva. LHC Experiments Committee. *LHCb : letter of intent*. Tech. rep. CERN-LHCC-95-5. LHCb Collaboration, 1995.
- 3951
- 3952 [16] L. Evans and P. Bryant. “LHC Machine”. In: *JINST* 3 (2008). S08001.
- 3953 [17] CMS Collaboration ATLAS Collaboration. “Combined Measurement of the Higgs Boson Mass in  $pp$  Collisions at  $\sqrt{s} = 7$  and  $8 \text{ TeV}$  with the ATLAS and CMS Experiments”. In: *Physical Review Letters* 114 (2015). 191803.
- 3954
- 3955
- 3956 [18] LHCb Collaboration. “Observation of  $J/\psi p$  Resonances Consistent with Pentaquark States in  $\Lambda_b^0 \rightarrow J/\psi K^- p$  Decays”. In: *Physical Review Letters* 115 (2015). 072001.
- 3957

- 3958 [19] LHCb Collaboration. “Observation of  $J/\psi\phi$  Structures Consistent with Exotic States from  
3959 Amplitude Analysis of  $B^+ \rightarrow J/\psi\phi K^+$  Decays”. In: *Physical Review Letters* 118 (2017).  
3960 022003.
- 3961 [20] CERN. Geneva. *High-Luminosity Large Hadron Collider (HL-LHC) Technical Design Re-*  
3962 *port V. 0.1*. Tech. rep. CERN-2017-007-M. 2017.
- 3963 [21] CERN. Geneva. LHC Experiments Committee. *The CMS muon project : Technical Design*  
3964 *Report*. Tech. rep. CERN-LHCC-97-032. CMS Collaboration, 1997.
- 3965 [22] CERN. Geneva. LHC Experiments Committee. *CMS, the Compact Muon Solenoid : technical*  
3966 *proposal*. Tech. rep. CERN-2015-005. 2015.
- 3967 [23] CERN. Geneva. LHC Experiments Committee. *The Phase-2 Upgrade of the CMS Muon*  
3968 *Detectors*. Tech. rep. CERN-LHCC-2017-012, CMS-TDR-016. CMS Collaboration, 2017.
- 3969 [24] CERN. Geneva. LHC Experiments Committee. *High-Luminosity Large Hadron Collider*  
3970 *(HL-LHC) Preliminary Design Report*. Tech. rep. CERN-LHCC-94-38. CMS Collaboration,  
3971 1994.
- 3972 [25] CERN. Geneva. LHC Experiments Committee. *The Phase-2 Upgrade of the CMS Level-1*  
3973 *Trigger - Interim Report to the LHCC*. Tech. rep. CERN-LHCC-2017-013, CMS-TDR-017.  
3974 CMS Collaboration, 2017.
- 3975 [26] CERN. Geneva. LHC Experiments Committee. *Technical Proposal for the Phase-II Upgrade*  
3976 *of the CMS Detector*. Tech. rep. CERN-LHCC-2015-010, CMS-TDR-15-02. CMS Collabo-  
3977 ration, 2015.
- 3978 [27] A. Gelmi. *CMS iRPC at HL-LHC: background study*. 2018. URL: [https://indico.cern.ch/event/732794/contributions/3021836/attachments/1657792/2654574/iRPC\\_bkg\\_study\\_Upgrade29\\_05\\_18.pdf](https://indico.cern.ch/event/732794/contributions/3021836/attachments/1657792/2654574/iRPC_bkg_study_Upgrade29_05_18.pdf).
- 3981 [28] F.Sauli. “GEM: A new concept for electron amplification in gas detectors”. In: *Nucl. Instr.*  
3982 *Meth. Phys. Res.* 386 (1997), pp. 531–534.
- 3983 [29] CERN. Geneva. LHC Experiments Committee. *CMS Technical Design Report for the Muon*  
3984 *Endcap GEM Upgrade*. Tech. rep. CERN-LHCC-2015-012, CMS-TDR-013. CMS Collabo-  
3985 ration, 2015.
- 3986 [30] The CMS collaboration. “The performance of the CMS muon detector in proton-proton col-  
3987 lisions at  $\sqrt{s} = 7$  TeV at the LHC”. In: *JINST* 8 (2013). P11002.
- 3988 [31] P.Bortignon. “Design and performance of the upgrade of the CMS L1 muon trigger”. In:  
3989 *Nucl. Instr. Meth. Phys. Res.* 824 (2016), pp. 256–257.
- 3990 [32] The European Parliament and the Council of the European Union. “Regulation (EU) No  
3991 517/2014 of 16 April 2014 on fluorinated greenhouse gases and repealing Regulation (EC)  
3992 No 842/2006”. In: *Official Journal of the European Union* 150 (2014), pp. 195–230.
- 3993 [33] R. Santonico and R. Cardarelli. “Development of resistive plate counters”. In: *Nucl. Instr.*  
3994 *Meth. Phys. Res.* 187 (1981), pp. 377–380.
- 3995 [34] Yu.N. Pestov and G.V. Fedotovich. *A picosecond time-of-flight spectrometer for the VEPP-2M*  
3996 *based on local-discharge spark counter*. Tech. rep. SLAC-TRANS-0184. SLAC, 1978.
- 3997 [35] W.W. Ash, ed. *Spark Counter With A Localized Discharge*. Vol. SLAC-R-250. 1982, pp. 127–  
3998 131.
- 3999 [36] I. Crotty et al. “The non-spark mode and high rate operation of resistive parallel plate cham-  
4000 bers”. In: *NIMA* 337 (1993), pp. 370–381.

---

## BIBLIOGRAPHY

---

- [37] I. Crotty et al. "Further studies of avalanche mode operation of resistive parallel plate chambers". In: *NIMA* 346 (1994), pp. 107–113.
- [38] R. Cardarelli et al. "Avalanche and streamer mode operation of resistive plate chambers". In: *NIMA* 382 (1996), pp. 470–474.
- [39] R. Cardarelli et al. "Performance of a resistive plate chamber operating with pure  $CF_3Br$ ". In: *NIMA* 333 (1993), pp. 399–403.
- [40] M. Abbrescia et al. "Performance of a Resistive Plate Chamber operated in avalanche mode under  $^{137}Cs$  irradiation". In: *NIMA* 392 (1997), pp. 155–160.
- [41] M. Abbrescia et al. "Properties of C2H2F4-based gas mixture for avalanche mode operation of resistive plate chambers". In: *NIMA* 398 (1997), pp. 173–179.
- [42] P. Camarri et al. "Streamer suppression with SF6 in RPCs operated in avalanche mode". In: *NIMA* 414 (1998), pp. 317–324.
- [43] E. Cerron Zeballos et al. "Effect of adding SF6 to the gas mixture in a multigap resistive plate chamber". In: *NIMA* 419 (1998), pp. 475–478.
- [44] E. Cerron Zeballos et al. "A new type of resistive plate chamber: The multigap RPC". In: *NIMA* 374 (1996), pp. 132–135.
- [45] M.C.S. Williams. "The development of the multigap resistive plate chamber". In: *Nucl. Phys. B* 61 (1998), pp. 250–257.
- [46] H. Czyrkowski et al. "New developments on resistive plate chambers for high rate operation". In: *NIMA* 419 (1998), pp. 490–496.
- [47] CERN. Geneva. LHC Experiments Committee. *ATLAS muon spectrometer: Technical design report*. Tech. rep. CERN-LHCC-97-22. ATLAS Collaboration, 1997.
- [48] CERN. Geneva. LHC Experiments Committee. *ALICE Time-Of-Flight system (TOF) : Technical Design Report*. Tech. rep. CERN-LHCC-2000-012. ALICE Collaboration, 2000.
- [49] The CALICE collaboration. "First results of the CALICE SDHCAL technological prototype". In: *JINST* 11 (2016).
- [50] PoS, ed. *Density Imaging of Volcanoes with Atmospheric Muons using GRPCs*. International Europhysics Conference on High Energy Physics - HEP 2011. 2011.
- [51] C. Lippmann. "Detector Physics of Resistive Plate Chambers". PhD thesis. Johann Wolfgang Goethe-Universität, 2003.
- [52] W. Riegler. "Induced signals in resistive plate chambers". In: *NIMA* 491 (2002), pp. 258–271.
- [53] M. Abbrescia et al. "Effect of the linseed oil surface treatment on the performance of resistive plate chambers". In: *NIMA* 394 (1997), pp. 13–20.
- [54] G. Battistoni et al. "Sensitivity of streamer mode to single ionization electrons". In: *NIMA* 235 (1985), pp. 91–97.
- [55] M. Abbrescia et al. "Cosmic ray tests of double-gap resistive plate chambers for the CMS experiment". In: *NIMA* 550 (2005), pp. 116–126.
- [56] JINST, ed. *Performance of the Resistive Plate Chambers in the CMS experiment*. The 9<sup>th</sup> International Conference on Positioin Sensitive Detectors. 2012.
- [57] PoS, ed. *The CMS RPC detector performance during Run-II data taking*. The European Physical Society Conference on High Energy Physics (EPS-HEP2017). 2018.
- [58] Honeywell International Inc. *Solstice(R) ze Refrigerant (HFO-1234ze): The Environmental Alternative to Traditional Refrigerants*. Tech. rep. FPR-003/2015-01. 2015.

- 4044 [59] E. Cerron Zeballos et al. “A comparison of the wide gap and narrow gap resistive plate  
4045 chamber”. In: *NIMA* 373 (1996), pp. 35–42.
- 4046 [60] ALICE Collaboration. “A study of the multigap RPC at the gamma irradiation facility at  
4047 CERN”. In: *NIMA* 490 (2002), pp. 58–70.
- 4048 [61] B. Bonner et al. “A multigap resistive plate chamber prototype for time-of-flight for the STAR  
4049 experiment at RHIC”. In: *NIMA* 478 (2002), pp. 176–179.
- 4050 [62] S. Yang et al. “Test of high time resolution MRPC with different readout modes for the  
4051 BESIII upgrade”. In: *NIMA* 763 (2014), pp. 190–196.
- 4052 [63] A. Akindinovg et al. “RPC with low-resistive phosphate glass electrodes as a candidate for  
4053 the CBM TOF”. In: *NIMA* 572 (2007), pp. 676–681.
- 4054 [64] JINST, ed. *Development of the MRPC for the TOF system of the MultiPurpose Detector*.  
4055 RPC2016: XII Workshop on Resistive Plate Chambers and Related Detectors. 2016.
- 4056 [65] M.C.S. Williams. “Particle identification using time of flight”. In: *Journal of Physics G* 39  
4057 (2012).
- 4058 [66] A. Alici et al. “Aging and rate effects of the Multigap RPC studied at the Gamma Irradiation  
4059 Facility at CERN”. In: *NIMA* 579 (2007), pp. 979–988.
- 4060 [67] M. Abbrescia et al. “The simulation of resistive plate chambers in avalanche mode: charge  
4061 spectra and efficiency”. In: *NIMA* 431 (1999), pp. 413–427.
- 4062 [68] C. Patrignani et al. (Particle Data Group). “Review of Particle Physics”. In: *Chin. Phys. C*  
4063 C40 (2016), p. 100001.
- 4064 [69] JINST, ed. *Description and simulation of physics of Resistive Plate Chambers*. RPC2016:  
4065 XII Workshop on Resistive Plate Chambers and Related Detectors. 2016.
- 4066 [70] V. Français. “Description and simulation of the physics of Resistive Plate Chambers”. PhD  
4067 thesis. LPC - Laboratoire de Physique Corpusculaire - Clermont-Ferrand, 2017.
- 4068 [71] H. Bethe. “Zur Theorie des Durchgangs schneller Korpuskularstrahlen durch Materie”. In:  
4069 *Annalen der Physik* 397 (1930), pp. 325–400.
- 4070 [72] International Commission on Radiation Units and Measurements. *Stopping Powers for Elec-*  
4071 *trons and Positions*. Tech. rep. Report 37. 1984.
- 4072 [73] International Commission on Radiation Units and Measurements. *Stopping Power and Ranges*  
4073 *for Protons and Alpha Particles*. Tech. rep. Report 49. 1994.
- 4074 [74] H. Bichsel. “A method to improve tracking and particle identification in TPCs and silicon  
4075 detectors”. In: *NIMA* 562 (2006), pp. 154–197.
- 4076 [75] W. W. M. Allison and J. H. Cobb. “Relativistic charged particle identification by energy loss”.  
4077 In: *Annual Review of Nuclear and Particle Science* 30 (1980), 253–298.
- 4078 [76] International Commission on Radiation Units and Measurements. *Average energy to produce*  
4079 *an ion pair*. Tech. rep. Report 31. 1994.
- 4080 [77] I.B. Smirnov. “Modeling of ionization produced by fast charged particles in gases”. In: *NIMA*  
4081 554 (2005), pp. 474–493.
- 4082 [78] <https://doi.org/10.1088/1742-6596/587/1/012035>.
- 4083 [79] W. Riegler et al. “Detector physics and simulation of resistive plate chambers”. In: *NIMA* 500  
4084 (2003), pp. 144–162.
- 4085 [80] I.B. Smirnov. *HEED++ simulation program*. 2010. URL: \href{http://ismirnov.  
4086 web . cern . ch / ismirnov / heed } {http : / / ismirnov . web . cern . ch /  
4087 ismirnov/heed}.

## BIBLIOGRAPHY

---

- 4088 [81] S.F. Biagi. “Monte Carlo simulation of electron drift and diffusion in counting gases under  
4089 the influence of electric and magnetic fields”. In: *NIMA* 421 (1999), pp. 234–240.
- 4090 [82] W. H. Furry. “On Fluctuation Phenomena in the Passage of High Energy Electrons through  
4091 Lead”. In: *Phys. Rev.* 52 (1937), pp. 569–581.
- 4092 [83] H. Genz. “Single electron detection in proportional gas counters”. In: *Nucl. Instr. and Meth.*  
4093 112 (1973), pp. 83–90.
- 4094 [84] M. Abbrescia et al. “Study of long-term performance of CMS RPC under irradiation at the  
4095 CERN GIF”. In: *NIMA* 533 (2004), pp. 102–106.
- 4096 [85] H.C. Kim et al. “Quantitative aging study with intense irradiation tests for the CMS forward  
4097 RPCs”. In: *NIMA* 602 (2009), pp. 771–774.
- 4098 [86] S. Agosteo et al. “A facility for the test of large-area muon chambers at high rates”. In: *NIMA*  
4099 452 (2000), pp. 94–104.
- 4100 [87] PoS, ed. *CERN GIF ++ : A new irradiation facility to test large-area particle detectors for*  
4101 *the high-luminosity LHC program*. Vol. TIPP2014. 2014, pp. 102–109.
- 4102 [88] A. Fagot. *GIF++ DAQ v4.0*. 2017. URL: [https://github.com/afagot/GIF\\_DAQ](https://github.com/afagot/GIF_DAQ).
- 4103 [89] CAEN. *Mod. V1190-VX1190 A/B, 128/64 Ch Multihit TDC*. 14th ed. 2016.
- 4104 [90] CAEN. *Mod. V1718 VME USB Bridge*. 9th ed. 2009.
- 4105 [91] W-Ie-Ne-R. *VME 6021-23 VXI*. 5th ed. 2016.
- 4106 [92] Wikipedia. *INI file*. 2017. URL: [https://en.wikipedia.org/wiki/INI\\_file](https://en.wikipedia.org/wiki/INI_file).
- 4107 [93] S. Carrillo A. Fagot. *GIF++ Offline Analysis v6*. 2017. URL: [https://github.com/afagot/GIF\\_OfflineAnalysis](https://github.com/afagot/GIF_OfflineAnalysis).
- 4108